Micromechanics, Macromechanics and Constitutive Modeling of the Elasto-Viscoplastic Deformation of Rubber-Toughened Glassy Polymers

by

Mats Danielsson

Submitted to the Department of Mechanical Engineering
in partial fulfillment of the requirements for the degree of

Doctor of Philosphy in Mechanical Engineering

at the

MASSACHUSETTS INSTITUTE OF TECHNOLOGY

June 2003

Author .....
Department of Mechanical Engineering
May 15, 2003

Certified by .....
Mary C. Boyce
Professor
Thesis Supervisor

Certified by .....
David M. Parks
Professor
Thesis Supervisor

Accepted by .....
Ain A. Sonin
Chairman, Department Committee on Graduate Students

Micromechanics, Macromechanics and Constitutive Modeling of the Elasto-Viscoplastic Deformation of Rubber-Toughened Glassy Polymers

by

Mats Danielsson

Submitted to the Department of Mechanical Engineering
on May 15, 2003, in partial fulfillment of the
requirements for the degree of
Doctor of Philosphy in Mechanical Engineering

Abstract

Glassy polymers, such as polystyrene (PS), poly(methyl methacrylate) (PMMA) and polycarbonate (PC), are common engineering polymers that have found uses in consumer products ranging from portable computers and optical lenses, to automotive components and appliance housings. PMMA and PS are typically considered to be brittle polymers, since they fail in a brittle manner under low triaxiality conditions, such as under uniaxial tension. Polycarbonate is considered to be a more ductile polymer than PMMA and PS, since it will deform plastically under uniaxial tension. However, PC does exhibit brittle behavior under certain loading conditions, such as low temperatures, high strain rates, or highly (tensile) triaxial stress states. A technique used for reducing the brittleness (increasing the fracture toughness) of glassy polymers is *rubber-toughening*. The technology of rubber-toughening, which involves blending a small volume fraction (5-20%) of rubber particles with the homopolymer, has been used commercially since the 1940s, and has been of major importance to the plastics industry. The technology of rubber-toughening is qualitatively well understood, but quantitative tools to study the material response are still at an early stage of development.

The purpose of this thesis is to develop numerical tools to investigate the mechanical behavior of rubber-toughened glassy polymers, with emphasis on rubber-toughened PC. To this end, several tools are developed. Three-dimensional micromechanical models of the hetereogeneous microstructure are developed to study the effects of particle volume fraction on the underlying elastic visco-plastic deformation mechanisms in the material, and how these mechanisms influence the macroscopic [continuum-level] response of the material. A continuum-level constitutive model is developed for the homogenized large-strain elastic-viscoplastic behavior of the material. The model is calibrated against micromechanical modeling results for rubber-toughened polycarbonate. The constitutive model is used to study boundary value problems such as notched tensile bars, where a multi-scale modeling approach en-

ables assessment of failure due to local stress and strain levels in the material. The results are compared to experimental studies to establish correlations between the continuum-level response of the material, and observed failure mechanisms in the material.

Thesis Supervisor: Mary C. Boyce
Title: Professor

Thesis Supervisor: David M. Parks
Title: Professor

A fool is a man who never tried an experiment in his life.

– Erasmus Darwin (1731-1802)

If you are going through hell, keep going.

– Sir Winston Churchill (1874-1965)

Contents

List of Figures

List of Tables

Chapter 1

Introduction

Glassy polymers, such as polystyrene (PS), poly(methyl methacrylate) (PMMA) and polycarbonate (PC), are common engineering materials that have found uses in consumer products ranging from portable computers and optical lenses, to automotive components and appliance housings. PMMA and PS are typically considered to be brittle polymers, since they fail in a brittle manner under low triaxiality conditions, such as under uniaxial tension. Polycarbonate is considered to be a more ductile polymer than PMMA and PS, since it will deform plastically under uniaxial tension at ambient temperatures and low strain-rates. However, PC exhibits brittle behavior under certain loading conditions, such as low temperatures and / or high strain-rates, as shown schematically by the Davidenkov construction in Fig. (1-1a,b). Brittle fracture is thought to initiate when a fracture stress is reached before ductile plastic flow occurs in the material. In addition to temperature and strain rate effects, highly triaxial (tensile) stress states, resulting from sharp geometry changes, such as notches and cracks, have been shown to promote brittle behavior of PC (see, for example, Hyakutake and Nisitani [37], Nimmer and Woods [51], and Tsuji, et al. [69]). In summary, at low temperatures, high strain rates, or highly triaxial stress states, PC shares the unfavorable failure characteristics displayed by "brittle" glassy polymers such as PS and PMMA. The increasing use of glassy polymers in areas traditionally dominated by metals, for example in the automotive industry, has motivated the development of new engineering polymers with improved mechanical properties, and, in

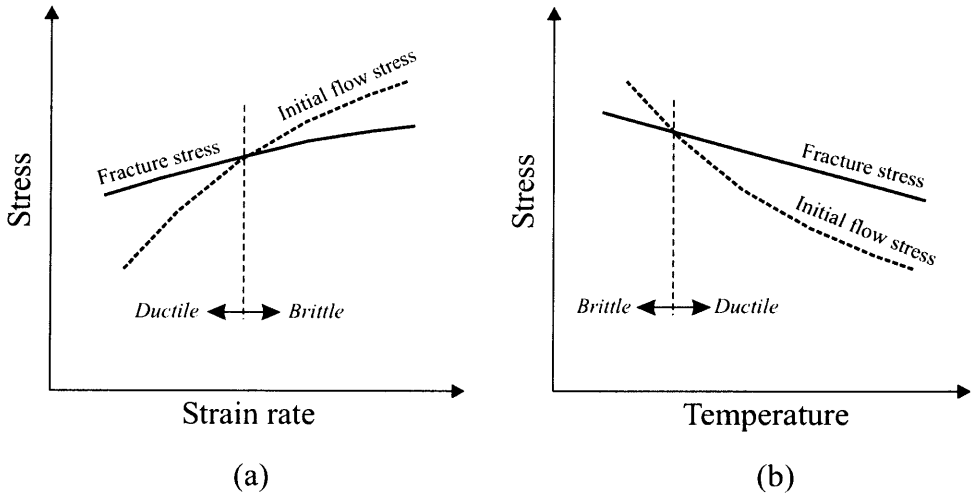

Figure 1-1: The Davidenkov construction illustrating the ductile-to-brittle transition in a glassy polymer: (a) effects of strain rate, (b) effects of temperature.

particular, an increased fracture toughness.

A technique often used to increase the fracture toughness of glassy polymers is *rubber-toughening*. The technology of rubber-toughening (Fig. 1-5a) involves blending a small volume fraction (5-20%) of [easily-cavitating] rubber particles with the homopolymer. Rubber-toughening has been used commercially since the 1940s, and has been of major importance to the plastics industry. In fact, rubber-toughening has proved so effective in improving toughness, that the technology has been applied to almost all commercial glassy polymers. Rubber particles of different morphologies can be used to toughen glassy polymers. At their simplest, the particles are homogeneous rubber spheres; however, in most toughened plastics, the morphology is more complex. Figure (1-2) shows the most commonly used particle morphologies. Figs. (1-2a-c) show different morphologies involving alternating concentric shells of rubber and glassy polymer. These "layered" particles are often used to toughen PMMA (Lovell, et al. [45]), and are also effective in toughening PC and poly(vinyl chloride) (PVC) (Lutz and Grossman [46]). Figure (1-2d) shows a "salami"-type particle morphology, often found in high-impact polystyrene (HIPS) (Bucknall [14]). These particles consist of PS subinclusions in a polybutadiene phase.

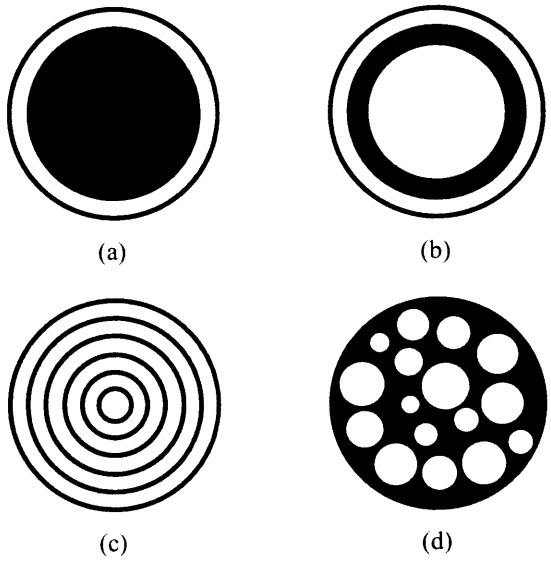

Figure 1-2: Rubber particle morphologies: (a) soft-core/hard-shell, (b) hard-core/soft-shell/hard-shell, (c) "onion" morphology, (d) "salami" structure.

From an engineering standpoint, toughness can be defined as the ability of a material to absorb and dissipate energy prior to final fracture. There are two major mechanisms by which energy is dissipated in rubber-toughened glassy polymers. Depending on the properties of the glassy polymer matrix, these mechanisms are either massive crazing or massive distortional plasticity[1]. High-impact polystyrene displays massive crazing; the rubber particles act to provide a profusion of craze initiation sites (Bucknall and Smith [16]). Figure (1-3a) shows a section of deformed HIPS with fibrillation in the rubber phase of the "salami" particles, and crazing in the polystyrene matrix (Bucknall [15]). Rubber-toughened polycarbonate, on the other hand, displays massive shear banding, as polycarbonate usually deforms through ductile shearing. Cavitation of the rubber particles is thought to relieve hydrostatic stresses, and the [cavitating] particles provide a profusion of stress concentrations throughout the polycarbonate matrix, which promotes ductile plastic shearing of inter-particle ligaments (see, for example, Yee [77]). This distributed shearing of the polycarbonate matrix is illustrated in Fig. (1-3b) where a [two-dimensional] porous polycarbonate film has

[1]Distortional plastic flow of glassy polymers is often referred to as *shear yielding* in the literature.

been stretched horizontally to 10% strain (van der Sanden [72]). Regardless of the specific deformation mechanism, the objectives of rubber-toughening in glassy polymers are to maximize the material volume that takes part in the deformation process, and to maximize the deformation at each contributing material point, thereby maximizing the total energy dissipation before final fracture.

The focus of this thesis is the mechanical behavior / performance of rubber-toughened polycarbonate. As discussed previously, homogeneous polycarbonate is generally considered to be a "tough" polymer, which will usually deform plastically through ductile shearing, and ultimately fracture subsequent to significant plastic straining. While polycarbonate is, in this sense, ductile in nature, the introduction of a modestly sharp notch has been shown to trigger brittle behavior due to the high hydrostatic (tensile) stresses near the notch tip. Polycarbonate also undergoes a ductile-to-brittle transition at high strain rates and / or low temperatures (Fig.1-1). Thus, rubber particles are introduced to decrease the "notch sensitivity" of the material, and to shift the ductile-to-brittle transition to higher strain-rates and lower temperatures. The conditions [stress triaxiality, strain-rate, temperature] for the ductile-to-brittle transition in rubber-toughened polycarbonate depend on the volume fraction of the rubber phase and the dispersion of the rubber particles in the polycarbonate matrix. Cheng, et al. [18] found that polycarbonate modified with linear polybutadiene resulted in a wide range of rubber particle sizes, and such a distribution did not enhance toughness of the blend, compared to the homopolymer. Core-shell rubber particles (Fig. 1-2a) allow for good dispersion in the matrix, and Kim [40] found that these particles are effective in enhancing toughness of polycarbonate. In summary, the major factors that influence the ductile-to-brittle transition in rubber-toughened polycarbonate are

- temperature,
- rate of deformation,
- level of stress triaxiality and magnitude of stress,
- volume fraction of rubber particles,

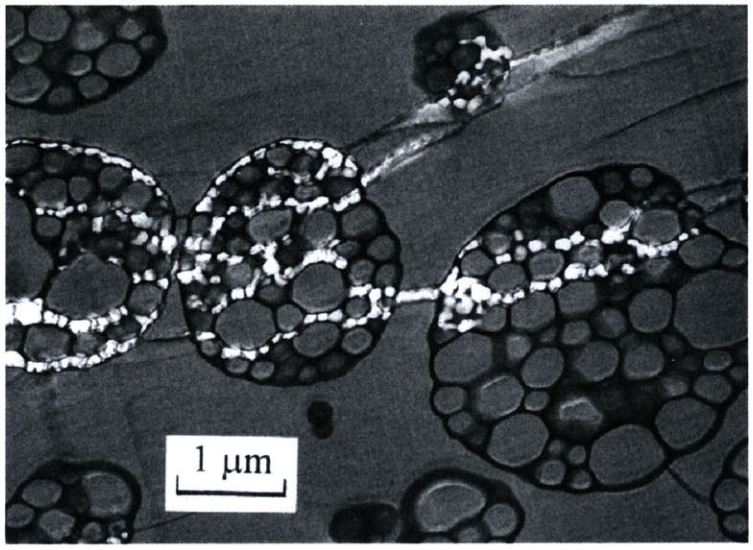

(a)

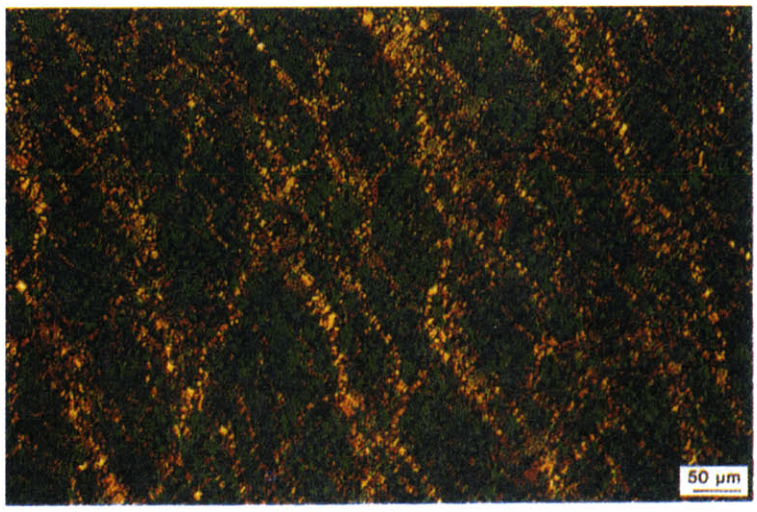

(b)

Figure 1-3: Deformation mechanisms: (a) Crazing between rubber particles in HIPS (Bucknall [15]), and (b) distributed shearing of the matrix in a porous polycarbonate film (van der Sanden [72]).

- dispersion of the rubber particles in the polycarbonate matrix.

While these factors are generally recognized as playing a role in the ductile-to-brittle transition of rubber-toughened polycarbonate, quantitative models to predict this transition are lacking; there are no ductile or brittle fracture criteria available in the literature[2]. If brittle fracture can be averted through an improvement of the local loading conditions of the polycarbonate matrix, the rubber-toughened polymer is able to undergo large plastic strains before final [ductile] fracture.

While substantial progress has been made in the development of constitutive models for *homogeneous* glassy polymers, there are no quantitative constitutive models for the large-strain deformation of *rubber-toughened* glassy polymers. The large-strain deformation of homogeneous glassy polymers has been successfully modeled by Boyce, Parks and Argon [12], and by Arruda and Boyce [7] (see Chapter 2 for a review). The addition of rubber particles to a glassy polymer significantly alters the mechanical response of the arising material. The large-strain deformation of rubber-toughened polycarbonate has been studied experimentally by, for example, Cheng, et al. [18], Kim, et al. [40] and Johnson [38]. Figure (1-4) shows experimentally-obtained uniaxial compression data for different rubber-toughened polycarbonate blends at room temperature and constant axial strain-rate ($\dot{E}_{axial} = -0.01s^{-1}$) (Johnson [38]). The curves in Fig. (1-4) show that, when compared to the homopolymer, the introduction of rubber particles to glassy polycarbonate

- decreases the elastic stiffness,
- lowers the yield stress,
- decreases the amount and rate of post-yield softening,
- decreases the strain-hardening slope.

As mentioned previously, constitutive models that account for these observed differences in constitutive response are lacking. Attempts have been made to model some

[2]The notion of "brittle fracture" is appropriate when the material fails early during deformation, with insignificant accompanying plastic straining and dissipation, whereas "ductile fracture" refers to failure subsequent to significant plastic straining and dissipation.

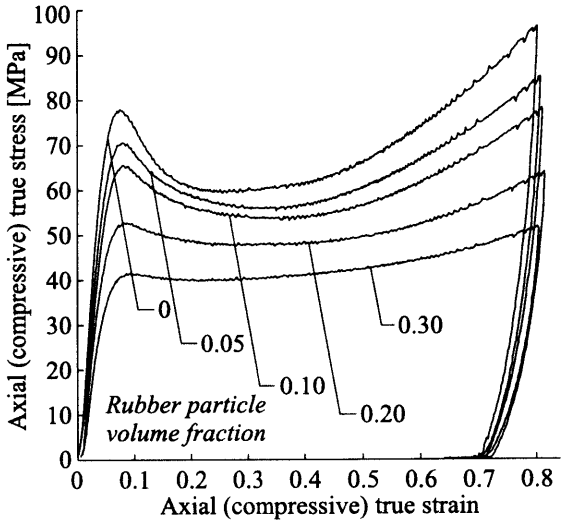

Figure 1-4: Stress-strain response under uniaxial compression ($\dot{E}_{axial} = -0.01s^{-1}$) for polycarbonate at room temperature and different rubber-particle volume fractions (Johnson [38]).

of the main features of deformation of rubber-toughened glassy polymers, including elastic properties and initial "yield surfaces" (see, for example, Steenbrink, et al. [65] and Pijnenburg and van der Giessen [56])[3]. These studies have modeled the rubber particles as voids, as the particles are assumed to have cavitated early during deformation. An inherent limitation of these models is that they were developed through modifications of porous plasticity models for dilute volume fractions of voids in a rate-independent, non-hardening matrix. Many issues were not addressed, such as the existence of a deformation-induced back-stress, the anisotropic growth of the rubber particles (or voids), etc.

The purpose of this thesis is to develop numerical tools to investigate the mechanical behavior of rubber-toughened glassy polymer blends, with emphasis on rubber-toughened polycarbonate (Fig. 1-5). Three-dimensional micromechanical models of the hetereogeneous microstructure are developed to study the effects of filler volume fraction on the underlying elasto-viscoplastic deformation mechanisms in the blend,

[3]The notion of *yield surface* for a viscoplastic material is formally incorrect, as it pertains to rate-independent plasticity. Nevertheless, at a given norm of [deviatoric + hydrostatic] strain-rate, it can be instructive to describe the onset of plastic flow by such a surface.

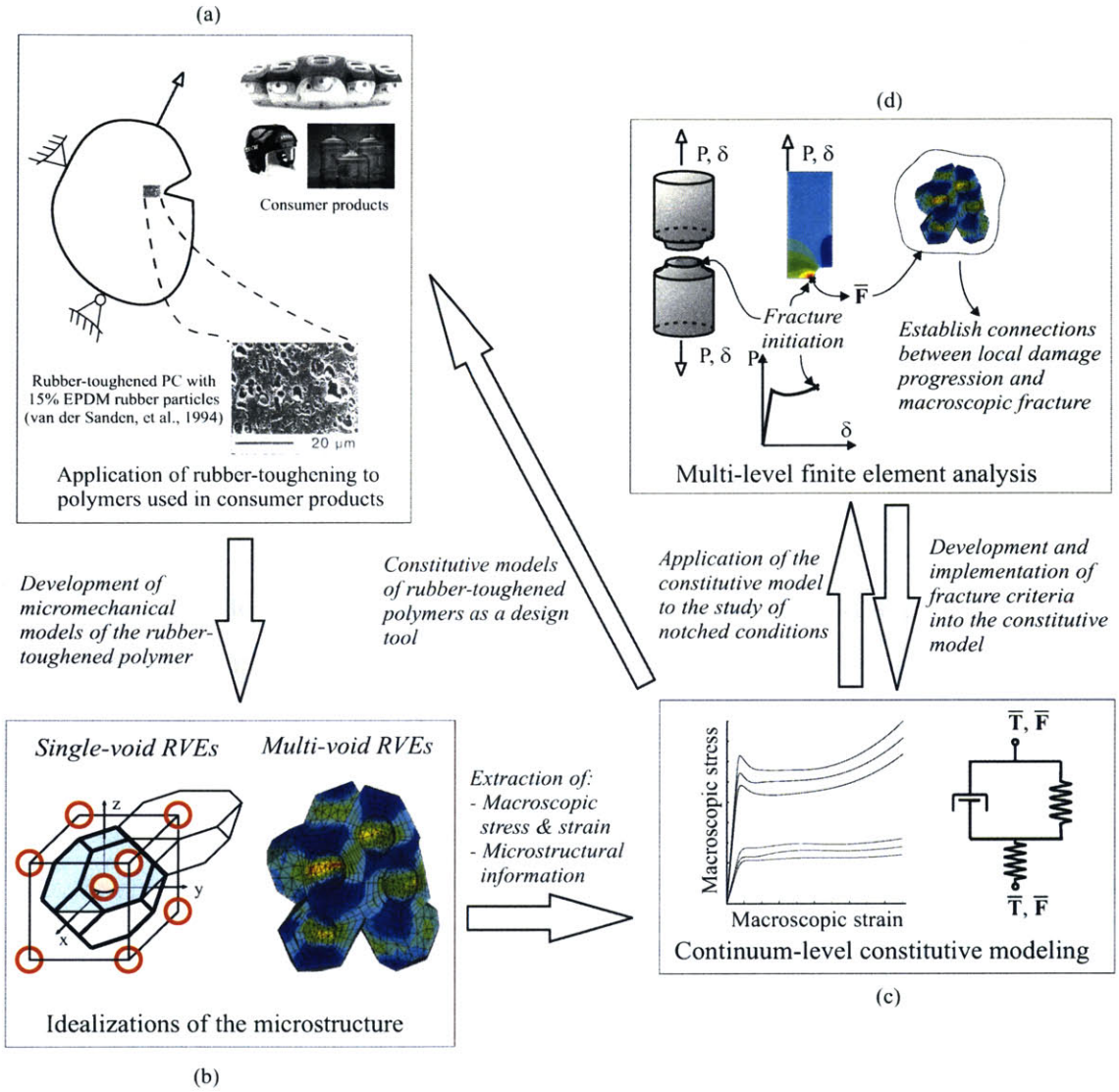

Figure 1-5: Investigation of the mechanical behavior of rubber-toughened glassy polymers: (a) improvement of consumer product performance through rubber-toughening, (b) idealizations of the microstructure, (c) continuum-level constitutive modeling, (d) multi-level finite element modeling to establish fracture criteria for rubber-toughened glassy polymers.

and how these mechanisms influence the macroscopic [continuum-level] response of the blend (Fig.1-5b). A continuum-level constitutive model is developed for the homogenized large-strain elastic-viscoplastic behavior of the blend (Fig.1-5c). The model is calibrated to micromechanical modeling results for rubber-toughened polycarbonate. The constitutive model is used to study boundary value problems such as notched tensile bars, where a multi-scale modeling approach enables assessment of failure due to local stress and strain levels in the blend. The results are compared to experimental studies to establish correlations between the continuum-level response of the blend, and observed failure mechanisms in the blend (Fig.1-5d). The availability of a multi-scale continuum-level constitutive modeling framework for rubber-toughened glassy polymers is important from an engineering standpoint. It can be utilized in the development of consumer products, thereby reducing the costs for mechanical testing and evaluation (Fig.1-5a).

The outline of the thesis is as follows: In Chapter 2, a constitutive model for the rate and temperature dependent deformation of glassy polymers is reviewed within a large-strain continuum-mechanics framework. The constitutive model has been implemented into the commercial finite element program ABAQUS [1]. The implementation of the model allows the analysis of boundary value problems, and, in particular, it provides the basis for modeling the porous polycarbonate microstructures in Chapter 3.

In Chapter 3 are developed several micromechanical models of the rubber-toughened polycarbonate (Fig. 1-5b). In these models, the rubber particles are replaced by voids, as the rubbery phase is assumed to cavitate at an early stage during deformation. The polycarbonate matrix behavior is modeled using the constitutive framework outlined in Chapter 2. The micromechanical models differ in their assumptions on the void arrangement, and in the number of voids considered. First, a model is presented in which the voids are assumed to be spherical and arranged on a BCC lattice, thereby enabling the use of a single void volume element. Two models are then introduced in which several voids, randomly placed on a cubic lattice, are considered. The two models differ in their respective idealizations of the void shapes; the voids are taken

as spherical or cubical. The last model considers spherical voids, randomly dispersed in the glassy polymer matrix; no underlying lattice structure confines the voids to certain locations. The developed models are used to study the micromechanics and macromechanics of rubber-toughened (here porous) glassy polycarbonate, and the relative merits and drawbacks of each model are discussed.

In Chapter 4, the results from Chapter 3 are used to elucidate the differences in mechanical response of porous polycarbonate, compared to the mechanical response of the homogeneous material for a range of moderate, yet industrially relevant, porosity levels: $f_0 = \{0.05, 0.10, 0.15\}$ (Fig. 1-5c). Equipped with the insight from Chapter 3, the merits and limitations of existing constitutive porous plasticity models in the literature are discussed. A constitutive model for the mechanical behavior of porous polycarbonate is then formulated within a large-strain continuum mechanics framework. The model is designed to capture the essential features of deformation of porous polycarbonate, observed in the micromechanical modeling of Chapter 3. We implement the developed constitutive model into the commercial finite element program ABAQUS [1]. The implementation of the constitutive model into a finite element program enables the study of boundary value problems, in which each material point represents the homogenized mechanical response of the porous material.

In Chapter 5, the developed constitutive model for porous polycarbonate is used to study the deformation and fracture processes in rubber-toughened tensile bars. The constitutive model enables studies of the macroscopic mechanical behavior of the bars, and it also enables studies of [homogenized] stress and strain fields in the bars. Various notched and un-notched tensile bars are simulated, and the results are compared to experimental observations. These comparative studies, when made over a wide range of temperatures, strain-rates and strain histories, can provide a basis for establishing brittle and ductile fracture criteria for rubber-toughened polycarbonate. A thorough experimental study is required to provide the data necessary to *quantitatively* establish fracture criteria, and at present, such a study is not available. In light of this, we are limited to a *qualitative* assessment of the mechanisms involved in the fracture process. To aid in gaining an understanding of the fracture process, a multi-

scale finite element modeling technique is employed in which the micromechanical models of the porous microstructure of Chapter 3 are revisited. The micromechanical models are used to study local stress and strain fields at [matrix] material points in a notched bar where fracture was observed to initiate. This modeling scheme enables the study of progression of local deformation and fracture in the polycarbonate matrix prior to macroscopically-observed fracture.

In Chapter 6, we summarize the work carried out in the thesis, and provide directions for future work. We discuss possible routes toward developing fracture criteria for rubber-toughened polycarbonate by means of the numerical tools devloped in this thesis. We also suggest modifications necessary to apply the developed tools to the study of other classes of materials, such as particle-toughened semi-crystalline polymers and polycrystalline metals.

Chapter 2

Constitutive Behavior of Homogeneous Glassy Polymers

The mechanical response of glassy polymers beyond the elastic regime can be broadly categorized into two modes: A glassy polymer can deform in a ductile manner through large-strain plastic shearing, or it can undergo brittle fracture through crazing, a dilatational process. For example, at ambient temperatures and low strain rates, polycarbonate is ductile under uniaxial tension, as it deforms plastically through shearing; the material is able to undergo large plastic strains without failing in a brittle manner. The brittle mode of crazing is encountered in glassy polymers such as polystyrene under uniaxial tension, and in polycarbonate under states of high hydrostatic stress, such as at crack tips. The topic of crazing will not be discussed in this chapter, but it is noted that the process of crazing is itself the product of large plastic strains which are localized within very small volumes of material. The large-strain mechanical behavior of glassy polymers has been studied over the past few decades, and several continuum-level constitutive models of increasing complexity have been developed for this class of materials. The purpose of this chapter is to give a brief review of these developments in order to provide a basis for the finite element simulations of Chapter 3 and the continuum-level constitutive modeling of *porous* glassy polymers in Chapter 4.

Haward and Thackray [33] proposed a one-dimensional spring-dashpot model to

characterize the major features of deformation of glassy polymers. The model consists of three constitutive elements (Fig. 2-2): A linear elastic spring (A) acts in series with a parallel arrangement of a dashpot (B) and a non-linear spring (C). The linear elastic spring is used to characterize the initial response of the glassy polymer as elastic (Hookean). The dashpot is used to model the viscous part (an intermolecular resistance) of the material behavior, and the non-linear spring is used to model the orientation-induced strain-hardening upon continued plastic straining. For the viscous part, a number of flow models have been proposed, which are appropriate for a solid polymer, and Haward and Thackray used the Eyring viscosity equation [26]. The non-linear spring was assumed to follow the laws of rubber elasticity, as presented by Treloar [68]. A model based on non-Gaussian statistics was selected, as it provided a limit to chain extensibility in accordance with experimental observations. Argon [4] pointed out that the use of rubber elasticity for the non-linear spring in the model by Haward and Thackray was a particular way of representing entropy changes in the molecular network.

Parks et al. [54] extended the one-dimensional spring-dashpot framework by Haward and Thackray to three dimensions. In their model, the intermolecular resistance was taken to be constant, leading to rate-independent plastic flow. The entropic resistance (strain-hardening) was modeled, as suggested by Haward and Thackray, using non-Gaussian rubber elasticity. The network response was represented using the three-chain model proposed by Wang and Guth [75]. This description of the entropic resistance results in a back-stress tensor having a one-to-one correspondence to the plastic distortion which reflects the molecular texture developed in the polymer.

Boyce et al. [12] extended the three-dimensional model by Parks, et al. to include the effects of deformation rate, pressure, strain-softening and temperature on the plastic resistance. In their model, the intermolecular resistance of the material was represented using the rate- and temperature-dependent model by Argon [4], modified to account for strain-softening and effects of pressure on plastic flow.

Arruda and Boyce [7] studied the strain-hardening characteristics of two glassy polymers, polycarbonate (PC) and poly(methyl methacrylate) (PMMA). They showed

that the network description used by Parks, et al., and Boyce, et al., does not predict correctly the state of deformation dependence observed in these polymers. Arruda and Boyce proposed a new statistical mechanics-based constitutive model for rubber elasticity using an eight-chain network model. This model has been shown to correctly account for the deformation dependence of several rubber materials [8]. Arruda and Boyce modified the glassy polymer model of Boyce, et al., by using the eight-chain rubber elasticity model, instead of the previously-used three-chain model, to model the strain-hardening response of the glassy polymer. Comparisons to experimental data for PC and PMMA showed that the eight-chain model description of the strain-hardening successfully captured the state of deformation dependence in both these polymers.

As its predecessors, the glassy polymer model by Arruda and Boyce involves three components (Fig. 2-2): a linear spring (A) used to characterize the initial response as elastic; and a non-linear spring (B) that accounts for an anisotropic resistance to molecular chain alignment, which develops as a back-stress with plastic straining; a viscoplastic dashpot (C) representing the rate and temperature-dependent plastic flow which corresponds to an isotropic resistance to chain segment rotation. Constitutive descriptions for each of these elements, as well as the finite strain kinematics of the constitutive model, are summarized below.

2.1 Kinematics

The constitutive model uses the multiplicative decomposition of the deformation gradient, $\mathbf{F}$, into elastic and plastic parts according to Lee [44],

$$\mathbf{F} = \mathbf{F}^e \mathbf{F}^p, \tag{2.1}$$

where the superscripts e and p denote the elastic and plastic (relaxed) configurations, respectively. The plastic deformation gradient, $\mathbf{F}^p$, is obtained in the relaxed configuration by elastically unloading to a stress-free state via $\mathbf{F}^{e-1}$ (Fig. 2-1). The elastic

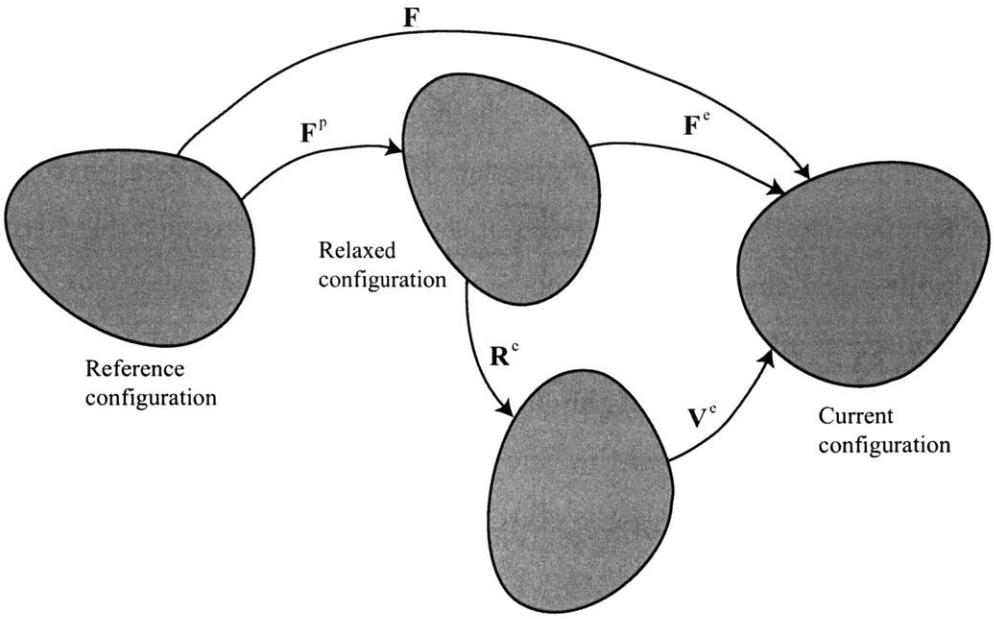

Figure 2-1: Finite strain kinematics of the glassy polymer.

deformation gradient, $\mathbf{F}^e$, can be decomposed as

$$\mathbf{F}^e = \mathbf{V}^e\mathbf{R}^e, \tag{2.2}$$

where $\mathbf{V}^e$ is the left elastic stretch tensor, and the proper orthogonal tensor $\mathbf{R}^e$ is an elastic rotation. The velocity gradient, $\mathbf{L}$, can be expressed as the sum of a (symmetric) stretching tensor, $\mathbf{D}$, and a (skew) spin tensor, $\mathbf{W}$, and it is given as follows:

$$\mathbf{L} = \dot{\mathbf{F}}\,\mathbf{F}^{-1} = \mathbf{D} + \mathbf{W} = \underbrace{\dot{\mathbf{F}}^e\,\mathbf{F}^{e-1}}_{\mathbf{L}^e} + \underbrace{\mathbf{F}^e\tilde{\mathbf{L}}^p\mathbf{F}^{e-1}}_{\mathbf{L}^p} = \mathbf{L}^e + \mathbf{L}^p, \tag{2.3}$$

where $\mathbf{L}^e$ and $\mathbf{L}^p$ are the "elastic" and "plastic" velocity gradients in the current configuration, respectively, and $\tilde{\mathbf{L}}^p$ is the "plastic velocity gradient" in the relaxed configuration[1]. The plastic velocity gradient in the current configuration can be

[1]The notion of "elastic" and "plastic" velocity gradients is widely accepted, but the terminology is formally inaccurate as there are, in general, no corresponding "elastic" or "plastic" velocity fields.

decomposed into symmetric and skew parts as,

$$\mathbf{L}^p = \mathbf{D}^p + \mathbf{W}^p. \tag{2.4}$$

In this formulation, we prescribe the skew part of the plastic velocity gradient in the current configuration to be zero, $\mathbf{W}^p \equiv \mathbf{0}$, and by this process eliminate the rotational indeterminacy of the $\mathbf{F}^e\,\mathbf{F}^p$ decomposition [13]. The evolution of the plastic deformation gradient (the flow rule) is then given by

$$\dot{\mathbf{F}}^p = \tilde{\mathbf{L}}^p\,\mathbf{F}^p = \mathbf{F}^{e-1}\,\mathbf{D}^p\,\mathbf{F}^e\,\mathbf{F}^p = \mathbf{F}^{e-1}\,\mathbf{D}^p\mathbf{F}, \tag{2.5}$$

where $\mathbf{D}^p$ is constitutively prescribed below.

2.2 Stress

The total Cauchy stress, $\mathbf{T}$, acting on the material is the sum of the contributions from the viscoplastic dashpot and the non-linear orientation hardening spring (back-stress):

$$\mathbf{T} = \mathbf{T}^* + \frac{1}{J^e}\mathbf{F}^e\mathbf{T}^B\mathbf{F}^{eT}, \tag{2.6}$$

where $J^e = \det \mathbf{F}^e$. The stress acting on the dashpot, $\mathbf{T}^*$, is defined in the current configuration. The back-stress, $\mathbf{T}^B$, is defined in the relaxed configuration, and is pushed forward to the current configuration via $\mathbf{F}^e$.

2.3 Linear elastic behavior

The isotropic linear elastic spring (A) used to characterize the initial response of the material is constitutively described by the fourth-order elasticity tensor, $\mathcal{C}^e$,

$$\mathcal{C}^e \equiv 2\mu\mathcal{I} + \{\kappa - 2/3\mu\}\,\mathbf{1}\otimes\mathbf{1}, \tag{2.7}$$

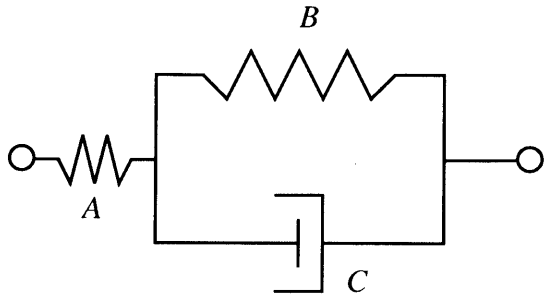

Figure 2-2: Schematic of the constitutive model for glassy polymers: (A) linear elastic spring, (B) non-linear orientation hardening spring, (C) viscoplastic dashpot.

where μ and κ are the shear and bulk moduli, respectively, and $\mathbf{1}$ and $\mathcal{I}$ are the second and fourth-order identity tensors, respectively. Elastic strains in glassy polymers are often on the order of a few percent, and a suitable strain measure is therefore the elastic logarithmic (Hencky) strain, $\mathbf{E}^e = \ln \mathbf{V}^e$. The Cauchy stress, $\mathbf{T}$, is then given by (Anand [2]),

$$\mathbf{T} = \frac{1}{J^e} C^e \left[\mathbf{E}^e\right]. \tag{2.8}$$

2.4 Viscoplastic flow

The plastic stretching, in the current configuration, is given by

$$\mathbf{D}^p = \dot{\gamma}^p \, \mathbf{N}, \tag{2.9}$$

where $\mathbf{N}$ is the tensorial direction of the plastic stretching, and $\dot{\gamma}^p$ is a plastic shear strain rate. The plastic flow is taken to be incompressible, and the tensor $\mathbf{N}$ is aligned with the deviator of the driving stress for plastic flow,

$$\mathbf{N} = \frac{\mathrm{dev}\left(\mathbf{T}^*\right)}{\|\mathrm{dev}\left(\mathbf{T}^*\right)\|}, \tag{2.10}$$

where $\|\ldots\|$ denotes the 2-norm of the argument. The plastic strain rate, $\dot{\gamma}^p$, is, in general, a function of the properties of the glassy polymer, temperature and stress.

The plastic flow has been successfully modeled by Argon [4] to include these effects. The expression for $\dot{\gamma}^p$ proposed by Argon is

$$\dot{\gamma}^p = \dot{\gamma}_0 \exp\left(-\frac{\Delta G}{k\theta}\left\{1 - \left(\frac{\tau^*}{s}\right)^{5/6}\right\}\right), \tag{2.11}$$

where $\dot{\gamma}_0$ is the pre-exponential factor, proportional to the attempt frequency, ΔG is the zero-stress level activation energy, k is Boltzmann's constant, $\tau^* = \|\text{dev}\,\mathbf{T}^*\|/\sqrt{2}$ is the effective shear stress, s is the athermal shear strength, and θ is the absolute temperature.

The viscoplastic flow in glassy polymers can also be modeled using a power-law expression for the viscous flow rate (see, for example, G'Sell and Jonas [30]). The power-law expression is given by

$$\dot{\nu}^p = \dot{\nu}_0 \left(\frac{\tau^*}{s}\right)^{1/m}, \tag{2.12}$$

where $\dot{\nu}_0$ is, in general, a function of temperature, and m is a plastic strain-rate sensitivity parameter. Using this formulation, the plastic stretching is expressed as

$$\mathbf{D}^p = \dot{\gamma}^p \mathbf{N} = \sqrt{\frac{3}{2}}\dot{\nu}^p \mathbf{N}, \tag{2.13}$$

where the factor $\sqrt{3/2}$ is a consequence of the manner in which the power-law viscosity is frequently formulated[2]. The limit of $m \to 0$ implies rate-independence, while $m \to 1$ models linear viscous behavior. The shear strength, s, in Eqs. (2.11) and (2.12) can be modified to account for the observed pressure-dependent yield in glassy polymers (Boyce et al. [12]) by the formal change,

$$s \to s + \alpha p, \tag{2.14}$$

[2]The plastic strain-rate potential for an isotropic incompressible power-law viscous behavior is given by $\Phi = \hat{\Phi}(T_{eq}, m) = \frac{\dot{\nu}_0 s}{1/m+1}\left(\frac{T_{eq}}{s}\right)^{1/m+1}$, where T_{eq} is the Mises equivalent tensile stress. Differentiation of this expression with respect to the driving stress for plastic flow gives the plastic stretching tensor as $\mathbf{D}^p = \sqrt{\frac{3}{2}}\dot{\nu}_0\left(\frac{\tau^*}{s}\right)^{1/m}\mathbf{N}$.

where α is a dimensionless constant, and $p = -\mathrm{tr}(\mathbf{T})/3$ is the pressure. Strain-softening in aged glassy polymers has been modeled by letting the shear strength s evolve from an initial value, s_0, to a [lower] constant saturation shear strength, s_{sat}, according to

$$\dot{s} = h\left(1 - \frac{s}{s_{sat}}\right)\dot{\gamma}^p, \tag{2.15}$$

where $h > 0$ is a softening parameter (Boyce et al. [12]). In Eq. (2.15), s_{sat} is taken to be independent of temperature and strain rate.

2.5 Back-stress

At large plastic deformations of the glassy polymer, the molecular chains become preferentially oriented. The work associated with the chain alignment is internally stored in entropic form, and it gives rise to a deviatoric back-stress in the material. The back-stress can successfully be described within the context of rubber elasticity using the Arruda-Boyce eight-chain material model [8]. The deviatoric back-stress, $\mathrm{dev}\left(\mathbf{T}^B\right)$, is given by

$$\mathrm{dev}\left(\mathbf{T}^B\right) = C_R \frac{\sqrt{N}}{\sqrt{3}\lambda_{ch}^p} \mathcal{L}^{-1}\left(\frac{\lambda_{ch}^p}{\sqrt{N}}\right) \mathrm{dev}\left(\mathbf{B}^p\right), \tag{2.16}$$

where $\mathrm{dev}\left(\mathbf{B}^p\right) = \mathrm{dev}\left(\mathbf{F}^p\mathbf{F}^{pT}\right)$ and $\lambda_{ch}^p = \left[\mathrm{tr}\left(\mathbf{B}^p\right)/3\right]^{1/2}$. The material properties describing the orientation-hardening characteristics are C_R, the initial hardening modulus, and N, the number of rigid molecular units between entanglements. The Langevin function $\mathcal{L}$ is given by

$$\mathcal{L}(\beta) = \coth(\beta) - \frac{1}{\beta}, \tag{2.17}$$

and the inverse Langevin function is implicitly defined by

$$\beta = \mathcal{L}^{-1}\left(\frac{\lambda_{ch}^{p}}{\sqrt{N}}\right). \tag{2.18}$$

2.5.1 Material parameters for glassy polycarbonate

Arruda [6] performed uniaxial compression and plane strain compression experiments on glassy polycarbonate and poly(methyl methacrylate). The experiments were carried out for a range of temperatures and [low] strain rates. The glassy polymer model, using the Argon expression (Eq. 2.11), modified to account for pressure effects (Eq. 2.14), was calibrated against the experimental results obtained for polycarbonate at room temperature, and the model parameters are given in Tables 2.1 and 2.2. Table 2.1 shows the linear elastic bulk (κ) and shear modulus (μ) at room temperature, as well as the two material parameters N and C_R required to model the orientation-hardening. Table 2.2 shows the parameters $\{\dot{\gamma}_0, \Delta G, s_0, s_{sat}, h, \alpha\}$ for the plastic flow part. The uniaxial tensile stress-strain response using the material parameters in Tables 2.1 and 2.2 is shown in Fig. (2-3a) for three strain rates: $\dot{E}_{axial} = \{0.001\text{s}^{-1}, 0.01\text{s}^{-1}, 0.1\text{s}^{-1}\}$.

Figure (2-3b) shows the effects of pressure on plastic flow ($\alpha = \{0, 0.075\}$). It is seen in the figure that under uniaxial tension and compression, the effect of pressure is indeed present, but does not have a major influence on the stress-strain response of the material. Under highly triaxial stress states, the effect of pressure on plastic flow increases, while under highly deviatoric stress states, this effect is diminishing. In Chapter 3, various idealizations of *porous* glassy polymers will be used to address the influence of porosity on the macroscopic stress-strain response of the material. In a porous glassy polymer, it is expected that presence of voids will act to relieve local negative pressures in the glassy polymer matrix, which reduces the influence of the parameter α of the matrix on the macroscopic stress-strain response of the porous material. In the following discussion, it will therefore be assumed that $\alpha = 0$.

As will be illustrated in Chapter 4, the mathematically simple power-law viscous flow description (Eq. 2.12) is suitable in the development of a constitutive descrip-

κ (MPa)	μ (MPa)	N	C_R (MPa)
2250	870	2.15	12.8

Table 2.1: Summary of the elastic and strain hardening parameters for annealed polycarbonate.

$\dot{\gamma}_0$ (s^{-1})	ΔG (J)	s_0 (MPa)	s_{sat} (MPa)	h (MPa)	α
$2 \cdot 10^{15}$	$3.3 \cdot 10^{-19}$	99.37	77.5	500	0.075

Table 2.2: Summary of the viscoplastic parameters for polycarbonate using Argon's expression.

tion for the plastic flow of porous glassy polymers. The constitutive model for the glassy polymer using the power-law description for the viscous flow (Eq. 2.12) was therefore calibrated against the stress-strain curves based on Tables 2.1 and 2.2. The resulting set of material parameters for the plastic flow are shown in Table 2.3. The constitutive model for glassy polymers will serve two purposes in the thesis: It will be used to represent the glassy polymer matrix phase in micromechanical modeling of rubber-toughened polymers, and it will provide a framework for the development of continuum-level constitutive models for rubber-toughened polymers.

$\dot{\nu}_0$ (s^{-1})	m	s_0 (MPa)	s_{sat} (MPa)	h (MPa)
0.009	0.033	73.5	39	245

Table 2.3: Summary of the viscoplastic parameters for polycarbonate using the power-law expression.

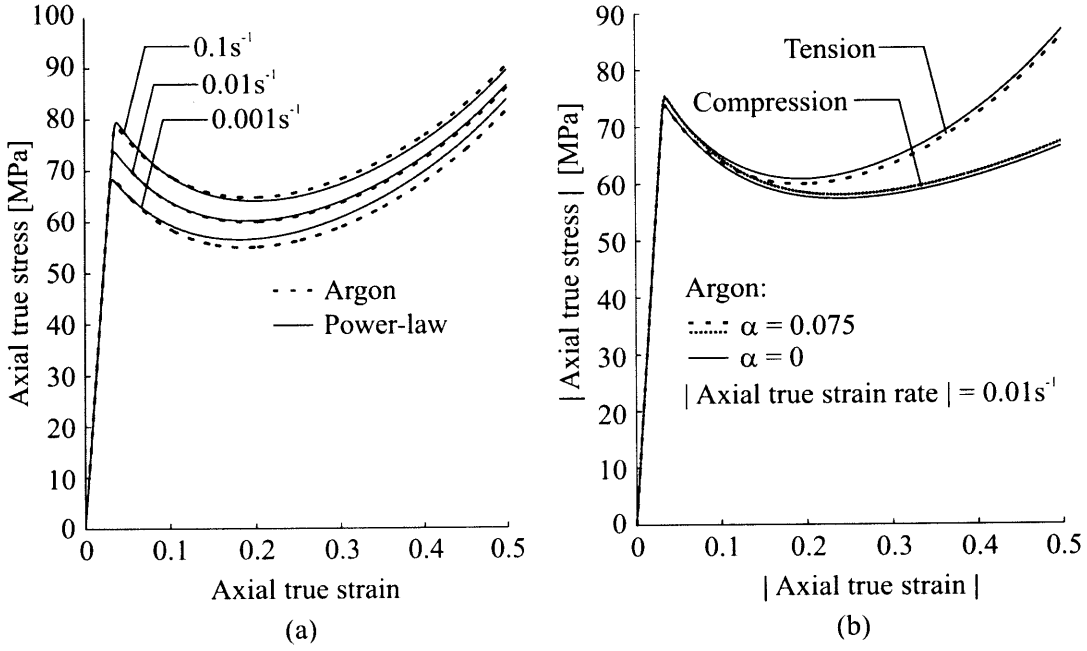

Figure 2-3: Homogeneous polycarbonate under axial loading: (a) uniaxial tension for a constitutive response using the Argon (Table 2.2) and power-law (Table 2.3) equations for the viscous flow, respectively, at different true strain rates, (b) uniaxial tension and compression, illustrating the influence of the pressure parameter α on the stress-strain response using the Argon equation for the viscous flow.

Chapter 3

Micromechanical Modeling

Micromechanical modeling, through the identification of a representative volume element (RVE) of material, has become an increasingly important tool for understanding deformation mechanisms in porous (or particle-modified) materials. Many micromechanical models have idealized the porous microstructure as a stacked hexagonal array (SHA) of identical, spherical voids in a matrix (Fig. 3-1a) (see, for example, Tvergaard [70], Koplik and Needleman [41], and Steenbrink, et al. [65]). The SHA void distribution enables the simplification of the porous material to a locally-periodic "unit cell", which is solved numerically as a two-dimensional axisymmetric boundary value problem. Socrate and Boyce showed that the axisymmetric SHA model gives realistic predictions of macroscopic stress and strain as long as the void volume fraction is low; that is, when the voids are essentially isolated, and there is limited interaction. At large void volume fractions, when the interactions between voids become stronger, the periodicity of the SHA model forces matrix deformation to localize through a thin inter-void ligament near the void equator, and this yields unrealistic predictions of the macromechanical and micromechanical behavior. A more suitable representation of the void distribution is obtained if the voids are staggered, rather than stacked. Socrate and Boyce [63] developed two axisymmetric cell models based on BCC and BCT arrangements of voids. The model based on a BCC arrangement of voids, termed the axisymmetric V-BCC model, is shown in Fig. (3-1a). These models were shown to give more realistic predictions of macroscopic stress and strain,

as well as micromechanical behavior, for higher void volume fractions. A limitation of any axisymmetric model, however, is that it can only be used to study macroscopic deformation and loading histories that are themselves axisymmetric, such as uniaxial tension, or uniaxial tension with a superimposed hydrostatic stress. The axisymmetric V-BCC model by Socrate and Boyce was extended by Danielsson, et al. [21], to a fully three-dimensional description of the geometry (Fig. 3-1b). This model (the 3D V-BCC model) can be used to study arbitrary macroscopic deformation histories, including plane strain tension and simple shear deformation, and it will be discussed in this chapter.

The idealization of the void distribution as stacked or staggered arrays is convenient, as it allows for single-void RVEs to be considered. By considering single-void RVEs, it is possible to accurately resolve local matrix field quantities in the vicinity of the void, such as stress, strain and strain-rate. In a single-void RVE, plastic deformation mechanisms, such as shear banding between voids, are forced to occur periodically throughout the composite. In a real porous material, where the voids are randomly distributed, such deformation events are expected to occur sequentially, giving rise to a percolation of plastic flow through the material. In order to account for the distribution of deformation events expected in a porous material, Smit, et al. [62] proposed a two-dimensional plane-strain cell model based on a random distribution of cylindrical voids in a polycarbonate matrix (Fig. 3-1c). The authors argued that the significant post-yield softening predicted in porous polycarbonate by single-void models is an artifact of the local periodicity of the voids, and that it is only through the introduction of a spatially random distribution of voids that a micromechanical model can capture the macroscopically stable blend behavior which results from the successive percolation of plastic flow through the matrix.

A limitation of the model proposed by Smit, et al. is its plane geometry, and idealization of a random distribution of spherical voids into a random array of cylindrical voids. The model by Smit, et al. showed the percolation of plastic flow through the matrix, but the plane geometry of the micromechanical model did not allow for strain or stress gradients in the direction of macroscopic constraint. When the real material

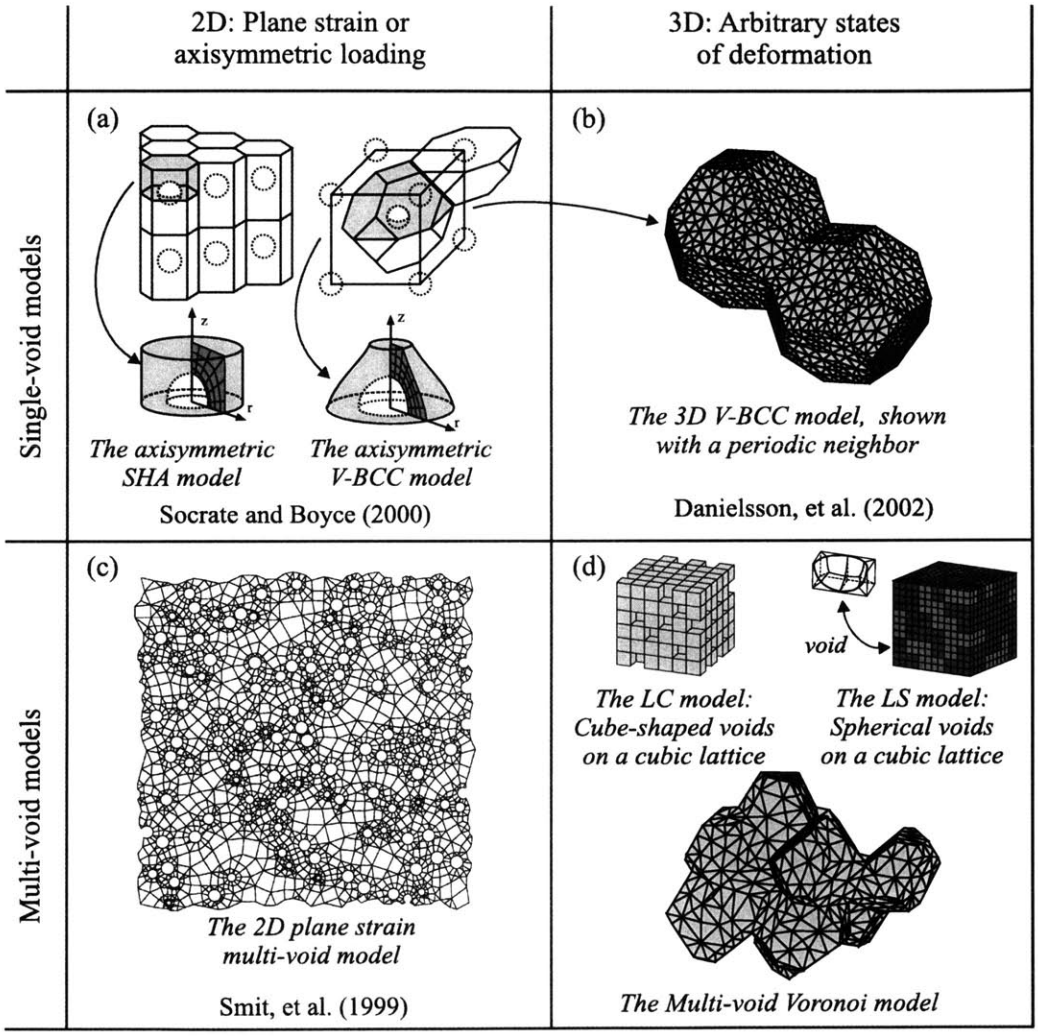

Figure 3-1: Different topological idealizations of the porous microstructure: (a) two-dimensional axisymmetric single-void models, (b) three-dimensional single-void models, (c) two-dimensional multi-void models, (d) three-dimensional multi-void models.

is subjected to macroscopic plane strain tension, it is reasonable to expect local plastic deformation also in the direction of macroscopic constraint. In order to successfully model any three-dimensional loading conditions, such as macroscopic plane strain tension, a fully three-dimensional micromechanical model is required. Three different micromechanical models of three-dimensional, random, distributions of voids (Fig. 3-1d) will be presented in this chapter, in addition to the single-void 3D V-BCC model. For each of the four micromechanical models, different macroscopic loading histories will be studied on micromechanical and macromechanical scales. The relative merits of the micromechanical models will be discussed.

3.1 Periodic boundary conditions and macroscopic response

Each representative volume element to be discussed in this chapter is space-filling and spatially periodic. When such an RVE is subjected to a macroscopic loading and/or deformation history, periodic boundary conditions must be applied to the surface of the RVE. This ensures that the RVE deforms in a periodically repeating manner, and that no overlaps or cavities form. Figure (3-2) shows a schematic of a periodically repeating RVE. Although in Fig. (3-2) the undeformed RVE geometry is schematically taken to be a unit cube, the following discussion is general and applicable to any space-filling, spatially periodic RVE. The RVE is subjected to a macroscopic deformation gradient, $\overline{\mathbf{F}}$. The two points A and B (Fig. 3-2) are periodically located on the RVE surface, and the requirement that no overlaps or cavities may form poses a constraint on the relative displacement of A with respect to B. The displacement of point A relative to point B is determined by the macroscopically applied displacement gradient, $\overline{\mathbf{H}} = \overline{\mathbf{F}} - \mathbf{1}$, through

$$\mathbf{u}(B) - \mathbf{u}(A) = \left(\overline{\mathbf{F}} - \mathbf{1}\right)\left\{\mathbf{X}(B) - \mathbf{X}(A)\right\} = \overline{\mathbf{H}}\left\{\mathbf{X}(B) - \mathbf{X}(A)\right\}, \qquad (3.1)$$

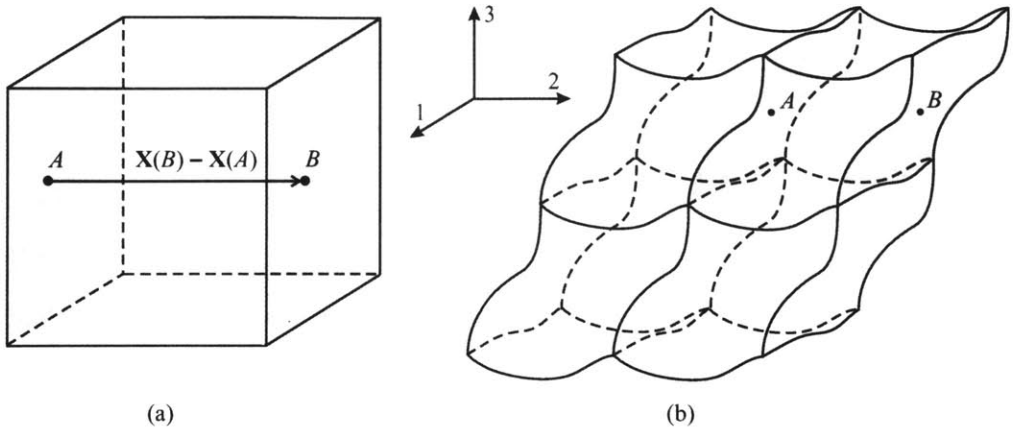

Figure 3-2: A spatially periodic RVE: (a) the undeformed RVE, (b) the deformed RVE with three of its periodic neighbors.

where $\mathbf{u}(\dots)$ denotes displacement, and $\mathbf{X}(\dots)$ denotes position in the reference configuration[1]. Every periodic surface point pair on the RVE must be constrained using Eq. (3.1). The macroscopic RVE deformation can then be imposed by prescribing the nine components of $\overline{\mathbf{F}}$. The macroscopic Cauchy stress, $\overline{\mathbf{T}}$, corresponding to the macroscopically applied deformation gradient $\overline{\mathbf{F}}$, can be extracted through virtual work considerations (Danielsson, et al. [21]). The procedure for obtaining the macroscopic Cauchy stress, $\overline{\mathbf{T}}$, is reviewed here for completeness.

The principle of virtual work states that the internal virtual work has to be equal to the external virtual work,

$$\delta W^{int} = \delta W^{ext}. \tag{3.2}$$

[1]Note that a frequently used constraint equation is $\mathbf{u}(A) = (\overline{\mathbf{F}} - \mathbf{1})\,\mathbf{X}(A)$ applied to all boundary points of the RVE. This constraint equation satisfies the requirement that the RVE deforms in a compatible manner, with no overlaps or cavities forming, but it imposes an over-constraint on the local deformation fields, and limits the deformation patterns through which the RVE can accommodate the macroscopically-applied $\overline{\mathbf{F}}$. Moreover, traction periodicity will not be satisfied on the surface of the RVE.

The external virtual work may be written as

$$\delta W^{ext} = \int_{S_0} \mathbf{S}\mathbf{n}_0 \cdot \delta\mathbf{u}(C)\mathrm{d}S_0 = \int_{S_0} \mathbf{s} \cdot \delta\mathbf{u}(C)\mathrm{d}S_0, \tag{3.3}$$

where $\mathbf{S}$ is the (pointwise) first Piola-Kirchhoff stress tensor, $\mathbf{n}_0$ is the outward unit normal to the surface of the RVE, S_0, in the reference configuration. $\delta\mathbf{u}(C)$ is the virtual displacement of a point C in the reference configuration, and $\mathbf{s}$ is the surface traction in the reference configuration[2]. The macroscopic (RVE average) first Piola-Kirchhoff stress, $\overline{\mathbf{S}}$, is given by

$$\overline{\mathbf{S}} = \frac{1}{V_0}\int_{V_0} \mathbf{S}\,\mathrm{d}V_0, \tag{3.4}$$

where V_0 is the volume of the RVE in the reference configuration, including contained voids where $\mathbf{S} = \mathbf{0}$. The first Piola-Kirchhoff stress is work-conjugate to the deformation gradient. Hence, the internal virtual work can be written as

$$\delta W^{int} = V_0\overline{\mathbf{S}} \cdot \delta\overline{\mathbf{F}}. \tag{3.5}$$

By using Eqs. (3.2), (3.3) and (3.5), we obtain

$$V_0\overline{\mathbf{S}} \cdot \delta\overline{\mathbf{F}} = \int_{S_0} \mathbf{s} \cdot \delta\mathbf{u}(C)\mathrm{d}S_0. \tag{3.6}$$

Hence, the macroscopic first Piola-Kirchhoff stress tensor, $\overline{\mathbf{S}}$, is expressed in terms of the local surface tractions, $\mathbf{s}$. The components of the macroscopic deformation gradient, $\overline{\mathbf{F}}$, are the quantities that drive the deformation of the RVE (Eqs. 3.15 and 3.18) in a finite element analysis of the corresponding boundary value problem. Operationally, the components of $\overline{\mathbf{F}}$ are provided to the RVE by introducing nine

[2]Note: The reference surface S_0 includes the internal void surfaces. However, these are traction-free, and do not contribute to the external virtual work.

generalized degrees of freedom, ξ_i,

$$\begin{bmatrix} \xi_1 & \xi_2 & \xi_3 \\ \xi_4 & \xi_5 & \xi_6 \\ \xi_7 & \xi_8 & \xi_9 \end{bmatrix} = \begin{bmatrix} (\overline{F}_{11} - 1) & \overline{F}_{12} & \overline{F}_{13} \\ \overline{F}_{21} & (\overline{F}_{22} - 1) & \overline{F}_{23} \\ \overline{F}_{31} & \overline{F}_{32} & (\overline{F}_{33} - 1) \end{bmatrix}. \tag{3.7}$$

These ξ_i are assigned to be the displacement components of three 'dummy' nodes in the finite element model, thus giving $\overline{\mathbf{F}}$ in Eq. (3.1). Virtual work is then used to determine the work-conjugate stress, $\overline{\mathbf{S}}$. The external virtual work (Eq. 3.3) may be re-stated in terms of the generalized degrees of freedom, ξ_i, and their work conjugate generalized forces, Ξ_i,

$$\delta W^{ext} = \sum_{i=1}^{9} \Xi_i \, \delta\xi_i. \tag{3.8}$$

Therefore, the Ξ_i are the "reaction forces" corresponding to the assigned "displacement components", ξ_i of the 'dummy' nodes. By using Eqs. (3.5) and (3.8), the components of the macroscopic first Piola-Kirchhoff stress tensor, $\overline{\mathbf{S}}$, are identified as

$$\begin{bmatrix} \overline{S}_{11} & \overline{S}_{12} & \overline{S}_{13} \\ \overline{S}_{21} & \overline{S}_{22} & \overline{S}_{23} \\ \overline{S}_{31} & \overline{S}_{32} & \overline{S}_{33} \end{bmatrix} = \frac{1}{V_0} \begin{bmatrix} \Xi_1 & \Xi_2 & \Xi_3 \\ \Xi_4 & \Xi_5 & \Xi_6 \\ \Xi_7 & \Xi_8 & \Xi_9 \end{bmatrix}. \tag{3.9}$$

The macroscopic Cauchy stress tensor, $\overline{\mathbf{T}}$, is calculated from $\overline{\mathbf{S}}$ and $\overline{\mathbf{F}}$ as

$$\overline{\mathbf{T}} = \frac{V_0}{V} \overline{\mathbf{S}} \, \overline{\mathbf{F}}^T = \frac{1}{\overline{J}} \overline{\mathbf{S}} \, \overline{\mathbf{F}}^T, \tag{3.10}$$

where V is the volume of the RVE in the current (deformed) configuration, and $\overline{J} = \det \overline{\mathbf{F}}$. The macroscopic deformation of the RVE can be characterized in terms of the macroscopic logarithmic strain tensor, $\overline{\mathbf{E}}$, given by

$$\overline{\mathbf{E}} = \ln \overline{\mathbf{V}}, \tag{3.11}$$

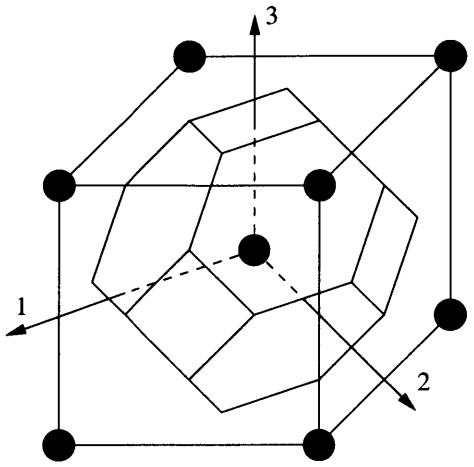

Figure 3-3: The 3D V-BCC cell.

where $\overline{\mathbf{V}}$ is the (macroscopic) left stretch tensor based on a polar decomposition of the macroscopic deformation gradient, $\overline{\mathbf{F}} = \overline{\mathbf{V}}\,\overline{\mathbf{R}}$.

3.2 The 3D V-BCC model

In the 3D V-BCC cell model, the random void distribution is idealized by arranging the particles on a body-centered cubic (BCC) lattice. The cell model is constructed through a three-dimensional Voronoi tessellation procedure, which results in a space-filling arrangement of tetrakaidecahedra (Fig. 3-3). The tessellation can be carried out in three elementary steps (Dib and Rodin [23]). First, the center of a reference cube is connected by lines to its eight corners and to the six nearest corresponding cube centers. Second, each of these lines is bisected by a plane. Third, the 3D V-BCC cell is given as the volume bounded by the planes. This 3D V-BCC cell, also known as the Wigner-Seitz cell (Wigner and Seitz [76]), is a highly symmetric polyhedron which possesses nine symmetry planes.

3.2.1 Boundary conditions

General periodic boundary conditions for the 3D V-BCC cell model are developed for three specific macroscopic loading cases: (1) axial deformation with imposed lateral stress; (2) plane strain deformation with imposed lateral stress; (3) simple shear deformation. The boundary conditions are then expressed in terms of the macroscopic deformation gradient, $\overline{\mathbf{F}}$ (Eq. 3.1). The different macroscopic load cases in this study allow for the cell model to be reduced, due to reflective symmetries. This reduction of the geometry is desired to lessen the computational requirement of the finite element analyses. The Cartesian reference system used in this study is shown in Fig. (3-3); Cartesian base vectors are $\{\mathbf{e}_i\}$. For the cases of principal stress states coaxial with the Cartesian reference system, 1/8 of the 3D V-BCC cell is considered, whereas the case of simple shear deformation requires 1/4 of the cell to be considered[3]. The principal direction of uniaxial tension is taken to be the 3-direction, which is a direction perpendicular to a pair of square facets (Fig. 3-3). In the case of simple shear deformation, the principal shearing planes are taken along a pair of square facets of the cell.

General case

The surface of the 3D V-BCC RVE consists of eight hexagonal and six square facets. The RVE is space-filling (Fig. 3-4), and periodically located surface points are related through the macroscopic deformation gradient (Eq. 3.1),

$$\mathbf{u}(B) - \mathbf{u}(A) = \left(\overline{\mathbf{F}} - \mathbf{1}\right)\{\mathbf{X}(B) - \mathbf{X}(A)\} = \overline{\mathbf{H}}\{\mathbf{X}(B) - \mathbf{X}(A)\}. \tag{3.12}$$

For certain load cases, the geometry of the RVE can be reduced due to reflective symmetries. If two points, A and B, are reflectively symmetric with respect to a

[3]For the case of uniaxial tension and tension with equal lateral stresses, only 1/16 of the 3D V-BCC cell model is needed. However, to facilitate the use of hexahedral meshes, 1/8 of the cell model is used instead.

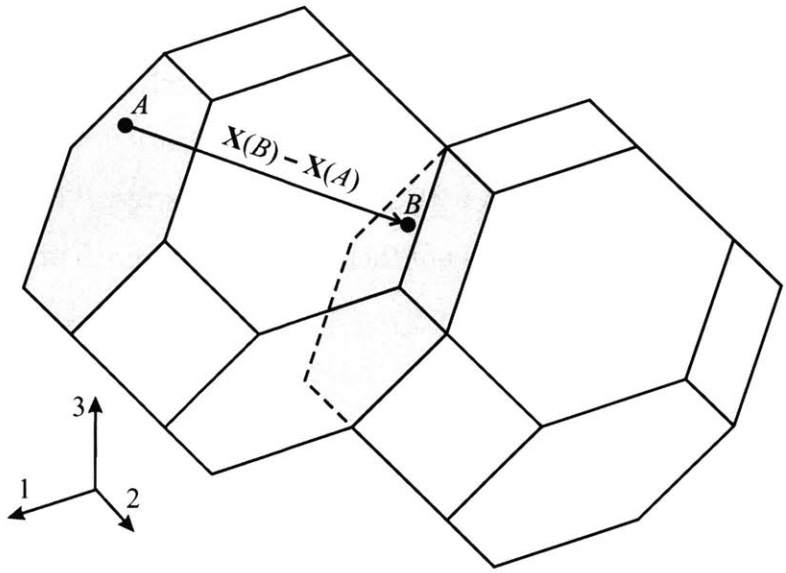

Figure 3-4: Two neighboring 3D V-BCC cells.

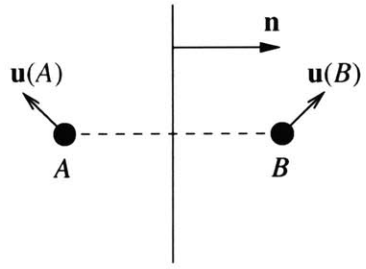

Figure 3-5: Two points, A and B, that are reflectively symmetric with respect to a plane with unit normal $\mathbf{n}$.

plane with unit normal $\mathbf{n}$ (Fig. 3-5), then their displacements are related through

$$\mathbf{u}(A) = (\mathbf{1} - 2\mathbf{n} \otimes \mathbf{n})\mathbf{u}(B) = \mathbf{Q}(\mathbf{n})\mathbf{u}(B), \tag{3.13}$$

where $\mathbf{u}(A)$ and $\mathbf{u}(B)$ are the displacements of A and B, $\mathbf{1}$ is the second-order identity tensor, the symbol $\otimes$ denotes the tensor (dyadic) product, and $\mathbf{Q}(\mathbf{n})$ is the reflection operator of the symmetry plane with normal direction $\mathbf{n}$. The reflection operator $\mathbf{Q}(\mathbf{n})$ is an orthogonal tensor, thus $\mathbf{Q}(\mathbf{n})^T\,\mathbf{Q}(\mathbf{n}) = \mathbf{1}$.

Plane strain deformation and principal stress states

The cases of plane strain deformation and principal stress states coincident with the coordinate directions perpendicular to the square facets of the cell, require 1/8 (Fig. 3-6) of the 3D V-BCC cell to be modeled. The coordinate planes are symmetry planes, and the general periodic boundary conditions (Eq. 3.1), together with appropriate reflections (Eq. 3.13) give rise to the following boundary conditions (Eqs. 3.14 and 3.15),

$$\begin{aligned} \mathbf{u}(S_6) + \mathbf{Q}(\mathbf{e}_3)\mathbf{u}(S_5) &= 2\mathbf{u}(P_1) \\ \mathbf{u}(S_1) + \mathbf{Q}(\mathbf{e}_1)\mathbf{u}(S_2) &= 2\mathbf{u}(P_2) \\ \mathbf{e}_3 \cdot \mathbf{u}(S_7) &= \mathbf{e}_3 \cdot \mathbf{u}(P_3) \\ \mathbf{u}(S_3) + \mathbf{Q}(\mathbf{e}_2)\mathbf{u}(S_4) &= 2\mathbf{u}(P_4) \end{aligned} \tag{3.14}$$

$$(\overline{\mathbf{F}} - \mathbf{1})\mathbf{X}(P_i) = \mathbf{u}(P_i), \quad i = 1..4 \tag{3.15}$$

where S_1-S_7 are points on the facets of the 3D V-BCC cell (Fig. 3-6). The macroscopic deformation gradient, $\overline{\mathbf{F}}$, corresponding to a macroscopic principal deformation state is given by

$$\overline{\mathbf{F}} = \sum_{i=1}^{3} \overline{\lambda}_i(t)\, \mathbf{e}_i \otimes \mathbf{e}_i, \tag{3.16}$$

where the time-dependent macroscopic principal stretches, $\overline{\lambda}_i(t)$, can be prescribed. In the case of macroscopic uniaxial tension in the three-direction, $\overline{\lambda}_3(t)$ is prescribed to produce a constant macroscopic axial true strain-rate, and $\overline{\lambda}_1(t)$ and $\overline{\lambda}_2(t)$ are left un-prescribed. In the case of macroscopic plane strain deformation, $\overline{\lambda}_3(t)$ is prescribed to produce a constant macroscopic axial true strain-rate, $\overline{\lambda}_1(t) = 1$, and $\overline{\lambda}_2(t)$ is left un-prescribed.

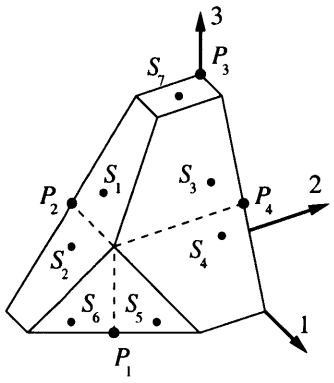

Figure 3-6: The (undeformed) 3D V-BCC cell model used for plane strain deformation and principal stress states.

Simple shear deformation

For the case of simple shear deformation in the 23-plane, 1/4 of the 3D V-BCC cell is modeled (Fig. 3-7). The 23-plane is here a plane of symmetry, and the 12-plane is a plane of antisymmetry. The boundary conditions for this case are summarized below (Eqs. 3.17 and 3.18),

$$\begin{aligned}
\mathbf{u}(S_6) - \mathbf{Q}(\mathbf{e}_1)\mathbf{u}(S_{11}) &= 2\mathbf{u}(P_1) \\
\mathbf{u}(S_1) + \mathbf{Q}(\mathbf{e}_1)\mathbf{u}(S_2) &= 2\mathbf{u}(P_2) \\
\mathbf{u}(S_7) + \mathbf{Q}(\mathbf{e}_1)\mathbf{u}(S_8) &= 2\mathbf{u}(P_3) \\
\mathbf{u}(S_4) + \mathbf{u}(S_9) &= 2\mathbf{u}(P_4) \\
\mathbf{u}(S_3) + \mathbf{u}(S_{10}) &= 2\mathbf{u}(P_4) \\
\mathbf{u}(S_{12}) - \mathbf{Q}(\mathbf{e}_1)\mathbf{u}(S_5) &= 2\mathbf{u}(P_5) \\
\mathbf{u}(S_{15}) + \mathbf{Q}(\mathbf{e}_1)\mathbf{u}(S_{16}) &= 2\mathbf{u}(P_6) \\
\mathbf{u}(S_{13}) + \mathbf{Q}(\mathbf{e}_1)\mathbf{u}(S_{14}) &= \mathbf{0}
\end{aligned} \tag{3.17}$$

$$(\overline{\mathbf{F}} - \mathbf{1})\mathbf{X}(P_i) = \mathbf{u}(P_i), \quad i = 1..6 \tag{3.18}$$

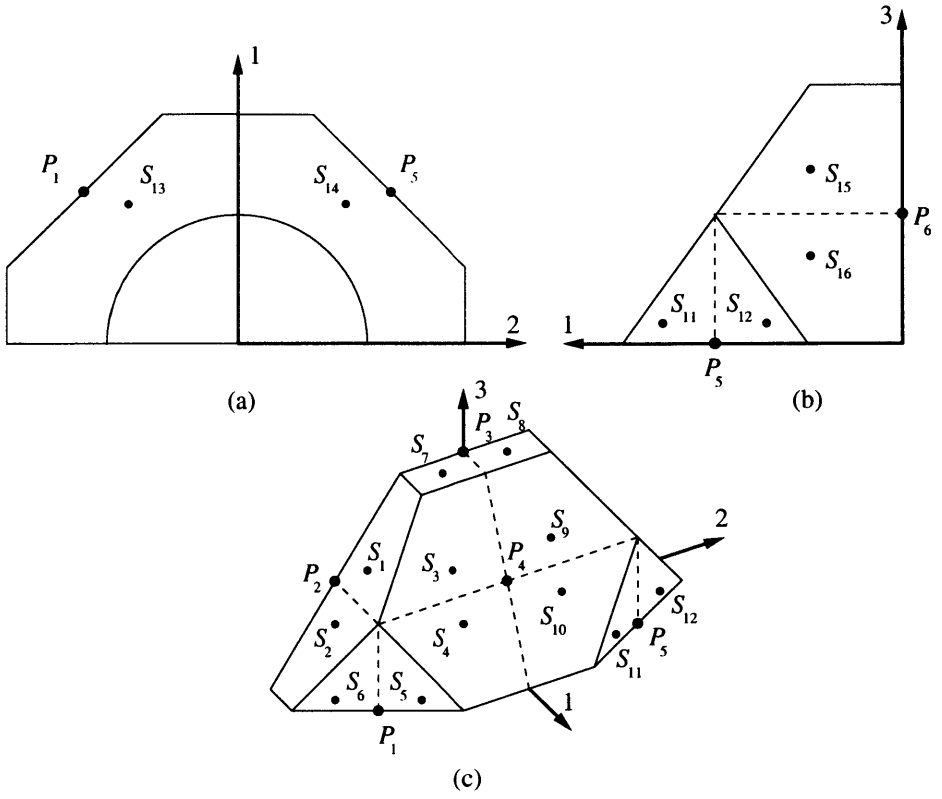

Figure 3-7: The (undeformed) 3D V-BCC cell model used for simple shear deformation: (a) 12-orthographic view; (b) 13-orthographic view; (c) 3D view.

where S_1-S_{16} are points on the facets of the 3D V-BCC cell (Fig. 3-7). The macroscopic deformation gradient, $\overline{\mathbf{F}}$, corresponding to macroscopic simple shear deformation is given by

$$\overline{\mathbf{F}} = \mathbf{1} + \dot{\overline{\Gamma}} t \, \mathbf{e}_2 \otimes \mathbf{e}_3, \tag{3.19}$$

where $\dot{\overline{\Gamma}}$ is the imposed nominal shear strain-rate.

3.2.2 Results for the 3D V-BCC model

The simulations in this section were performed using twenty-node hexahedral finite elements with reduced integration. The benefit of using reduced integration is that the computational cost is significantly reduced compared to the fully-integrated elements,

but more importantly, that numerical problems pertaining to hydrostatic modes of deformation are relieved; reduced integration is suitable for nearly-incompressible analyses.

Uniaxial tension

The 3D V-BCC model was subjected to uniaxial tension for three levels of initial void volume fraction $f_0 = \{0.05, 0.10, 0.15\}$. The macroscopic axial-stress / axial-strain curves are shown in Fig. (3-9a), and the evolution of volumetric strain, $E_{vol} = \mathrm{tr}\,\mathbf{E}$, with axial strain is shown in Fig. (3-9b). The macroscopic yield of the porous material is defined as the point on the axial-stress / axial-strain curve where the stress experiences a peak, with subsequent softening. The microscopic response, in terms of contour plots of plastic shear strain-rate, $\dot{\gamma}^p$, is shown for the case of $f_0 = 0.15$ in Fig. (3-8). The contour plots (Fig. 3-8) indicate that plastic flow initiates in the equatorial region of the void surface (a). At this point in the deformation, most of the surrounding material is still in the elastic regime. A close examination of the stress-strain curves (Fig. 3-9a) shows that, prior to macroscopic yield, the curves deviate slightly from linearity. This is due to the initial local plastic deformation in the equatorial region of the void, which begins to soften the porous material. As the flowing material strain-hardens due to molecular orientation, surrounding material starts to flow. Eventually, shear bands form across inter-void ligaments. This "net section" flow corresponds to macroscopic yield of the porous material. The stress-strain curves show a decrease in the macroscopic "yield stress" of the porous material with increasing initial void volume fraction. The stress-strain curves also show that the post-yield softening, appreciable in the homopolymer, is reduced through the introduction of voids, and that this reduction is more substantial with an increasing volume fraction of voids.

The hardening behavior is consistent over the studied range of initial void volume fractions. As the shear bands strain-harden, surrounding matrix material begins to flow plastically. This flow propagates up and down the ligaments in a manner similar to the stable necking and drawing of a tensile bar. As the plastic flow propagates, a

greater volume of matrix material is encompassed by the flow. This increases the total plastic flow resistance of the porous material, since more matrix material is forced to undergo plastic deformation simultaneously. For low void volume fractions, the increase in fraction of matrix material encompassed by the flow occurs more rapidly with applied macroscopic axial strain (Fig. 3-8c, Appendix A), which results in a higher hardening rate than for higher void volume fractions. The predictions of the evolution of macroscopic volumetric strain with axial deformation, shown in Fig. (3-9b), reflect the initial Poisson effect of the porous material, followed by plastic void growth due to plastic shearing of the matrix material. The predicted magnitude and evolution of volumetric strain are in good agreement with the axisymmetric version of the V-BCC cell model (Socrate and Boyce [63]); small differences are due to the axisymmetric vs. fully three-dimensional formulation.

Plane strain tension

The case of plane strain tension was studied for three levels of initial void volume fractions, $f_0 = \{0.05, 0.10, 0.15\}$. The main macroscopic loading direction is the 3-direction, and the macroscopically constrained direction is the 1-direction. The macroscopic 2-direction is left unconstrained. The macroscopic stress vs. macroscopic strain in the 3-direction is shown in Fig. (3-11a) for the range of initial void volume fractions, and Fig. (3-11b) shows the corresponding predictions of macroscopic volumetric strain. The underlying microscopic behavior is characterized by plotting contours of plastic shear strain-rate at different levels of macroscopic axial strain (Fig. 3-10). The macroscopic yield stress for the material is defined as the point where the stress-strain response exhibits a peak in axial stress, followed by softening. Figure (3-11a) shows that, prior to macroscopic yield, the stress-strain curves deviate slightly from linearity. Similar to the case of uniaxial tension, where local plastic flow in the equatorial region of the void gave rise to this non-linearity, the contours of plastic shear strain-rate also show this initial local plastic flow in the matrix (Fig. 3-10a, Appendix A).

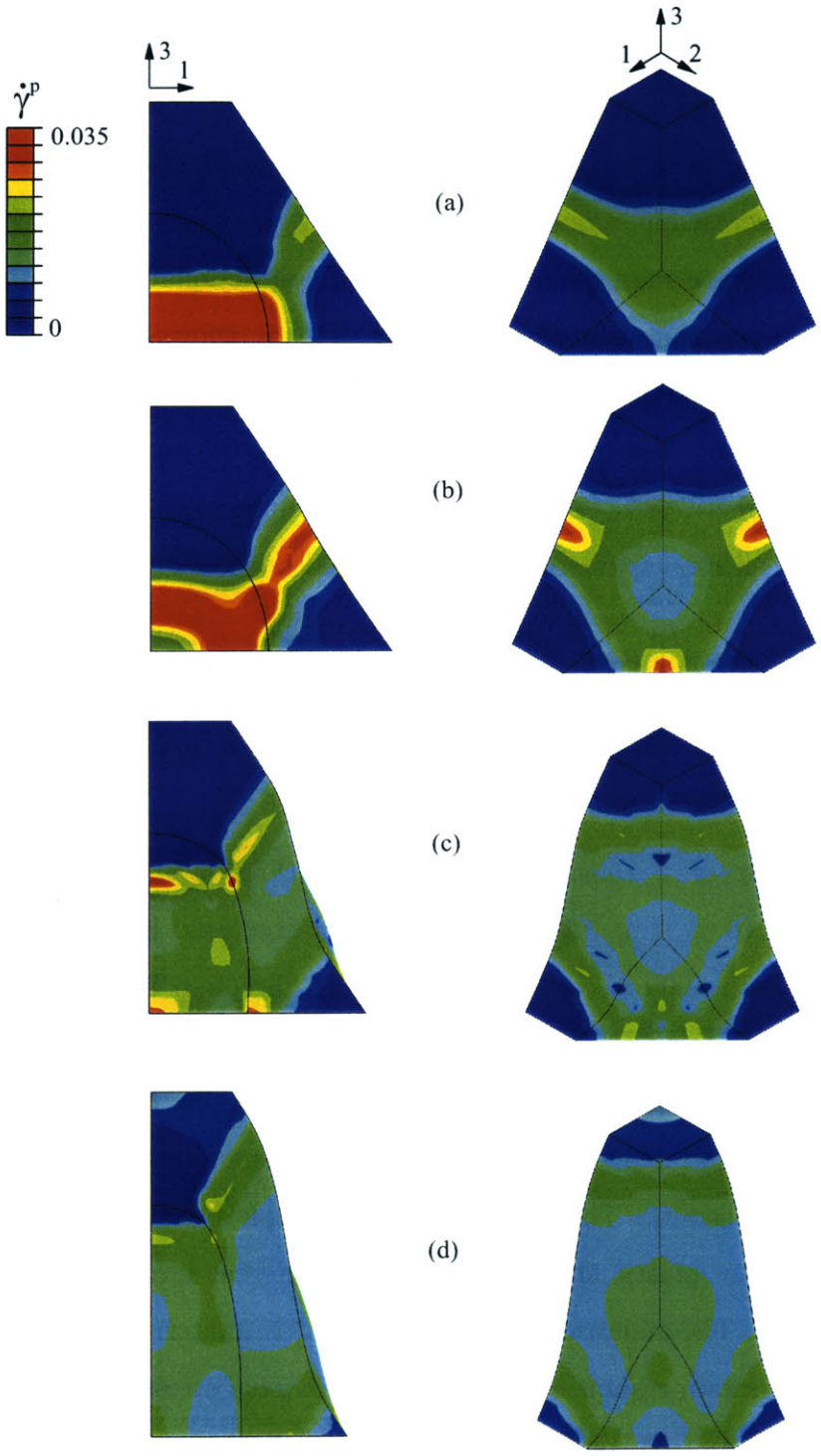

Figure 3-8: Contours of $\dot{\gamma}^p$ under macroscopic uniaxial tension for an initial void volume fraction, $f_0 = 0.15$. The development of plastic shear localization is shown for increasing levels of macroscopic axial strain: (a) $E_{33} \simeq 0.034$, (b) $\overline{E}_{33} \simeq 0.05$, (c) $\overline{E}_{33} \simeq 0.23$ and (d) $\overline{E}_{33} \simeq 0.40$.

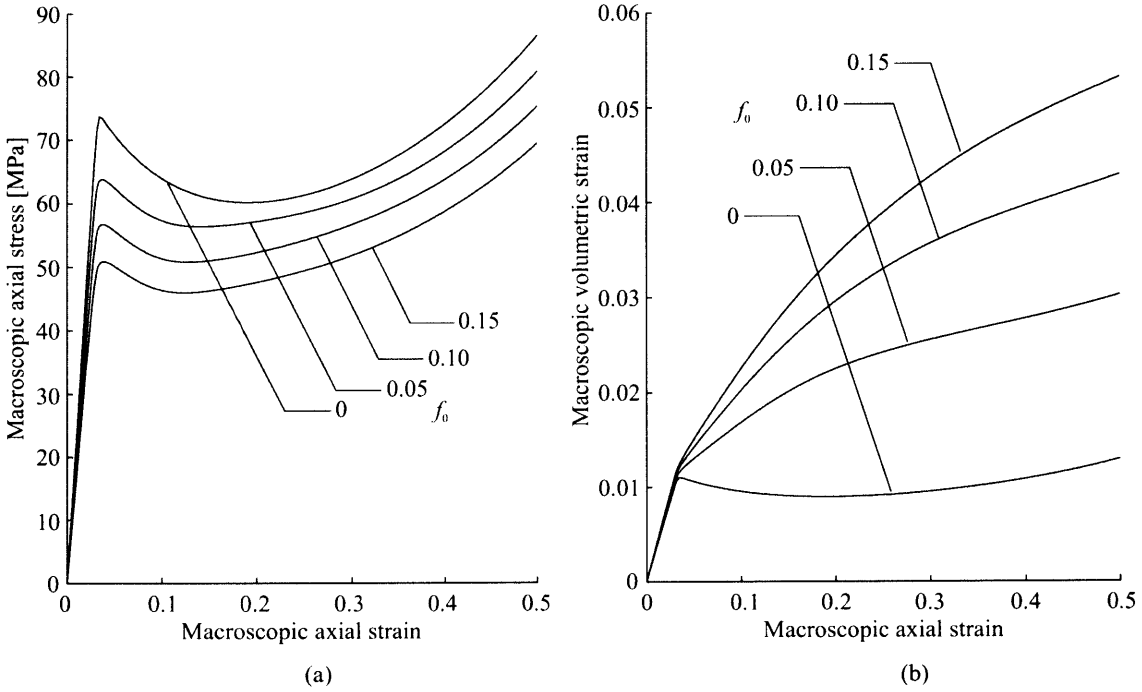

Figure 3-9: Macroscopic response of the 3D V-BCC model under macroscopic uniaxial tension at different initial void volume fractions: (a) evolution of macroscopic axial stress with macroscopic axial strain, (b) evolution of macroscopic volumetric strain with macroscopic axial strain.

For the case of $f_0 = 0.15$, shown in Fig. (3-10), the contours of plastic shear strain-rate reveal that plastic flow of the matrix initiates in the equatorial region of the void, and then successively spreads and grows across the inter-void ligament in the constrained direction. At this point, the inter-void ligament in the unconstrained direction is not encompassed by plastic flow. The plastic flow in the constrained direction is a feature which could not have been captured in a traditional two-dimensional plane-strain analysis in which the spherical voids are approximated as cylindrical. As the macroscopic axial strain continues to increase, the plastic flow spreads across the inter-void ligament in the (unconstrained) 2-direction. At this point, macroscopic yield of the porous material is reached. Interestingly, the interaction of the plastic flow in the constrained direction with that in the unconstrained direction results in the formation of two shear bands (Figs. (3-10d), Appendix A). The distributed plastic flow in the matrix reduces the post-yield strain softening as compared to that of the homopolymer, a feature which was also observed in the case of uniaxial tension. As the deformation progresses, all of the shear bands strain-harden and propagate up and down the inter-void ligaments as previously discussed for the case of uniaxial tension. This propagation coincides with macroscopic strain-hardening.

Simple shear deformation

The 3D V-BCC model was subjected to macroscopic simple shear deformation in the 23-plane. The macroscopic deformation gradient is given by

$$\overline{\mathbf{F}} = \mathbf{1} + \dot{\overline{\Gamma}} t \, \mathbf{e}_2 \otimes \mathbf{e}_3, \tag{3.20}$$

where $\dot{\overline{\Gamma}} = 0.0173 s^{-1}$ is the imposed nominal shear strain-rate. Three different initial void volume fractions were studied, $f_0 = \{0.05, 0.10, 0.15\}$, and the deformation was taken in each case to a final nominal shear strain $\overline{\Gamma} = \dot{\overline{\Gamma}} t = 0.35$. The macroscopic

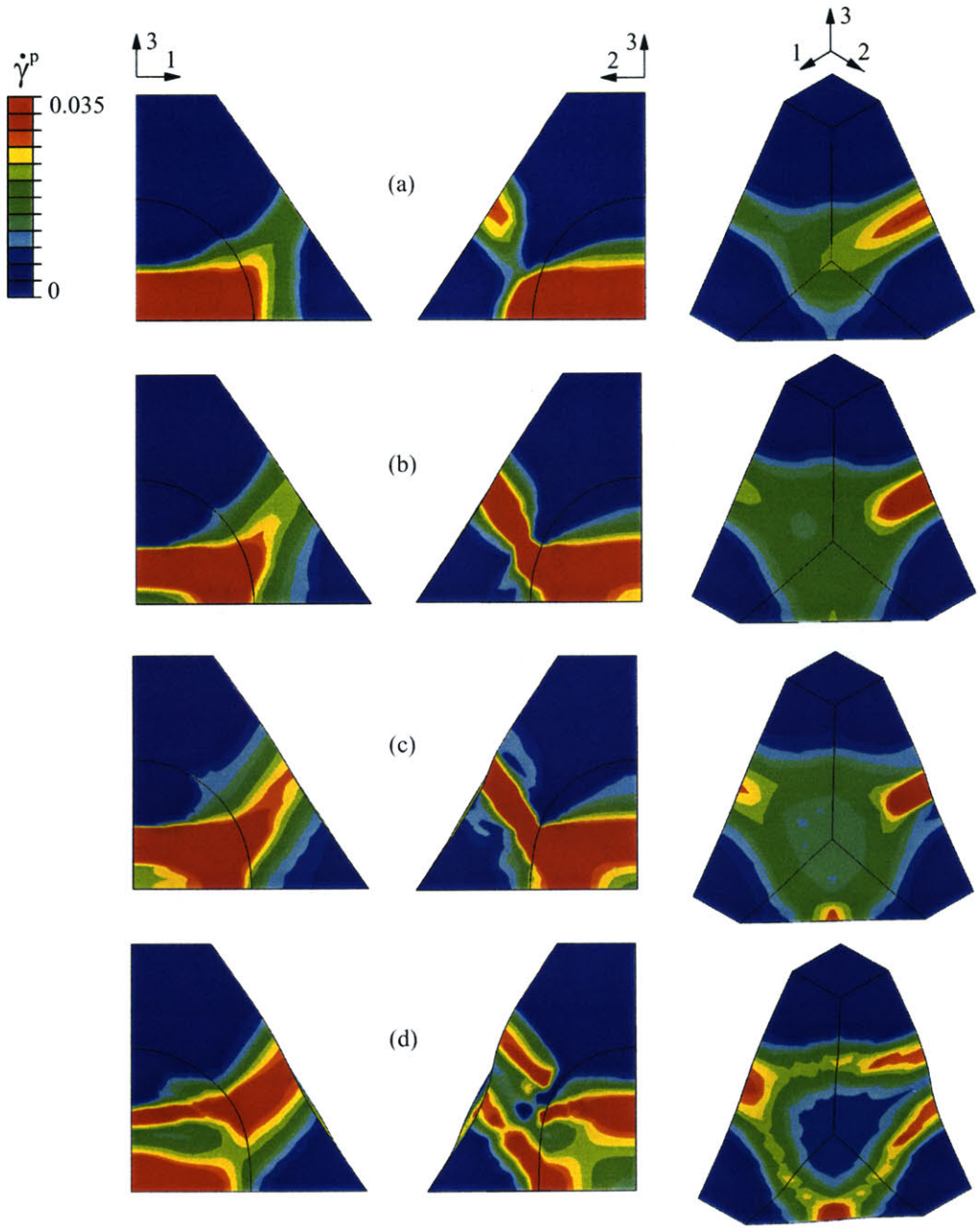

Figure 3-10: Contours of $\dot{\gamma}^p$ under macroscopic plane strain tension for an initial void volume fraction, $f_0 = 0.15$. The development of plastic shear localization is shown for increasing levels of macroscopic axial strain: (a) $\overline{E}_{33} \simeq 0.035$, (b) $\overline{E}_{33} \simeq 0.045$, (c) $\overline{E}_{33} \simeq 0.069$ and (d) $\overline{E}_{33} \simeq 0.127$.

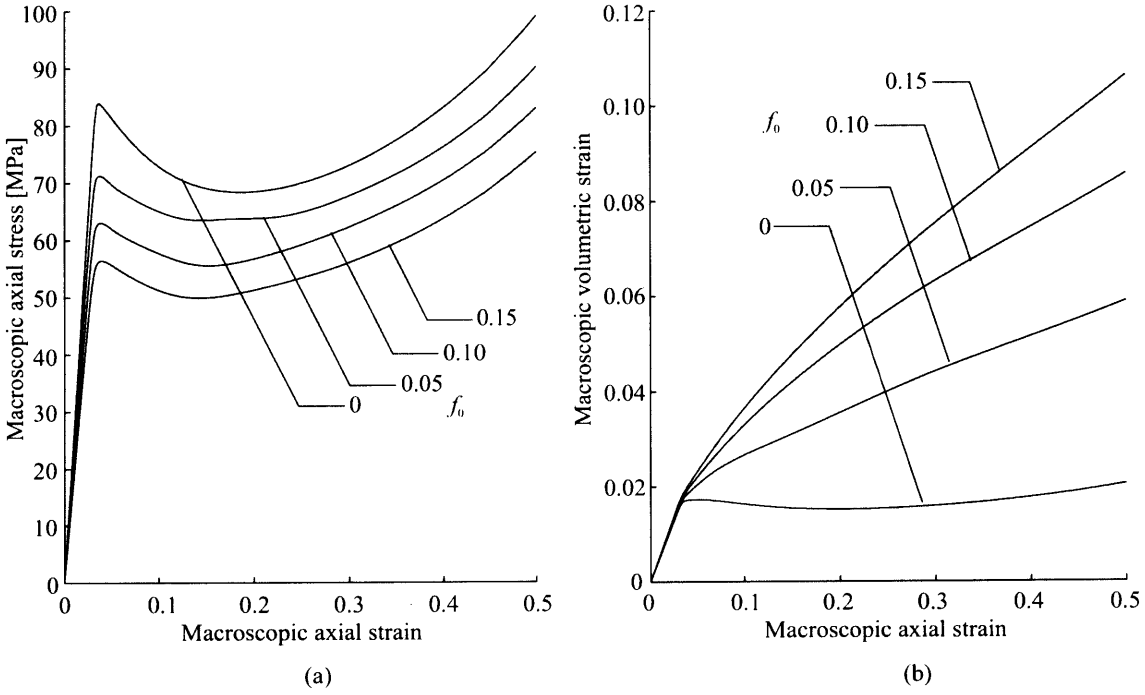

Figure 3-11: Macroscopic response of the 3D V-BCC model under macroscopic plane strain tension at different initial void volume fractions: (a) evolution of macroscopic axial stress with macroscopic axial strain, (b) evolution of macroscopic volumetric strain with macroscopic axial strain.

response of the porous material is computed in terms of the macroscopic nominal shear stress, $\overline{S}_{23}$, as a function of the macroscopically-applied nominal shear strain $\overline{\Gamma}$ (Fig. 3-13). Contours of plastic shear strain-rate are shown in Fig. (3-12) for the case of $f_0 = 0.15$. The plastic flow initiates at two locations on the void equator (Fig. 3-12a). At this point in the deformation, the onset of macroscopic yield has not yet been reached; the matrix is still predominantly in the elastic regime. As the deformation progresses, the plastic flow spreads in a Y-pattern until it penetrates the ligament thickness (Fig. 3-12a). As discussed previously, the local plastic flow prior to macroscopic yield appears in the stress-strain response as a slight non-linearity. The plastic flow then spreads across the inter-void ligament in the vertical direction. This "net section yield" corresponds to macroscopic yield of the porous material. Immediately after macroscopic yield (Fig. 3-13), the stress exhibits a sharp drop. The drop corresponds to the localization of yield and strain softening to a thin vertical shear band which penetrates the entire ligament thickness. The sudden drop is thought to be an artifact of the specific choice of macroscopic shearing direction, relative to the BCC lattice, and of the assumption of local (single-void) periodicity of the array. For the case of $f_0 = 0.05$, the macroscopic nominal shear stress, $\overline{S}_{23}$, exceeds that of the homopolymer around $\overline{\Gamma} = 0.2$ and at $\overline{\Gamma} = 0.27$ and beyond. Again, this is believed to be an artifact of the direction of shear relative to the underlying BCC void lattice. Macroscopic shearing of the porous material in a different direction would alter the predicted macroscopic response, as the 3D V-BCC model is not initially isotropic due to the underlying BCC lattice.

3.3 The lattice-based multi-void models

In the previous section, the 3D V-BCC cell model was introduced. The 3D V-BCC model assumes that voids are periodically located on a three-dimensional BCC lattice. In a single-void model, deformation events, such as shear-localization between voids, are forced to occur in a periodically repeating (void-to-void) manner. In a random porous microstructure, deformation events will, in general, occur in a se-

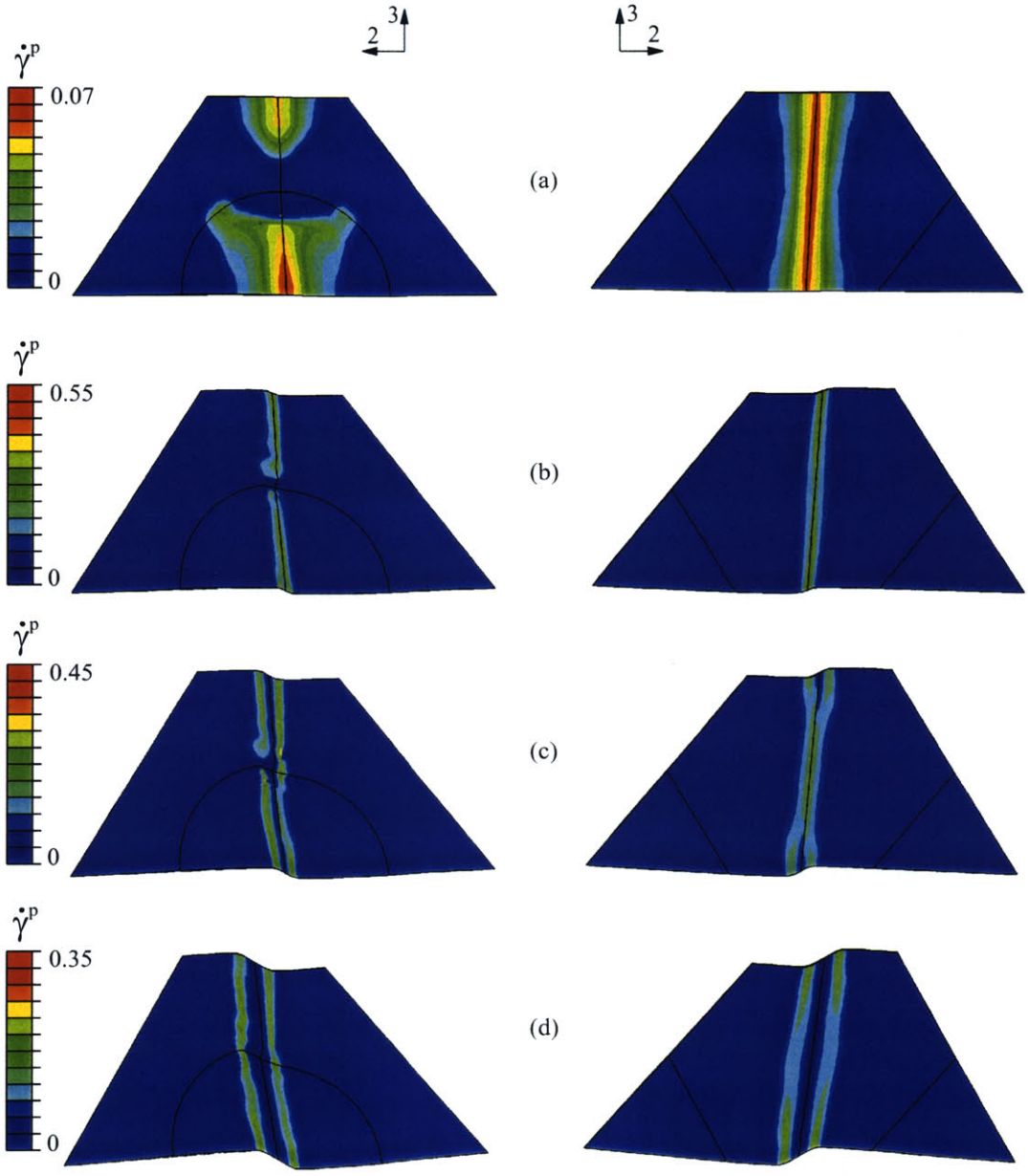

Figure 3-12: Contours of $\dot{\gamma}^p$ under simple shear deformation for an initial void volume fraction, $f_0 = 0.15$. The development of plastic shear localization is shown for increasing levels of macroscopic nominal shear strain, $\overline{\Gamma}$: (a) $\overline{\Gamma} \simeq 0.048$, (b) $\overline{\Gamma} \simeq 0.068$, (c) $\overline{\Gamma} \simeq 0.085$ and (d) $\overline{\Gamma} \simeq 0.122$.

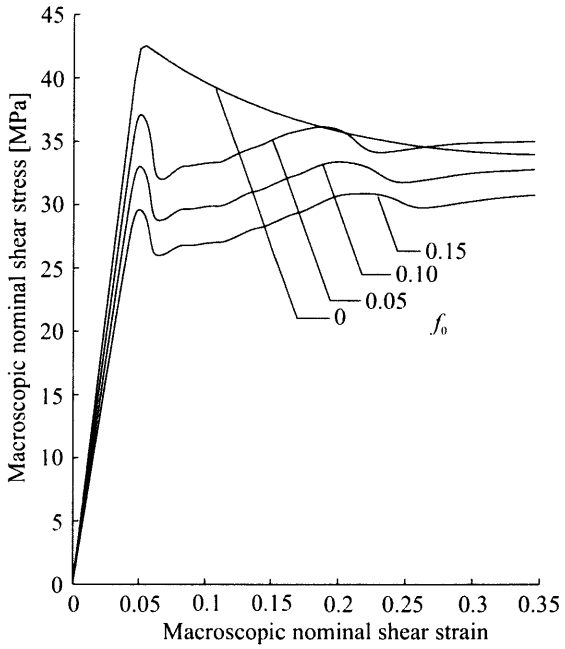

Figure 3-13: Macroscopic response of the 3D V-BCC model under simple shear deformation at different initial void volume fractions: evolution of macroscopic nominal shear stress with macroscopic nominal shear strain.

quential, percolating, manner. This type of deformation cannot be captured using a single-void model such as the 3D V-BCC model. In this section, two simplified idealizations (RVEs) of a random porous microstructure are introduced. Both models consider randomly distributed voids on a cubic lattice. The first model assumes, for sake of meshing simplicity, that the voids are cubic (Fig. 3-15). The second model is a refinement of the first model as it more accurately represents void shapes, by considering them to be spherical (Fig. 3-18). In the following discussion, these two RVEs are examined and compared. Macroscopic hydrostatic deformation and macroscopic simple shear deformation are used to establish a suitable number of voids for each RVE, and a suitable finite element mesh density, as well as to compare the relative merits of the two models.

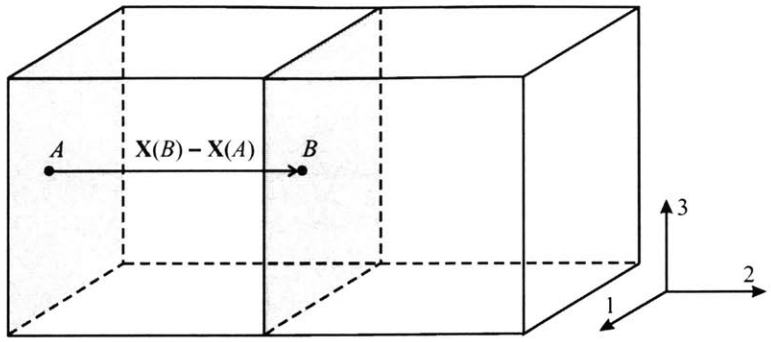

Figure 3-14: Periodically located points on the surface of the lattice-based multi -void models.

3.3.1 Boundary conditions

The lattice-based multi-void models (RVEs) consist of cubes which contain cubic or spherical voids, The RVEs are space-filling and spatially periodic (Fig.3-2). Periodic boundary conditions are applied to each RVE. Each pair of surface points is related through the macroscopic deformation gradient (Eq. 3.1) as,

$$\mathbf{u}(B) - \mathbf{u}(A) = \left(\overline{\mathbf{F}} - \mathbf{1}\right)\{\mathbf{X}(B) - \mathbf{X}(A)\} = \overline{\mathbf{H}}\{\mathbf{X}(B) - \mathbf{X}(A)\}. \tag{3.21}$$

3.3.2 The LC model (cubic voids on a lattice)

The LC model assumes that the voids are cubic and randomly dispersed on a cubic lattice of unit volume (Fig. 3-15). The initial void volume fraction, f_0, is determined as

$$f_0 = \frac{M}{N^3}, \tag{3.22}$$

where M is the number of voids, and N is the number of lattice positions along each edge of the RVE. In order to avoid unrealistic, worm-like, cavities in the matrix, no voids are allowed to be located face-to-face in the matrix. The M voids can be arranged on any of the N^3 sites as long as this constraint is satisfied. Thus,

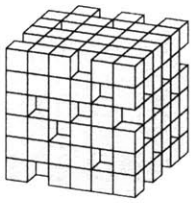

Figure 3-15: The lattice-based multi-void RVE with cubic voids. $N = 6$.

N	M (number of voids)	f_0
4	10	0.156
6	32	0.148
8	77	0.15

Table 3.1: Resulting initial void volume fraction, f_0, as a function of RVE size (N) and number of voids (M) for the RVE with cubic voids.

a number of possible void distributions in the RVE can be selected to represent the actual porous microstructure. For very large RVE sizes and a large number of randomly distributed voids, the RVE response should become independent of the particular void distribution, and different initial void topologies should give rise to the same macroscopic and microscopic features. However, if an insufficient number of voids is considered, the RVE response will display a dependence on the topology of the initial void distribution and will deviate from the isotropic response of a truly random porous microstructure. In order to find the minimal number of voids required to represent the microstructure, the cases of macroscopic hydrostatic deformation and macroscopic simple shear deformation are considered for an initial void volume fraction $f_0 = 0.15$. Three RVE 'sizes' are considered: $N = \{4, 6, 8\}$. Since M and N are integers, the initial void volume fraction is restricted to certain values (Eq. 3.22). The RVE size, N, and the desired initial void volume fraction result in certain values of M, and corresponding values of f_0 which are the best attainable approximations for the desired level of porosity of the RVE (Table 3.1). Twenty-node hexahedral finite elements with reduced integration were used to discretize the RVE. As discussed in the case of the 3D V-BCC model, reduced integration is suitable for nearly-incompressible

analyses. Figures (3-16a,c,e) show the macroscopic hydrostatic stress ($\overline{T}_m = \mathrm{tr}\,\overline{\mathbf{T}}/3$) vs. macroscopic volumetric change ($\overline{J} = \det \overline{\mathbf{F}}$), averaged over ten different initial void distributions, for the three values of N, and Figs. (3-16b,d,f) show the corresponding average macroscopic nominal shear stress ($\overline{S}_{23}$) vs. macroscopic nominal shear strain ($\overline{\Gamma}$) for the case of macroscopic simple shear deformation. The standard deviation in the predicted response is shown in each case as vertical error bars at discrete strain levels. The figures show that as the number of voids is increased, the standard deviation of the predicted average response decreases. For the case of $N = 4$ and hydrostatic deformation, there is a significant scatter in the predicted macroscopic response of the RVE. Macroscopic plastic volume change is accommodated through local plastic shearing of the matrix material. In the case of macroscopic hydrostatic deformation, there is no preferential orientation for the percolation of plastic flow, and the possible shearing directions in the matrix are governed by the spatial distribution of the voids. When few voids are considered, there are only a few available shearing directions, and these are a strong function of the void distribution. This explains the large standard deviation in the predicted average response under hydrostatic deformation, compared to simple shear deformation. Moreover, the corners of the cubic voids introduce artificial stress and deformation concentrations in the matrix. The effects of a certain distribution of voids on the macroscopic stress-strain response are accentuated by these stress concentrations. The sharp corners resulting from the cubic voids also imply that the localized nature of plastic flow in the glassy polymer matrix cannot be accurately resolved. Any interpretation of local field quantities, such as stress, strain and strain-rate, is therefore meaningless.

Predictions using the medium-sized RVE ($N = 6$) provide a reasonably low standard deviation in the macroscopic response under both hydrostatic deformation and simple shear deformation (Fig. 3-16). Thus, an RVE of this size can be used to obtain a fairly adequate representation of the macroscopic stress-strain response. The *average* response of the ten simulations at $N = 6$ is similar to the *average* response of the ten simulations at $N = 8$ (Fig. 3-17). This suggests that the dependence of the macroscopic response on the specific void distribution, which is reflected by the

magnitude of the error bars in the curves, can be circumvented by considering the average of several simulations with $N = 6$ and different void topologies.

It is expected that the number of simulations required for a given RVE size to obtain accurate results is a strong function of the matrix material under consideration. For example, hyperelastic materials, which undergo large deformation in absence of the localized plastic flow in glassy polymers, are likely to exhibit much lower void topology dependence, and therefore require fewer simulations. For these materials, the LC model constitutes an effective, computationally inexpensive model of the porous microstructure.

The simulations used to find the minimal number of voids in the RVE were performed on relatively coarse finite element meshes. In order to find a suitable finite element mesh density, a thorough mesh refinement study is required. As the LC model is not suitable for the study of porous glassy polymers, in view of the stress concentrations resulting from the cubic voids, such a study will not be pursued here. In the following section, an extension of the LC model will be presented (the LS model), where the voids are modeled as spherical. The LS model is more suitable for the study of porous glassy polymers, and a finite element mesh density study was then performed for this improved model.

3.3.3 The LS model (spherical voids on a lattice)

The model with initially spherical voids is an extension of the model with cubic voids: the voids are also randomly dispersed on a cubic lattice, and the RVE 'size' is given by the number of lattice units, N, along the edge of the RVE. Figure (3-18) shows that each lattice unit in the cube is either solid, or contains a void. The voids are restricted to the fixed lattice positions, but the relative size of each void can be varied. In this study, a uniform initial void size is considered. The initial void volume fraction, f_0, is then given by

$$f_0 = f_0^{local} \frac{M}{N^3}, \tag{3.23}$$

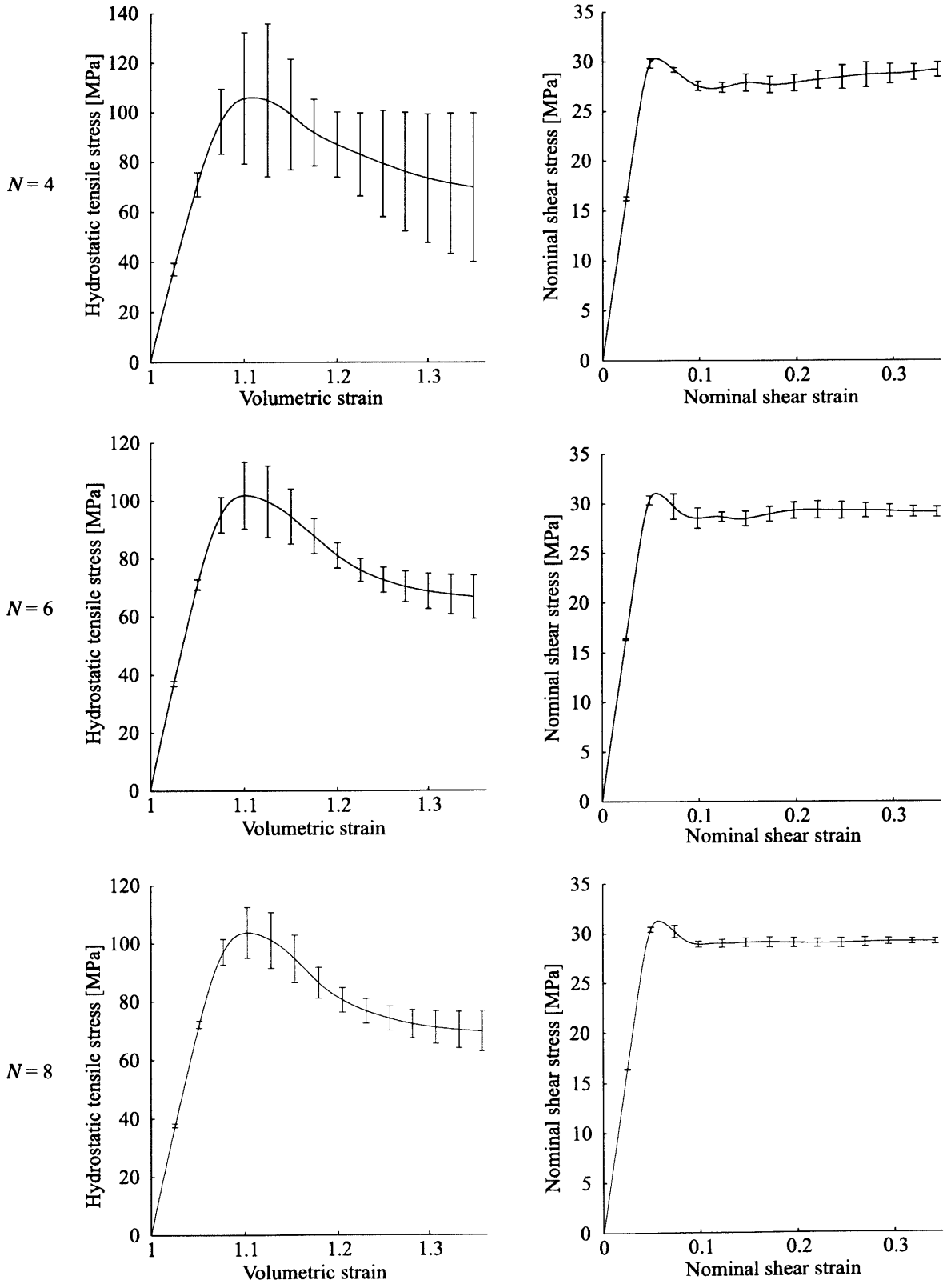

Figure 3-16: The LC model: Influence of the number of voids, M, on the predicted macroscopic stress-strain response ($f_0 = 0.15$).

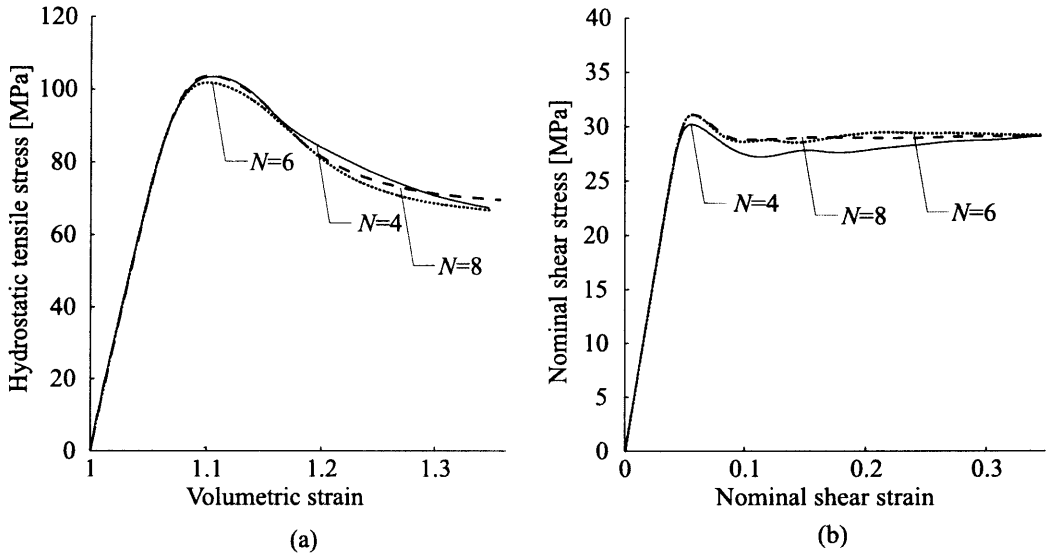

Figure 3-17: The LC model: Superposition of the mean response at $N = \{4, 6, 8\}$ and $f_0 = 0.15$ for (a) macroscopic hydrostatic deformation and (b) macroscopic simple shear deformation.

where f_0^{local} is the volume fraction occupied by a void in a voided lattice site unit (Fig. 3-18a), and M and N are defined in Eq. (3.22). The local void volume fraction f_0^{local} is an upper bound on the macroscopically-attainable initial void volume fraction, f_0 for this type of RVE. In the limit $M \to N^3$, where every lattice site in the RVE contains a void, the macroscopic void volume fraction approaches the local void volume fraction $f_0 \to f_0^{local}$. In this limit, there is no purpose in considering multiple voids, as a single-void periodic RVE can model this distribution. It is therefore desirable to choose a large local void volume fraction. In the present simulations $f_0^{local} = 0.45$ is used. This value results in voids that are large compared to the voided unit, while maintaining a reasonable inter-void ligament thickness (Fig. 3-18b).

As in the case of the LC model, it is important to determine the minimal RVE size, N, required to represent a random porous microstructure with sufficient approximation. For this purpose, the case of $f_0 = 0.15$ is studied for the case of macroscopic hydrostatic deformation and macroscopic simple shear deformation. Three RVE sizes are considered: $N = \{4, 6, 8\}$ with $k = 1$. The choice of the local void volume fraction, together with the integers M and N, restrict the initial macroscopic void

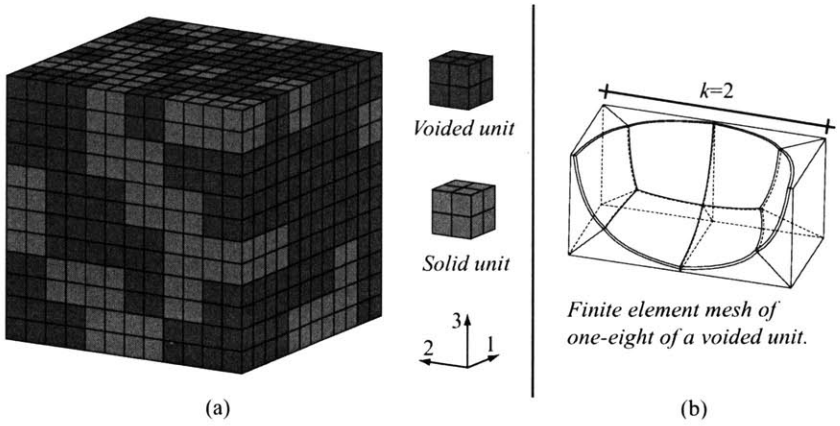

Figure 3-18: The LS model: Example topology for the case of $N = 6$, $f_0 = 0.15$ and a mesh density given by $k = 2$ (number of divisions in each direction of the lattice units).

N	M (number of voids)	f_0
4	21	0.147
6	72	0.15
8	171	0.15

Table 3.2: Resulting initial void volume fraction, f_0, as a function of RVE size (N) and number of voids (M) for the RVE with spherical voids, using $f_0^{local} = 0.45$.

volume fraction to certain values. The desired initial void volume fraction together with the RVE size N result in certain values of M, and corresponding values of f_0 (Table 3.2). In the simulations, twenty-node hexahedral finite elements with reduced integration are used. As discussed in preceding sections, this element type is suitable for nearly-incompressible analyses. Figures (3-19a,c,e) show the macroscopic hydrostatic tension ($\overline{T}_m = \mathrm{tr}\,\overline{\mathbf{T}}/3$) vs. macroscopic volumetric change ($\overline{J} = \det \overline{\mathbf{F}}$) averaged over ten different initial void distributions for the three values of N, and Figs. (3-19b,d,f) show the average macroscopic nominal shear stress ($\overline{S}_{23}$) vs. macroscopic nominal shear strain ($\overline{\Gamma}$) for the case of macroscopic simple shear deformation. The standard deviation in the predicted response in each case is shown as vertical error bars. It is seen that as the RVE size, and therefore the number of voids, increases,

the standard deviation in the predicted macroscopic response decreases. As in the case of the LC model, macroscopic volume change is accommodated through local plastic shearing of the matrix material. In the case of macroscopic hydrostatic deformation, there is no preferential orientation for the plastic flow, and the possible shearing directions are governed by the spatial distribution of voids. When a small number of voids is considered, there are only few shearing directions, and these are a strong function of the spatial distribution of voids. This explains the comparatively large standard deviations for the cases of hydrostatic deformation compared to simple shear deformation. In the LS model, the volume of each spherical void is smaller than the volume of the cubic voids in the LC model, and therefore a larger number of voids is considered for the same RVE size and void volume fraction. The larger number of voids in the LS model produces a larger number of possible shearing directions in the material, and the spherical shape of the voids removes the stress concentrations associated with the cubic voids in the LC model. As discussed previously, both these features significantly affect the macroscopic response of the RVE under macroscopic hydrostatic deformation, and Figs.(3-16b,d,e) and (3-19b,d,e) show that the standard deviation in the macroscopic response is overall lower in the LS model.

Predictions using the medium-sized RVE ($N = 6$) provide a reasonably low standard deviation in the macroscopic response under both hydrostatic deformation and simple shear deformation (Fig. 3-19). Thus, an RVE of this size can be used to obtain a fairly adequate representation of the macroscopic stress-strain response. The *average* response of the ten simulations at $N = 6$ is similar to the *average* response of the ten simulations at $N = 8$; small discrepancies are seen in the simple shear response (Fig. 3-20). This suggests that the dependence of the macroscopic response on the specific void distribution can be circumvented by considering the average of several simulations with $N = 6$ and different void topologies.

Each of the simulations used to determine an appropriate number of voids for the LS model were performed using a single finite element mesh density ($k = 1$). In order to investigate the effects of successive finite element mesh refinements on the macroscopic response, a small RVE with $N = 3$ ($M = 3$ voids) and $f_0 = 0.15$, and a

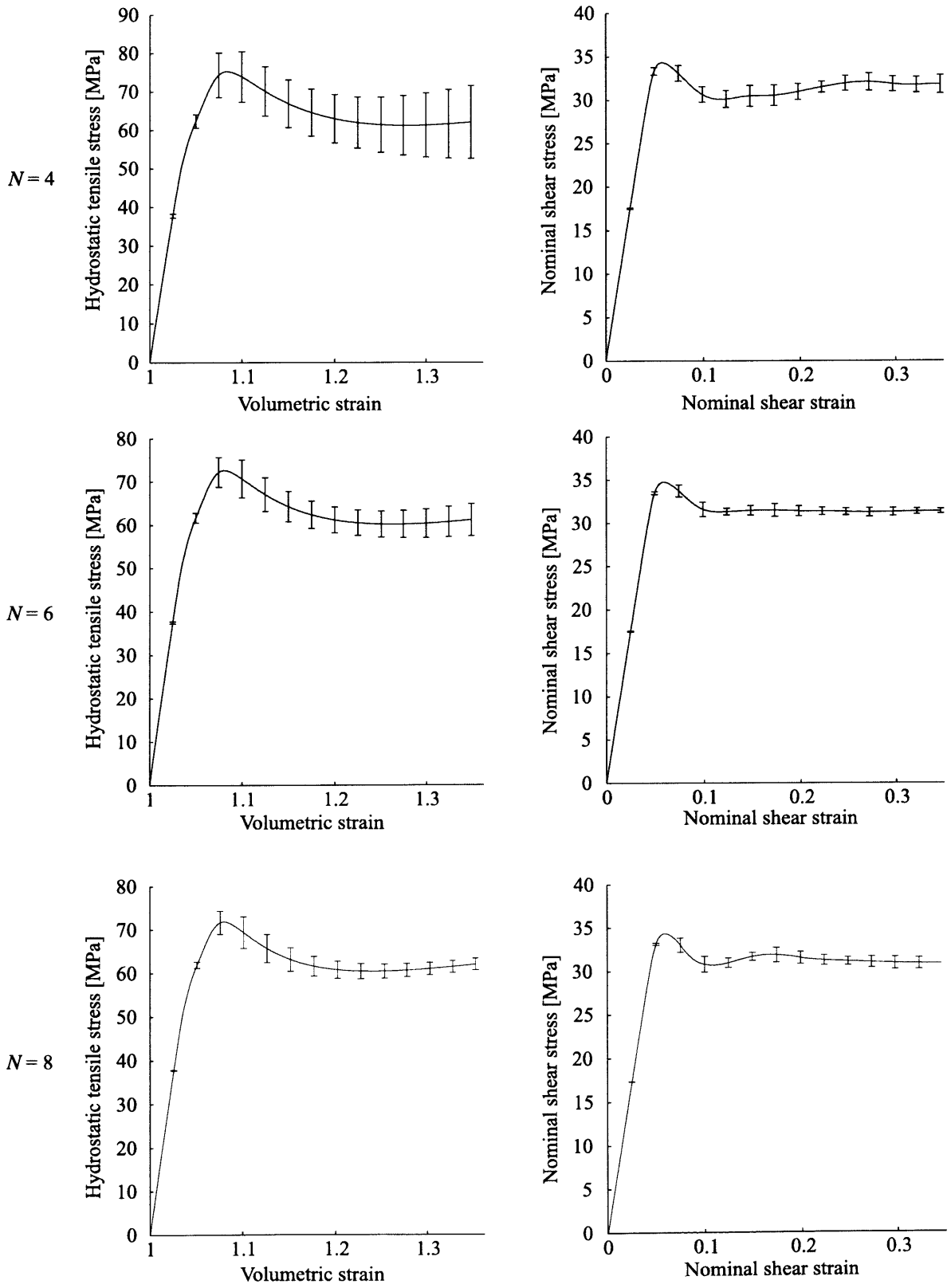

Figure 3-19: The LS model: Influence of the number of voids, M, on the predicted macroscopic stress-strain response ($f_0 = 0.15$).

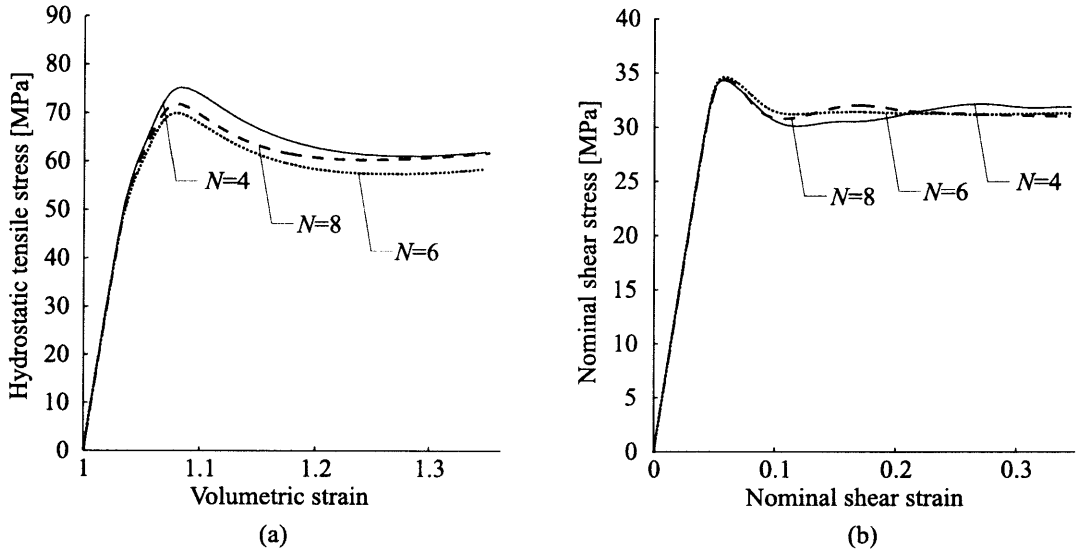

Figure 3-20: The LS model: Superposition of the response at $N = \{4, 6, 8\}$ and $f_0 = 0.15$ for (a) macroscopic hydrostatic deformation and (b) macroscopic simple shear deformation.

given void topology is considered. The RVE is subjected to macroscopic hydrostatic deformation, and the change in the stress-strain response upon mesh refinements is studied. The mesh density in the LS model is controlled by the parameter k (Fig. 3-21a). The parameter k controls the number of edge divisions of each lattice unit in the mesh. For example, if $k = 2$, the total number of finite elements along the side of the RVE is $2N$. In the case of a void-containing lattice unit, the parameter k also controls the number of elements in the radial direction of the void (Fig. 3-21c). Figure (3-21) shows that the predicted macroscopic stress decreases as the finite element mesh is refined. The figure also shows that the predicted stress level appears to converge for an increasing value of k. The computational expense involved in solving the boundary value problem associated with the mesh density $k = 3$ is considerable. Although the stress-strain response for $k = 2$ has not converged, this mesh density is used in the following discussion, as it provides a reasonable balance between computational expense and numerical accuracy.

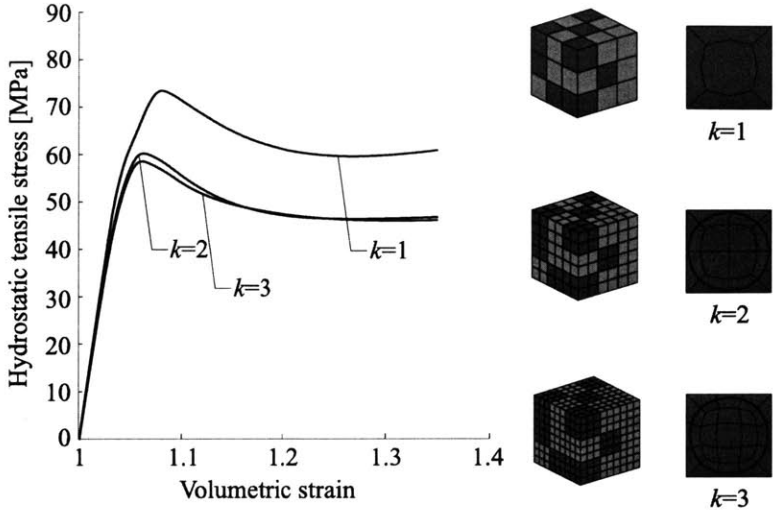

Figure 3-21: The LS model: Influence of mesh refinements on the predicted macroscopic stress-strain response ($f_0 = 0.15$).

3.3.4 Lattice-based multi-void models: Summary

Two multi-void RVEs have been introduced to model a random porous microstructure by placing voids on a cubic lattice. The LC model considered cube-shaped voids, and the LS model considered spherical voids. Both models were used in conjunction with a glassy polymer matrix. The relative macromechanical and micromechanical merits of the models are discussed below.

In general, the number of voids necessary in each RVE to accurately capture the macroscopic response of a porous microstructure is a strong function of the constitutive behavior of the matrix material. When the RVE does not contain a sufficient number of voids, the predicted macroscopic response displays a dependence on the specific topology of the void distribution in the RVE. For both the LC and the LS models, it was found that the standard deviation in the predicted stress-strain response decreased with an increasing number of voids. For the present application to glassy polycarbonate, predictions obtained using RVEs with $N = 6$ provided a suffi-

ciently low standard deviation for the macroscopic response [4]. Any RVE of this size can then be used to obtain a fairly adequate representation of the macroscopic material response. The dependence of the predicted macroscopic response on the specific location of voids in the RVE can be further reduced by considering the average of ten simulations with different void topologies. The average response for ten simulations with medium size ($N = 6$) RVEs was found to closely resemble the macroscopic response predicted by larger ($N = 8$) RVEs. Topology-independent predictions can thus be obtained either by relying on a single large RVE or by averaging out the predictions over a number of smaller RVEs. Note that the RVE size studies for the two models were carried out on finite element meshes of different densities. In order to directly compare the macroscopic predictions of the two models, a thorough mesh refinement study is required.

In the LC model, the corners of the cube-shaped voids result in artificial stress concentrations in the material. This means that local field quantities, such as stress and strain, are not realistically represented in the matrix. In the application of micromechanical models to investigate the brittle to ductile transition in porous, or rubber-toughened glassy polymers, it is of critical importance to be able to continuously and accurately monitor the local deformation history and the local stress state of the matrix material. From this point of view, the LC model is an inadequate representation of the porous microstructure. However, for the purpose of studying the macroscopic stress-strain response of materials that do not exhibit a ductile-to-brittle transition under the loading situations of interest, the LC model is an inexpensive alternative to more elaborate and computationally expensive models.

The LS model, in which the voids are modeled as spherical, is an improvement over the LC model, as the stress concentrations associated with the corners of the cube-shaped voids in the LC model are alleviated[5]. The LS model more accurately represents local field quantities in the matrix material. As mentioned previously, mi-

[4]In the LC model, this corresponds to $M = 32$ voids, and in the LS model, it corresponds to 72 voids.

[5]Spurious stress concentrations are not entirely eliminated due to the coarseness of the finite element representation of the spherical void surface for the selected level of mesh refinement.

croscopic field information is important in understanding the ductile-to-brittle transition in porous glassy polymers, and the ability to provide such information is a considerable advantage of the LS model.

In the LS model, the diameter of each void is restricted by the lattice spacing $1/N$. This poses a constraint on the maximum-attainable macroscopic void volume fraction in the LS model. In the limit where every lattice site is occupied by a void, the purpose of considering multiple voids is defeated, and the ability of the LS model to represent the spatial randomness of voids, at high macroscopic voids volume fractions, is therefore limited.

In summary, the two models presented in this section display topological similarities; they both consider voids that are randomly distributed on a cubic lattice. The focus of the present work is the study of porous glassy polymers on a macroscopic and microscopic level. The LC model is inadequate to study these types of matrix materials, as the cube-shaped voids in the model misrepresent local field quantities in the matrix material. In view of the similarities of the two models, and the limitations of the LC model, the LC model is abandoned in the following discussion. The LS model is instead used to study the two cases of macroscopic uniaxial tension and macroscopic simple shear deformation on a microscopic and macroscopic level.

3.3.5 Results

Uniaxial tension

The LS model was subjected to macroscopic uniaxial tension for different initial void volume fractions, $f_0 = \{0.05, 0.10, 0.15\}$. The macroscopic axial-stress / axial-strain response is given in Fig. (3-22a), and the evolution of volumetric strain with axial deformation is shown in Fig. (3-22b). Each curve in (a), and the corresponding curve in (b), is the average of the response of ten different RVEs. In the curves in (a), macroscopic yield is defined as the point where the macroscopic axial stress exhibits a peak, followed by softening. The microscopic response of the porous material is characterized by plotting the evolution of plastic shear strain-rate, $\dot{\gamma}^p$, with axial de-

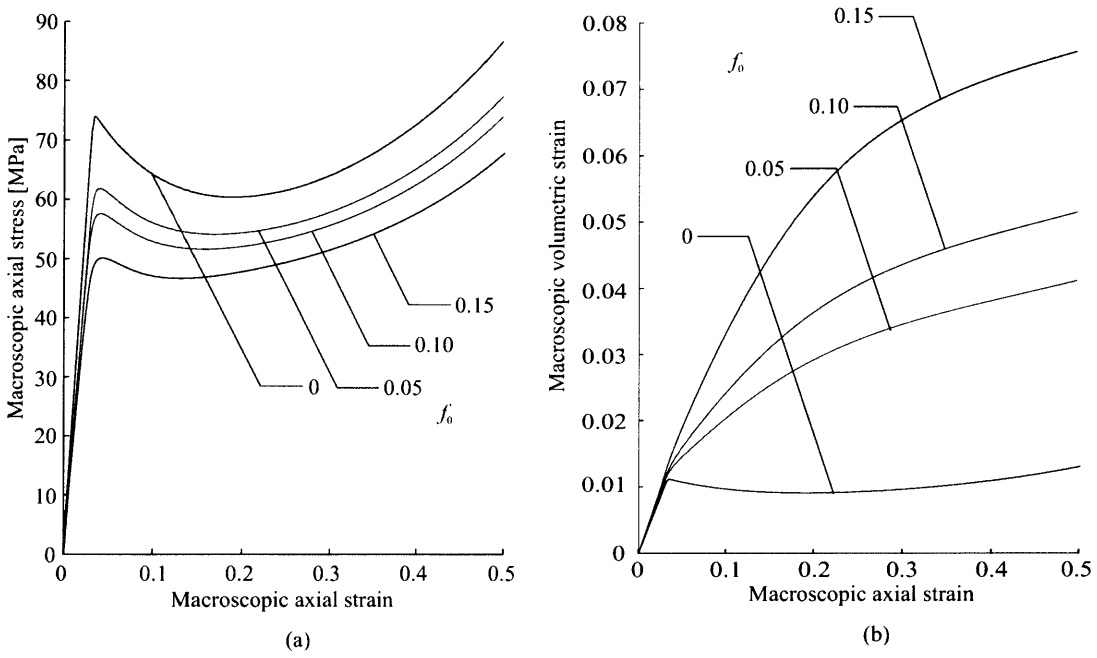

Figure 3-22: Macroscopic response of the LS model under uniaxial tension at different initial void volume fractions ($N = 6$, $k = 2$): (a) evolution of macroscopic axial stress with macroscopic axial strain, (b) evolution of macroscopic volumetric strain with macroscopic axial strain.

formation, for an RVE with $f_0 = 0.15$. Figure (3-23a) shows that plastic flow initiates in the equatorial region of the voids. The figure shows that voids that have side-to-side neighbors, with respect to the macroscopic principal loading direction, deform more rapidly than voids that do not. Due to the nature of the void arrangement in the LS model, voids that are located side-to-side are separated by a very thin inter-void ligament. The thin ligament carries only a limited load, and the voids essentially act as a single, large void. At the point in macroscopic deformation corresponding to Fig. (3-23a), macroscopic yield has not been reached; the plastic flow in the RVE is confined to the vicinity of the voids, and the matrix is predominantly in the elastic regime. As the macroscopic deformation progresses, macroscopic yield of the blend is reached (Fig. 3-22a). This corresponds to the development of local shear bands between voids, and coalescence of these shear bands into macroscopic shear bands which span the entire RVE (Fig. 3-23b). The matrix material in the macroscopic

shear bands begins to strain-harden as the deformation progresses, and the plastic flow spreads to neighboring matrix material; existing shear bands between voids become broader (less sharp), and previously undeformed inter-void ligaments begin to flow plastically (Fig. 3-23c). This corresponds to the strain-softening regime of the stress-strain response (Fig. 3-22a). At higher levels of macroscopic axial strain, the plastic flow in the matrix becomes more homogeneous, and the blend displays macroscopic strain-hardening. Figure (3-23d) shows the RVE at $\overline{E}_{33} \simeq 0.5$. Figure (3-23) shows the anisotropic growth of voids in the blend; the voids are stretched in the main loading direction, and contracted in the lateral direction (the void shapes are outlined in red for clarity). Figure (3-23d) also illustrates the necessity of imposing periodic boundary conditions on the RVE. The highly localized nature of plastic flow in the matrix causes the RVE surfaces to deform at every point markedly different from the macroscopically-imposed deformation gradient. As discussed previously, boundary conditions of the type $\mathbf{u}(A) = \left(\overline{\mathbf{F}} - \mathbf{1}\right) \mathbf{X}(A)$, applied to all boundary points, A, of the RVE are overconstraining the RVE and are therefore highly unsuitable, whereas boundary conditions based on Eq. (3.1) are appropriate for this type of analysis.

The evolution of macroscopic volumetric strain is shown in Fig. (3-22b) for the studied levels of initial void volume fraction. As in the case of the 3D V-BCC model, the evolution of macroscopic volumetric strain with axial deformation reflects the initial elastic Poisson effect, followed by volumetric straining associated with the plastic growth of voids in the matrix. However, compared to the 3D V-BCC model, the LS model predicts notably higher levels of macroscopic volumetric strain. In the LS model, the voids are arranged randomly on a cubic lattice. In effect, the voids are located along certain planes in the matrix, separated by a solid layer of matrix material. When macroscopic uniaxial tension is imposed along the principal cube directions, these solid matrix layers introduce an artificial lateral stiffness to the RVE, which reduces lateral constraction of the RVE, as inter-void ligaments are prevented from deforming through shearing and rotation. Socrate and Boyce [63] report a similar finding for a single-void model based on a stacked hexagonal array of voids (the axisymmetric SHA model) (Fig. 3-1a), where a stiff matrix layer resulted

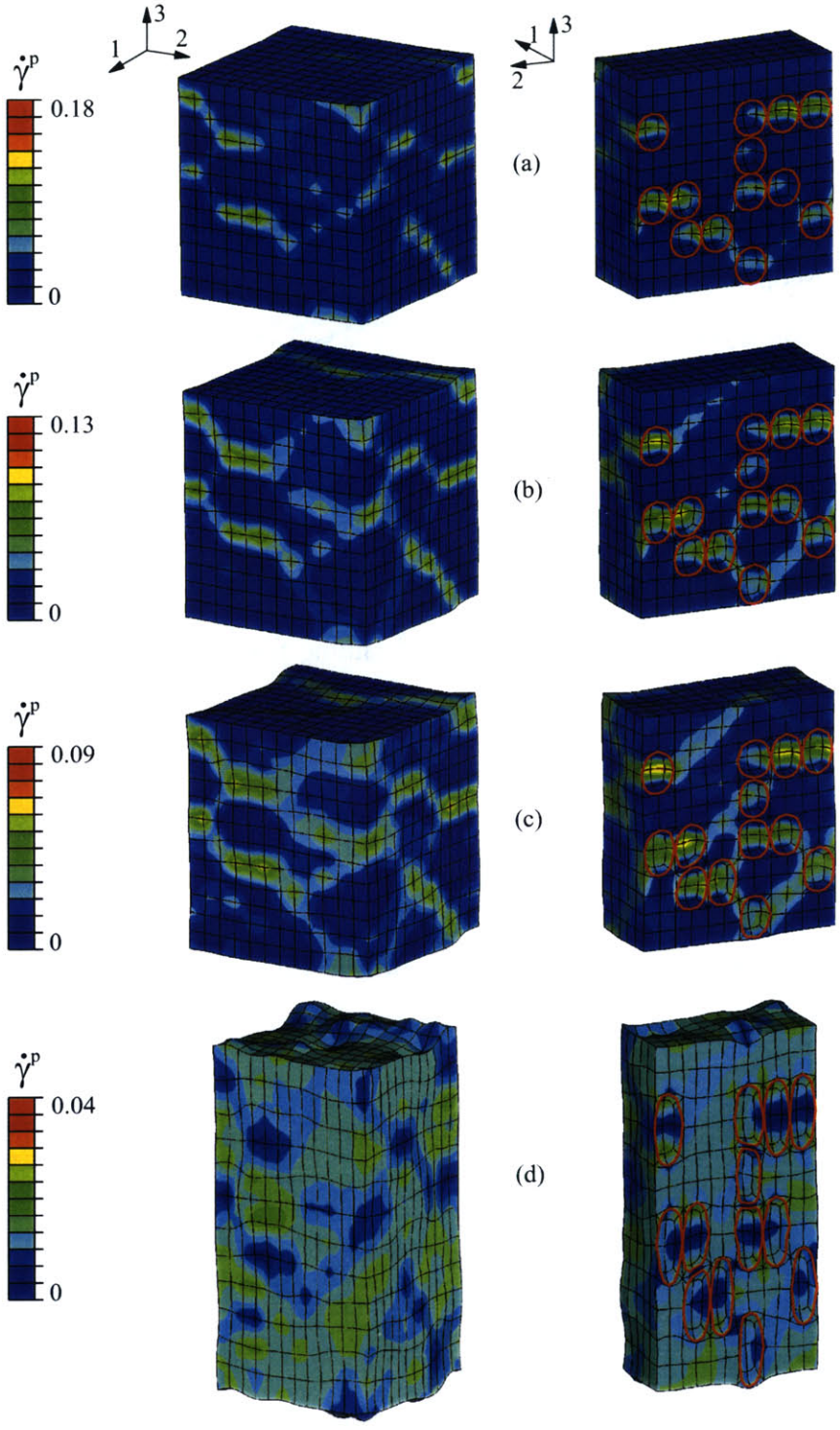

Figure 3-23: Contours of $\dot{\gamma}^p$ under uniaxial tension for an initial void volume fraction, $f_0 = 0.15$. The development of plastic shear localization is shown for increasing levels of macroscopic axial strain: (a) $\overline{E}_{33} \simeq 0.040$, (b) $\overline{E}_{33} \simeq 0.075$, (c) $\overline{E}_{33} \simeq 0.11$ and (d) $\overline{E}_{33} \simeq 0.50$.

in unrealistically high levels of volumetric strain.

Since macroscopic uniaxial tension was imposed along the principal cube directions, it would indeed be interesting to investigate how the micromechanical and macromechanical material response would change if the RVE was deformed along different axes. This has not been carried out in the present work, but we note that if the macroscopic deformation gradient, $\overline{\mathbf{F}}$, is imposed using Eq. (3.1), macroscopic uniaxial tension along different coordinate axes can be readily studied by applying a rotation to $\overline{\mathbf{F}}$.

Simple shear deformation

The LS model with $N = 6$ and $k = 2$ is subjected to macroscopic simple shear deformation for three different initial void volume fractions, $f_0 = \{0.05, 0.10, 0.15\}$. Simple shear is taken to occur perpendicular to the 23-plane, and the macroscopic deformation gradient is given by

$$\overline{\mathbf{F}} = \mathbf{1} + \dot{\overline{\Gamma}} t \mathbf{e}_2 \otimes \mathbf{e}_3, \tag{3.24}$$

where the imposed nominal shear strain-rate is taken to be $\dot{\overline{\Gamma}} = 0.0173 s^{-1}$. The macroscopic nominal shear stress, $\overline{S}_{23}$, vs. macroscopic nominal shear strain, $\overline{\Gamma}$, is shown in Fig. (3-24) for the three levels of void volume fraction. Each curve in the figure corresponds to an average of the stress-strain response for ten different RVEs. In the curves, macroscopic yield is defined as the point in the deformation where the macroscopic nominal shear stress exhibits an initial peak, followed by a drop. The microscopic response is characterized by plotting contours of plastic shear strain-rate, $\dot{\gamma}^p$, at various stages of the deformation, for one of the RVEs at $f_0 = 0.15$ (Fig. 3-25). In the present case of $f_0 = 0.15$ and $N = 6$, there are 72 voids in the RVE. Relative to the cubic directions of the RVE, the void centers are located on six distinct planes. When the RVE is subjected to macroscopic simple shear deformation according to Eq. (3.24), a "weakest" plane can be identified as the plane with unit normal $\mathbf{e}_3$ on which the largest number of voids is located. In the particular RVE used here, the

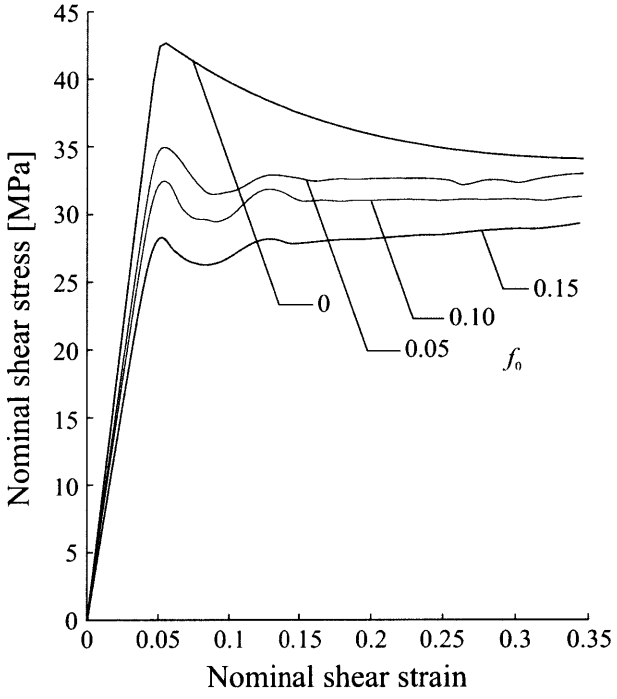

Figure 3-24: Macroscopic response of the LS model under simple shear deformation at different initial void volume fractions: evolution of macroscopic nominal shear stress with macroscopic nominal shear strain.

number of voids on the weakest plane is 16 (out of the total 72). Figure (3-24a) shows that plastic flow in the RVE develops on this weakest plane. At this point in the deformation, the plastic flow has not yet developed into a macroscopic shear band; there are still regions on the weak plane that are in the elastic regime, and macroscopic yield of the blend has not been reached (Fig. 3-24a). As the macroscopic deformation progresses, the plastic flow along the weakest plane forms a macroscopic shear band, and macroscopic yield of the blend is reached. Figure (3-25b) shows, at a later stage of macroscopic deformation, that the plastic flow is still confined to the weakest plane, and that the localized deformation in the shear band causes voids to deform and rotate to accommodate the macroscopic deformation (the void shapes are outlined in red in the figure for clarity). As the matrix material in the shear band continues to deform plastically, it begins to strain-harden, and deformation ceases. Instead, plastic flow develops on another plane in the RVE (Fig. 3-25c). Similar to the location for initial plastic flow in the RVE, this plane contains the largest number of voids, compared to the four other "undeformed" planes, and a shear band forms along this plane. As before, the localized deformation in the layer causes voids to deform and rotate to accommodate continued macroscopic deformation, and the matrix material in the shear band subsequently strain-hardens. This successive activation of "weak" planes in the RVE continues with macroscopic deformation, and Fig. (3-25d) shows, at a later stage, how a shear band has formed along a third plane which is deforming plastically while the plastic flow on the previous plane has ceased. The figure also shows the deformed and rotated voids on the previously-deformed void planes.

The successive deformation along specific planes in the RVE is an artifact of the underlying cubic lattice for the void locations in the RVE, in combination with the direction of macroscopically-applied shear. It would be interesting to subject the LS model to macroscopic simple shear deformation in a rotated coordinate system in order to investigate the effects of the orientation of the lattice with respect to the macroscopic loading direction. However, this has not been carried out in the present work, but we note, similar to the case of macroscopic uniaxial tension, that if the macroscopic deformation gradient, $\overline{\mathbf{F}}$, is imposed using Eq. (3.1), macroscopic simple

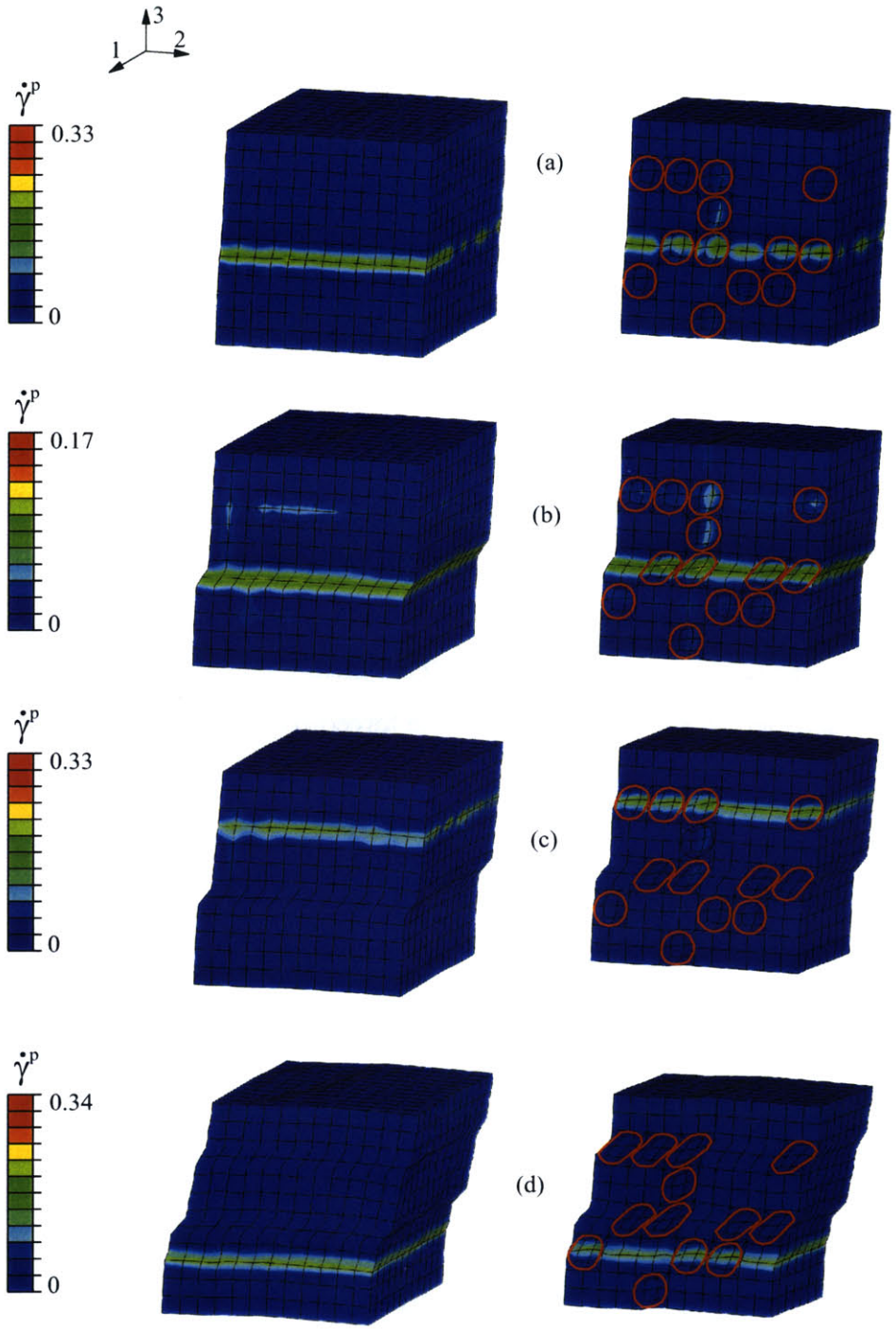

Figure 3-25: Contours of $\dot{\gamma}^p$ under simple shear deformation for an initial void volume fraction, $f_0 = 0.15$. The development of plastic shear localization is shown for increasing levels of macroscopic nominal shear strain: (a) $\overline{\Gamma} \simeq 0.048$, (b) $\overline{\Gamma} \simeq 0.12$, (c) $\overline{\Gamma} \simeq 0.15$ and (d) $\overline{\Gamma} \simeq 0.25$.

shear deformation along different coordinate axes can be readily studied by applying a rotation to $\overline{\mathbf{F}}$.

3.4 The multi-void Voronoi model

The lattice-based multi-void models considered aggregates of cube-shaped voids (the LC model) or spherical voids (LS model) arranged on a cubic lattice. The voids were distributed randomly on the lattice in order to capture the major topological features of a random porous microstructure. The underlying cubic lattice in these two models raises some doubts as to how well the models mimic a truly random porous microstructure. The modeling assumption of an underlying lattice limits the number of available void locations in the RVE, as the voids are restricted to the fixed lattice positions. Neighboring voids are always mutually located at distances and directions corresponding to the lattice spacing $1/N$. This means that deformation mechanisms between voids, such as shear localization, are forced to occur in preset directions and over preset distances. In this section, we consider an aggregate of M voids whose centers are randomly located within a unit cube, in the absence of an underlying lattice.

A space-filling, periodic RVE is generated through a Voronoi tessellation of the M void centers. The steps involved in generating the RVE geometry and corresponding finite element discretization are described below.

3.4.1 Geometry

The following procedure for generating a space-filling, periodic RVE based on a Voronoi tessellation is general. It can be applied to different material classes, such as particle-filled or voided glassy polymers or metals, where the particles or voids are nearly spherical, as well as to polycrystalline materials. In two dimensions, porous media have been studied using Voronoi-tessellation-based representative volume elements (Cruz and Patera [20]), and polycrystalline materials have been studied in both two and three dimensions (Nygårds and Gudmundson [52],[53], and Besdo [49]).

In the present case of a porous glassy polymer, the M spherical voids occupy a volume fraction, f_0, of the unit cube. Although this is not a requirement of the general procedure, the voids are taken to be uniform in size. The procedure for generating the RVE is summarized below, and the two-dimensional analogy, using ten voids, of the procedure is shown in Fig. (3-26).

1. The M void centers are sequentially located within a reference unit box. As a "primary" void is added to the reference box, its 26 (eight, in the two-dimensional case) periodic "image" voids are also added to the 26 unit boxes surrounding the reference box (Fig. 3-26a). The 26 image voids are those that are offset from the primary void by a linear unit combination of the Cartesian base vectors. A new void is added to the reference box only if it does not conflict with an existing primary or image void. In order to ensure a reasonable finite element mesh between the voids, a spatial constraint of $2.5r$ on the separation of voids is enforced, where r is the void radius. At the end of this step, there are $27M$ (primary+image) voids ($9M$ in the two-dimensional case).

2. A Voronoi tessellation of the $27M$ void centers is performed (Fig. 3-26b). The resulting $27M$ Voronoi cells are of two types: The Voronoi cells on the surface of the tessellation are unbounded (and extend to infinity), while the interior Voronoi cells are bounded. In the two-dimensional analogous case depicted in Fig. (3-26b), the unbounded cells are not shown.

3. The final step is to only consider the M Voronoi cells corresponding to primary voids, and discard the other $26M$ ($8M$ in the two-dimensional case) Voronoi cells (Fig. 3-26c). The resulting aggregate of Voronoi cells constitutes a space-filling, periodic volume element. Figure (3-26d) illustrates the compatibility of the volume element with its periodic neighbors. Figure (3-27a) shows a three-dimensional example RVE with three void-containing Voronoi cells. A neighboring RVE that fits periodically with the original RVE is also shown (Fig. 3-27b).

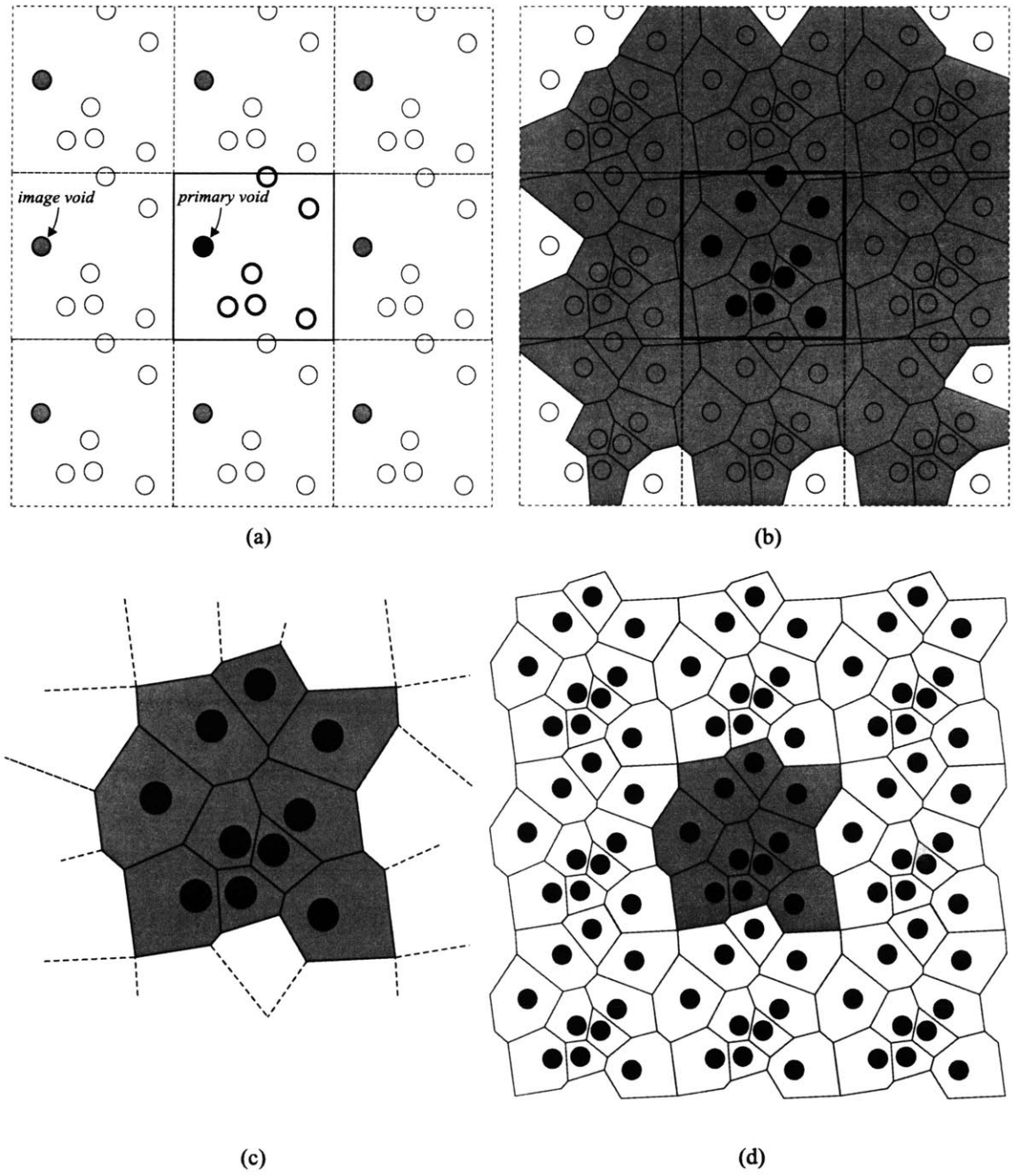

Figure 3-26: Geometry generation for the multi-void Voronoi model: (a) insertion of a non-conflicting primary void, and its periodic image voids, (b) Voronoi tessellation of the set of primary and image void centers, (c) the Voronoi cells containing the primary voids, comprising the space-filling, periodic RVE, (d) the RVE with its neighbors.

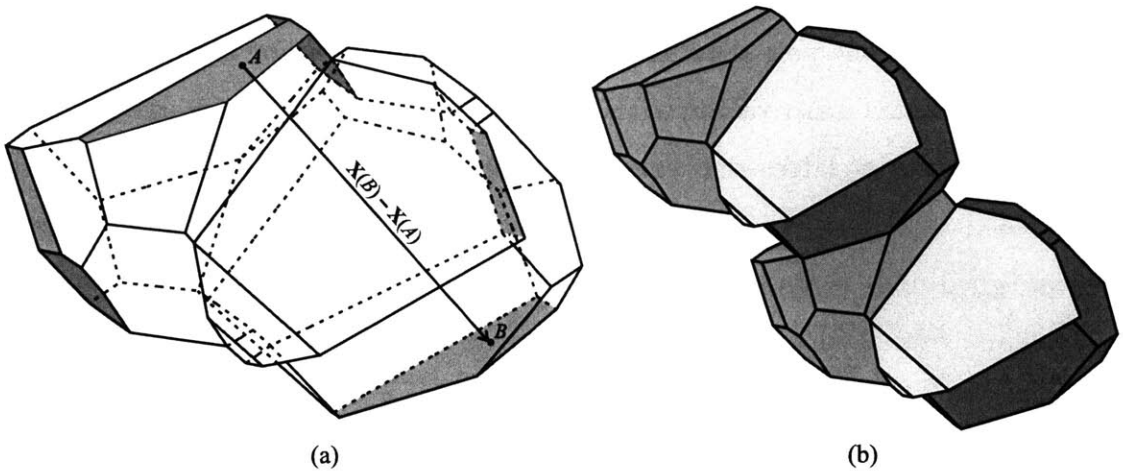

Figure 3-27: The multi-void Voronoi model with three void-containing cells: (a) three pairs of periodic surface segments, (b) two three-void RVEs, fitting together.

3.4.2 Finite element discretization

In Section 3.1, periodic boundary conditions were developed for a space-filling, periodic RVE, and an expression for the corresponding macroscopic state of stress was obtained. The periodic boundary conditions were applied to periodic pairs of points on the surface of the RVE (Fig. 3-2a). In the context of finite elements, this means that the topology of the finite element mesh on the surface of the RVE must be periodically repeated, so as to provide periodic node pairs. Here, we describe how to generate a periodic surface node topology for the present RVE, which enables the direct application of the periodic boundary conditions (Eq. 3.1).

The developed RVE consists of four distinctly different geometrical entities: convex polyhedra (the Voronoi cells), convex polygons (the Voronoi cell facets), lines (the edges bounding each Voronoi cell facet), and vertices (bounding the edges). By breaking down the geometry into these different entities, it is possible to create a structured database which greatly facilitates the task of creating a periodic surface node topology. The procedure for generating a periodic topology of surface nodes can be summarized as follows:

1. The edges in the RVE are identified. There are external edges that lie on the

surface of the RVE, and edges that are internal to the RVE. Each external edge has at least one periodic "image" edge, offset by a linear unit combination of the Cartesian base vectors. (For example, each of the edges of a unit cube possesses three edges that are its periodic images.) The edges in the RVE are seeded with nodes for the finite element discretization. The external edges are assigned node seeds that are themselves periodic. This means that every node on an external edge in the mesh will have at least one other periodic image node to which the periodic boundary condition (Eq. 3.1) can be applied.

2. The facets of the Voronoi cells in the RVE are identified. There are facets that are internal to the RVE, and facets that are external. The internal facets are shared by exactly two Voronoi cells in the RVE. Each external facet has exactly one identical periodic image facet. The external facets are shared by one Voronoi cell in the RVE and exactly one of its 26 periodic images. Each facet is discretized using, for example, triangular elements. When the external facets are discretized, an identical triangulation is enforced on its periodic image facet (Fig. 3-28a).

When each cell contains a spherical void, the interior of the cells can be discretized by taking advantage of the convexity of the Voronoi cells. It is then possible to project the surface triangulation of the cell facets onto the surface of the spherical void. Triangular prismatic finite elements can be used to fill the volume between the Voronoi cell surface and the void surface (Fig. 3-28b). In the present study, we consider triangular prismatic elements with linear interpolation functions. These elements are computationally inexpensive, compared to the [quadratic] hexahedral elements used for the LS model. However, the linear element formulation in the prismatic elements can cause spurious integration point pressures under volumetrically constrained modes of deformation. As will be discussed below, this indicates that a hybrid (constant-pressure) formulation of the element should be used in order to accurately resolve the distribution of pressure in the matrix.

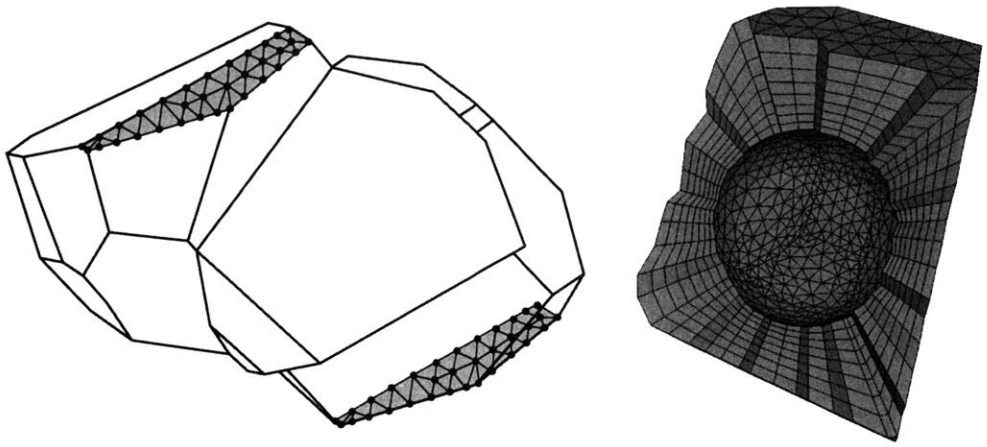

(a) (b)

Figure 3-28: The multi-void Voronoi model: (a) two periodically located external surfaces with the same node and element topology, (b) finite element topology for a Voronoi cell containing a spherical void.

3.4.3 Evaluation of the multi-void Voronoi model

As in the case of the lattice-based multi-void models, issues related to the minimal number of voids required to represent a random microstructure with sufficient accuracy must be addressed. The LS model represents an improvement over the LC model as it can model spherical voids, thus providing access to local microstructural information, such as matrix stress and strain levels around the voids. Compared to the LS model, the random Voronoi model resolves fields in the matrix in even greater detail, as the density of the finite element mesh can be refined between voids. However, this added detail of local fields by virtue of a finer finite element mesh also increases the computational size of the associated boundary value problem. As a consequence, fewer voids can be considered as compared to the LS model. The cases of hydrostatic deformation and simple shear deformation are used to study the influence of the number of voids, and the distribution of voids, on the macroscopic response of the porous material. For the purpose of studying these effects, we use a constant, low mesh density consisting of regular [non-hybrid] finite elements. Thus, the obtained macroscopic stress-strain responses only represent the mechanical response of

the porous material in a relative sense. Figure (3-29) shows the hydrostatic and simple shear response for a fixed initial macroscopic void volume fraction of $f_0 = 0.15$ and three sizes of the RVE with $P = \{5, 10, 15\}$ voids. Each stress-strain curve shows the average of ten simulations for different void distributions, and the standard deviation of the response is shown as error bars in the curves. As the number of voids increases, the standard deviation of the response is expected to decrease. However, Figs. (3-29a-f) show that, in contrast with the results for the LS model, the standard deviation does not decrease with an increasing number of voids. This suggests that in the case of the multi-void Voronoi model, the low number of voids that can be considered in view of computational constraints is not sufficient to reach the regime where the RVE responses begin to mimic a random porous microstructure[6].

As mentioned above, considering a larger number of voids is computationally prohibitive, and a limited number of voids must be used instead. In view of this restriction, it is intriguing to consider the notion of a methodology that would, among different void distributions, distinguish those that more closely mimic a random microstructure from those that show significant anisotropy. It is thus relevant to try to characterize the level of randomness of a given ensemble of voids.

In order to try to establish correlations between the void topology and results from micromechanical modeling, ten simulations of RVEs with 15 voids were carried out under macroscopic hydrostatic deformation. The responses of four of these ten simulations are shown in Fig. (3-30). In each of the plots (Figs. 3-30a-d), three orthogonal normal stress curves resulting from the imposed hydrostatic deformation are shown, together with the mean hydrostatic stress, T_m, averaged over all ten simulations. For a sufficiently large, random, isotropic RVE, the three normal stress curves should collapse onto the mean hydrostatic stress curve. For the four plots in Fig. (3-30) the three stresses deviate from the mean stress, which is symptomatic of an anisotropic behavior for the corresponding RVEs. Depending on the spatial distribution of the

[6]The voids in the multi-void Voronoi model are not restricted to fixed lattice sites, as in the LS model; distributions of voids in the former are thus allowed an even greater spatial variation, suggesting that a larger number of voids should be considered.

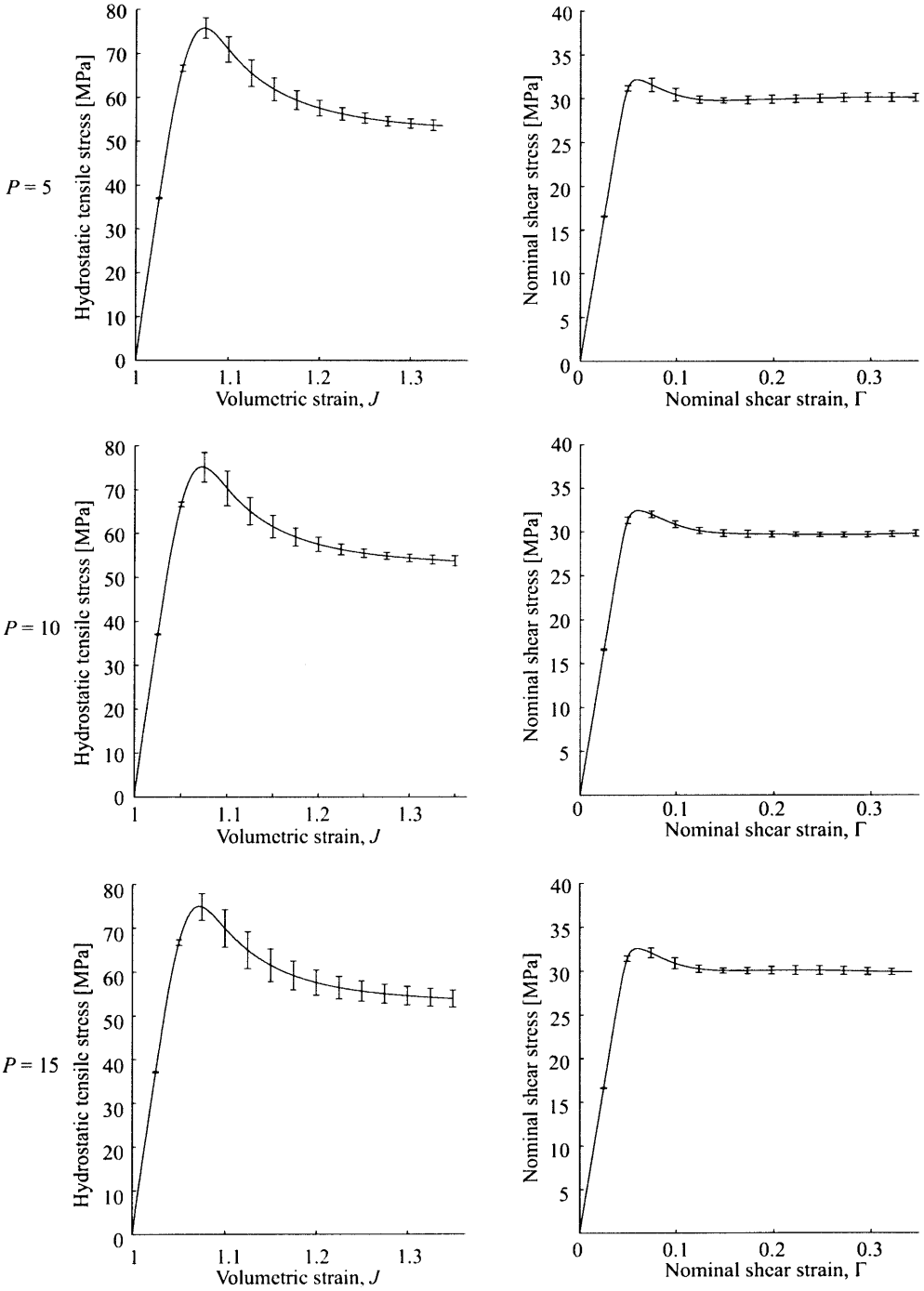

Figure 3-29: The multi-void Voronoi model: Macroscopic response for different number of voids ($f_0 = 0.15$).

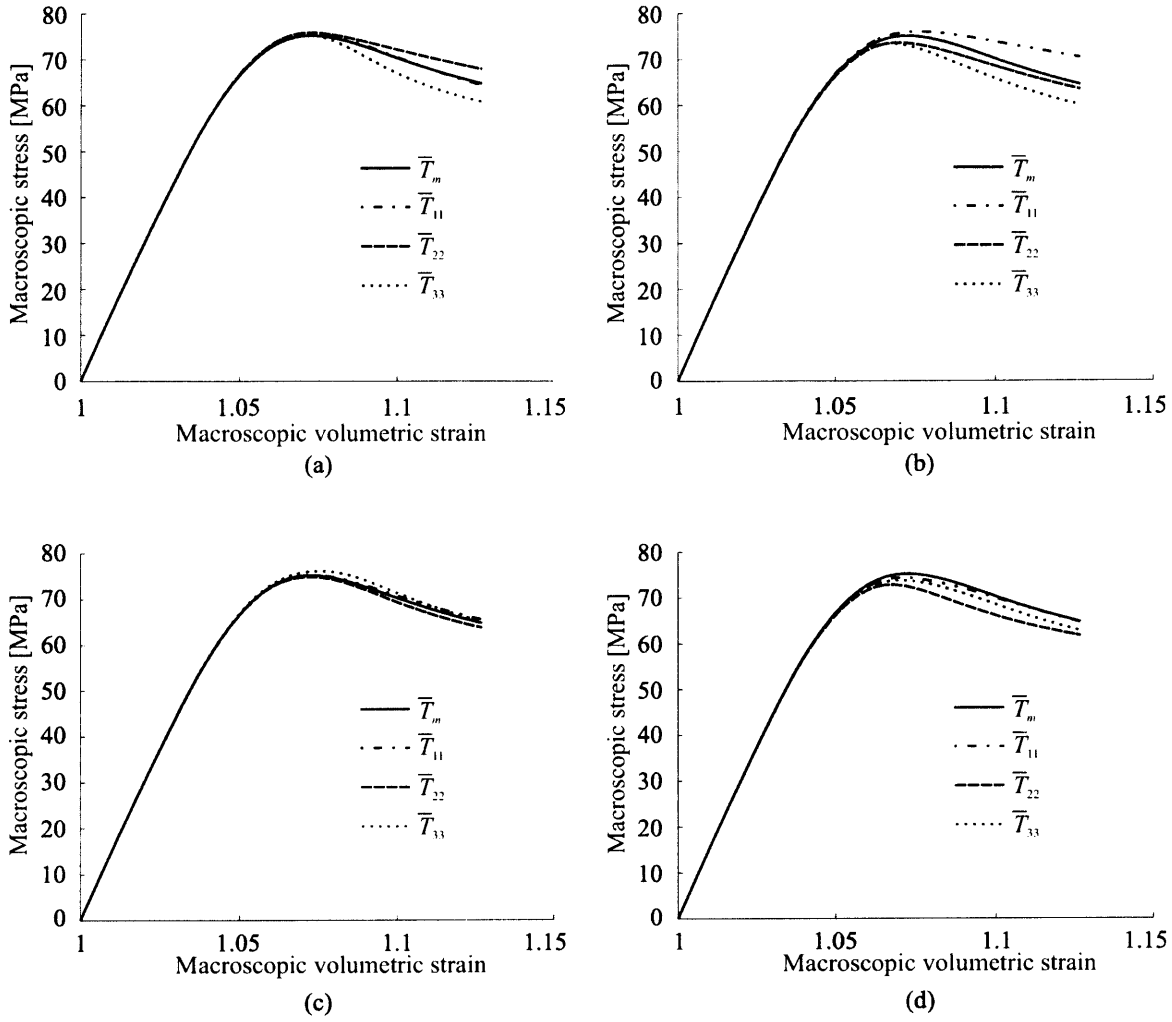

Figure 3-30: Four simulations (a-d) using 15 voids ($f_0 = 0.15$): Three normal stresses corresponding to a macroscopically-imposed state of hydrostatic deformation.

voids, the amount of deviation will differ, reflecting different degrees of anisotropy. For example, Fig. (3-30b) suggests that the corresponding void distribution cannot be used to represent an isotropic microstructure, as the stresses deviate significantly from the mean hydrostatic stress. While this is an adequate measure to evaluate the performance of a specific RVE *a posteriori*, it does not provide any guidance to select an optimal RVE from a large number of alternative void distributions. This task would requires the ability to evaluate a specific RVE *a priori*, simply based on the RVE void topology. Several methods for characterizing porous and particulate

Simulation	$\frac{\sigma_1}{f_0}$	$\frac{\sigma_2}{f_0}$	$\frac{\sigma_3}{f_0}$	$\|\|\text{dev}(\mathbf{I})\|\|$	$\frac{6\,I_{11}}{1-f_0}$	$\frac{6\,I_{22}}{1-f_0}$	$\frac{6\,I_{33}}{1-f_0}$
(a)	0.2313	0.3560	0.4273	0.0023	0.9988	1.008	0.9960
(b)	0.3033	0.3247	0.2247	0.0096	0.9967	0.9791	0.9882
(c)	0.2687	0.3220	0.2280	0.0054	0.9699	0.9861	0.9769
(d)	0.2133	0.2267	0.2133	0.0037	0.9861	0.9875	0.9847

Table 3.3: Microstructural information for the four simulations using 15 voids ($f_0 = 0.15$).

microstructures exist in the literature (see, for example, Torquato [67]). Here, two measures are used: First, the moments of inertia of a given void distribution are used to measure initial isotropy. Second, the local distribution of voids in the matrix is examined by monitoring the spatial fluctuation of void area fraction through the material.

Segurado and Llorca [61] have used moments of inertia to characterize the randomness of particle-reinforced composites. The authors calculated the moments of inertia in three perpendicular directions, $\{I_{11}, I_{22}, I_{33}\}$ of a given ensemble of thirty particles, and compared them to the moments of inertia of a unit cube of the same effective density as the ensemble of particles, $(1 - f_0)/6$. The authors used this information to identify a sufficiently isotropic distribution of particles, and calculated effective small-strain elastic constants for different composites, at different particle volume fractions. Here, the moment of inertia tensor, $\mathbf{I}$, is calculated for a given distribution of voids. The norm of the deviator of the inertia tensor, $||\text{dev}(\mathbf{I})||$, is taken as a measure of isotropy. For an isotropic material, this norm should vanish, indicating that there are no preferred orientations in the material. Table 3.3 shows this norm for the four simulations in Figs. (3-30a-d). Table 3.3 also shows the moments of inertia in three perpendicular directions, normalized by the moment of inertia for a truly random distribution of voids. Unfortunately, it is not possible to establish a strong correlation between the values of the inertia tensor deviator and the relative isotropy of the corresponding macroscopic response of the RVE. The inadequacy of this topological parameter to serve as a predictor of RVE performance is illustrated

by the cases (a) and (c), where a lower value of the deviator corresponds to a higher degree of anisotropy in the macroscopic response. Yet, this same topological measure of isotropy was found to be adequate in the Segurado and Llorca study, where an elastic matrix material was considered. The underlying cause of this discrepancy is to be found in the different deformation mechanisms through which the dilatation of the RVE is accomplished. For a glassy polymer matrix, the macroscopic dilatancy is associated with the creation of localized shear bands which percolate through the RVE, connecting voids along the weaker planes of resistance. The orientation and inherent shear resistance of these planes are a direct consequence of the RVE topology and relative location of the voids. The moment of inertia tensor of a given ensemble of voids can provide information about the degree of anisotropy of the entire ensemble, but it does not provide local information about the porous microstructure, such as void-to-void distances, void-to-void orientations, and clustering of voids in the matrix. Therefore, we conclude that $||\mathrm{dev}\,(\mathbf{I})||$ is not a sufficient measure of isotropy for a [small] system whose macroscopic response is controlled by shear localization events.

In a random porous material with an initial void volume fraction f_0, a topological feature is that any cross section of the porous material shows a void area fraction equal to the void volume fraction f_0. For a finite number of voids, the area fraction of voids at different cross sections of the RVE will, in general, not be equal to the macroscopic void volume fraction, but it will fluctuate about this value. Socrate and Boyce [63] used the concept of local void area fraction to compare the performance of the axisymmetric SHA (stacked hexagonal array) and V-BCC (Voronoi body centered cubic) models (Fig. 3-1a) applied to glassy polycarbonate. The authors found that the variation in local void area fraction was much higher in the SHA model, compared to the V-BCC model, and that the existence of planes of very high and very low void area fraction in the SHA model resulted in unrealistic shear localization in the cross sections of high void area fraction.

In the present case of multiple-void RVEs, the distribution of local void area fraction is calculated for three sets of planes scanning the RVE along three perpendicular

directions. The mean value of each distribution is the macroscopic void volume fraction, f_0, and the standard deviation of the distribution, σ_i, $i = 1..3$, is a measure of the spread about the mean. The standard deviation in the three perpendicular directions is shown in Table 3.3, for the four simulations in Fig. (3-30). Standard deviations close to zero indicate that the voids are well distributed in the matrix, whereas larger standard deviations imply higher degrees of void clustering or void alignment along preferential planes. High values for this topological measure were expected to correlate with a higher propensity of the RVE to display preferential shear localization along specific planes, and therefore a higher degree of anisotropy in its macroscopic response. However, a comparison of the area fraction standard deviations in Table 3.3 and the corresponding macroscopic response curves in Fig. (3-30) fails to demonstrate a clear correlation. The inadequacy of area fraction standard deviations to serve as predictors of RVE performance is illustrated by the cases (b) and (c), where almost identical levels of area fraction deviations are associated with substantial differences in the macroscopic response. Also, the case with the lowest area deviations among the ones considered in this study, (d), exhibited a higher degree of anisotropy in its macroscopic response than RVEs with higher area deviations (c). Therefore we conclude that the standard deviations of the area fraction distributions are not a sufficient measure to determine *a priori* the relative merit of different void distributions.

The reasons for this lack of success are probably to be found in the very limited size of RVEs that can be considered within the current computational constraints. With only 15 voids in the RVE, most of the critical shear deformation is localized along one or two planes. If such a model is used to represent a sample of a porous material undergoing homogeneous hydrostatic deformation, the periodic boundary conditions on the RVE are essentially enforcing a repetition of this simple RVE shear pattern over the entire sample. This is clearly a crude approximation for the complex pattern of percolating shear localization that will occur in the actual material sample over a multiplicity of randomly oriented planes. It is unrealistic to expect that this complex shear pattern could be reproduced over an RVE with only 15 voids (note

that a 3x3x3 void array corresponds to 27 voids!).

These considerations lead to the conclusion that it is impossible to construct a single 15-void RVE which can be considered representative for the behavior of the actual random microstructure under all deformation states. Instead, we will consider an alternative approach to obtain macroscopic and microscopic information for the behavior of porous glassy polymers from micromechanical modeling.

Figure (3-29) displayed the macroscopic predictions in hydrostatic and simple shear deformation for increasing RVE sizes. While the individual predictions of each RVE display a degree of void topology dependence (hence the error bars), the average stresses from the ten simulations for each RVE size are remarkably similar. These average curves are superposed in Fig. (3-31) for direct comparison. It is remarkable that RVEs with 5, 10 and 15 voids give rise to the same average macroscopic response. From a physical standpoint, these results for hydrostatic and simple shear deformation can be discussed in the context of a Taylor model interpretation. Each simulation is sampling a "material point" with a specific local void topology. By sampling a number of "material points", subjecting them to the same macroscopic deformation history[7], and taking the average stress response, we are obtaining a fairly accurate, repeatable representation of the actual material behavior. These considerations apply to the macroscopic response as well as to local field quantities.

In view of the results in Fig. (3-31), the average macroscopic response over ten simulations for five-void RVEs will be considered representative of the porous glassy polymer macroscopic response under all modes of deformation This simulated material response will constitute the basis to develop and validate a continuum level constitutive model for glassy polymers as further discussed in Chapter 4.

The approach of using several RVEs can be also employed to probe the evolution of local field quantities under specific macroscopic deformation histories. Thus several RVEs of different void topologies can be subjected to the same loading histories and

[7]Under macroscopic loading conditions where not every component of $\overline{\mathbf{F}}$ is prescribed, the Taylor model interpretation is formally not correct. For example, under uniaxial tension, the macroscopic lateral stretches are unprescribed, and in general different for different RVEs.

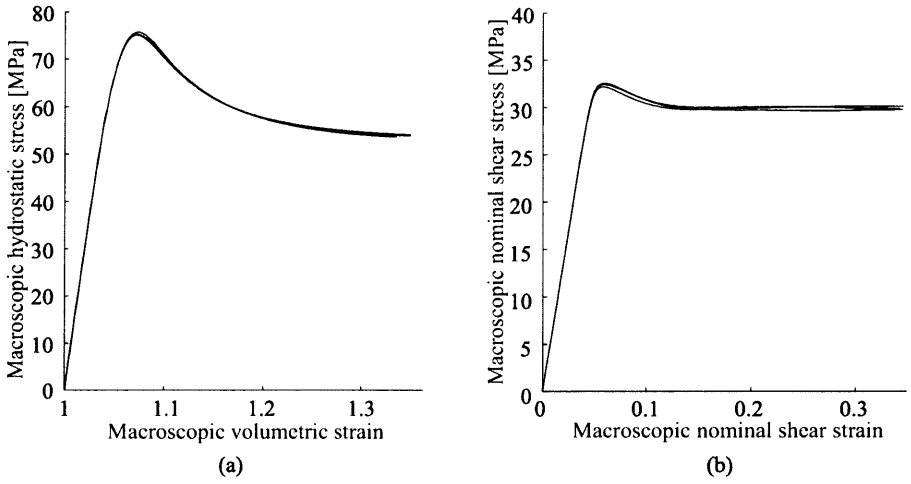

Figure 3-31: The multi-void Voronoi model ($f_0 = 0.15$): Superposition of the responses at 5, 10 and 15 voids for (a) macroscopic hydrostatic deformation and (b) macroscopic simple shear deformation.

local stress and strain levels over all the simulations can be monitored and correlated to observed failure mechanisms, as further discussed in Chapter 5.

The simulations to study the effects of the number of voids on the macroscopic stress-strain response were performed using constant-density, coarse, finite element meshes of regular [non-hybrid] elements. In order to investigate the effects of finite element mesh refinements on the macroscopic stress-strain response, an RVE with $P = 3$ voids, an initial void volume fraction $f_0 = 0.15$, and a fixed topology is subjected to macroscopic hydrostatic deformation. As discussed previously, the linear element formulation may cause spurious pressure modes in the matrix. It is important to resolve local fields in the matrix, in addition to the macroscopic stress-strain behavior of the porous material. We therefore carry out the mesh refinement study using hybrid (constant-pressure) finite elements.

The mesh refinements in the case of the LS model were controlled by the parameter k (Fig. 3-32). We first constructed a coarse hexahedral finite element mesh ($k = 1$) and then considered two levels of mesh refinement ($k = 2$, $k = 3$). This corresponded to dividing each hexahedral finite element into eight and 27 elements, respectively. In the present case of a triangular prismatic finite element mesh for the multi void

Voronoi RVE, the mesh is refined in a consistent manner. A first coarse mesh is created ($k = 1$) for a selected RVE topology. The mesh density corresponding to $k = 1$ was chosen as to provide the coarsest mesh possible, while maintaining reasonably-shaped element facets on the surfaces of the Voronoi cells. The first refinement level ($k = 2$) corresponds to dividing each surface triangle on the coarsely meshed Voronoi facets into four triangles, and increasing the number of prisms by a factor of two in the radial direction. The second mesh refinement level ($k = 3$), corresponds to dividing each coarse surface triangle on the facets of the Voronoi cells into nine triangles, and increasing the original number of prismatic elements radially by a factor of three.

The finite element mesh is successively refined according to the refinement scheme above ($k = \{1, 2, 3\}$), and the macroscopic hydrostatic response is shown in Fig. (3-32). The macroscopic RVE responses show that the stress decreases with an increasingly fine mesh, and the response appears to converge as the mesh is refined. However, the computational expense involved in solving the boundary value problem associated with the highest mesh density ($k = 3$) is considerable. As in the case of the LS model, the intermediate mesh density ($k = 2$) provides a reasonable balance between computational expense and numerical accuracy. This mesh density is used in the following.

3.4.4 Results

Uniaxial tension

Ten RVEs with $P = 5$ voids are subjected to macroscopic uniaxial tension for three different initial void volume fractions, $f_0 = \{0.05, 0.10, 0.15\}$. Macroscopic uniaxial tension in the 3-direction corresponds to a macroscopic deformation gradient given by

$$\overline{\mathbf{F}} = \overline{\lambda}_1(t)\ \mathbf{e}_1 \otimes \mathbf{e}_1 + \overline{\lambda}_2(t)\ \mathbf{e}_2 \otimes \mathbf{e}_2 + \overline{\lambda}_3(t)\ \mathbf{e}_3 \otimes \mathbf{e}_3, \tag{3.25}$$

where $\overline{\lambda}_1(t)$ and $\overline{\lambda}_2(t)$ are un-prescribed, and a constant macroscopic axial strain-rate $\dot{\overline{E}}_{33} = 0.01 s^{-1}$ is imposed by prescribing $\overline{\lambda}_3(t) = \exp \dot{\overline{E}}_{33} t$. The average macroscopic

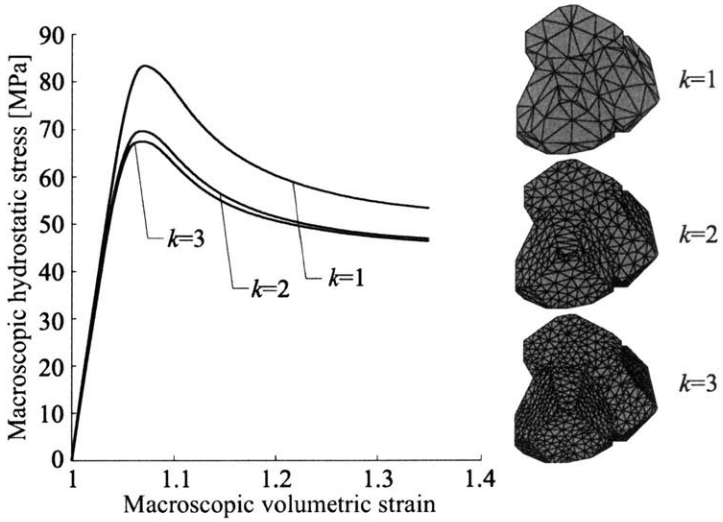

Figure 3-32: The multi-void Voronoi model: effects of finite element mesh refinements on the macroscopic hydrostatic response.

axial-stress / axial-strain response of the simulations is given in Fig. (3-33a) for each of the initial void volume fractions, and the corresponding evolution of volumetric strain with axial deformation is shown in Fig. (3-33b). In order to better illustrate the microscopic features of deformation of the porous material, contours of plastic shear strain-rate, $\dot{\gamma}^p$, are shown for a larger RVE ($P = 10$). The case of $f_0 = 0.15$ is shown in Fig. (3-34) for different levels of macroscopic axial strain.

As in the previously discussed 3D V-BCC and LS models, the plastic flow in the matrix initiates in the equatorial region of the voids. Macroscopic yield, defined as the point in the deformation where the macroscopic stress-strain response exhibits a peak, has not yet been reached; the matrix material is still predominantly in the elastic regime. Similar to the previous models, the axial-stress/axial-strain curves display a slight non-linearity prior to macroscopic yield of the material. This is explained by the local plastic flow in the matrix, which increases the overall compliance of the porous material. As the macroscopic deformation progresses, the plastic flow in the equatorial regions of the voids spreads from void to void as local shear bands (Fig. 3-34a). Macroscopic yield of the porous material is reached when these local shear bands, that run from void to void, span the entire RVE to form a macroscopic

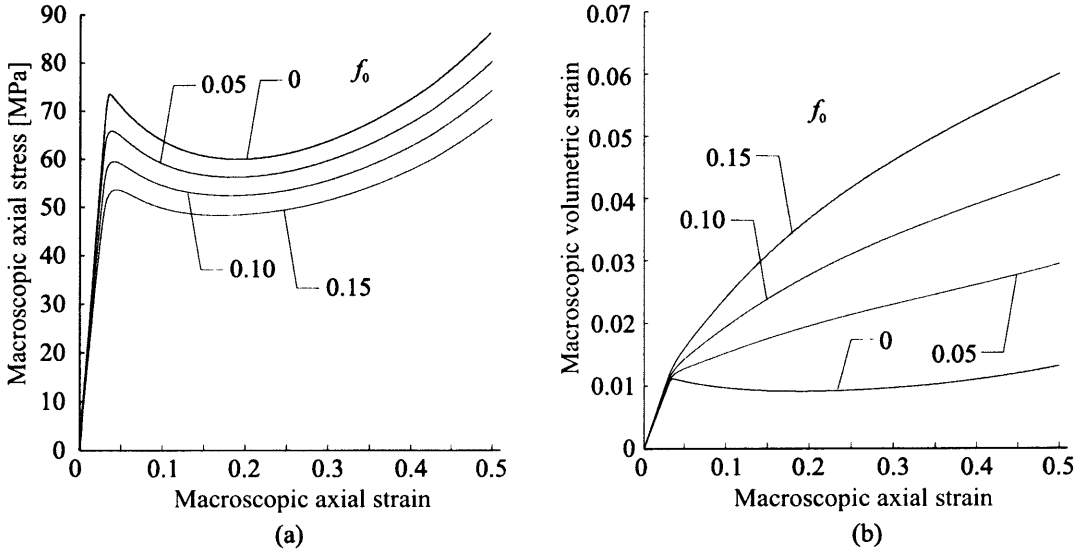

Figure 3-33: Macroscopic uniaxial tension: (a) axial stress-strain response, (b) evolution of volumetric strain with axial deformation.

shear band (Fig. 3-34b). The porous material subsequently strain-softens as the shear bands continue to flow. As the matrix material in the shear bands continues to deform, the molecular chains become oriented, and the resistance to continued plastic flow increases. The plastic flow then spreads to neighboring matrix material which then yields and strain-softens. This progression of plastic flow in the matrix encompasses an increasing amount of matrix material, as the flow spreads away from the voids. As this happens, the flow stabilizes, and the macroscopic stress-strain response for the porous material eventually enters the hardening regime.

Figure (3-33b) shows the evolution of macroscopic volumetric strain, $\overline{E}_{vol} = \ln \overline{J}$, of the porous material. The evolution of macroscopic volumetric strain with axial strain reflects the initial Poisson effect, followed by volumetric straining associated with the plastic growth of voids in the matrix. In the LS model, neighboring voids are placed side by side, with respect to the macroscopic loading direction, and this particular void arrangement has been shown to unrealistically prevent lateral contraction of the RVE, thus over-predicting the macroscopic volumetric response of the porous material (Socrate and Boyce [63]). In the 3D V-BCC model, neighboring voids are diagonally offest, with respect to the macroscopic loading direction, and this void

arrangement enables significant lateral contraction of the RVE (Socrate and Boyce [63], Danielsson, et al. [21]). In the present multi-void Voronoi RVE, the voids are not confined to these "lattice extremes", and the prediction of volumetric strain lies in between the predictions of the LS and 3D V-BCC models.

Plane strain tension

The case of plane strain tension is studied for three levels of initial void volume fraction, $f_0 = \{0.05, 0.10, 0.15\}$. The main macroscopic loading direction is the 3-direction, and the macroscopically constrained direction is the 1-direction. The macroscopic 2-direction is left un-constrained. Macroscopic plane strain tension in the 3-direction is then given by a macroscopic deformation gradient corresponding to

$$\overline{\mathbf{F}} = \mathbf{e}_1 \otimes \mathbf{e}_1 + \overline{\lambda}_2(t)\, \mathbf{e}_2 \otimes \mathbf{e}_2 + \overline{\lambda}_3(t)\, \mathbf{e}_3 \otimes \mathbf{e}_3, \tag{3.26}$$

where $\overline{\lambda}_2(t)$ is un-prescribed, and a constant macroscopic axial strain-rate $\dot{\overline{E}}_{33} = 0.01 s^{-1}$ is imposed by prescribing $\overline{\lambda}_3(t) = \exp \dot{\overline{E}}_{33} t$.

The macroscopic axial stress vs. macroscopic axial strain in the 3-direction, averaged over ten simulations using $P = 5$ voids, is shown in Fig. (3-35a) for the studied initial void volume fractions. Figure (3-35b) shows the corresponding predictions of macroscopic volumetric strain, $\overline{E}_{vol} = \ln \overline{J}$. As in the case of macroscopic uniaxial tension, the underlying microscopic behavior is characterized by plotting contours of plastic shear strain-rate, $\dot{\gamma}^p$, for a larger RVE ($P = 10$) at different levels of macroscopic axial strain (Fig. 3-36). Macroscopic yield stress for the porous material is defined as the point where the stress-strain response exhibits a peak in axial stress, followed by softening. Figure (3-35a) shows that, prior to macroscopic yield, the stress-strain curves deviate slightly from linearity. Similar to the case of uniaxial tension, where local plastic flow in the equatorial region of the voids gave rise to this non-linearity, the contours of plastic shear strain-rate also show this initial local plastic flow in the matrix (Fig. 3-36a).

Macroscopic yield of the porous material is reached when the local plastic flow

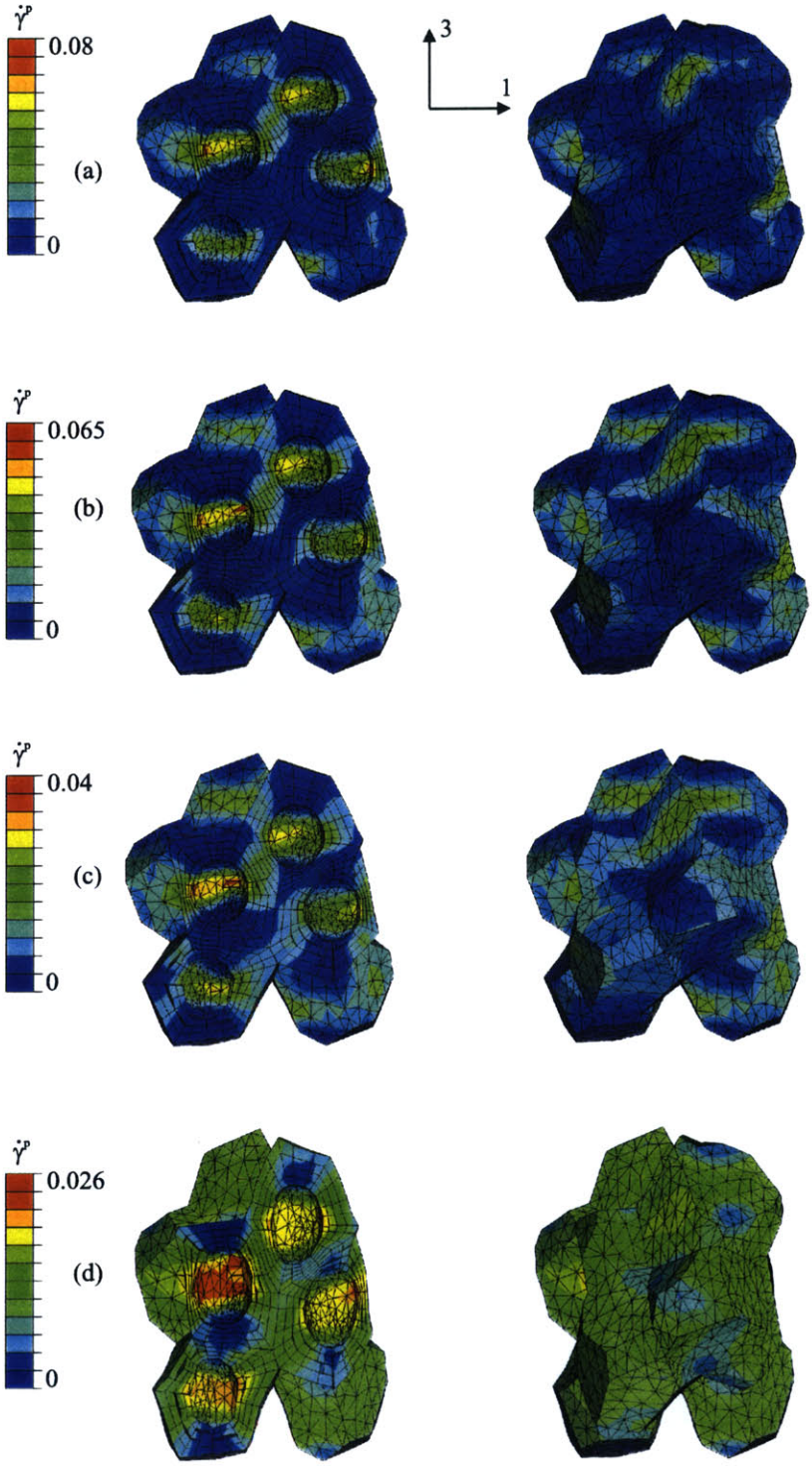

Figure 3-34: Contours of plastic shear strain-rate, $\dot{\gamma}^p$, for a ten-void RVE under macroscopic uniaxial tension ($f_0 = 0.15$): (a) $\overline{E}_{33} = 0.034$, (b) $\overline{E}_{33} = 0.044$, (c) $\overline{E}_{33} = 0.055$, (d) $\overline{E}_{33} = 0.18$.

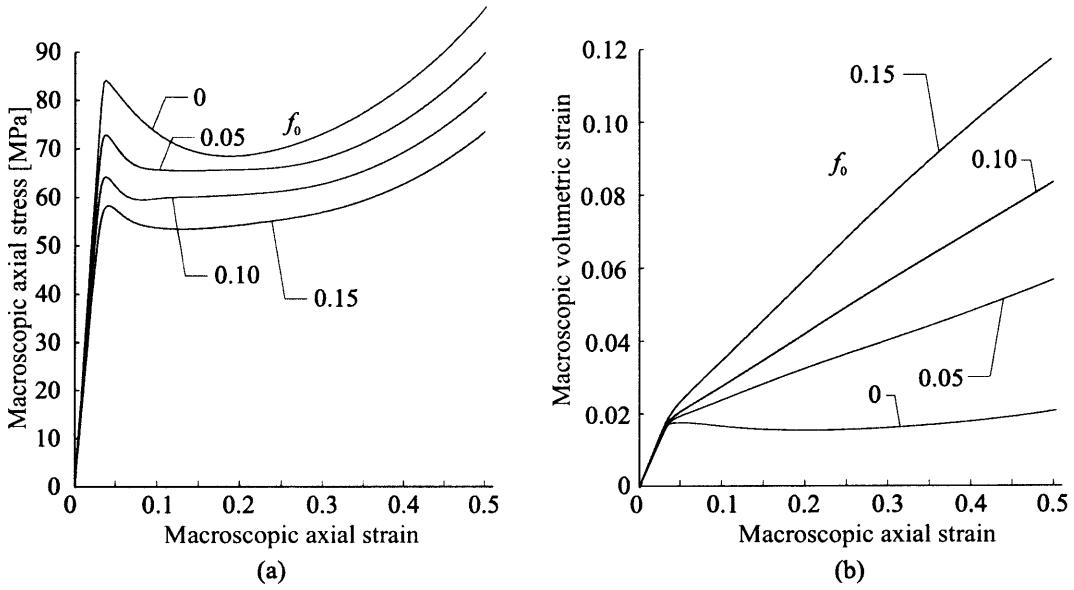

Figure 3-35: Macroscopic plane strain tension: (a) axial stress-strain response, (b) evolution of volumetric strain with axial deformation.

near the voids spreads from void to void, and forms macroscopically running shear bands (Fig. 3-36b-c). Recall that in the V-BCC model, a shear band first developed in the direction of macroscopic plane-strain constraint, followed by shear banding in the un-constrained direction. This type of deformation sequence is a consequence of the biaxial stress state resulting from the macroscopic axial stress and the stress due to the macroscopically-imposed constraint. It is expected that the formation of macroscopically running shear bands in the present RVE should follow the same sequence of events. However, initial macroscopic shear bands do not form only in the direction of macroscopic constraint, but also in the macroscopically unconstrained direction (Fig. 3-36b-c); the deformation patterns in the matrix look very similar to those of the previous case of macroscopic uniaxial tension. When a limited number of voids is considered, the shearing directions in the material are strongly affected by the mutual orientations of neighboring voids. In the present ten-void example, the void distribution does not promote the shearing directions observed in the 3D V-BCC model. However, it is likely that other void distributions would display macroscopic shear banding in the direction of macroscopic constraint, and that several simulations

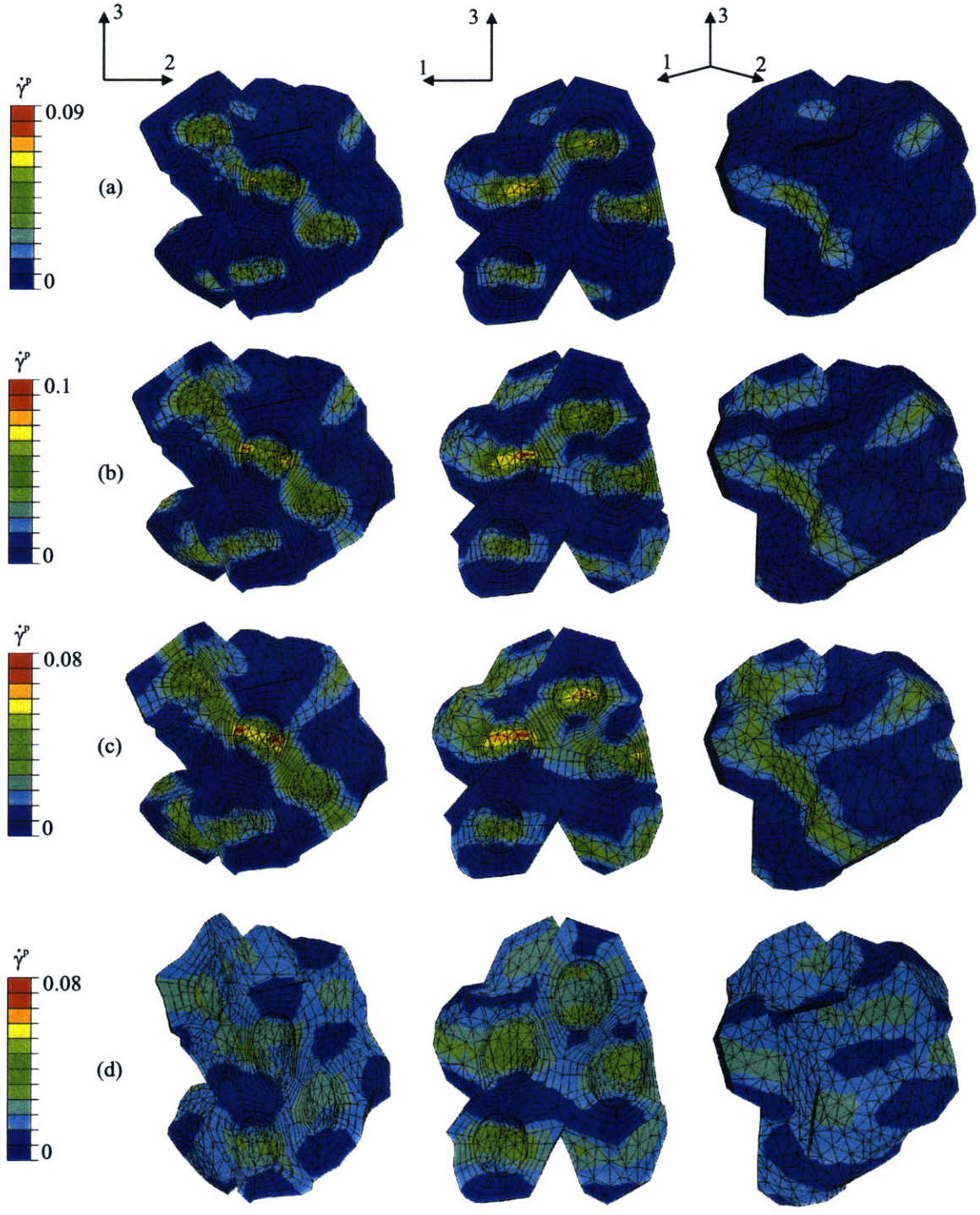

Figure 3-36: Contours of plastic shear strain-rate, $\dot{\gamma}^p$, for the case of macroscopic plane strain tension and $f_0 = 0.15$, using $P = 10$ voids: (a) $\overline{E}_{33} = 0.033$, (b) $\overline{E}_{33} = 0.043$, (c) $\overline{E}_{33} = 0.053$, (d) $\overline{E}_{33} = 0.18$. The macroscopic plane-strain constraint is imposed in the 1-direction.

using ten voids would display this deformation pattern "on average".

The plastic flow of the material in the shear bands causes strain-softening in the macroscopic stress-strain response. As the deformation progresses, the plastic flow in the shear bands orients the associated matrix material, which increases the plastic resistance in these regions. The increase in plastic resistance causes the plastic flow to spread to neighboring matrix material. As an increasing amount of matrix material is encompassed by the flow, the overall plastic resistance of the porous material increases, and the macroscopic stress-strain curves exhibit strain-hardening.

Compared to the case of macroscopic uniaxial tension, the predicted levels of macroscopic volumetric strain with axial deformation are significantly higher. The imposed macroscopic constraint prevents the RVE from contracting, and this results in higher macroscopic volumetric straining with axial deformation. The contour plots of plastic shear strain-rate (Fig. 3-36) reveal, in addition to shear localization events, that with increasing macroscopic axial strain, the voids do not contract, on average, in the direction of macroscopic constraint. However, in the macroscopically unconstrained direction, the voids do contract. This illustrates the evolving anisotropy of the porous material, resulting from anisotropic void growth. A continuum-level constitutive model should include the effects of evolving anisotropy due to anisotropic void growth.

Simple shear deformation

The case of macroscopic simple shear deformation is studied for three cases of initial void volume fraction, $f_0 = \{0.05, 0.10, 0.15\}$. As in the previous cases of macroscopic uniaxial and plane strain tension, the macroscopic response of the material is taken as the average of ten simulations using $P = 5$ voids. In the simulations, simple shear was taken to occur perpendicular to the 23-plane, thus, the macroscopic deformation gradient is given by

$$\overline{\mathbf{F}} = \mathbf{1} + \dot{\overline{\Gamma}} t \, \mathbf{e}_2 \otimes \mathbf{e}_3, \tag{3.27}$$

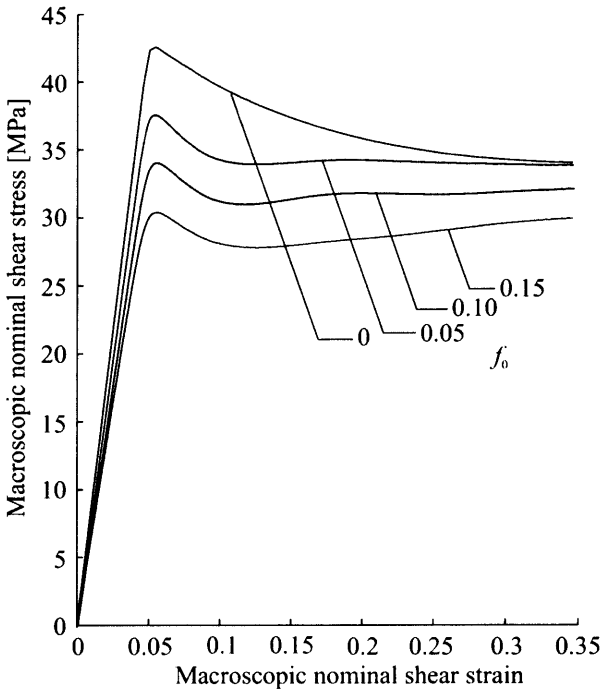

Figure 3-37: Macroscopic simple shear deformation.

where the imposed nominal shear rate was taken to be $\dot{\overline{\Gamma}} = 0.0173s^{-1}$. The macroscopic nominal shear stress, $\overline{S}_{23}$, is shown in Fig. (3-37b) for the three values of initial void volume fraction, f_0. Macroscopic yield of the blend is defined as the point where the macroscopic nominal shear stress exhibits a peak, followed by softening. The microscopic response of the material was characterized by plotting contours of plastic shear strain-rate at various stages of the deformation, for the case of $f_0 = 0.15$ (Fig. 3-38). As in the previous load cases, an RVE with $P = 10$ voids is shown in order to better illustrate micromechanical features of deformation. Figure (3-37b) shows that the elastic shear stiffness of the different blends decreases with an increasing initial void volume fraction f_0, as expected. The slight non-linearity prior to macroscopic yield, seen in Fig. (3-37b), results from initial plastic flow in the matrix (Fig. 3-38a). At this point in the macroscopic deformation, the plastic flow in the matrix is local, and does not completely bridge the ligaments between the voids. As the macroscopic deformation progresses, the local plastic flow forms a macroscopic shear band which is oriented in the 12-plane (Fig. 3-38b). The plastic flow of this 'net section' results in

macroscopic yield of the blend (Fig. 3-37). Recall that in the case of the 3D V-BCC model subjected to macroscopic simple shear deformation according to Eq. (3.27), a distinct shear band developed in the 13-plane (Fig. 3-12a-c). This response to the macroscopically-applied deformation is believed to be an artifact of the assumed BCC arrangement of the voids. As the deformation progresses, the macroscopic shear band broadens, as an increasing amount of matrix material is encompassed by the plastic flow. Similar to the previous cases, the matrix material in the shear band becomes oriented, and its resistance to continued plastic flow increases. The plastic flow then spreads to neighboring matrix material, and the shear band moves upward in the RVE (Fig. 3-38c-d).

At higher levels of macroscopic deformation, the voids in the matrix begin to rotate and elongate as a result of the macroscopic state of deformation (Fig. 3-38d). This indicates that a continuum-level constitutive model for the porous glassy polymer should take into account the shape change and change in orientation of voids with macroscopically-applied deformation.

Hydrostatic deformation

The case of macroscopic hydrostatic deformation was studied for the three initial void volume fractions, $f_0 = \{0.05, 0.10, 0.15\}$. As previously, the macroscopic response is obtained by averaging over ten simulations using $P = 5$ voids. The macroscopic deformation gradient corresponding to hydrostatic deformation is given by

$$\overline{\mathbf{F}} = \overline{J}(t)^{1/3}\ \mathbf{1}, \tag{3.28}$$

where a macroscopic dilatational strain-rate $\dot{\overline{E}}_{vol} = 0.03s^{-1}$ is imposed through $\overline{J}(t) = \det \overline{\mathbf{F}} = \exp \dot{\overline{E}}_{vol} t$. The macroscopic stress-strain response is characterized by plotting the macroscopic hydrostatic stress, $\overline{T}_m = (\overline{T}_{11} + \overline{T}_{22} + \overline{T}_{33})/3$, against macroscopic volume change, $\overline{J}$. The microscopic response is characterized by plotting contours of plastic shear strain-rate, $\dot{\gamma}^p$, at different stages of the deformation for a ten-void RVE with $f_0 = 0.15$ (Fig. 3-40).

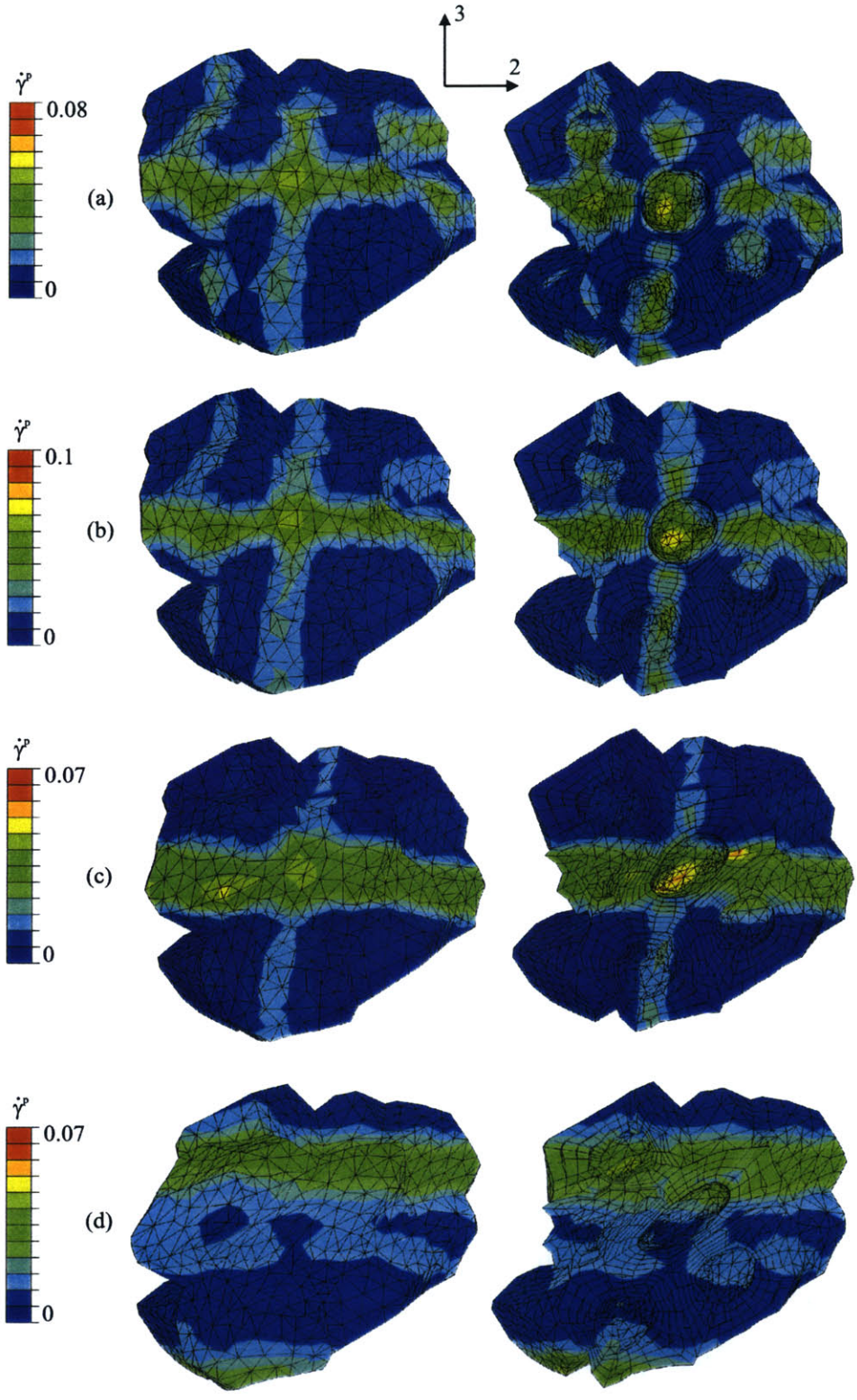

Figure 3-38: Contours of plastic shear strain-rate, $\dot{\gamma}^p$, for the case of macroscopic simple shear deformation and $f_0 = 0.15$: (a) $\overline{\Gamma} = 0.032$, (b) $\overline{\Gamma} = 0.042$, (c) $\overline{\Gamma} = 0.093$, (d) $\overline{\Gamma} = 0.20$.

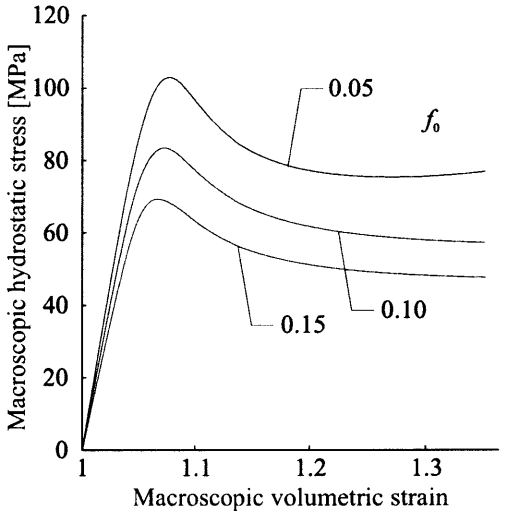

Figure 3-39: Macroscopic hydrostatic deformation.

The stress-strain curves (Fig. 3-39) show that the elastic bulk stiffness of the porous material decreases with increasing initial void volume fraction. Local plastic flow in the matrix initiates on the void surfaces (Fig. 3-40a). This local plastic flow results in a pre-peak non-linearity in the predicted macroscopic hydrostatic stress (Fig. 3-39). The plastic flow on the void surfaces successively spreads through the matrix as local shear bands, which bridge the ligaments between neighboring voids (Fig. 3-40b). As the macroscopic deformation progresses, macroscopically running shear bands develop, and macroscopic yield of the porous material is reached (Fig. 3-40c). In the case of the homogeneous glassy polymer, the plastic flow is volume-preserving, and no plastic flow would be predicted under purely hydrostatic deformation. Thus, the 'macroscopic yielding' of the porous material results from local [volume-preserving] plastic shearing of the matrix material, which in turn gives rise to plastic void growth, and macroscopic plastic dilatation of the material.

3.5 Summary of the developed RVEs

In the preceding discussion, four micromechanical models (RVEs) of a porous microstructure were introduced. Three of the models (the 3D V-BCC, LS and multi-void

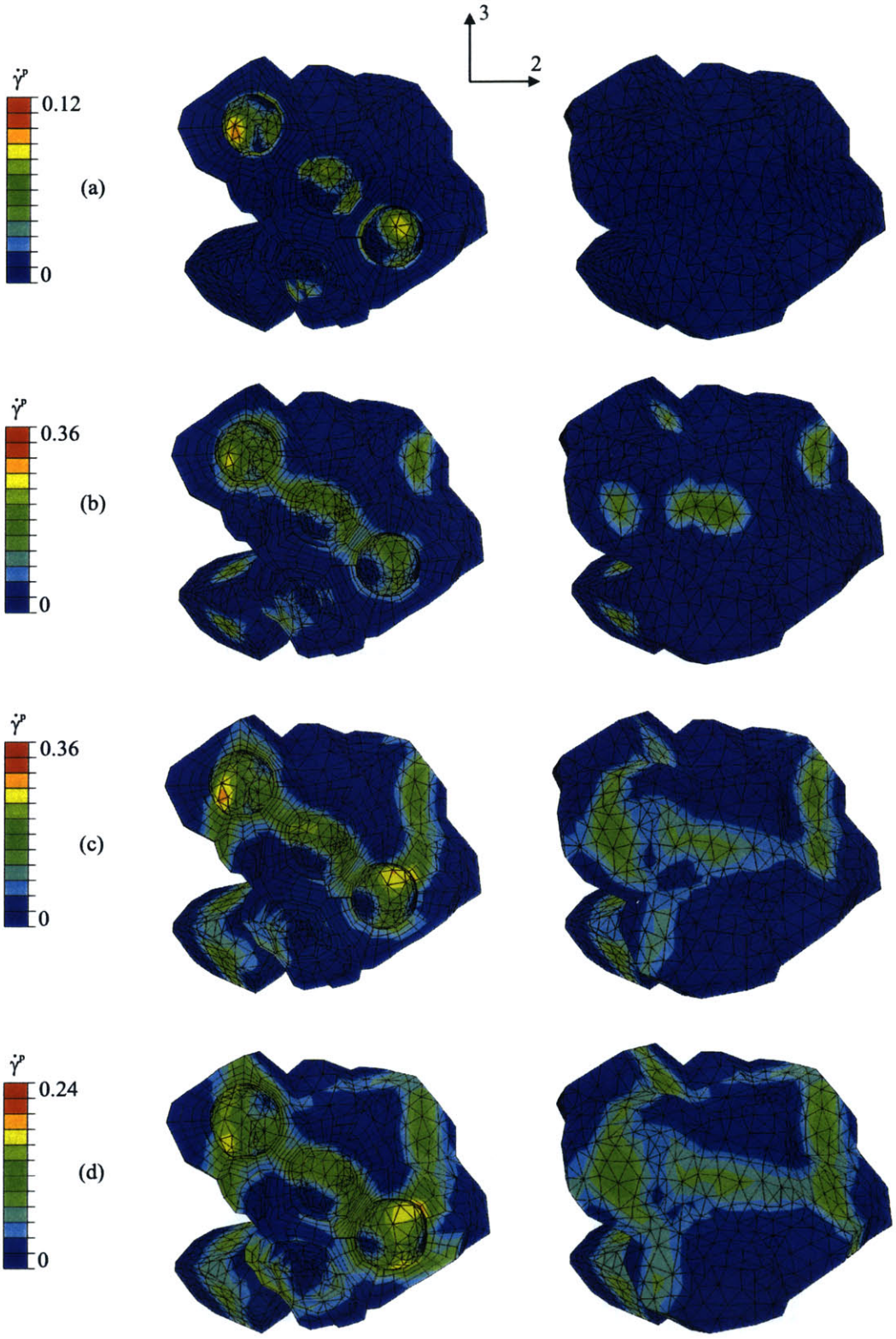

Figure 3-40: Contours of plastic shear strain-rate, $\dot{\gamma}^p$, for the case of macroscopic hydrostatic deformation and $f_0 = 0.15$: (a) $\overline{J} = 1.04$, (b) $\overline{J} = 1.07$, (c) $\overline{J} = 1.09$, (d) $\overline{J} = 1.14$.

Voronoi models) were used to study the micromechanical and macromechanical behavior of porous glassy polycarbonate under various macroscopic loading situations. The loading conditions included simple shear deformation, uniaxial tension, plane strain tension and hydrostatic tension, and for each studied load case, a range of initial void volume fractions was studied. In this concluding section, we highlight the merits and drawbacks of each of the three RVEs mentioned above. The suitability of each RVE for interpreting local stresses and strains is discussed, and the predictions of the macroscopic stress-strain behavior of each RVE are compared and discussed.

3.5.1 Micromechanics

Toughness of rubber-toughened polycarbonate is intrinsically connected to the distribution of stress and strain in the polycarbonate matrix. The RVEs developed in the preceding discussion can be used to study such distributions, and provide important information that might aid in understanding the deformation and eventual fracture processes in the material. However, in order for such a study to be relevant, the employed RVE should represent as realistically as possible the void distribution [cavitated rubber particles] of the real porous microstructure, as the local fields are strongly affected by void-to-void distances and orientations. In the 3D V-BCC model, there are only two characteristic void-to-void distances at two corresponding orientations, and the 3D V-BCC model therefore does not provide a sufficient basis for interpreting local stress and strain fields in the matrix. For example, the issue of ductile-to-brittle transition in the presence of rubber particle clusters in the real material cannot be addressed. The LS model is an improvement from this point of view. In the LS model, there is a larger variation in void-to-void interactions since the voids are randomly placed on a cubic lattice. However, the local void volume fraction in the LS model (Eq. 3.23) was assigned a relatively large value ($f_0^{local} = 0.45$) as to prevent the void distribution from resembling that of a single-void model. The large value on f_0^{local} produces unrealistically thin inter-void ligaments between adjacent voids, and any interpretation of local fields in these regions therefore has to be made with caution. In the multi-void Voronoi model, there is no underlying lattice that decides

admissible positions of the voids in the matrix. Thus, for a given ensemble of voids, there is a greater variation in the void-to-void distances and orientations, compared to the LS model. Using the multi-void Voronoi model, it is also possible to study the effects of particle (or void) clustering. In view of this discussion, we conclude that when addressing issues of toughening through the monitoring of matrix field quantities, the multi-void Voronoi model constitutes the most appropriate tool.

3.5.2 Macromechanics

As discussed previously, the different void distributions in each of the three studied RVEs give rise to different predictions of local [matrix-level] stress and strain fields. Similarly, the different void distributions give rise to different predictions of macroscopic stress and strain fields. Here, we compare the predictions of macroscopic response of the three models in order to elucidate the effects of void distribution on the macroscopic response. Figure (3-41) shows the case of macroscopic uniaxial tension for $f_0 = 0.15$ for the 3D V-BCC, LS and multi-void Voronoi models, respectively; the uniaxial stress-strain response is shown in (a), and the evolution of volumetric strain, $\overline{E}_{vol} = \ln \overline{J}$, is shown in (b). Figure (3-42) shows the macroscopic response to simple shear deformation for the 3D V-BCC, LS and Multi-void Voronoi models, respectively.

We first consider the case of macroscopic uniaxial tension. Figure (3-41a) shows that the predictions by the three models are in close agreement in the elastic region and in the strain-hardening region. In the region around macroscopic yield, and in the strain-softening region, the multi-void Voronoi model prediction of stress is higher than those of the LS and 3D V-BCC models. As discussed previously, the presence of an underlying lattice in the case of the 3D V-BCC and LS models enables the formation of local shear bands between voids in a few, pre-determined directions, whereas in the multi-void Voronoi model, the random void distribution provides a greater variation in possible shearing directions. Onset of macroscopic yield is reached when local void-to-void shear bands coalesce into a macroscopic shear band spanning the entire RVE. The formation of a macroscopic shear band in the LS model is

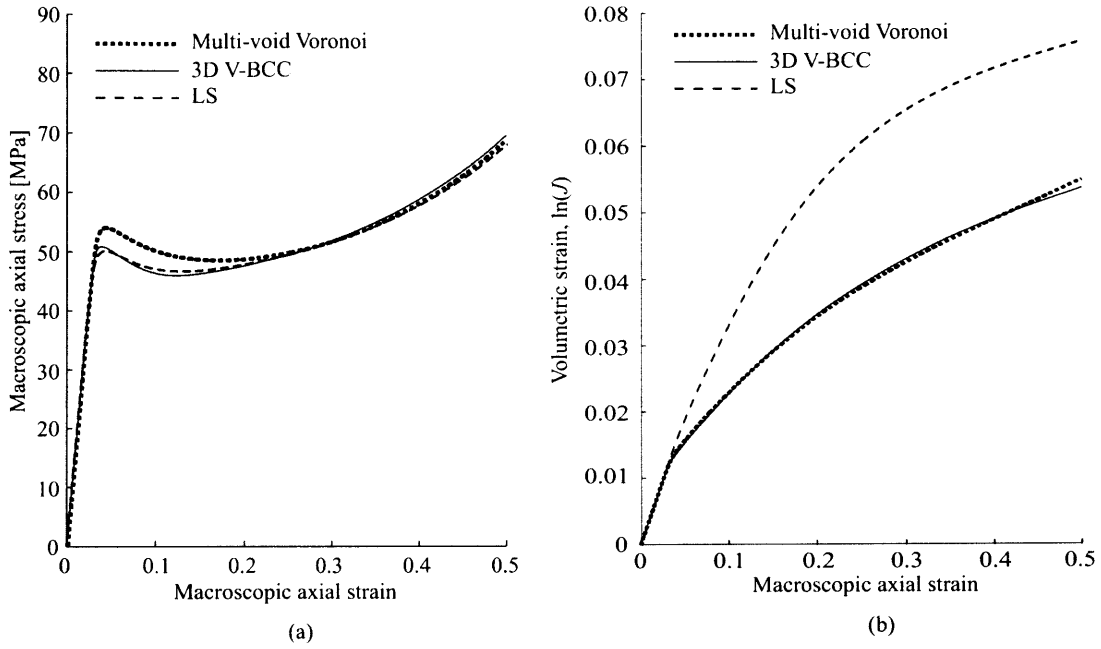

Figure 3-41: Comparison of the micromechanical models under macroscopic uniaxial tension ($f_0 = 0.15$): (a) macroscopic axial stress vs. macroscopic axial strain, (b) macroscopic volumetric strain vs. macroscopic axial strain.

facilitated by the presence of an underlying lattice; the formation of a local shear band between two voids promotes the formation of subsequent shear bands in the same direction, to a neighboring void on the lattice (Fig. 3-23b-c). It is important to emphasize that the macroscopic stress response of the two models with an underlying lattice is likely to be different for a different choice of macroscopic loading direction. For example, the 3D V-BCC model could be subjected to macroscopic uniaxial tension with the principal loading direction bisecting a hexagonal facet (Fig. 3-3), and the LS model could be subjected to macroscopic uniaxial tension along an RVE diagonal (Fig. 3-18).

Figure (3-41b) shows the evolution of macroscopic volumetric strain corresponding to the case of macroscopic uniaxial tension. Here, the response of the LS model differs markedly from those of the 3D V-BCC and multi-void Voronoi models. In the LS model, the voids are arranged randomly on a cubic lattice. In effect, the voids are located along certain planes in the matrix, separated by a solid layer of matrix

material. When macroscopic uniaxial tension is imposed along the principal cube directions, these solid matrix layers introduce an artificial lateral stiffness to the RVE, which prevents the RVE from contracting upon axial loading. Socrate and Boyce [63] report a similar finding for a single-void model based on a stacked hexagonal array of voids (the axisymmetric SHA model) (Fig. 3-1a), where a stiff matrix layer resulted in unrealistically high levels of volumetric strain. Socrate and Boyce also showed that by staggering the voids in the matrix, these laterally-stiff matrix layers were avoided, and the RVE was able to deform laterally through inter-void ligament shearing and rotation. The present 3D V-BCC model, in which the voids are staggered rather than stacked, displays volumetric strain levels that are similar to those of the axisymmetric V-BCC model, but significantly lower than those of the LS model. The volumetric strain response of the 3D V-BCC model is very close to that of the multi-void Voronoi model. This suggests that when voids are staggered in space, the volumetric response resembles that of a truly random distribution, whereas a "stacked" void arrangement is not suitable from this point of view. As discussed previously, the higher levels of volumetric strain in the LS model are associated with the existence of laterally stiff layers of matrix material in the RVE. The volumetric response of the RVE is therefore likely to change if the LS model was deformed along a diagonal.

Lastly, we compare predictions of the three RVEs for the case of macroscopic simple shear deformation. The three models give identical predictions of the initial elastic response. However, initial yield, and the predictions of the stress-strain response beyond initial yield, differ markedly between the models. The 3D V-BCC model displays an abrupt drop in stress immediately after yield. The abrupt drop in stress corresponds to the formation of a sharp vertical shear band (Fig. 3-12a-b). The formation and progression of this shear band through the RVE, described in Section 3.2.2, gives rise to an unrealistically fluctuating stress-strain response. Recall that for the case of $f_0 = 0.05$ (Fig. 3-13), the macroscopic shear stress even exceeded that of the homopolymer for certain strain levels. The stress-strain response in Fig. (3-13) is an artifact of the modeling simplification of the void distribution into a single void, and the chosen shearing direction with respect to the staggered BCC

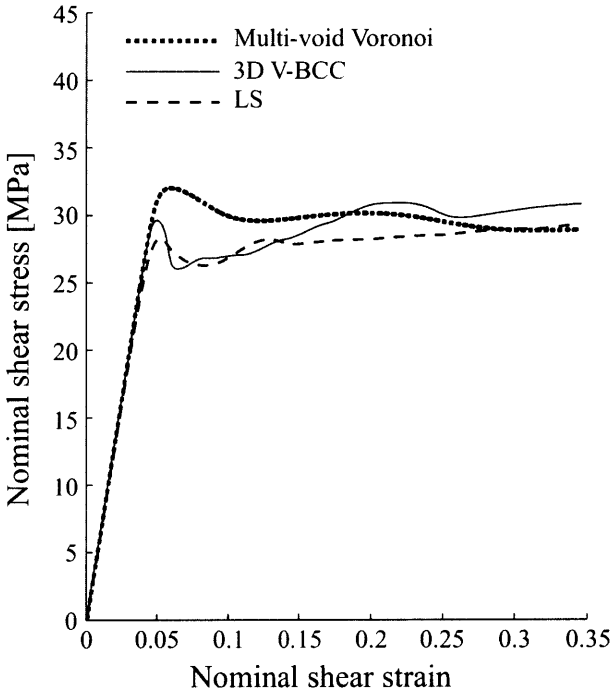

Figure 3-42: Comparison of the micromechanical models under macroscopic simple shear deformation: macroscopic nominal stress vs. macroscopic nominal shear strain ($f_0 = 0.15$).

void arrangement. The LS model displays a more realistic stress-strain response than the 3D V-BCC model; the inital macroscopic yield is followed by a less abrupt drop in stress and a less fluctuating post-yield stress. Rather than forming a vertical shear band through the RVE, macroscopic yield of the RVE corresponds to plastic shearing of a "weak" layer of voids, with unit normal $\mathbf{e}_3$, containing the largest number of voids. In the multi-void Voronoi model, such a layer of voids is not present, and Fig. (3-42) shows that the macroscopic stress required to cause macroscopic yield of the material is higher, and the post-yield drop in stress is less abrupt.

As discussed for the previous case of macroscopic uniaxial tension, it is likely that the predicted stress-strain response of the 3D V-BCC and LS models would be different if the macroscopic simple shear deformation was imposed in a different direction with respect to the underlying lattices. In particular, the cubic lattice in the LS model resulted in "weak" void layers along which shear bands readily formed. A different shearing direction is therefore expected to alter the prediction of initial yield stress, and the post-yield stress-strain response.

In conclusion, any stress-strain predictions by lattice-based models of the porous microstructure will be affected by lattice symmetries and spacings. In order to avoid issues pertaining to the particular choice of loading direction with respect to the lattice symmetries of the RVE, any load case should be averaged over a wide range of directions, as to reduce the lattice effects. As this is computationally prohibitive, it becomes necessary to use an RVE absent an underlying lattice. We therefore conclude that the multi-void Voronoi model, which lacks an underlying lattice, is superior to any lattice-based [single-void or multi-void] models of a random, porous microstructure.

Chapter 4

Constitutive Modeling of Porous Glassy Polymers

As discussed in Chapter 2, the constitutive behavior of glassy polymers has been successfully described within a continuum mechanics framework by Boyce, et al. [12], and Arruda and Boyce [7]. Their model captures the effects of strain, strain rate and temperature on the elastic-viscoplastic behavior of glassy polymers, and it has been applied to various glassy polymers, such as poly(methyl methacrylate) (PMMA) and polycarbonate (PC), the latter being the focus of this work.

As evidenced by the micromechanical modeling results of Chapter 3, the addition of rubber particles, modeled as voids, to polycarbonate alters its mechanical behavior. Under tensile loading conditions, where the rubber particles may be approximated as voids, in view of their deformation-induced cavitation, the rubber-toughened polycarbonate displays the following macroscopic features, when compared to the homopolymer (Fig. 4a,b):

- reduced elastic stiffness,
- decreased yield stress,
- reduced post-yield softening,
- reduced strain-hardening,

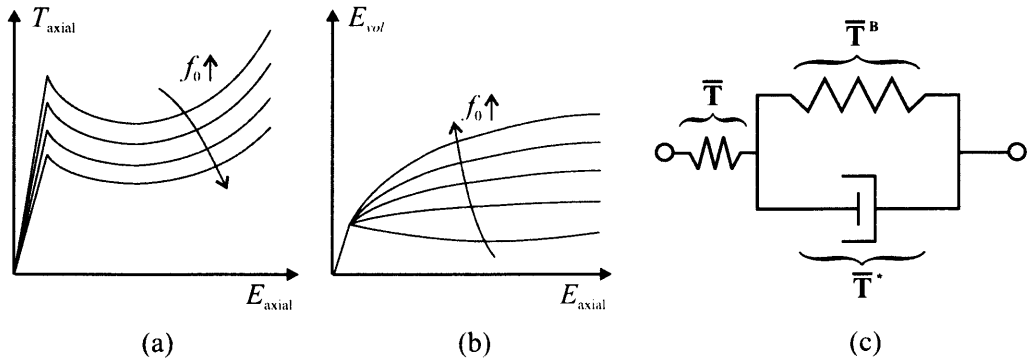

Figure 4-1: The porous glassy polymer: (a,b) features of macroscopic deformation, (c) schematic of the proposed model.

- plastic dilatation through plastic void growth.

These features of the mechanical behavior of the material need to be addressed and included in a continuum-level constitutive model for the mechanical behavior of rubber-toughened polycarbonate. Several constitutive models have been proposed over the past decades within the context of *rate-independent* porous *metal* plasticity; see for example McClintock [47] and Gurson [31]. The Gurson model was developed for the small-strain behavior of rigid, perfectly-plastic materials (metals) with dilute concentrations of spherical voids, subjected to highly triaxial stress states. This suggests that a mere application of the Gurson model to rubber-toughened polycarbonate would not be successful. The Gurson model has been modified to account for some of the intrinsic constitutive differences between metals and polymers. For example, large elastic strains in polymers have been accounted for by Steenbrink, et al. [65], and Lazzeri and Bucknall [43] modeled the matrix pressure dependence on the onset of macroscopic yield of a porous glassy polymer containing spherical voids. These modifications might make a "Gurson-type" model more suitable for the application to rubber-toughened polycarbonate. However, the intrinsic rate-dependence observed in glassy polymers raises some doubts about the validity of the "Gurson-type" models. Furthermore, previous work has mostly focused on macroscopic yield of the material, and the porosity-dependence of the observed back-stress at large macroscopic strain levels has not been addressed.

Zavaliangos and Anand [78] developed a constitutive modeling framework for rate-dependent porous materials. Their work showed applicability to a broad range of matrix strain-rate sensitivities, from nearly rate-independent materials at low homologous temperatures, to strongly rate-dependent materials at high homologous temperatures. However, their work did not include (kinematic) strain-hardening of the porous matrix material, which is characteristic of glassy polymers. In conclusion, there is no constitutive model in the literature able to fully account for the major features of deformation of porous glassy polymers.

We propose to model the constitutive behavior of rubber-toughened glassy polymers (here porous polycarbonate) by modifying the components of the Arruda-Boyce "spring-dashpot" structure to account for porosity. The porosity will be modeled using one scalar parameter, f, which evolves with macroscopic deformation. The initial value of f represents the initial volume fraction of rubber particles in the rubber-polycarbonate blend, and is denoted f_0. The introduction of the void volume fraction, f, should modify the glassy polymer model as follows (Figs. 3-33, 3-35, 3-37 and 3-39):

- The initial elastic response should include effects of porosity, as there is an observed decrease in stiffness with increasing porosity.

- The flow rule should include a dilatational component, as the porous material deforms volumetrically through plastic void growth.

- The back-stress (from orientation hardening of the polycarbonate matrix) should include a porosity-dependent hydrostatic term, as the porous material strain-hardens under macroscopic volumetric deformation.

- A requirement for the proposed approach, where the porous model is defined by modifying the Arruda-Boyce model, is that in the limit of zero initial porosity, $f_0 \rightarrow 0$, the original Arruda-Boyce model (Chapter 2) should be recovered.

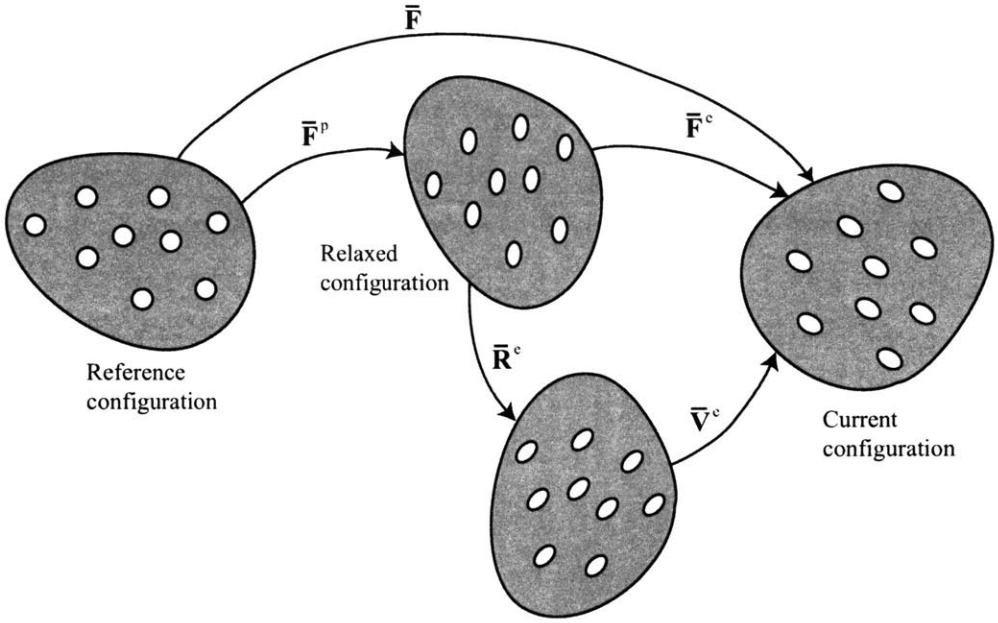

Figure 4-2: Finite strain kinematics of the porous glassy polymer.

4.1 Kinematics

The total deformation gradient, $\overline{\mathbf{F}}$, of the porous material is multiplicatively decomposed into elastic and plastic parts according to Lee [44],

$$\overline{\mathbf{F}} = \overline{\mathbf{F}}^{e}\,\overline{\mathbf{F}}^{p}, \tag{4.1}$$

where the superscripts e and p denote the elastic and plastic (relaxed) configurations, respectively[1]. The plastic deformation gradient, $\overline{\mathbf{F}}^{p}$, is obtained in the relaxed configuration by elastically unloading to a stress-free state via $\overline{\mathbf{F}}^{e-1}$ (Fig. 4.1). The elastic deformation gradient, $\overline{\mathbf{F}}^{e}$, can be polar-decomposed as

$$\overline{\mathbf{F}}^{e} = \overline{\mathbf{V}}^{e}\,\overline{\mathbf{R}}^{e}, \tag{4.2}$$

[1]In order to distinguish between the macroscopic behavior of the porous glassy polymer, and the behavior of the homogeneous glassy polymer matrix, tensor quantities pertaining to the former are indicated by a bar, e.g. $\overline{\mathbf{F}}$ and $\mathbf{F}$ for macroscopic vs. pointwise (matrix-level) deformation gradients, respectively.

where $\overline{\mathbf{V}}^e$ is the left elastic stretch tensor, and the elastic rotation $\overline{\mathbf{R}}^e$ is a proper orthogonal tensor. The velocity gradient, $\overline{\mathbf{L}}$, can be expressed as the sum of a (symmetric) stretching tensor, $\overline{\mathbf{D}}$, and a (skew) spin tensor $\overline{\mathbf{W}}$, and it is given as follows:

$$\overline{\mathbf{L}} = \dot{\overline{\mathbf{F}}}\,\overline{\mathbf{F}}^{-1} = \overline{\mathbf{D}} + \overline{\mathbf{W}} = \underbrace{\dot{\overline{\mathbf{F}}}^e\,\overline{\mathbf{F}}^{e-1}}_{\overline{\mathbf{L}}^e} + \underbrace{\overline{\mathbf{F}}^e\tilde{\overline{\mathbf{L}}}^p\overline{\mathbf{F}}^{e-1}}_{\overline{\mathbf{L}}^p} = \overline{\mathbf{L}}^e + \overline{\mathbf{L}}^p, \tag{4.3}$$

where $\overline{\mathbf{L}}^e$ and $\overline{\mathbf{L}}^p$ are the elastic and plastic velocity gradients in the current configuration, respectively, and $\tilde{\overline{\mathbf{L}}}^p = \dot{\overline{\mathbf{F}}}^p\,\overline{\mathbf{F}}^{p-1}$ is the plastic velocity gradient in the relaxed configuration. The plastic velocity gradient in the current configuration can be decomposed into symmetric and skew parts as,

$$\overline{\mathbf{L}}^p = \overline{\mathbf{D}}^p + \overline{\mathbf{W}}^p. \tag{4.4}$$

In this formulation, we prescribe the skew part of the plastic velocity gradient in the current configuration to be zero, $\overline{\mathbf{W}}^p \equiv \mathbf{0}$. The evolution of the plastic deformation gradient (the flow rule) is then given by

$$\dot{\overline{\mathbf{F}}}^p = \tilde{\overline{\mathbf{L}}}^p\,\overline{\mathbf{F}}^p = \overline{\mathbf{F}}^{e-1}\,\overline{\mathbf{D}}^p\,\overline{\mathbf{F}}^e\,\overline{\mathbf{F}}^p, \tag{4.5}$$

where $\overline{\mathbf{D}}^p$ is prescribed as discussed in the following sections. The void volume fraction, f, is defined in the relaxed configuration. From plastic incompressibility of the matrix material, and balance of mass, a relation between the initial void volume fraction, f_0, and current void volume fraction, f, is given by

$$\det \overline{\mathbf{F}}^p = \frac{1 - f_0}{1 - f}. \tag{4.6}$$

4.2 Stress

The macroscopic (Cauchy) stress, $\overline{\mathbf{T}}$, acting on the material is the sum of the contributions from the viscoplastic dashpot and the non-linear hardening spring (macroscopic

back-stress):

$$\overline{\mathbf{T}} = \overline{\mathbf{T}}^{*} + \frac{1}{\overline{J}^{e}} \overline{\mathbf{F}}^{e} \overline{\mathbf{T}}^{B} \overline{\mathbf{F}}^{eT}, \tag{4.7}$$

where $\overline{J}^{e} = \det \overline{\mathbf{F}}^{e}$. The macroscopic stress acting on the dashpot, $\overline{\mathbf{T}}^{*}$, is defined in the current configuration. The macroscopic back-stress, $\overline{\mathbf{T}}^{B}$, is defined in the relaxed configuration, and pushed forward to the current configuration via $\overline{\mathbf{F}}^{e}$.

4.3 Linear elastic behavior

The elastic response of the porous glassy polymer is assumed to be isotropic and therefore characterized by two effective elastic moduli. The elastic stiffness of the porous glassy polymer is described by the fourth-order elasticity tensor, $\overline{\mathcal{C}}^{e}$,

$$\overline{\mathcal{C}}^{e} \equiv 2\,\overline{\mu}\,\mathcal{I} + \{\overline{\kappa} - 2/3\,\overline{\mu}\}\,\mathbf{1} \otimes \mathbf{1}, \tag{4.8}$$

where $\overline{\mu}$ and $\overline{\kappa}$ are the effective shear and bulk moduli, respectively, and $\mathbf{1}$ and $\mathcal{I}$ are the second and fourth-order identity tensors, respectively. The effective elastic shear and bulk moduli, $\overline{\mu}$ and $\overline{\kappa}$, are functions of the matrix elastic moduli and the void volume fraction f. The effective elastic moduli of a void-containing matrix has been studied extensively in the literature (e.g. Budiansky [17], Hill [34], Mori and Tanaka [50]). Here, we use the Mori and Tanaka estimates, as expressed by Benveniste [10], to describe the porosity dependence on the effective elastic moduli,

$$\overline{\mu} = \frac{\mu(1-f)}{1 + 6f\left(\frac{\kappa+2\mu}{9\kappa+8\mu}\right)}, \tag{4.9}$$

$$\overline{\kappa} = \frac{4(1-f)}{\frac{4}{\kappa} + \frac{3f}{\mu}}. \tag{4.10}$$

Using an elastic logarithmic strain measure, $\overline{\mathbf{E}}^e = \ln \overline{\mathbf{V}}^e$, the total (Cauchy) stress is then given by

$$\overline{\mathbf{T}} = \frac{1}{\overline{J}^e} \overline{\mathcal{C}}^e \left(\overline{\mathbf{E}}^e \right). \tag{4.11}$$

4.4 Back-stress

The orientation hardening of glassy polymers is attributed to the alignment of molecular chains with deformation. As the molecular chains approach their limiting extensibility, the resulting back-stress in the glassy polymer increases rapidly, and the material 'locks'. In the case of homogeneous glassy polymers, this orientation hardening and terminal locking has been successfully described using the (incompressible) eight-chain model for rubber elasticity (Arruda and Boyce [8]). The strain energy density function Ψ for the eight-chain model is given by

$$\Psi = \hat{\Psi}(I_1^p; C_R, N) = C_R \sqrt{N} \left(\beta \sqrt{\frac{I_1^p}{3}} + \sqrt{N} \ln \frac{\beta}{\sinh \beta} \right) + c, \tag{4.12}$$

where, in the application to the orientation hardening of glassy polymers, the parameters C_R, $\sqrt{N}$ and c are the initial hardening modulus, the limiting plastic stretch (locking stretch) of the molecular network, and a temperature-dependent constant, respectively. The first invariant of plastic stretch, I_1^p, is defined as $I_1^p = \operatorname{tr} \mathbf{B}^p = \operatorname{tr}(\mathbf{F}^p \mathbf{F}^{pT})$, and the inverse Langevin function, β, is given by

$$\beta = \mathcal{L}^{-1} \left(\sqrt{\frac{I_1^p}{3N}} \right) \; ; \; \mathcal{L}(\beta) = \coth \beta - \frac{1}{\beta}. \tag{4.13}$$

The back-stress in the plastically incompressible ($J^p = \det \mathbf{F}^p = 1$) homogeneous glassy polymer can be determined, to within an arbitrary pressure p^B, as

$$\mathbf{T}^B = 2 \frac{\partial \Psi}{\partial \mathbf{B}^p} \mathbf{B}^p = C_R \frac{\sqrt{3N}}{\sqrt{I_1^p}} \mathcal{L}^{-1} \left(\sqrt{\frac{I_1^p}{3N}} \right) \operatorname{dev} \mathbf{B}^p - p^B \mathbf{1}, \tag{4.14}$$

where $\mathrm{dev}\,\mathbf{B}^p = \mathrm{dev}\left(\mathbf{F}^p\mathbf{F}^{pT}\right)$ and $\lambda^p_{ch} = [\mathrm{tr}\,\mathbf{B}^p/3]^{1/2}$.

In the case of a porous glassy polymer, the void-containing material is not plastically incompressible ($\overline{J}^p = \det\overline{\mathbf{F}}^p \neq 1$), as it can accommodate macroscopically dilatant deformations through plastic void growth. In order to accurately describe the orientation hardening behavior of porous glassy polymers we therefore use a recently-proposed framework for constitutive modeling of porous hyperelastic materials (Danielsson, et al. [22], Appendix B). The macroscopic strain energy density function for a given (pointwise incompressible) hyperelastic matrix material, and a prescribed macroscopic state of deformation, was expressed by Danielsson, et al. [22], using a spherical (hollow) volume element, of initial outer radius B, to represent the porous material. For the present application to the orientation hardening of porous glassy polymers, this expression becomes

$$\overline{\Psi} = \frac{1}{V_0}\int_{Bf_0^{1/3}}^{B}\int_0^{2\pi}\int_0^{\pi}\hat{\Psi}(I_1^p; C_R, N)\,R^2\sin\Theta\,\mathrm{d}\Theta\,\mathrm{d}\Phi\,\mathrm{d}R, \tag{4.15}$$

where $\hat{\Psi}$ the local strain energy density function of the incompressible hyperelastic matrix material is integrated over the reference volume $V_0 = 4\pi B^3/3$ of the spherical volume element. The pointwise first invariant of plastic stretch, I_1^p, is expressed in the sphere in terms of the macroscopically-applied plastic deformation, as

$$I_1^p = \frac{1}{\left(\overline{J}^p\right)^{2/3}}\left\{\overline{I}_1^p\,\psi^2 + \frac{1}{R^2}\left(\left(\overline{\lambda}_1^p\right)^2 X_1^2 + \left(\overline{\lambda}_2^p\right)^2 X_2^2 + \left(\overline{\lambda}_3^p\right)^2 X_3^2\right)\left(\frac{1}{\psi^4} - \psi^2\right)\right\}, \tag{4.16}$$

where $\overline{\lambda}_i^p$ are the macroscopic principal plastic stretches, $\overline{I}_1^p = \mathrm{tr}\overline{\mathbf{B}}^p = \mathrm{tr}(\overline{\mathbf{F}}^p\overline{\mathbf{F}}^{pT})$, $\psi = \hat{\psi}(R) = \left(1 + \left(\overline{J}^p - 1\right)(B/R)^3\right)^{1/3}$, and X_i are the Cartesian reference coordinates of a point in the sphere. This expression is based on an approximate form for the deformation field in the volume element (Danielsson, et al. [22], Hou and Abeyaratne [35]).

The macroscopic back-stress tensor is obtained by differentiation of the macroscopic strain energy density function, $\overline{\Psi}$, with respect to the plastic left Cauchy-Green

strain tensor, $\overline{\mathbf{B}}^p$,

$$\overline{\mathbf{T}}^B = \frac{2}{\overline{J}^p} \frac{\partial \overline{\Psi}}{\partial \overline{\mathbf{B}}^p} \overline{\mathbf{B}}^p. \tag{4.17}$$

The differentiation of $\overline{\Psi}$ with respect to $\overline{\mathbf{B}}^p$ is not straightforward, as the expression for the pointwise first invariant of plastic stretch (Eq. 4.16) has explicit occurences of the macroscopic principal plastic stretches, $\overline{\lambda}_i^p$. Since the principal directions of the macroscopic back-stress tensor, $\overline{\mathbf{T}}^B$, and the macroscopic plastic left Cauchy-Green strain tensor, $\overline{\mathbf{B}}^p$, coincide, the evaluation of $\overline{\mathbf{T}}^B$ can be readily carried out in the principal frame of $\overline{\mathbf{B}}^p$.

The macroscopic plastic left Cauchy-Green strain tensor, $\overline{\mathbf{B}}^p$, can be decomposed into an orthogonal rotation tensor, $\overline{\mathbf{Q}}$ and a diagonal tensor $\overline{\mathbf{b}}^p$, as

$$\overline{\mathbf{B}}^p = \overline{\mathbf{Q}}\, \overline{\mathbf{b}}^p\, \overline{\mathbf{Q}}^T, \tag{4.18}$$

where $\overline{\mathbf{b}}^p$ is the macroscopic plastic left Cauchy-Green strain tensor rotated into its principal frame. The diagonal components of $\overline{\mathbf{b}}^p$ are expressed in terms of the macroscopically-applied plastic stretches, $\overline{\lambda}_i^p$, as

$$[\overline{\mathbf{b}}^p]_i = \left(\overline{\lambda}_i^p\right)^2. \tag{4.19}$$

Since the principal directions of the macroscopic back-stress tensor, $\overline{\mathbf{T}}^B$, and the macroscopic plastic left Cauchy-Green strain tensor, $\overline{\mathbf{B}}^p$, coincide, the latter may be decomposed as,

$$\overline{\mathbf{T}}^B = \overline{\mathbf{Q}}\, \overline{\mathbf{t}}^B\, \overline{\mathbf{Q}}^T, \tag{4.20}$$

where $\overline{\mathbf{t}}^B$ is the macroscopic back-stress tensor, expressed in its principal frame. By combining Eqs. (4.17), (4.18) and (4.20), the macroscopic principal back-stress tensor

can be expressed as

$$\bar{\mathbf{t}}^B = \frac{2}{\overline{J}^p}\,\overline{\mathbf{Q}}^T\,\frac{\partial\overline{\Psi}}{\partial\overline{\mathbf{B}}^p}\,\overline{\mathbf{Q}}\,\overline{\mathbf{Q}}^T\,\overline{\mathbf{B}}^p\,\overline{\mathbf{Q}} = \frac{2}{\overline{J}^p}\,\frac{\partial\overline{\Psi}}{\partial\overline{\mathbf{b}}^p}\,\overline{\mathbf{b}}^p. \tag{4.21}$$

Using Eq. (4.21), the diagonal components of the macroscopic principal back-stress tensor, $\bar{\mathbf{t}}^B$, are then expressed as

$$[\bar{\mathbf{t}}^B]_i = \left[\frac{2}{\overline{J}^p}\,\frac{\partial\overline{\Psi}}{\partial\overline{\mathbf{b}}^p}\,\overline{\mathbf{b}}^p\right]_i = \frac{2}{\overline{J}^p}\,\frac{\partial\overline{\Psi}}{\partial\left(\left(\overline{\lambda}_i^p\right)^2\right)}\left(\overline{\lambda}_i^p\right)^2 = \frac{\overline{\lambda}_i^p}{\overline{J}^p}\,\frac{\partial\overline{\Psi}}{\partial\overline{\lambda}_i^p} \quad \text{(no sum on } i\text{)}. \tag{4.22}$$

By using Eq. (4.22) and (4.15), the diagonal components of the macroscopic back-stress tensor can be expressed as

$$[\bar{\mathbf{t}}^B]_i = \frac{\overline{\lambda}_i^p}{\overline{J}^p V_0}\int_{Bf_0^{1/3}}^{B}\int_0^{2\pi}\int_0^{\pi}\frac{\partial\hat{\Psi}}{\partial I_1^p}\,\frac{\partial I_1^p}{\partial\overline{\lambda}_i^p}\,R^2\sin\Theta\,\mathrm{d}\Theta\,\mathrm{d}\Phi\,\mathrm{d}R. \tag{4.23}$$

The integral in Eq. (4.23) can be evaluated numerically using an appropriate numerical quadrature rule, such as Gauss-Legendre quadrature (see, for example Stroud and Secrest [66]). The macroscopic back-stress tensor, $\overline{\mathbf{T}}^B$, can then be readily obtained through the rotation of $\bar{\mathbf{t}}^B$ by $\overline{\mathbf{Q}}$ (Eq. 4.20).

A back-stress tensor based on the preceding discussion accounts for the evolving plastic anisotropy of the porous material, which arises from evolving molecular alignment in the matrix material with plastic deformation, and the anisotropic growth of voids. However, it does not fully take into account possible effects of [strong] void-to-void interactions on the back-stress in the real material. Danielsson, et al. [22] compared predictions of their model, using a Neo-Hookean matrix material, to results obtained from micromechanical modeling. The authors found that while the stress-strain response was well-predicted over the range of studied load cases and void volume fractions, the predictions of volumetric straining under plane strain tension showed differences. As will be discussed below, some of the possible shortcomings of the present [eight-chain Langevin statistics-based] back-stress model can be compensated for by the specific choice of functional form for the macroscopic plastic

stretching, $\overline{\mathbf{D}}^p$.

4.5 Viscoplastic flow

The visco-plastic flow in the Arruda-Boyce model is modeled as purely deviatoric, and thus volume-preserving. The plastic stretching tensor, $\mathbf{D}^p$ is aligned with the deviator of the driving stress, dev $(\mathbf{T}^*)$. The micromechanical modeling results of Chapter 3 indicate that the visco-plastic flow of the porous glassy polymer is different from that of the homopolymer. The functional form of the plastic stretching tensor, $\overline{\mathbf{D}}^p$, of the porous material should include the following major features:

- The "yield stress" of the porous material decreases with increasing volume fraction of voids.
- The post-yield softening decreases with increasing volume fraction of voids.
- The presence of voids in the plastically-incompressible glassy polymer matrix enables plastic dilatation of the porous material through void growth.

The objective of this section is to develop functional forms for the macroscopic plastic stretching tensor, $\overline{\mathbf{D}}^p$, for the porous glassy polymer. In Chapter 2, two functions for the effective plastic shear strain-rate were presented: the exponential expression by Argon (Eq. 2.11) and the power-law expression (Eq. 2.12). The power-law expression will be used in the following discussion, as its simple form provides [convexity and homogeneity] information about admissible forms for $\overline{\mathbf{D}}^p$. The subject of porous, rate-sensitive, materials has been studied in the past by various researchers. This work has mainly focused on materials that do not possess a significant back-stress. The previous work is reviewed in the following section, and the application to porous glassy polymers in the presence of a back-stress is subsequently presented.

4.5.1 Porous viscoplasticity

The flow in visco-plastic solids is often characterized by a plastic strain-rate potential, Φ. The plastic stretching, $\mathbf{D}^p$, is defined as the gradient with respect to stress of this

plastic strain-rate potential,

$$\mathbf{D}^p = \frac{\partial \Phi}{\partial \mathbf{T}}. \tag{4.24}$$

The (scalar) plastic strain-rate potential, Φ, for an incompressible power-law material is given by

$$\Phi = \hat{\Phi}\left(T_{eq}, m\right) = \frac{\dot{\nu}_0 s}{1/m+1}\left(\frac{T_{eq}}{s}\right)^{1/m+1}, \tag{4.25}$$

where m is a strain-rate sensitivity parameter. This plastic strain-rate potential is a function only of T_{eq}, the second invariant of the stress deviator $\mathrm{dev}\,(\mathbf{T})$. The plastic stretching, $\mathbf{D}^p$, in a constitutive formulation based on Eq. (4.24), is therefore deviatoric. Equations (4.24) and (4.25) give the plastic stretching for the homopolymer,

$$\mathbf{D}^p = \dot{\gamma}^p \frac{\mathrm{dev}\,(\mathbf{T})}{\|\mathrm{dev}\,(\mathbf{T})\|}, \tag{4.26}$$

which is consistent with Eq. (2.13). The macroscopic strain-rate potential, $\overline{\Phi}$, of a *porous* material should be a function of porosity, and it should reduce to the plastic strain-rate potential of the matrix material in the limit of zero porosity. Duva and Hutchinson [25] proposed a plastic strain-rate potential for the macroscopic plastic stretching of a power-law matrix containing a dilute concentration of spherical voids on the form

$$\overline{\Phi} = \Phi\left(\overline{\mathbf{T}}\right) + f\Phi_V\left(\overline{\mathbf{T}}\right), \tag{4.27}$$

where Φ is the strain-rate potential for the power-law matrix material (Eq. 4.25), evaluated at $\overline{T}_{eq}$, and Φ_V is an appropriately defined change in potential caused by the introduction of an isolated spherical void in an infinite block of the matrix material which is subjected to the macroscopic stress $\overline{\mathbf{T}}$. This proposition of the macroscopic plastic strain-rate potential is only applicable to dilute volume fractions of voids, where void-to-void interactions can be neglected. For the present application

to porous glassy polymers, where void volume fractions are typically in the order of $5 - 15\%$, the interactions between voids are significant and cannot be neglected, and the dilute assumption breaks down. Cocks [19] presented (one-sided) bounds on the macroscopic plastic strain-rate potential for porous materials of non-dilute concentrations of voids. Cocks extended the formalism of Duva and Hutchinson by using a macroscopic plastic strain-rate potential on the form

$$\overline{\Phi} = \hat{\overline{\Phi}}\left(\overline{T}_{eq}, \overline{T}_m, f, m\right) = F\left(X, f, m\right)\Phi\left(\overline{T}_{eq}, m\right), \tag{4.28}$$

where $\overline{T}_{eq}$ and $\overline{T}_m$ are the macroscopic Mises and mean stresses, respectively, $X = \overline{T}_m/\overline{T}_{eq}$ is the triaxiality of macroscopic stress, and F is an elliptical interpolation of the predicted behavior at purely deviatoric and purely hydrostatic macroscopic states of stress. As pointed out by Hutchinson [36], the convexity and homogeneity of the power-law strain-rate potential must be preserved in the transition to a macroscopic strain-rate potential for the porous material. By differentiating Eq. (4.28) with respect to the macroscopic stress $\overline{\mathbf{T}}$, the expression for the macroscopic plastic stretching becomes

$$\overline{\mathbf{D}}^p = \dot{\nu}_0 \left[\frac{3}{2}\left(F - \frac{F'X}{1/m+1}\right)\frac{\operatorname{dev}\overline{\mathbf{T}}}{\overline{T}_{eq}} + \frac{F'}{3\left(1/m+1\right)}\mathbf{1}\right]\left(\frac{\overline{T}_{eq}}{s}\right)^{1/m}, \tag{4.29}$$

where $(\ldots)'$ denotes differention with respect to X, and s here represents an effective shear strength of the matrix material. Convexity of the macroscopic strain-rate potential, $\overline{\Phi}$, is satisfied if the following inequality holds (Rodin and Parks [59]):

$$F\,F'' - \frac{1}{m+1}F'^2 > 0, \tag{4.30}$$

where $(\ldots)''$ denotes the second derivative with respect to X. The required homogeneity of the macroscopic strain-rate potential is satisfied if the following requirements are met (Zavaliangos [79]):

- In the limit of zero-porosity, the plastic strain-rate potential of the homogeneous

material should be recovered:

$$\lim_{f \to 0} F(X, f, m) = 1. \tag{4.31}$$

- Under purely hydrostatic tension, the requirement that $\operatorname{tr} \overline{\mathbf{D}}^p \neq 0$ from Eq. (4.29) requires

$$\lim_{X \to \infty} F(X, f, m) \propto X^{1/m+1}. \tag{4.32}$$

Several investigators, for example Haghi and Anand [32], Sofronis and McMeeking [64] and Michel and Suquet [48], have proposed models for rate-dependent porous power-law materials using a macroscopic strain-rate-potential based on Eq. (4.27), with F given by

$$F = A_1 + \left(A_2 X^2 + A_3\right)^{\frac{1/m+1}{2}} \tag{4.33}$$

where $A_i = \hat{A}_i(f, m)$. The function A_2 governs the plastic flow of the material under purely hydrostatic states of stress ($X \to \infty$). The models by Haghi and Anand, Sofronis and McMeeking, and Michel and Suquet all have in common an A_2 selected to reproduce the analytical solution for the dilatational behavior of a thick-walled sphere made from an isotropic, pointwise incompressible, power-law viscoplastic matrix material, subjected to external hydrostatic stress. The functions A_1 and A_3 influence the plastic flow of the porous material under purely deviatoric, and under mixed [deviatoric + hydrostatic] states of stress. Several approaches can be followed to select appropriate forms for these functions. For example, Michel and Suquet set $A_1 = 0$, and estimated A_3 from lower bounds (Ponte-Castañeda and Willis [57]). Sofronis and McMeeking also set $A_1 = 0$, and estimated A_3 through comparisons with finite element results for a sphere subjected to purely deviatoric ($X = 0$) states of stress. Zavaliangos and Anand noted that for linear viscous ($m = 1$) matrix materials of constant strength ($s = s_0$), any proposed potential for the porous material should agree with the known dilute-limit potential of Duva and Hutchinson [25]. Based

on this, Zavaliangos and Anand adopted the functional forms of Haghi and Anand, where $A_1 = 1$, and A_3 was obtained by fitting the model to numerical results from axisymmetric finite element simulations. The particular choice of the functions A_i will, in general, have certain ranges of applicability. For example, choices of A_2 to match known solutions for thick-walled spheres under hydrostatic tension, are only valid for low to moderate void volume fractions, as these "sphere solutions" imply that the voids do not interact significantly.

For a general [deviatoric + hydrostatic] state of macroscopic stress, $\overline{\mathbf{T}}$, the exact distribution of stress and [evolved] shear strength in the matrix is unknown. In Eq. (4.29), the matrix shear strength is defined by an effective value, s. In order to relate this effective shear strength to the macroscopic stress state, an effective matrix shear stress, τ, is defined through plastic dissipation arguments. The external plastic dissipation of the porous material is equal to the internal plastic dissipation, which arises from plastic shearing of the matrix:

$$\overline{\mathbf{T}} \cdot \overline{\mathbf{D}}^p = \sqrt{2}\tau\dot{\gamma}^p (1 - f), \tag{4.34}$$

where $\dot{\gamma}^p$ is a plastic shear strain-rate. By combining Eqs. (4.29) and (4.34), the effective shear stress in the matrix can be expressed as

$$\tau = \frac{1}{\sqrt{3}} \left(\frac{F}{1-f} \right)^{\frac{1}{1/m+1}} \overline{T}_{eq}. \tag{4.35}$$

The effective shear strength, s, in the matrix (Eq. 4.29) is taken to evolve according to

$$\dot{s} = h \left(1 - \frac{s}{s_{sat}} \right) \dot{\gamma}^p \tag{4.36}$$

where h is a [hardening or softening] parameter, and $\dot{\gamma}^p$ is here given by the power-law expression

$$\dot{\gamma}^p = \dot{\nu}_0 \left(\frac{\tau}{s} \right)^{1/m}, \tag{4.37}$$

where τ is the effective matrix shear stress, given by Eq. (4.34).

4.5.2 Application to glassy polymers

In the presence of an orientation-induced back-stress, the stress that drives the visco-plastic flow is given by the tensorial difference between the macroscopic Cauchy stress, $\overline{\mathbf{T}}$, and the back-stress, $\overline{\mathbf{T}}^B$ (Eq. 4.7). The macroscopic plastic strain-rate potential, $\overline{\Phi}$, (Eq. 4.28) is therefore expressed in terms of the invariants of the macroscopic driving stress for plastic flow, $\overline{\mathbf{T}}^*$, rather than the total stress, $\overline{\mathbf{T}}$. As discussed previously, the model for the back-stress does not take into account possible effects of void-to-void interactions. In order to compensate for possible shortcomings of the back-stress model pertaining to its volumetric response, the form for the functions A_i is altered to include macroscopic plastic volumetric strain. Moreover, the primary objective of the present work is to develop a continuum-level constitutive model using a specific matrix material, namely glassy polycarbonate. The general dependence on the strain-rate sensitivity m of the functions A_i is therefore removed. The [matrix-specific] functional forms for A_i become

$$A_i = \hat{A}_i(f, f_0), \tag{4.38}$$

where the dependence of macroscopic plastic volumetric strain on the macroscopic plastic stretching is taken into account by including the initial void volume fraction, f_0, in addition to the current void volume fraction, f. The expression for the macroscopic plastic stretching, $\overline{\mathbf{D}}^p$, becomes

$$\overline{\mathbf{D}}^p = \dot{\nu}_0 \left[\frac{3}{2} \left(F - \frac{F' X^*}{1/m + 1} \right) \frac{\operatorname{dev} \overline{\mathbf{T}}^*}{\overline{T}^*_{eq}} + \frac{F'}{3\,(1/m+1)} \mathbf{1} \right] \left(\frac{\overline{T}^*_{eq}}{s} \right)^{1/m}, \tag{4.39}$$

where $X^* = \overline{T}^*_m / \overline{T}^*_{eq}$ here represents the triaxiality of macroscopic driving stress for plastic flow, and $(\ldots)'$ implies differentiation with respect to X^*. The plastic dissipation in the matrix can, as in Section 4.5.1, be used to define an effective driving

shear stress in the matrix, τ^*,

$$\overline{\mathbf{T}}^* \cdot \overline{\mathbf{D}}^p = \sqrt{2}\tau^* \dot{\gamma}^p (1 - f) . \tag{4.40}$$

This effective shear stress can then be used to evolve the effective matrix shear strength, s, in Eq. (4.39), using Eqs. (4.36) and (4.37). The matrix shear stress and shear strength fields are thus represented by two single, scalar, quantities s and τ^*. Clearly, in a porous material, there is a distribution of matrix shear stress and [evolved] shear strength, and, as pointed out by Zavaliangos [79], it is not obvious that these fields can be successfully related through Eq. (4.37). The effects of the distributed nature of these fields may be important in the case of a softening glassy polymer matrix. The micromechanical modeling results of Chapter 3 suggest that the stress state in the porous glassy polymer is non-uniform as a result of shear-localization. The attractive but minimalist approach of representing the matrix shear stress and matrix shear strength by two effective quantities may therefore warrant additional consideration / modeling.

4.6 Calibration of constitutive model parameters

The function F modifies the plastic strain-rate potential of the homogeneous glassy polymer to account for porosity through the three functions A_1, A_2 and A_3 (Eq. 4.33). As discussed previously, these functions generally depend on the matrix strain-rate sensitivity parameter m. However, for a given matrix material, the parameter m can be omitted, making the three functions A_i matrix-specific. In order to compensate for possible shortcomings of the employed back-stress model in its volumetric response, the effect of plastic volumetric strain was included in the functional forms for A_i (Eq. 4.38). In this section, we determine suitable forms for these functions $A_i = \hat{A}_i (f, f_0)$ for a glassy polycarbonate matrix material, containing $5 - 15\%$ voids. The functional forms for A_i are obtained by comparing the resulting constitutive model predictions to micromechanical modeling results from the previous chapter.

4.6.1 Calibration of the functions A_1, A_2 and A_3

Under macroscopic hydrostatic tension, the macroscopic driving stress for plastic flow is also hydrostatic. The macroscopic plastic stretching for this state of driving stress is not dependent on the functions A_1 and A_3, and a suitable form for A_2 can be easily obtained by direct comparisons to micromechanical modeling results. The expression

$$A_2 = \left(9.8f - 30f^2 + 95f^3\right)\left(\frac{f_0}{f}\right)^{0.05} \tag{4.41}$$

provides a good fit under this mode of deformation and under the range of initial void volume fractions of interest (Fig. 4-3f). The functions A_1 and A_3 influence the plastic flow of the material under macroscopic deviatoric and mixed [deviatoric + hydrostatic] states of driving stress. It is noted that in the presence of an evolving back-stress in the porous material, it is difficult to use micromechanical models and impose a constant triaxiality of macroscopic *driving* stress, $X^* = T_m^*/T_{eq}^*$, as the back-stress is, in general, not co-axial with the total Cauchy stress acting on the material. It is therefore difficult to carry out a systematic parametric study over a range of driving stress triaxialities. Functional forms for A_1 and A_3 were therefore sought that, given the assumed elastic and orientation-hardening behavior of the porous material, provide good total-stress/total-strain predictions against corresponding micromechanical modeling results. Studied load cases were simple shear deformation, uniaxial tension, plane strain tension and hydrostatic deformation. Given the results from Chapter 3, and the already established form for A_2, the following choices for A_1 and A_3 give good fits to the macroscopic stress-strain curves of Chapter 3:

$$A_1 = \left(\left(1 + 6f^{1.1}\right)\left(\frac{f_0}{f}\right)^{g_1}\right)^{(1/m+1)/2} - \left(1 - \left(\frac{f_0}{f}\right)^{g_2\,(1/m+1)/2}\right), \tag{4.42}$$

with $m = 0.033$, and

$$g_1 = -0.2 + 11.5f_0 - 30f_0^2 \tag{4.43}$$

$$g_2 = 0.5 + 4f_0. \tag{4.44}$$

$$A_3 = \left(1 + 6f^{1.1}\right)\left(\frac{f_0}{f}\right)^{g_1+g_2} . \tag{4.45}$$

The functional forms for A_1, A_2 and A_3 give rise to the stress-strain predictions shown in Fig. (4-3). The cases of simple shear deformation, uniaxial tension, plane strain tension and hydrostatic deformation are shown. The cases of uniaxial tension and plane strain tension are the most relevant load cases from an engineering standpoint; it is unlikely that material points in a component will experience either simple shear deformation or pure hydrostatic deformation. Figures (4-3a-d) show the cases of uniaxial tension and plane strain tension. The constitutive model predictions of axial stress are in excellent agreement with the micromechanical model predictions, over the studied levels of initial porosity (Fig. 4-3a,c). In the case of plane strain tension (Fig. 4-3c), the predicted constraint stress, arising from the imposed plane strain constraint, is also in good agreement with the micromechanical model results. The evolution of volumetric strain (Fig. 4-3b,d) is well-predicted in both cases.

Under simple shear deformation (Fig. 4-3e), the constitutive model predictions are in reasonable agreement with the micromechanical model predictions: The initial elastic response and initial "yield" are well-predicted, but the constitutive model does not accurately predict the post-yield response of the porous glassy polymer. The micromechanical models respond to macroscopic simple shear deformation by forming a macroscopic shear band. This mode of highly localized deformation causes the macroscopic shear stress to decrease rapidly before the deformation stabilizes, and the shear band begins to propagate through the porous material. The highly localized deformation produces a large distribution in [evolved] shear strength in the polycarbonate matrix. As discussed previously, this is not captured in the constitutive model; the shear strength is represented using a single, scalar value (See Section 4.5.2 for a discussion).

The case of macroscopic hydrostatic deformation is shown in Fig. (4-3f). The macroscopic hydrostatic tensile stress is well-predicted for the two highest levels of initial porosity ($f_0 = \{0.10\,,\,0.15\}$). The prediction for the lowest initial porosity ($f_0 = 0.05$) differs markedly from the micromechanical modeling results: the ini-

tial "yield" stress is over-predicted, and the predicted strain-hardening is too strong. An explanation for the former is, again, the [insufficient] modeling simplification of the distribution of evolved matrix shear strength into a single, scalar value (see Section 4.5.2 for a discussion). At higher levels of macroscopic dilatation, the constitutive model with $f_0 = 0.05$ over-predicts the macroscopic hydrostatic tensile stress. Under pure dilatation, the back-stress in the constitutive model is given by the expansion of a hollow sphere. For low levels of initial porosity, the inner surface of the hollow sphere reaches its limiting extensibility early during macroscopic deformation, which produces the strong upturn in stress. In the micromechanical models, the macroscopic hydrostatic deformation can, in addition to purely spherical void growth, be accommodated by inter-void ligament bending and rotation.

4.6.2 Comments on the choices of A_i

The choice of the functions A_i in the preceding discussion was found to give good predictions for the macroscopic stress-strain and volumetric strain response under different macroscopic loading conditions. It is important to realize, however, that the functions $A_i = \hat{A}(f, f_0)$ are matrix-specific. Their functional dependence of f_0 and f is likely to be different if the orientation-hardening properties C_R and $\sqrt{N}$ of the matrix change. Even for a given matrix material, the particular choice of functions is not unique. Moreover, it is important to emphasize that the chosen functions A_i were only calibrated over a narrow range of void volume fractions ($5-15\%$), and that the study of materials of higher (or lower) void volume fractions is likely to require additional numerical fitting.

4.7 Conclusions

A continuum-level constitutive model has been developed to describe the large-strain elasto-viscoplastic deformation of rubber-toughened [here porous] glassy polymers.

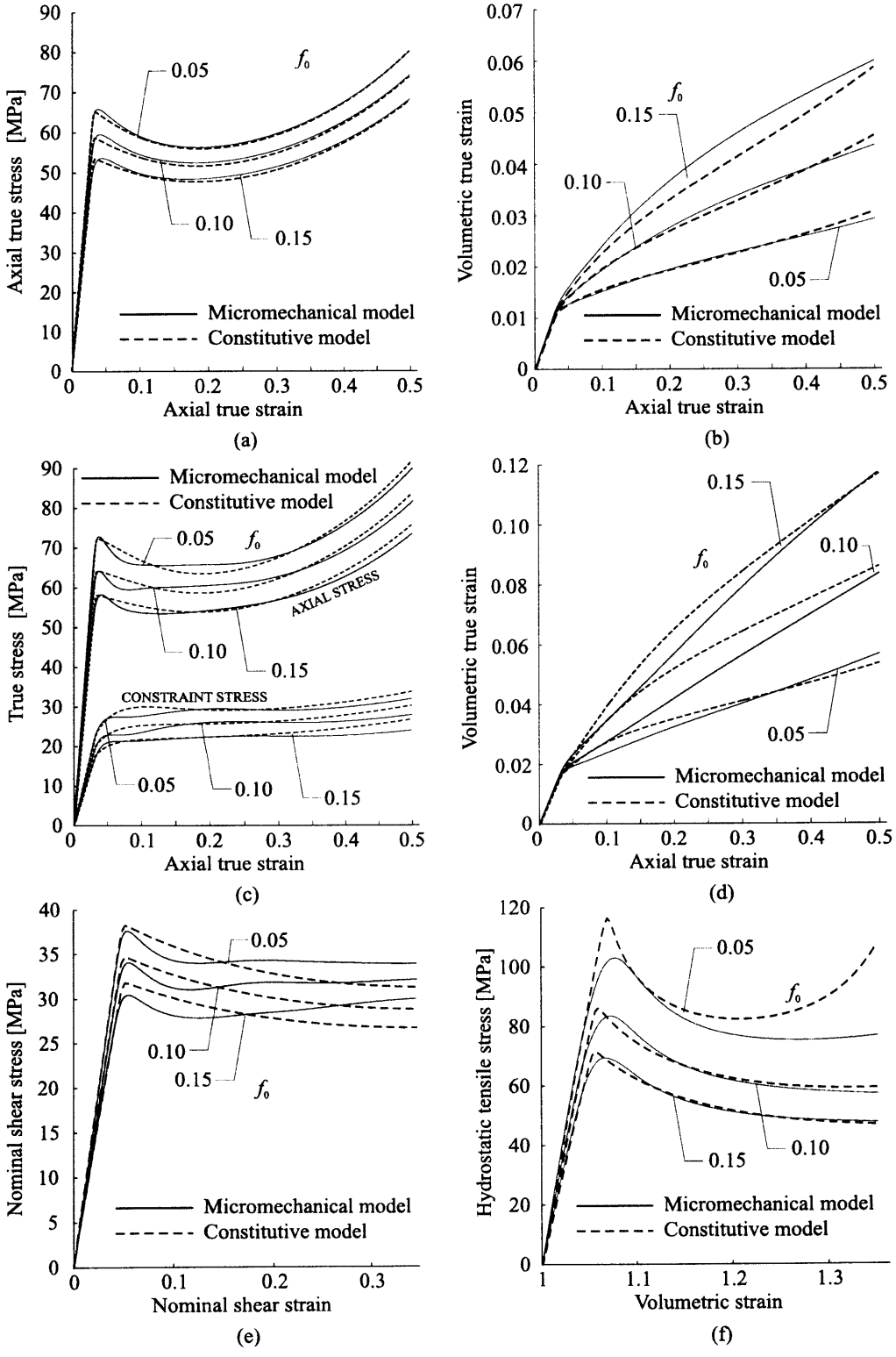

Figure 4-3: Constitutive model predictions using the fits on A_i: (a-b) uniaxial tension, (c-d) plane strain tension, (e) simple shear deformation, and (f) hydrostatic deformation.

The model was used in conjunction with a glassy polycarbonate matrix at ambient temperature, where the [porosity and matrix-dependent] functions A_i in the model were calibrated against micromechanical modeling results from Chapter 3. Using these functions, the constitutive model predicted well the macroscopic stress-strain and volumetric strain response across a range of load cases and initial void volume fractions.

The developed constitutive model is an essential tool for analyzing boundary value problems involving porous, or rubber-toughened [pre-cavitated] glassy polymers. In the following chapter, the constitutive model will be utilized in a finite element framework to study the tensile behavior of round notched bars of different notch radii, as a function of deformation rate, porosity, etc. By comparing the obtained results to existing experimental data on the tensile behavior of such tensile bars (Johnson [38]), it is possible to identify the critical local deformation / stress histories which give rise to brittle fracture, and which do not.

Chapter 5

Fracture Processes in Rubber-Toughened Polycarbonate

In the previous chapter, a continuum-level constitutive model for rubber-toughened glassy polymers was developed. The model treats the rubber particles as voids, in view of their deformation-induced cavitation, which occurs at early stages of deformation. The constitutive model was calibrated against micromechanical simulations of the deformation of porous glassy polycarbonate at room temperature. Predictions by the constitutive model were found to be in good overall agreement with the micromechanical modeling results of Chapter 3 over a range of porosity levels, and loading cases ranging from simple shear to hydrostatic deformation. As discussed in Chapter 2, the purpose of blending rubber particles into glassy polymers is to attain an improvement of the ductility of the material under severe loading situations, by preventing or delaying the brittle fracture processes that are observed in the homopolymer. The developed constitutive model for porous glassy polymers does not include fracture criteria; ductility is implicit in the model formulation, and [brittle or ductile] fracture events cannot be predicted using the model alone. In order to predict occurrences of fracture in the porous material, suitable fracture criteria must be incorporated into the constitutive model.

Failure events in glassy polymers can be interpreted within the framework of thermally activated processes (Zhurkov [80]). Zhurkov and Korsukov [81] introduced

a kinetic theory for stress-assisted damage evolution in polymers, where the time to failure, t, is expressed in terms of three kinetic parameters, t_0, U_0, γ, reflecting fundamental material properties:

$$t = t_0 \exp\left(\frac{U_0 - \gamma\sigma}{k\Theta}\right). \tag{5.1}$$

Here, t_0 coincides with the reciprocal of the natural oscillation frequency of atoms in solids; the magnitude of the energy barrier, U_0, determines the probability of bond breakage and was found to be closely related to the energy of chemical bonds along the backbone; the stress-assisted nature of the fracture process is reflected in the $\gamma\sigma$ term, where σ is a measure of the applied stress, and the activation volume, γ, is found to be strongly influenced by the molecular orientation of the polymer chains (see, for example, Kausch [39]). The parameter γ is taken to account for the effects of bond overstress, based on the supposition of a non-uniform distribution of stresses over the chain bond orientations (Zhurkov [80]). The activation volume γ is found to decrease sharply with molecular network orientation (Kausch [39], Rosen [60]), which implies that highly drawn polymer domains can sustain large tensile stresses before failure. In more pragmatic approaches to establishing fracture criteria for amorphous polymers, this kinetic treatment is often simplified. The time-dependent nature of the failure process is neglected, and the effects of a continuum spectrum of molecular orientation on the failure stress is often reduced to consider only two extreme cases:

- A *brittle* failure mode associated with cavitation events in the unoriented, hydrostatically loaded material.

- A *ductile* failure mode due to chain scission and disentanglement events in the highly aligned, plastically deformed material.

While macroscopic fracture is ultimately governed by extrinsic factors (defects, notches, etc.) that give rise to local stress concentrations, the failure process must be understood in terms of the flaw-free response of the polymer (Argon and Cohen [5]). In homogeneous polycarbonate, *brittle* failure modes are controlled by intrinsic cavita-

tion phenomena. Although the complex interactions controlling fracture initiation in polycarbonate have not yet been entirely resolved, there is a general consensus in the literature that brittle fracture in glassy polycarbonate occurs when the local elastic volumetric strain reaches a critical value prior to the onset of plastic shearing. In this regime, the polymer network is in its isotropic (unoriented) state, and a volumetric strain criterion can be equivalently expressed in terms of a critical negative pressure for intrinsic cavitation.

Under deformation histories dominated by deviatoric stress states, high levels of plastic deformation can develop in the material prior to the onset of *ductile* failure processes. The alignment of molecular chains in the polymer results in a significant increase of the material strength along the extension direction [a reflection of the decreased activation volume γ]. However, strain-hardening also increases the plastic deformation resistance, resulting in ductile fracture at a critical level of plastic stretching, due to chain scission and disentanglement events. These two extreme cases of failure mechanisms in homogeneous polycarbonate can be expressed as the following two fracture criteria (see, for example, Gearing and Anand [28]):

- Brittle fracture is taken to occur when a local elastic volumetric strain, E^e_{vol}, reaches a failure value E^e_f, in the *absence of molecular orientation*:

$$E^e_{vol} = E^e_f. \tag{5.2}$$

- Ductile fracture is taken to occur when the effective plastic stretch, λ^p, reaches a critical value λ^p_f:

$$\lambda^p = \lambda^p_f. \tag{5.3}$$

It is not obvious how [ductile or brittle] fracture criteria, based on critical levels of field quantities defined for the homogeneous polycarbonate should be extended to predict fracture in a rubber-toughened polymer blend. Although the underlying reasons for fracture in rubber-toughened polycarbonate are likely to be found in the

polycarbonate matrix, fracture criteria based on stress and/or strain levels in the homopolymer cannot be directly applied to the homogenized fields of the blend. Homogenized [continuum-level] fields can provide an indication of the severity of the loading conditions, but they provide very limited insight into the criticality of *local* fields. The polycarbonate matrix can fail in a ductile manner, subsequent to extensive local plastic shearing, or it can fail due to cavitation events associated with large elastic volumetric strains in unoriented domains. Due to the statistical nature of the particle distribution, and the stress-concentration effect of the particles themselves, there is a significant variation in stress and strain levels throughout the matrix material. The gradients of stress and strain fields in the matrix are likely to produce progressive degradation of the blend through local accumulation of submicrocracks. If the matrix fails locally, the blend might be able to accommodate this local fracture by shedding load to surrounding matrix material without resulting macroscopic failure, thus allowing large macroscopic plastic strains and dissipation before final fracture. The successive degradation of the matrix material will eventually lead to coalescence of voids, as entire inter-void ligaments fracture. As voids coalesce, larger cavities of higher aspect ratio form. These high-aspect ratio cavities are more effective stress concentrators and ultimately lead to macroscopic fracture of the blend.

The progression of local fracture in the polycarbonate matrix can be studied using the micromechanical models (RVEs) developed in Chapter 3. If fracture criteria, such as those described above for homogeneous polycarbonate, are applied to the polycarbonate matrix, the progression of local fracture in the matrix of the RVE can be studied using a finite element removal technique. When either of the two fracture criteria is met at an integration point in the mesh, the corresponding finite element is removed, and the load carried by that element is redistributed to neighboring elements. Finite element removal will eventually lead to fracture of inter-void ligaments and void coalescence. When the local fracture has extended to a significant portion of the matrix, further damage cannot be accommodated by the blend, and macroscopic fracture occurs. This detailed multi-level study of damage progression in the blend is beyond the scope of this work and is proposed for future study.

Here, we simply assess the propensity to macroscopic fracture at a [macroscopic] material point in the homogenized blend, subjected to a prescribed deformation history. We perform RVE micromechanical studies, and monitor, in the polycarbonate matrix, [microscopic] material points experiencing field levels in excess of the critical failure levels for homogeneous polycarbonate (Eqs. 5.2 and 5.3).

It is important to emphasize that, since failure of the polycarbonate matrix is not modeled in the RVE studies, the progressive degradation of the blend leading to macroscopic fracture cannot be captured. In particular, the rapid increase of void volume fraction associated with void coalescence is not modeled. Similarly, the continuum-level constitutive model for porous polycarbonate, which was fitted to micromechanical modeling results, does not account for rapid increases in void volume fraction associated with void coalescence[1].

5.1 Multiscale studies of failure processes

The modeling tools introduced in Chapter 3 and Chapter 4 are ideally suited to investigate the relationship between macroscopic fracture in the blend and failure conditions in the [porous] polycarbonate matrix. Finite element simulations of mechanical tests on rubber-toughened specimens can be performed using the continuum constitutive model for the blend, and local deformation histories in critical regions can be extracted. The micromechanical models developed in Chapter 3 can then be used to study local field quantities in the matrix (Fig. 5-1c). The [continuum-level] deformation history leading to fracture in the blend can be imposed as a macroscopic state of deformation on an RVE, and correlations between fracture of the porous material, and local stress and strain distributions in the matrix can be analyzed (Fig. 5-1d). For example, the hypothesis that critical negative pressure levels in the matrix control the onset of brittle fracture of the porous material can be tested in this fashion.

[1] At the continuum-level, effects of rapid void coalescence have been modeled by Tvergaard and Needleman [71] in the context of porous metal plasticity. Tvergaard and Needleman modified the void volume fraction, f, in the Gurson model by introducing a critical void volume fraction, f_c, associated with the onset of rapid void coalescence, and a failure void fraction, f_f. As $f \rightarrow f_f$, the material loses all stress-carrying capacity. (See Gurson [31] for a review of the constitutive model.)

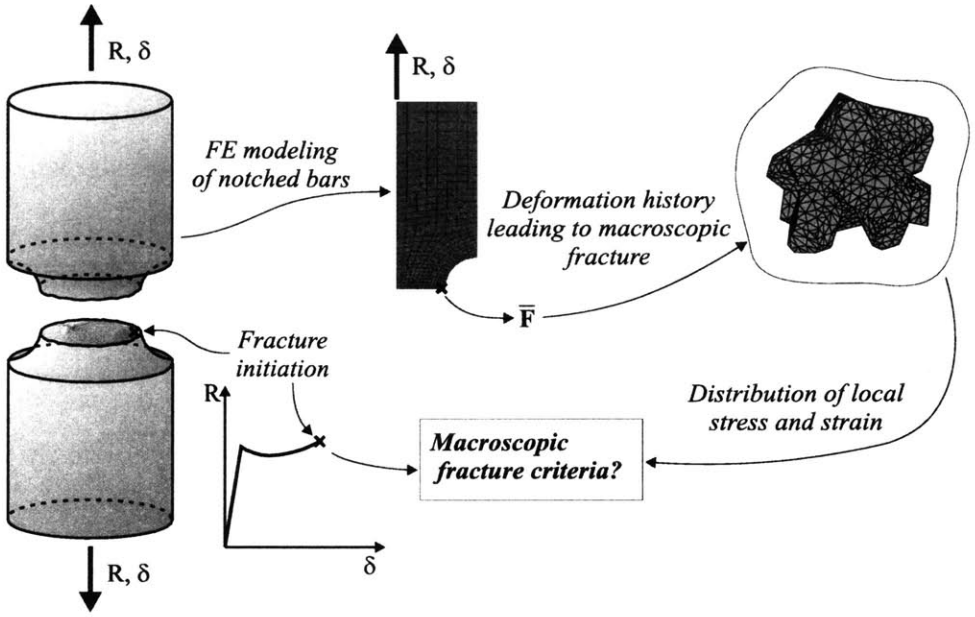

Figure 5-1: Correlation between experiments and simulations: (a) experimentally observed fracture, (b) simulation of notched conditions using the developed constitutive model, (c) simulation of material point behavior by means of an RVE, (d) development of fracture criteria.

Similarly, events leading to macroscopic ductile fracture can be investigated.

In order to establish robust fracture criteria for rubber-toughened polycarbonate based on comparisons between constitutive modeling predictions and results of mechanical tests, an extensive experimental study is required. In such a study, several aspects need to be carefully investigated, both at the microscopic and at the macroscopic levels. For example, at the microscopic level, it is important to characterize the nature of the particle dispersion in the matrix, as well as the particle size distribution, as these are likely to affect local stress and strain quantities. For example, well-dispersed particles have been observed to increase the toughness of the blend, whereas poorly dispersed particles can actually increase the brittleness of the blend (Cheng, et al. [18], Kim, et al. [40]). It is also important to determine the specific modes of local fracture under a given mode of applied deformation; whether the polycarbonate matrix displayed brittle crack propagation, or if the onset of macroscopic

fracture was associated with large levels of plastic stretches leading to localized matrix ligament drawing and subsequent chain scission events. On a macroscopic scale, it is important to obtain results that are repeatable, and statistically representative. Factors such as specimen surface roughness, or the possible existence of flaws in the material need careful evaluation. Mechanical tests can be designed so as to favor either brittle or ductile fracture. As an example, notched tensile bars with different notch radii can be used to favor one fracture mode over the other.

Johnson [38] performed tensile experiments on homogeneous and rubber-toughened polycarbonate using un-notched and [stress triaxiality enhancing] notched bars. The effects of temperature, deformation rate, and stress triaxiality on the material response were investigated. The rubber-toughened polycarbonate used in the study had core-shell rubber particles with a methyl-methacrylate / styrene shell. Johnson measured the size distribution of the particles using scanning electron microscopy, and found that the sizes ranged from 0.3μm to 0.8μm, with an average of 0.52μm. However, the spatial distribution of the rubber particles in the matrix was not measured. Due to the possible existence of internal flaws associated with the injection molding of the specimens, or surface flaws resulting from machining, several experiments need to be performed for each loading case, in order for the results to be statistically representative. Unfortunately, the results from the tensile tests on rubber-toughened polycarbonate were obtained using a very limited number of experiments for each considered case, and some degree of uncertainty is associated with the reported experimental findings. Furthermore, the geometry and loading conditions for the specimens tested by Johnson are conducive to loading histories in the notch region where high levels of triaxial stresses are accompanied by large plastic stretches. Under these conditions, brittle and ductile fracture mechanisms compete, and indeed many of the specimens display fracture surfaces with mixed characteristics.

In this chapter, we use the experimental data collected by Johnson as a basis for comparison to simulations of un-notched and notched tensile bars. Simulations of rubber-toughened polycarbonate tensile bars are performed using the developed constitutive model for porous polycarbonate described in Chapter 4; simulations of

neat polycarbonate tensile bars are performed using the constitutive model for polycarbonate outlined in Chapter 2. It is expected that the simulations will follow the same trends as the experiments; however, in view of the previous discussion, we recognize that the results obtained in the simulations may not yield a close quantitative agreement with the experimental data.

Results of the tensile tests simulations are analyzed to extract local homogenized stress and deformation histories for the blend across the neck of the specimens. Local deformation histories are then imposed as a macroscopic state of deformation on porous RVEs to investigate the local stress and strain distribution in the polycarbonate matrix using the micromechanical modeling tools of Chapter 3. These micromechanical studies allow us to investigate the connections between local field quantities in the matrix, corresponding homogenized stress and strain levels, and the [experimentally-obtained] onset of fracture.

5.2 Macroscopic response

The deformation of homogeneous and rubber-toughened (here porous) polycarbonate is simulated using two-dimensional axisymmetric tensile bars. Three different specimen geometries are modeled, as shown in Fig. (5-2). Figure (5-2a) shows a bar with a homogeneous gage section, and Figs. (5-2b,c) show notched bars with different notch radii reflecting two of the geometries tested by Johnson. The mildest notch (c) has a radius of 1.905 mm, and the most severe notch (b) has a radius of 0.76 mm. The two-dimensional axisymmetric finite element meshes corresponding to the geometries shown in Fig. (5-2), are shown in Fig. (5-3).

Figure (5-4a) shows the experimental force-displacement responses obtained by Johnson for different void volume fractions ($f_0 = \{0, 0.05, 0.10\}$) for the case of the un-notched bar, deformed at 5 mm/min, at room temperature. The experimental results obtained for the neat polycarbonate displays an initial elastic response, followed by a peak in applied force. The applied force drops abruptly after this peak, and a plateau is subsequently reached. The plateau corresponds to stable neck prop-

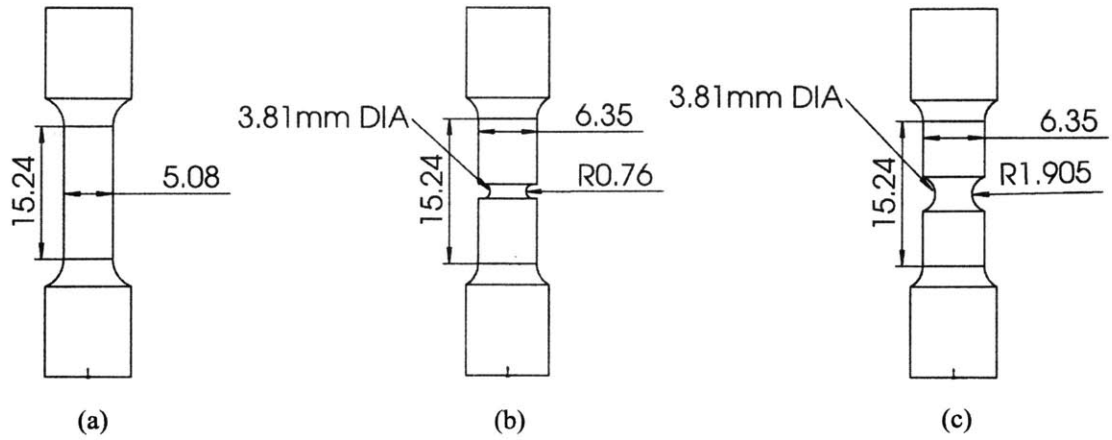

Figure 5-2: Geometries of the axisymmetric tension bars: (a) unnotched bar, (b) $R = 0.76$ mm notched bar, (c) $R = 1.905$ mm notched bar.

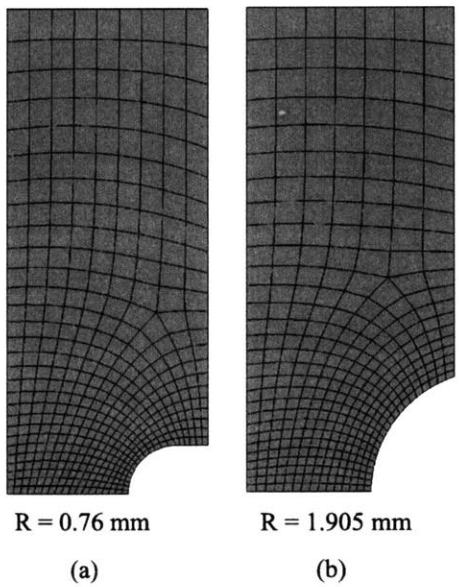

Figure 5-3: The finite element meshes of the notched axisymmetric bars: (a) $R = 0.76$ mm notched bar, and (b) $R = 1.905$ mm notched bar.

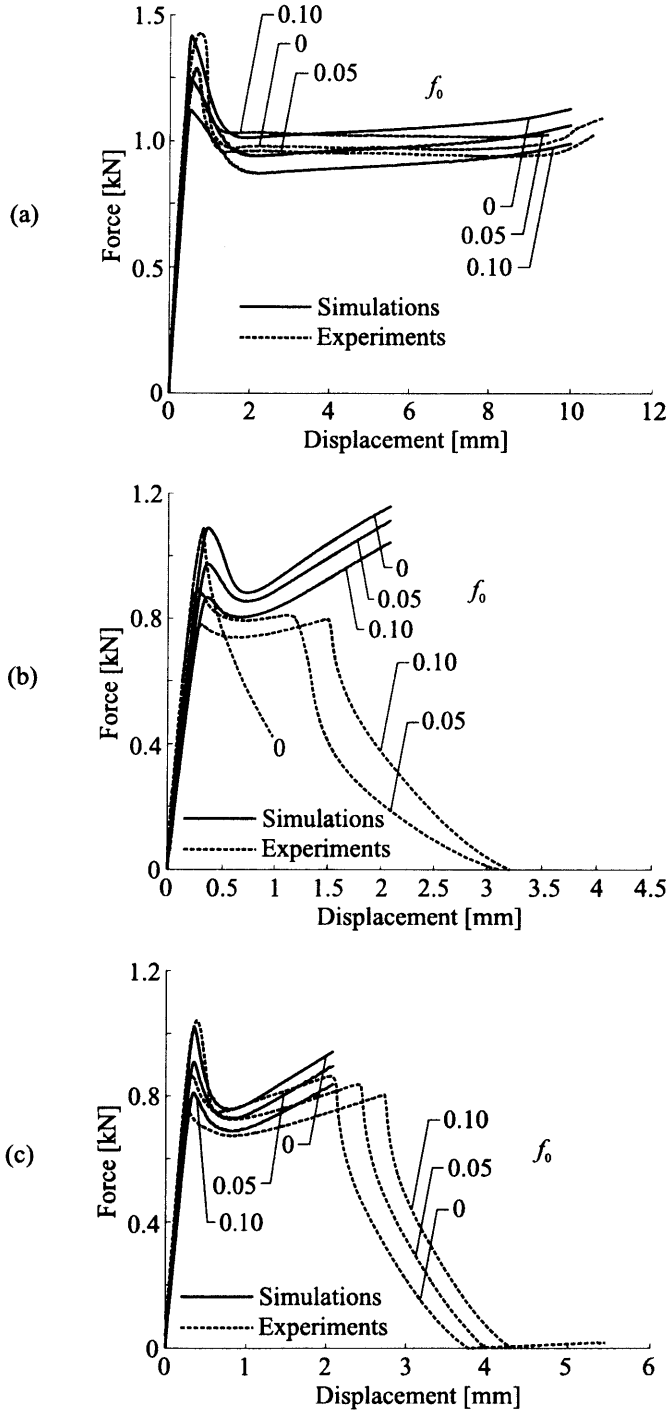

Figure 5-4: Force-displacement curves for different tensile bar geometries: (a) unnotched, (b) $R = 0.76$ mm notched bar; The gray zone indicates an approximate displacement range for fracture of the 10% rubber-toughened specimen, (c) $R = 1.905$ mm notched bar.

agation in the specimen, and it progresses until the grip section of the specimen is reached, after which the force again increases and the specimen eventually breaks. The experimental case of 5% rubber volume fraction displays the same trend as the homogeneous material, with the expected decrease in elastic stiffness, peak force and level of force for stable neck propagation. However, the experimental case for 10% particle volume fraction displays the opposite trend. The exact reason for this unexpected behavior is not clear, but it emphasizes the need for several tests for each case in order to obtain a representative and repeatable experimental behavior.

In Fig. (5-4a), simulated force-displacement responses for the unnotched bar configuration are also shown. Simulations results were obtained using the developed constitutive model for porous polycarbonate to simulate the rubber-toughened polycarbonate at different rubber volume fractions. The simulations are in qualitative agreement with the experimental results: the initial response is elastic, and the applied force experiences a peak with a subsequent drop and stable neck propagation. In order to promote localized necking on the midplane of the simulated specimen, the specimen geometry was tapered slightly, leading to a moderate rise in the predicted level of axial force necessary to stably propagate the neck. The simulation results display a consistent trend for the three cases: with an increasing level of initial porosity, the elastic stiffness decreases, the peak in applied force decreases, and the force level at which the specimen undergoes stable neck propagation decreases.

Figures (5-4b,c) show comparisons between experimental and simulated force-displacement responses for the two notched bar geometries. As pointed out previously, the constitutive model formulation does not include a fracture initiation criterion, and therefore no fracture events occur in the simulations. Figures (5-4b,c) display the same qualitative trends for the simulations and for the experimental data of Johnson: The initial force-displacement response is elastic, and the applied force experiences a peak followed by a "softening" regime. As the deformation progresses, the force gradually increases as the plastic deformation propagates axially from the root of the notch.

The simulations of notched and un-notched tensile bars are overall in good quali-

(a) (b) (c)

Figure 5-5: Fracture surfaces: (a) 0.76mm notched specimen of homogeneous polycarbonate, (b) 1.905mm notched specimen of homogenous polycarbonate, (c) 0.76mm notched specimen of 5% rubber-toughened polycarbonate (Johnson [38]).

tative agreement with experimental observations of Johnson. However, quantitative differences are present; the predicted peak in applied force differs from the experimental results, and the predicted increases in the axial force in notched bars are more pronounced than the experimentally recorded levels. There are several possible reasons for these differences. First, it is important to recognize that the glassy polycarbonate material parameters, to which the homogeneous and porous glassy polymer models of Chapters 2 and 4 were fitted, differ from those obtained by Johnson from uniaxial compression experiments. For example, the polycarbonate used by Johnson [38] displayed a higher plastic locking stretch ($\sqrt{N} = 1.52$, compared to the present $\sqrt{N} = 1.47$). This difference in material parameters can be a contributing factor leading to the variation in "hardening rate" at high levels of deformation. Second, it is important to realize that the data of Johnson was obtained using a very limited number of specimens for each load case. Statistical variations due to flaws in the interior of the specimen, or on the specimen surface cannot be quantified from such a small set of data. Nevertheless, we will use the obtained results from the simulations to attempt to develop a *qualitative* understanding of the local conditions corresponding to the onset of fracture in the blend.

5.3 Microscopic response

As discussed previously, brittle fracture in the homogeneous polymer is associated with reaching a critical elastic volumetric strain[2]. The homopolymer tensile bar with the sharpest notch ($R = 0.76$ mm) fails in a brittle manner while the macroscopic response is still in the "elastic" regime, and the critical elastic volumetric strain for brittle fracture can therefore equivalently be expressed in terms of a critical negative pressure. Simulation results for this notch geometry are thus used to investigate brittle fracture mechanisms by studying the local variation and evolution of negative pressure in the material with axial deformation. As seen in Fig. (5-4b), Johnson's experimental data *for the homopolymer* show that the specimen experienced brittle fracture at an axial deformation of 0.3 mm, which is immediately prior to the peak in applied force as predicted by the numerical simulation. The fracture surface corresponding to this event is shown in Fig. (5-5a). Brittle fracture appears to have initiated internally, at a short distance from the notch outer surface on the midplane of the specimen. If we want to explore the hypothesis that brittle fracture initiated at a point where a critical negative pressure was reached, it is relevant to follow the evolution of negative pressure levels in the specimen, along the specimen midplane at the root of the notch, where fracture is observed to initiate. The evolution of negative pressure is obtained at every numerical integration point along the midplane of the simulated specimen, and plotted against macroscopic imposed axial elongation. The resulting set of negative-pressure/displacement curves, together with an indication of peak negative pressure locations in the specimen at various stages of the deformation history, are shown in Fig. (5-6a-c). By constructing the envelope of maximum negative pressure about this set of curves, it is possible to determine the location and magnitude of maximum negative pressure in the specimen, at a given level of macroscopic specimen deformation. Figure (5-6b) shows that the maximum negative pressure corresponding to the level of macroscopic deformation where the real speci-

[2]Note that the plastic flow of the homogeneous polymer is isochoric, and that the elastic volumetric strain is equal to the total volumetric strain.

men failed, is about 70MPa, and that it is located just below the outer surface of the notch. The location is in reasonable agreement with the initial fracture site identifiable on the fractured surface of the specimen. This value for the negative pressure is similar to what was reported by Johnson, who used a similar approach. However, estimates of a critical negative pressure for brittle fracture initiation reported elsewhere for PC tend to be higher. Data in the literature range between 80 to 100 MPa (Lai and van der Giessen [42]; Nimmer and Woods [51]; Socrate and Boyce [63]; Parvin and Williams [55]; Gearing [27]). This difference can be explained in terms of statistical variations in brittle fracture initiation, as this is significantly affected by stress concentrations introduced by impurities and specimen flaws. Notched homopolymer specimens with milder notch radii deform plastically before failure. The mildest notch specimen ($R = 1.905$ mm) experiences ductile fracture at an axial specimen elongation of 2 mm. The fracture surface corresponding to this event is shown in Fig. (5-5b). Johnson describes the fracture surface as exhibiting the same tearing and yielding observed for the ductile failure of the un-notched tensile bar. The failure initiated at the notch surface in the region of highest plastic strain. If we want to explore the hypothesis that ductile fracture initiated at a point where a critical level of local plastic stretch was reached, it is relevant to follow the evolution of plastic stretch levels, expressed in terms of the first invariant of plastic stretch, I_1^p, along the specimen midplane at the root of the notch, where fracture is observed to initiate. The evolution of I_1^p is obtained at every numerical integration point along the midplane of the simulated specimen, and plotted against macroscopic imposed axial elongation. The resulting set of I_1^p-displacement curves are shown in Fig. (5-7). The figure shows that the maximum I_1^p corresponding to the level of macroscopic deformation where the real specimen failed, is $I_1^p \simeq 5.2$ on the notch surface. This corresponds to an effective plastic stretch $\lambda^p = 1.3$ which is 88% of the limiting extensibility of the molecular network, $\sqrt{N} = 1.47$. Gearing [27] reported a similar value (82%) for the fraction of the limiting extensibility leading to ductile fracture in polycarbonate.

We now examine fracture events in the rubber-toughened polymer blends. Due

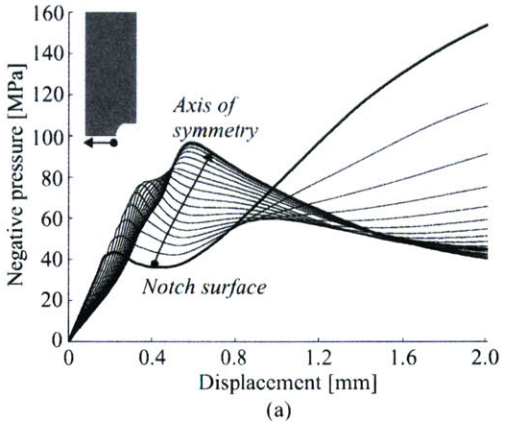

(a)

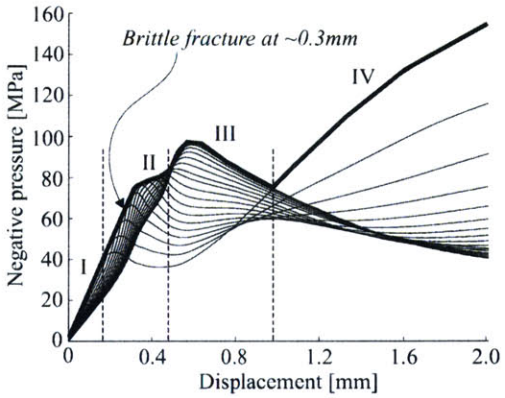

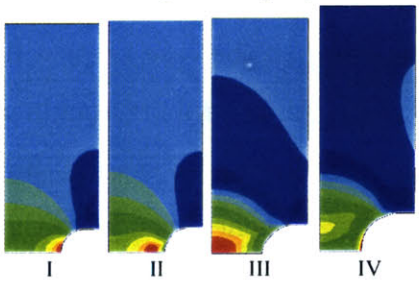

I) Maximum negative pressure on the notch surface.
II) Maximum negative pressure below the notch surface.
III) Maximum negative pressure in the specimen center.
IV) Maximum negative pressure on the notch surface due to molecular alignment.

(b)

Figure 5-6: Negative pressure distribution along a specimen midplane for the case of $f_0 = 0$ and $R = 0.76$ mm: (a) evolution of negative pressure on the specimen midplane as a function of axial specimen deformation, (b) indication of peak negative pressure locations along the specimen midplane as a function of axial specimen deformation.

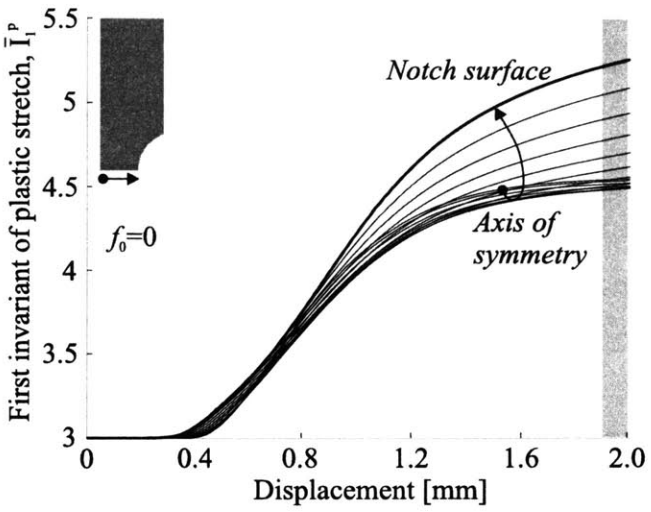

Figure 5-7: Distribution of I_1^p along the specimen midplane ($f_0 = 0$, $R = 1.905$ mm).

to the qualitative nature of the agreement between experimental data and model predictions, we can expect to attain only a qualitative understanding of the connections between microscopic and macroscopic parameters. Here our aim is mainly to demonstrate the use of the developed tools to gain an understanding of the fracture conditions, rather than to obtain quantitative estimates of fracture parameters. In this light, we limit our discussion to the case of $f_0 = 0.05$ and 0.10 for the sharpest notch geometry ($R = 0.76$ mm). All the rubber-toughened specimens tested by Johnson failed in a ductile manner following substantial amounts of macroscopic plastic deformation. In our analysis of toughened blends we therefore focus on ductile failure processes.

The macroscopic plastic deformation in the porous material includes a volumetric contribution from plastic void growth; we therefore monitor its evolution in terms of the two macroscopic invariants of macroscopic plastic stretch, $\overline{I}_1^p$ and $\overline{J}^p$. The sharpest-notched specimens experienced ductile fracture at axial elongations of 1.2 mm (for the 5% particle volume fraction) and 1.5 mm (for the 10% particle volume fraction). The fracture surface corresponding to the case of 5% particle volume fraction is shown in Fig. (5-5c). Again, ductile fracture initiated at the surface of the notch in the region of highest plastic strain. Similar to the approach followed

for the study of failure in the homopolymer, we follow the evolution of macroscopic plastic stretch, expressed in terms of $\overline{I}_1^p$ and $\overline{J}^p$, along the specimen midplane at the root of the notch, where fracture is observed to initiate. The resulting set of $\overline{I}_1^p$-displacement, and $\overline{J}^p$-displacement curves are shown in Fig. (5-8a-d) for the two volume fractions. Similar to the parallel findings for the [milder] notched homopolymer bar, Figure (5-8a,c) shows that the maximum $\overline{I}_p$ corresponding to the level of macroscopic deformation where the real specimen failed, are to be found on the notch surface. Coincidentally, the critical levels of $\overline{I}_1^p$ are found to be similar to the corresponding critical I_1^p levels in the homopolymer: $\overline{I}_1^p \simeq 5.2$ for both volume fractions. Conversely, $\overline{J}^p$ displays maximum values at the center of the specimens.

When the porous polymer is subjected to a specific loading or deformation history, there is a distribution of stress and strain in the matrix as the voids act as stress and strain concentrators. At the surface of the notch, where the real specimen failed, the porous material has undergone a specific deformation history, given by the deformation gradient $\mathbf{F}(t)$. This deformation history is extracted from the simulation and imposed as a macroscopic deformation history, $\overline{\mathbf{F}}(t)$, on five different five-void multi-void Voronoi RVEs (Fig. 5-9).

As discussed previously, the underlying reasons for fracture in rubber-toughened polycarbonate are likely to be found in the polycarbonate matrix itself. The multi-void Voronoi model ($f_0 = 0.10$), when subjected to the deformation history $\overline{\mathbf{F}}(t)$, provides a connection between the macroscopic plastic deformation and local field quantities in the matrix. Figure (5-10) shows, at various stages of the specimen elongation, contour plots of negative pressure and effective plastic stretch in the matrix. The figure shows that much prior to macroscopic ductile fracture of the blend, regions around the voids experience negative pressures in excess of 100 MPa. However, the matrix material in these regions has undergone substantial plastic shearing, and a brittle fracture criterion based on Eq. (5.2) is no longer valid. The high effective plastic stretch levels in the regions around the voids (Fig. 5-10) seem to support the notion of a successive [macroscopically non-critical] degradation of the blend through local fracture events. It is possible that the voids prevent formed micro-cracks from

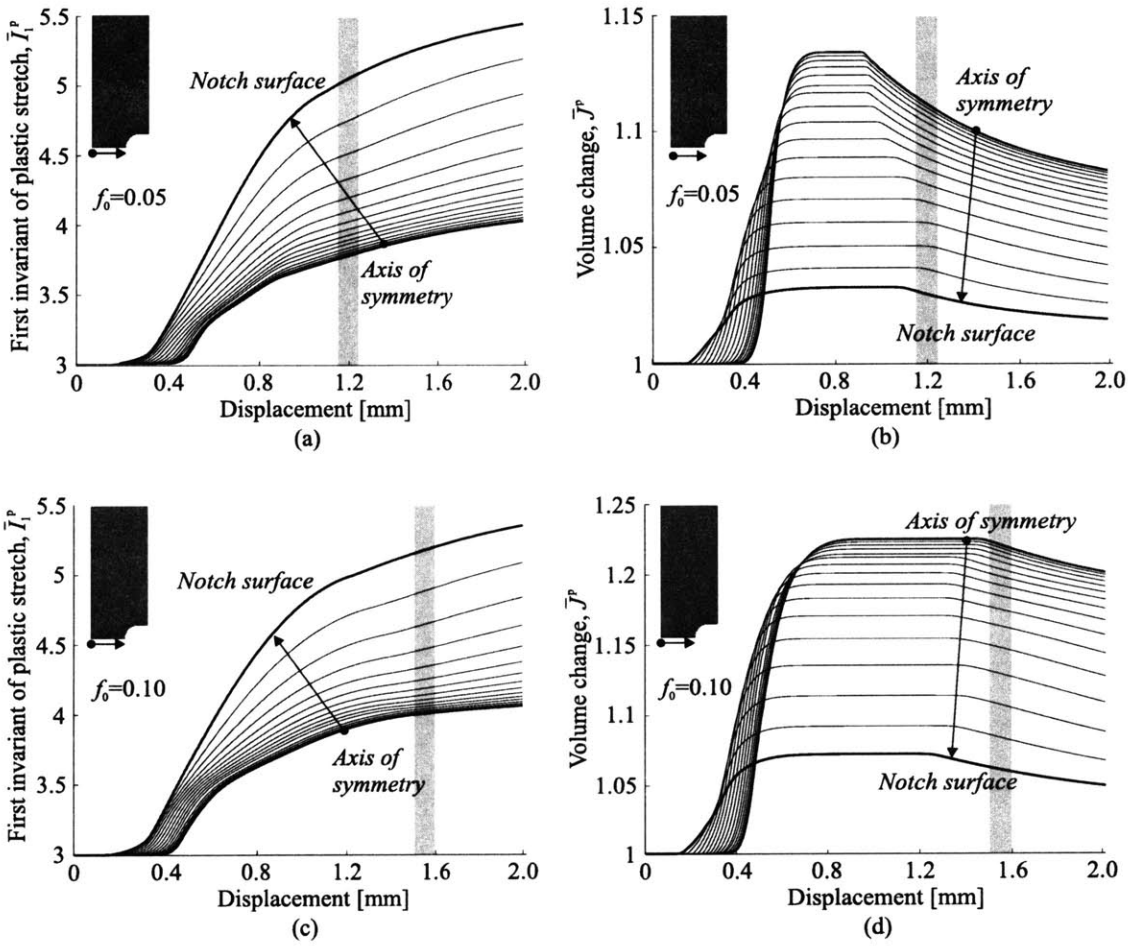

Figure 5-8: Macroscopic stretch invariant distribution along the specimen midplane ($f_0 = 0$): (a) $\overline{I}_1^p$-curves for $f_0 = 0.05$, (b) $\overline{J}^p$-curves for $f_0 = 0.05$, (c) $\overline{I}_1^p$-curves for $f_0 = 0.10$, (d) $\overline{J}^p$-curves for $f_0 = 0.10$. The gray zones indicate axial specimen deformation at observed fracture.

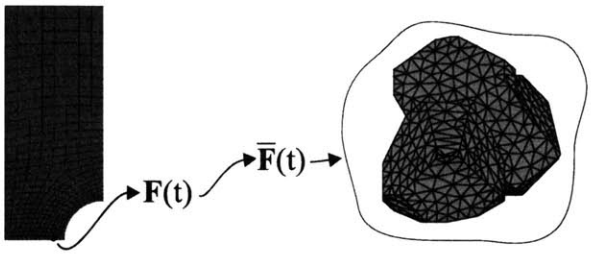

Figure 5-9: Extraction of the deformation gradient at a point in the specimen, and the subsequent application of the deformation to the multi-void Voronoi model.

propagating through the material, thereby keeping the fracture events local. At high levels of specimen deformation, a successive degradation of the material would be reflected in the macroscopic force-displacement response; for example, it would explain the lower "hardening" rate seen in experiments compared to simulations. The possibility of local fracture events has implications on the micromechanical modeling tools developed in Chapter 3, and on the constitutive modeling of Chapter 4. In the micromechanical models, local fracture criteria can be included by using finite element removal techniques. In the constitutive model for porous glassy polymers, the evolution of void volume fraction should allow for a nucleation term, corresponding to the formation and growth of cavities in the matrix.

5.4 Quality of the constitutive model calibration

The constitutive model for porous glassy polymers, developed in Chapter 4, was calibrated against micromechanical modeling results from Chapter 3. Different load cases and porosity levels were used in the calibration process; the load cases were simple shear deformation, uniaxial tension, plane strain tension and hydrostatic deformation, and three [industrially relevant] porosity levels, $f_0 = \{0.05, 0.10, 0.15\}$, were used for each of the load cases. A limitation of a calibration process involving the fundamental load cases above is that in a numerical boundary value problem associated with, for example, the design of a consumer product, certain material points will inevitably experience a more complicated load or deformation history; a material

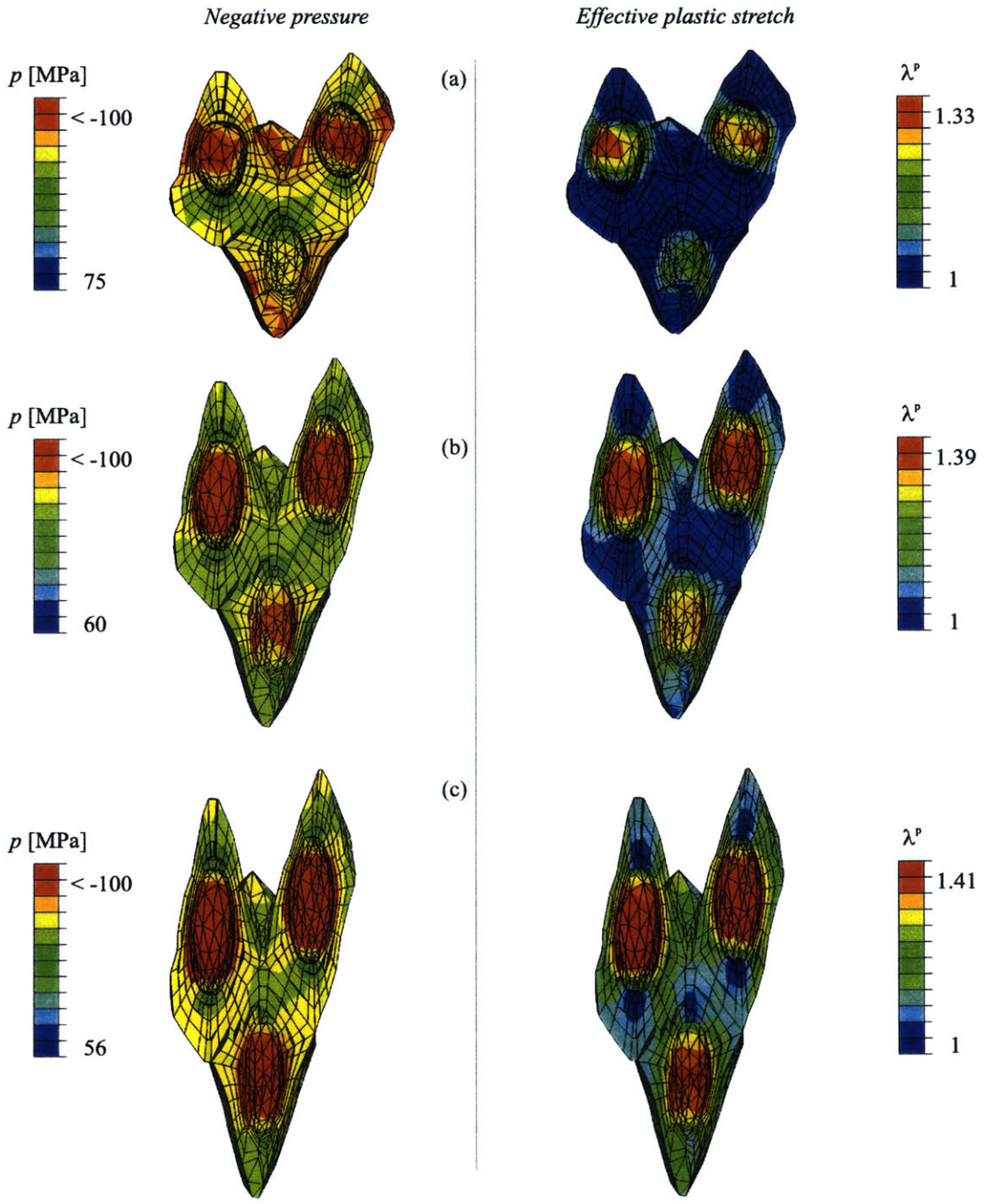

Figure 5-10: Contours of pressure and effective plastic stretch in the polycarbonate matrix at various stages of the specimen deformation: (a) 0.4 mm, (b) 1.3 mm, (c) 1.5 mm.

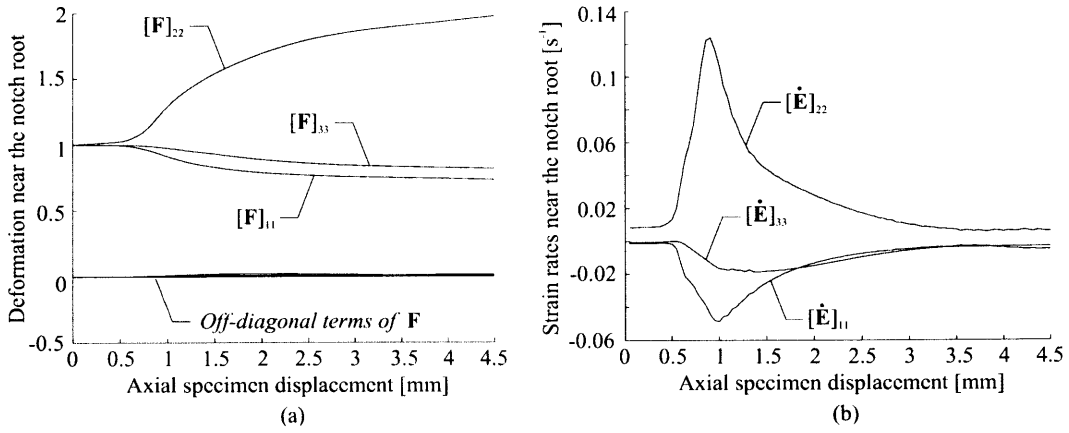

Figure 5-11: Deformation history of the monitored material point: (a) Components of the deformation gradient, (b) true normal strain rates.

point may experience larger strain levels than those of the fundamental load cases, and the rate at which a material point deforms may vary markedly throughout the deformation history. To illustrate this, we consider the simulated case of an axisymmetric notched bar ($R = 0.76$ mm) using the developed and calibrated constitutive model for the case of an initial porosity of $f_0 = 0.1$. The deformation history of a material point near the surface of the notch is monitored, and the components of the deformation gradient, expressed in Cartesian coordinates, are shown in Fig. (5-11a). The radial direction corresponds to the 1-direction, the axial direction corresponds to the 2-direction, and the out-of-plane direction corresponds to the 3-direction. Figure (5-11a) shows that the deformation state near the root of the notch corresponds to a deformation gradient with the off-diagonal terms close to zero. The diagonal terms show that the material point is highly stretched in the 2-direction, whereas it experiences compressive deformation in the two other directions. Figure (5-11b) shows the three true normal strain rates, $\dot{E}_{11}$, $\dot{E}_{22}$ and $\dot{E}_{33}$. The figure shows that the material point deforms most rapidly in the 2-direction (axial direction), with the strain rate shifting markedly throughout the deformation history.

As the constitutive model was calibrated against deformation histories noticeably different from that of the material point near the root of the notch in the specimen, it is unclear whether the predictions of material response in this region are indeed re-

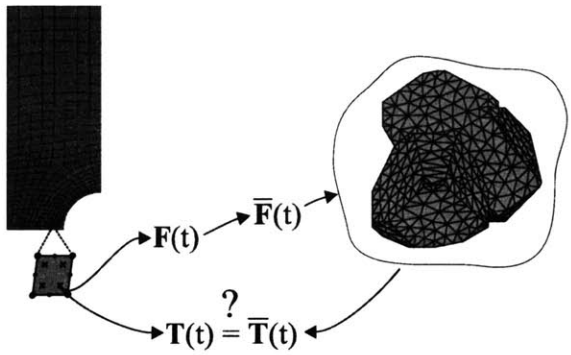

Figure 5-12: Self-consistency scheme to ascertain the quality of the consitutive model calibration.

liable. In this section, we employ a self-consistency scheme to ascertain the quality of the calibration of the constitutive model. A description of the scheme (Fig. 5-12) is as follows: The deformation history $\mathbf{F}(t)$ of the monitored material point is imposed as a macroscopic deformation gradient, $\overline{\mathbf{F}}(t)$, on ten five-void RVEs. The average stress history, $\overline{\mathbf{T}}(t)$, of the ten simulations is calculated. This stress history is then compared to the stress history, $\mathbf{T}(t)$, of the monitored material point in the specimen, as predicted by the previously-calibrated constitutive model. A close agreement between the two stress histories would indicate that the constitutive model was properly calibrated to characterize the stress and strain state near the root of the notch, whereas poor agreement would indicate the opposite. Figure (5-13a) shows the three normal stresses, as predicted by the constitutive model, and the three corresponding normal stresses obtained as ten-simulation RVE averages. The figure shows that the stresses are in reasonable agreement for the two cases; each stress component experiences an initial elastic response, followed by "yield" and [large-strain] plastic deformation. The present differences between the constitutive model predictions and the ten-simulation RVE averages can be explained by examining the specific nature of the predicted and simulated states of stress ahead of the notch. Figure (5-13b) shows the stress triaxiality, X, defined as the ratio between hydrostatic stress and Mises stress, corresponding to the respective stress histories. The two stress triaxiality curves are in general agreement; the RVE simulations predict a slightly higher peak stress triaxi-

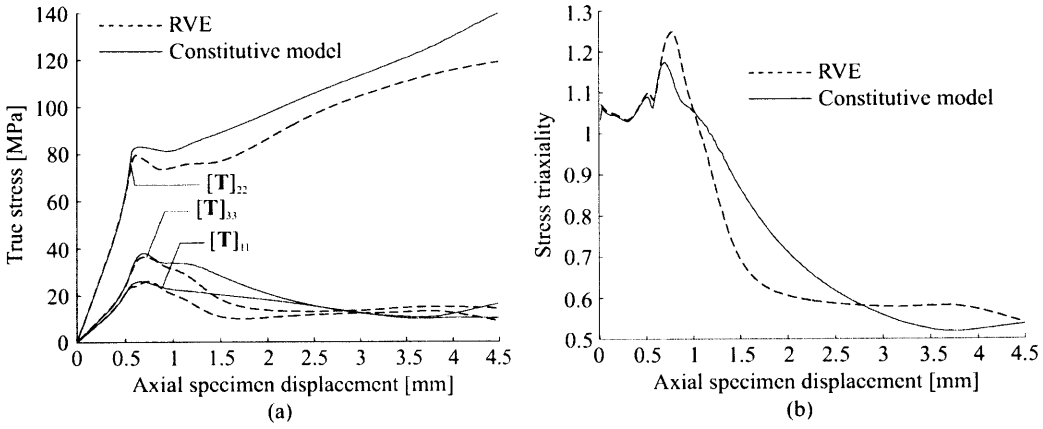

Figure 5-13: Stress history of the monitored material point: (a) Components of Cauchy stress, (b) stress triaxiality.

ality ($X \simeq 1.26$) than the constitutive model ($X \simeq 1.18$). As discussed previously, four load cases were used to calibrate the constitutive model. With the exception of hydrostatic deformation[3], the most triaxial load case used in the calibration process was plane strain tension (Fig. 4-3c-d). For the present case of $f_0 = 0.1$, the highest stress triaxiality for this case is $X \simeq 0.55$. This level of stress triaxiality is considerably lower than the highest level predicted by the RVE simulations ($X \simeq 1.26$). The differences in stress triaxiality suggest that, in addition to the four load cases used in the calibration process for the constitutive model, higher stress triaxialities should be considered as well. This would require additional micromechanical simulations of the porous material. However, for the present purposes, the current calibration of the constitutive model, as summarized in Section 4.6.1, is deemed sufficient.

5.5 Conclusions

There is insufficient experimental data at this point to explicitly express ductile fracture criteria for the rubber-toughened polycarbonate blends. Our qualitative findings indicate that the onset of ductile fracture in the porous material can be expressed

[3]The case of pure hydrostatic deformation is an extreme case corresponding to an infinite stress triaxiality, and it is not expected to be encountered in real boundary value problems.

in terms of the macroscopic first invariant of plastic stretch, $\overline{I}_1^p$. This invariant of macroscopic plastic stretch is, in turn, a function of local stress and strain fields in the matrix. Micromechanical modeling was used to provide a connection between the macroscopic plastic deformation, and local field quantities. Simulations of the conditions at a notch tip seem to indicate that local fracture events occur even prior to macroscopic ductile fracture of the blend. As discussed previously, the possibility of local fracture events has implications on the micromechanical modeling tools developed in Chapter 3, and on the constitutive modeling of Chapter 4. In the micromechanical models, local fracture criteria can be included by using finite element removal techniques. In the constitutive model for porous glassy polymers, the void volume fraction should allow for a nucleation term, corresponding to the formation and growth of cavities in the matrix.

Chapter 6

Summary and Future Work

As discussed previously, common engineering polymers, such as polystyrene, polycarbonate and poly(methyl methacrylate), display brittleness under certain loading conditions. The ductile-to-brittle transition in these materials depends on the rate of loading, temperature and level of stress triaxiality (see, for example, Johnson [38]). A technique for reducing the proneness for brittle fracture in these materials is to blend a small (5-20%) volume fraction of second-phase rubber particles with the polymer. To date, the effects of the rubber particles on the mechanical response of the arising blend have been qualitatively well understood, but a quantitative understanding of the mechanical response of rubber-toughened polymers has been lacking.

The purpose of this thesis was to develop numerical tools to investigate the mechanical behavior of rubber-toughened glassy polymers, with emphasis on rubber-toughened polycarbonate. To this end, several numerical tools were developed. Three-dimensional micromechanical models of the heterogeneous microstructure were developed to study the effects of rubber particle volume fraction on the underlying elasto-viscoplastic deformation mechanisms in the matrix material, and how these mechanisms influenced the macroscopic [continuum-level] multiaxial stress-strain response of the blend. In these developed models, the rubber particles were modeled as voids, in view of their deformation-induced cavitation early during deformation. A continuum-level constitutive model was developed for the homogenized large-strain elastic-viscoplastic behavior of the material, and it was calibrated against microme-

chanical modeling results for rubber-toughened (porous) polycarbonate. A multi-scale modeling approach was then used to assess proneness of fracture due to local stress and strain levels in the material.

In this chapter, we summarize the work that was accomplished in the preceding chapters in the areas of numerical tool development and multi-scale modeling. Directions for future work in the field of numerical modeling of rubber-toughened glassy polymers are provided in light of the current state of numerical tool development. Applications of the developed numerical tools to other material systems are also discussed.

6.1 Micromechanical modeling

Micromechanical models of a porous microstructure were developed to study the effects of void volume fraction on the mechanical behavior of porous polycarbonate. The developed micromechanical models differ in their respective assumptions concerning spatial void distributions and void shapes. Each micromechanical model (RVE) of the porous microstructure developed in the thesis is space-filling and spatially periodic. As discussed in Chapter 3, when such an RVE is subjected to a macroscopic loading and/or deformation history, periodic boundary conditions must be applied to the RVE. In Chapter 3, periodic boundary conditions were therefore developed for a general, periodic, space-filling RVE. A methodology was developed for extracting the macroscopic stress, corresponding to an arbitrary macroscopically-applied deformation history, based on virtual work considerations. The micromechanical models developed in the thesis can be broadly categorized into single-void and multi-void models.

The 3D V-BCC model is based on the assumption that spherical voids are arranged on a BCC lattice. This assumption enables the reduction of the micromechanical model to a single void (Danielsson, et al. [21]). The 3D V-BCC model displays significant improvements over traditional single-void models; it can be used to study arbitrary three-dimensional deformation histories, and it was shown to realistically

capture the dilatational response of the material at high porosity levels. A limitation of any single-void model, however, is that any deformation event that occurs in the matrix material around the void occurs simultaneously throughout the material by virtue of the assumed periodic void arrangement. In order to capture the successive percolation of deformation mechanisms in the matrix material, three micromechanical multiple-void models were constructed.

The LS and LC models consider multiple spherical or cubic voids, respectively, distributed "randomly" on an underlying cubic lattice. It was found that the LC model is not well suited for the application to porous glassy polymers. The corners associated with the cubic voids introduce artificial stress concentrations, which alter the character of local stress fields and introduce spurious modes of deformation. The LS model overcomes this specific limitation by considering spherical voids. However, both the LS and LC models are based on the assumption that the voids are arranged on a cubic lattice. This spatial constraint for the voids introduces a significant limitation on the number of available inter-void ligament directions and distances. In the porous microstructure, local deformation mechanisms are governed by inter-void shearing events, and the limitations, imposed by the cubic lattice, prevent the model from realistically mimicking a random porous microstructure. This limitation was overcome with the development of a multi-void model which does not rely on the existence of an underlying lattice.

The multi-void Voronoi model considers multiple randomly-distributed [but non-overlapping] spherical voids. Contrary to the LS and LC multi-void models, the void locations are not restricted by an underlying lattice. The only spatial constraint on the void locations is a minimum-separation constraint, employed to facilitate finite element meshing of the regions in between voids. The micromechanical model geometry is obtained through a Voronoi tessellation of the void centers, resulting in a space-filling, periodic RVE (see Chapter 3 for a complete description).

Similar to previous micromechanical models, the multi-void Voronoi model was used to study porous polycarbonate of various void volume fractions, under a range of macroscopic loading conditions, including simple shear, uniaxial tension, plane strain

tension and hydrostatic deformation. The main deformation mechanism in the void-containing polycarbonate matrix was identified as shear banding between voids upon macroscopic loading. The shear bands were, in every load case, observed to initiate on the surfaces of voids, where stress concentrations introduced by the voids were strong. The shear banding was observed to control the onset of macroscopic yield of the blend; as shear bands between voids developed to span the RVE, a macroscopic yield point was reached. Continued macroscopic deformation was enabled through percolation of plastic flow through the polycarbonate matrix. For load cases with a hydrostatic tensile stress component, the blends displayed volumetric plastic straining resulting from plastic volumetric straining of the voids.

In summary, the absence of an underlying lattice controlling the void locations makes the multi-void Voronoi model superior to its lattice-based predecessors. The former models all displayed unrealistic aspects of both microscopic and macroscopic deformation under certain load cases. For example, the underlying cubic lattice in the LS model, and the underlying BCC lattice in the 3D V-BCC model, resulted in unrealistic macroscopic stress predictions under macroscopic simple shear deformation. The random distribution of voids in the multi-void Voronoi model produces a greater variation in local field quantities. Contrary to the previous models, the multi-void Voronoi model is therefore a more reliable tool when studying the effects of macroscopic loading histories on local fields in the matrix. See Chapter 3 for a more extensive discussion on the differences and similarities of the developed micromechanical models.

6.2 Constitutive modeling

Previous constitutive models in the literature for the macroscopic response of porous glassy polymers have been predominantly extensions of the Gurson model [31]. As the Gurson model was developed for the small-strain deformation of dilute concentrations of voids in a rigid-perfectly plastic matrix, its applicability to porous glassy polymers is limited. Several models have been proposed (see Chapter 4 for a review) to account

for some inherent differences between the fundamental assumptions of the Gurson model and the observed features of deformation of porous glassy polymers. However, these studies have been restricted to the region around the "yield" condition of the material, and none of the proposed models is able to capture the large-strain response of the material. In this thesis, a homogenized description of the large-strain elastic-viscoplastic behavior of porous glassy polymers was developed. The constitutive model captures the following major features of deformation:

- Porosity-dependent elastic response.
- Rate and porosity-dependent plastic flow.
- A description of an evolving back-stress arising from molecular orientation of the matrix and the anisotropic growth of voids.

The model was calibrated against micromechanical modeling results using the multi-void Voronoi model, and it was found to be predictive of the large-strain mechanical response of the material under a range of load cases and porosity levels. To our knowledge, it is the first and only *large-strain constitutive model for porous glassy polymers that includes rate-dependence, and a back-stress arising from molecular orientation of the matrix material and the anisotropic growth of voids.* The constitutive model can be used in the finite element design process of consumer products, thereby reducing the costs associated with mechanical testing and evaluation.

6.3 Multi-scale modeling

As discussed above, the constitutive model for porous polycarbonate can be used in the design process of various consumer products. However, it cannot be used to predict final fracture of the blend which occurs under certain unfavorable combinations of loading and loading histories. The constitutive model for porous polycarbonate was therefore used to study tensile loading of notched bars. The results were compared to results from experimental studies in the literature, to establish preliminary correlations between the continuum-level response of the material, and observed fracture

events in the tensile bars. As discussed in Chapter 5, fracture initiates locally in the polycarbonate matrix, and the successive fracture of inter-void ligaments eventually results in macroscopic fracture of the blend. To this date, quantitative criteria for the fracture process in *homogeneous* polycarbonate have only begun to emerge. The fracture process in *porous* polycarbonate is far more complicated, and a multi-scale modeling approach to ascertain the proneness to macroscopic fracture was employed. Using the constitutive model, the calculated history of deformation corresponding to experimentally-observed fracture at a specific point in a notched bar was imposed as a macroscopic deformation history on the multi-void Voronoi model. This multi-scale modeling approach enabled a preliminary study of the evolution of local stress and strain fields in the polycarbonate matrix for a macroscopically-critical deformation history. However, the lack of fracture criteria for the polycarbonate matrix prevented any study of the progression of fracture within the polycarbonate matrix. Given this present limitation, we were only able to make preliminary assessments of the fracture process in porous polycarbonate. However, the multi-scale modeling technique introduced in Chapter 5 seems to be a promising avenue for future work aimed at understanding the connections between local fracture events in the matrix, and macroscopic fracture of the blend.

6.4 Future work

Numerical tools have been developed to investigate the mechanical behavior of rubber-toughened glassy polymers, with emphasis on rubber-toughened polycarbonate. In this section, we provide suggestions and directions for future work on this topic. Suggestions as to the application of the models to other classes of materials are also discussed.

6.4.1 Micromechanical modeling

The multi-void Voronoi model was used to simulate the mechanical response of rubber-toughened polycarbonate, where the rubber particles were modeled as voids.

Under highly deviatoric loading conditions, the modeling assumption that the rubber particles can be treated as voids is adequate, as the shear modulus of the rubber is considerably lower than the elastic moduli of the glassy polycarbonate matrix. Under loading conditions with a hydrostatic tensile component, the particles cavitate, and the model is again adequate. However, under macroscopic compressive loading conditions, the assumption that the rubber particles can be treated as voids breaks down. The multi-void Voronoi model can be modified to become a multi-particle Voronoi model, where rubber particles are present at the center of each Voronoi cell. The model can then be used to investigate the effects of variations in particle properties. Alternatively, a cavitating, shear-compliant particle can be modeled in a finite element code using a fluid pressure cavity instead of a void (Baumann [9]). This modeling approach provides a means of prescribing a pressure-dependent cavitation criterion for the particles without explicitly introducing detailed volumetric finite element meshing of particles in the model. A critical negative pressure for particle cavitation is likely to depend on the particle *size*, as larger particles are likely to contain more flaws than smaller particles. By using fluid pressure cavities to represent the particles, it is thus possible to study the effects of particle *size* on the response of the material. The micromechanical modeling thus far considered randomly dispersed voids of uniform size. In rubber-toughened polycarbonate, there is typically a distribution of particle sizes with variations about the mean; Johnson [38] reports, for polycarbonate toughened with core-shell rubber particles, sizes ranging from $0.3\,\mu$m to $0.8\,\mu$m, with a mean of $0.52\,\mu$m. The multi-void Voronoi model can be easily modified to incorporate a given statistical distribution of void sizes. Similarly, the spatial distribution of the rubber particles can be controlled and altered to reflect the microstructure of the actual material. It has been experimentally observed that the existence of particle clusters in the polycarbonate matrix strongly affects the ductility of the blend (Cheng, et al. [18]). The ability to control the spatial distribution of voids in the multi-void Voronoi model can be exploited in future studies to investigate the effects of particle clustering. From a numerical standpoint, a number of possible improvements to the model can be considered. For example, the separation constraint

between voids in the matrix could be relaxed if the finite element mesh in the inter-void regions were refined to a sufficient level. Currently, the structured finite element discretization in the radial direction of the Voronoi cells does not permit this kind of mesh refinement control. An un-structured finite element discretization scheme of the Voronoi cell interiors using tetrahedral elements could be employed to attain this objective. The multi-void Voronoi model can be also be used to study other classes of particle-modified materials. For example, ceramic matrix composites, metal matrix composites, filled elastomers, and [rubber or hard mineral] particle-toughened semi-crystalline polymers can be studied. In the latter case, [stiff] mineral particles would need to be introduced in a multi-particle Voronoi model at the center of each cell. The current structured finite element topology in the radial direction of the particles provides for a convenient means of modeling crystallites extending radially from the particles. The ductility of particle-toughened semicrystalline materials, using stiff filler particles, hinges on the debonding of the particles from the matrix. Debonding criteria can be developed and imposed on the particle-matrix interface to study these effects on the ductile-to-brittle transition in the material. These classes of problems have been studied in the context of two-dimensional, axisymmetric analyses (see, for example, Parsons, et al. [24]), and in three dimensions by van Dommelen [73] and van Dommelen, et al. [74] using a simplistic multi-particle model of the microstructure. However, to our knowledge, a full three-dimensional micromechanical analysis, using correctly implemented periodic boundary conditions according to Eq. (3.1), has not been performed at present. The developed methodology to generate a space-filling, periodic multi-void Voronoi model, can also be applied to studies in crystal plasticity. The developed finite element meshing algorithms can be modified to fill completely every Voronoi cell, to resemble a homogeneous solid crystal grain. Pole figure measurements can be used to obtain the texture of a polycrystalline material (Anand and Kothari [3]), and this texture can then be approximated using a finite number of grains, where each grain with a given crystal orientation is represented by a Voronoi cell. The concept of Voronoi diagrams to represent a crystalline microstructure is not new. It has been performed in both two-dimensional plane strain analyses (see,

for example, Ghosh, et al. [29]), and in three-dimensional analyses (see, for example, Quilici and Cailletaud [58], Besdo [49], and Nygårds and Gudmundson [53]). However, periodic boundary conditions have either been implemented incorrectly, or in a manner suitable only for small-strain analyses. As discussed previously, the current algorithm triangulates the surfaces of the grains prior to discretizing the grain interiors. The resulting nodal compatibility between periodic points on the surface of the RVE enables the imposition of periodic boundary conditions according to Eq. (3.1). This enables large-strain analyses of polycrystalline aggregates subjected to arbitrary deformation histories.

6.4.2 Constitutive modeling

The developed constitutive model for porous glassy polymers can be improved / extended in a number of ways.

1. The matrix shear stress and shear strength fields were represented by two single, scalar quantities. The effects of the distributed nature of these fields in the actual porous material (as observed in the micromechanical studies) is significant in the case of a softening glassy polymer matrix. The micromechanical models display a succession of plastic deformation events through the matrix, and the attractive but minimalist approach of representing the matrix shear stress and shear strength by two "effective" quantities may therefore warrant additional consideration / modeling.

2. The developed constitutive model for porous glassy polymers was based on an isothermal formulation for the matrix material. This is usually an adequate modeling assumption under loading conditions characterized by low strain rates. However, the micromechanical modeling results of Chapter 3 show that the inter-void ligaments in the porous glassy polymer can experience local strain rates that are an order of magnitude higher than the macroscopic strain rates. It is therefore not clear whether an isothermal formulation for the matrix material is adequate / sufficient, and how possible local heating of the glassy polymer

matrix affects the macroscopic [continuum-level] response of the porous glassy polymer. Boyce et al. [11] extended the glassy polymer model of Boyce et al [12] to account for deformation-induced heating in glassy polymers. A similar extension can be made to the constitutive model for the homogeneous glassy polymer described in Chapter 2, and the effects of local heating of the glassy polymer matrix on the macroscopic response can be studied, and quantified, using the micromechanical models of Chapter 3. The [continuum-level] constitutive model for porous glassy polymers can then be modified to account for these effects.

3. Ductile and brittle fracture criteria should be developed and implemented. This step requires substantial work in the areas of experiments and multi-scale finite element modeling. Fracture criteria can be developed if correlations between experimental results and multi-scale finite element results are found (see below).

6.4.3 Multi-scale modeling

The multi-scale modeling approach, described in Chapter 5, can provide information about local stresses and strains in the polycarbonate matrix, given a macroscopic loading history corresponding to macroscopic fracture. However, the absence of local fracture criteria prevents the study of local progression of fracture in the matrix. The development of macroscopic fracture criteria for porous polycarbonate therefore requires the development of local fracture criteria.

6.4.4 Experiments

In Chapter 5, we considered two possible causes for matrix-initiated failure of the material: a brittle failure mechanism, triggered by critical negative pressure levels in the matrix, and a ductile failure mechanism triggered at high levels of plastic stretch in the matrix. At present, there is not a sufficient experimental basis to firmly establish quantitative failure criteria for the rubber-toughened polycarbonate. An experimental program should be designed to carefully study the effects of temperature, deformation

rate and deformation history and deformation state (stress triaxiality level) on the failure of rubber-toughened polycarbonate. Experiments should be designed so as to enable a separation of possible failure mechanisms by controlling the geometry of the specimens and the loading conditions.

Appendix A

Paper I

Reprinted from J. Mech. Phys. Solids, Vol 50, M. Danielsson, D.M. Parks and M.C. Boyce, "Three-dimensional micromechanical modeling of voided polymeric materials", pp 351-379, 2002, with permission from Elsevier.

THREE-DIMENSIONAL MICROMECHANICAL MODELING OF VOIDED POLYMERIC MATERIALS

M. Danielsson, D.M. Parks and M.C. Boyce*

Department of Mechanical Engineering,
Center for Materials Science and Engineering,
Massachusetts Institute of Technology,
Cambridge, USA,
March 2001.

Abstract

A three-dimensional micromechanical unit cell model for particle-filled materials is presented. The cell model is based on a Voronoi tessellation of particles arranged on a Body-Centered Cubic (BCC) array. The three-dimensionality of the present cell model enables the study of several deformation modes, including uniaxial, plane strain and simple shear deformations, as well as arbitrary principal stress states.

The unit cell model is applied to studies on the micromechanical and macromechanical behavior of rubber-toughened polycarbonate. Different load cases are examined, including plane strain deformation, simple shear deformation and principal stress states. For a constant macroscopic strain rate, the different load cases show that the macroscopic flow strength of the blend decreases with an increase in void volume fraction, as expected. The main mechanism for plastic deformation is broad shear banding across inter-particle ligaments. The distributed nature of plastic straining acts to reduce the amount of macroscopic strain softening in the blend as the initial void volume fraction is increased. In the case of plane strain deformation, the plastic flow is observed to initiate across inter-particle ligaments in the direction of constraint. This particular mode of deformation could not have been captured using a two-dimensional, plane strain idealization of cylindrical voids in a matrix.

*Corresponding author. Tel: +1-617-253-2342; facsimile: +1-617-258-8742; e-mail: mcboyce@mit.edu.

The potential for localized crazing and/or cavitation in the matrix is addressed. It is observed that the introduction of voids acts to relieve hydrostatic stress in the matrix material, compared to the homopolymer. It is also seen that the predicted peak hydrostatic stress in the matrix is higher under plane strain deformation than under triaxial tension (with equal lateral stresses), for the same macroscopic stress triaxiality.

The effect of void volume fraction on the macroscopic uniaxial tension behavior of the different blends is examined using a Considère construction for dilatant materials. The natural draw ratio was predicted to decrease with an increase in void volume fraction.

Keywords: A. voids and inclusions, B. constitutive behavior, B. polymeric materials, B. porous material, C. finite elements.

1 Introduction

Micromechanical modeling has become an increasingly important tool for understanding deformation mechanisms in particle-modified materials. The particle distribution in such materials is typically random. Many micromechanical models have idealized the microstructure as a stacked hexagonal array (SHA) of particles or voids in a matrix (see for example Tvergaard (1982), Koplik and Needleman (1988) and Steenbrink, et al. (1997)). The SHA particle distribution enables the simplification of the composite material to a periodic "unit cell", which is solved numerically as a two-dimensional axisymmetric boundary value problem. The SHA model gives realistic predictions of the macroscopic stress-strain behavior as long as the particle volume fraction is low; that is, when the particles are essentially isolated (Socrate and Boyce (2000)). At large particle volume fractions, when particles can no longer be treated as isolated entities, the periodicity of the SHA model forces matrix deformation to localize through a thin inter-particle ligament at the particle equator, and this yields unrealistic predictions of the micromechanical and macromechanial behavior. A more suitable representation of the particle distribution is obtained if the particles are staggered, rather than stacked. Socrate and Boyce (2000) introduced two axisymmetric cell models which capture three-dimensional staggered distributions of particles; one cell model considers a body-centered tetragonal (BCT) array of particles, and the second is based on a Voronoi tessellation of a body-centered cubic (BCC) array of particles (the axisymmetric V-BCC cell model). These cell models capture features of the three-dimensional microstructure of the composite aggregate, while retaining axisymmetry. The models have been found to provide more realistic predictions of the macroscopic behavior than that predicted by the SHA model on various material systems (Socrate and Boyce (2000), Socrate, et al. (2001), Ishikawa, et al. (2000)). This paper extends the axisymmetric V-BCC model of Socrate and Boyce to introduce a fully three-dimensional Voronoi cell model (the 3D V-BCC model). The new model enables simulation of plane strain and simple shear loading conditions in addition to the uniaxial and the axisymmetric triaxial conditions that have been

captured with the axisymmetric V-BCC model. The ability to simulate the effects of the plane strain constraint on these 3D microstructures is of particular relevance in these material systems since it is under plane strain, notch-like conditions that many homopolymers (that are ductile in uniaxial tension) are found to be brittle. Polycarbonate is an example of such a polymer. The high triaxiality ahead of a notch is observed to initiate crazing and/or cavitation in polycarbonate and that results in brittle behavior under plane strain notch conditions (Nimmer and Woods (1992)). The controlled introduction of elastomeric particles into the polycarbonate matrix has been effective in restoring toughness (Yee (1977)). The particles are thought to promote diffuse plastic flow in the matrix material, with extensive distortional plasticity (shear yielding) being the most prominent mode of deformation. In order to explore the underlying micromechanics of deformation in rubber-filled polycarbonate, the proposed three-dimensional unit cell model is used to study different loading conditions including uniaxial, plane strain and simple shear loading. Implications of the results on toughening mechanisms in filled polymers are then discussed.

2 Description of the 3D V-BCC cell model

In order to understand the underlying mechanisms that govern the toughness of rubber-modified polycarbonate, micromechanical cell models of the composite material are constructed and deformed under various conditions. The particle distribution is typically random in the filled polymers. To fully simulate the actual microstructure, a three-dimensional model of a random distribution of particles is required. However, a model of this size is computationally intensive. The basic features of the structure and its behavior can be approximated by an idealized, staggered array of particles in which the staggered nature of the particle arrangement captures the major effects of particle-particle interactions. In this study, the random particle distribution is idealized by arranging the particles on a body-centered cubic (BCC) lattice. The cell model is then constructed through a three-dimensional Voronoi tessellation procedure, which results in a space-filling arrangement of tetrakaidecahedra (Figure 1).

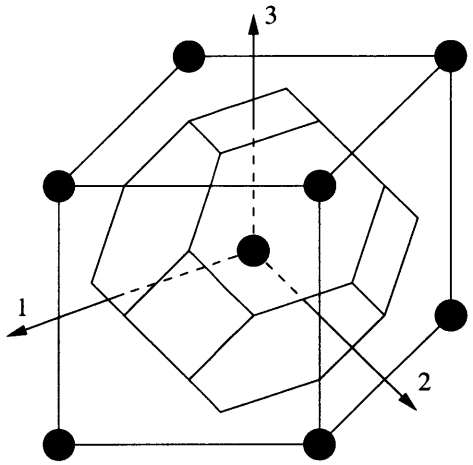

Figure 1: The 3D V-BCC cell.

The tessellation procedure can be carried out in three elementary steps (Dib and Rodin (1993); Socrate and Boyce (2000)). First, the center of a reference cube is connected by lines to its eight corners and to the six nearest corresponding cube centers. Second, each of these lines is bisected by a plane. Third, the 3D V-BCC cell is given as the volume bounded by the planes. This 3D V-BCC cell, also known as the Wigner-Seitz cell (Wigner and Seitz (1933)), is a highly symmetric polyhedron which possesses nine symmetry planes.

2.1 Boundary conditions

General periodic boundary conditions for the 3D V-BCC cell model are developed for three specific loading cases: (1) axial deformation with imposed lateral stress; (2) plane strain deformation with imposed lateral stress; (3) simple shear deformation. The boundary conditions are then expressed in terms of the macroscopic deformation gradient, $\mathbf{F}$. The different load cases in this study allow for the cell model to be reduced, due to reflective symmetries. This reduction of the geometry is necessary because of the substantial computational requirement of the finite element analyses. The Cartesian reference system used in this study is shown in Figure 1; Cartesian base vectors are $\{\mathbf{e}_i\}$. For the cases of plane strain deformation and principal stress states,

1/8 of the 3D V-BCC cell is considered, whereas the case of simple shear deformation requires 1/4 to be considered[1]. The principal direction of uniaxial tension is taken to be the 3-direction, which is a direction perpendicular to a pair of square facets (Figure 1). In the case of simple shear deformation, the principal shearing planes are taken along a pair of square facets of the cell.

2.1.1 General case

The surface of the 3D V-BCC cell consists of eight hexagonal and six square facets. Figure 2 shows a pair of hexagonal facets, where S_J is the facet diagonally opposite facet S_I. The center point of cell I is denoted O_I, and the center point of the adjacent cell, J, is denoted O_J. The (non-displacing) origin is taken to be O_I, and consequently $\mathbf{u}(O_I) = \mathbf{0}$. The two cells I and J have the facet S_J as a common boundary. The periodicity and symmetry of the microstructure force diametrically opposite points with respect to O_I to have equal and opposite displacements. The displacements of the points I_1 and J_3 (Figure 2) are thus related through

$$\mathbf{u}(I_1) = -\mathbf{u}(J_3). \tag{1}$$

The displacements of the points J_3 and I_3, relative to the respective cell centers O_J and O_I, are given by

$$\mathbf{u}(J_3) - \mathbf{u}(O_J) = \mathbf{u}(I_3) - \mathbf{u}(O_I). \tag{2}$$

By combining (1) and (2), we obtain

$$\mathbf{u}(I_1) + \mathbf{u}(I_3) = -\mathbf{u}(O_J). \tag{3}$$

[1]For the case of uniaxial tension and tension with equal lateral stresses, only 1/16 of the 3D V-BCC cell model is needed. However, due to topological difficulties with meshing, 1/8 of the cell model is used instead.

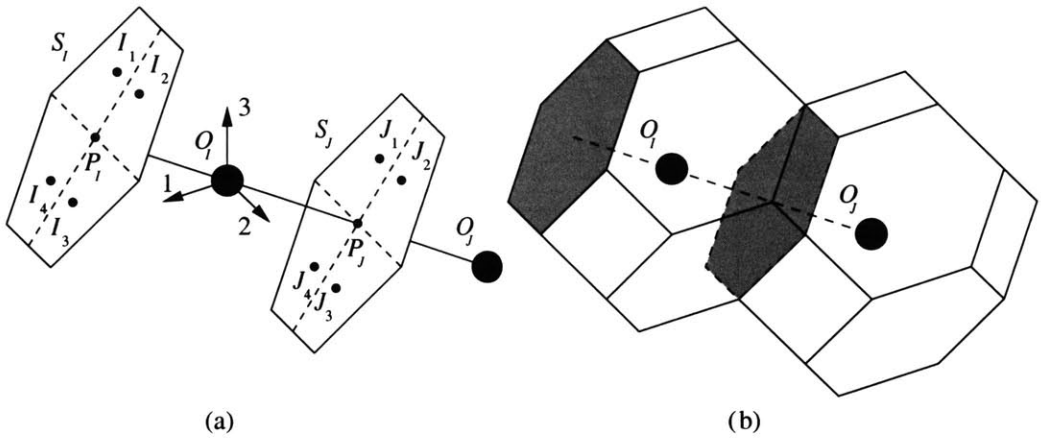

Figure 2: The 3D V-BCC cell: (a) characteristic points on diametrically opposite facets; (b) two adjacent 3D V-BCC cells.

The displacement of the point O_J can be related to the macroscopic deformation gradient through

$$\mathbf{u}(O_J) = (\mathbf{F} - \mathbf{1})\mathbf{p}(O_J), \tag{4}$$

where $\mathbf{F}$ is the macroscopic deformation gradient, $\mathbf{1}$ is the second-order identity tensor, and $\mathbf{p}(O_J)$ is the coordinate of O_J in the reference configuration. The displacement of the centroidal point of the facet, P_J, is given by

$$\mathbf{u}(P_J) = \frac{1}{2}\mathbf{u}(O_J) = -\mathbf{u}(P_I). \tag{5}$$

Hence, the displacements of the points I_1, I_3, and P_I are related through

$$\mathbf{u}(I_1) + \mathbf{u}(I_3) = 2\mathbf{u}(P_I) = 2(\mathbf{F} - \mathbf{1})\mathbf{p}(P_I), \tag{6}$$

where $\mathbf{p}(P_I)$ is the coordinate of P_I in the reference configuration.

If two points, A and B, are reflectively symmetric with respect to a plane with unit normal $\mathbf{n}$ (Figure 3), then their displacements are related through

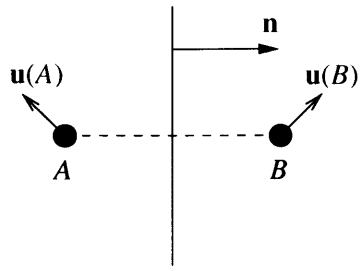

Figure 3: Two points, A and B, that are reflectively symmetric with respect to a plane with unit normal $\mathbf{n}$.

$$\mathbf{u}(A) = (\mathbf{1} - 2\mathbf{n} \otimes \mathbf{n})\mathbf{u}(B) = \mathbf{Q}(\mathbf{n})\mathbf{u}(B), \tag{7}$$

where $\mathbf{u}(A)$ and $\mathbf{u}(B)$ are the displacements of A and B, $\mathbf{1}$ is the second-order identity tensor, the symbol $\otimes$ denotes the tensor (dyadic) product, and $\mathbf{Q}(\mathbf{n})$ is the reflection operator of the symmetry plane with normal direction $\mathbf{n}$. The reflection operator $\mathbf{Q}(\mathbf{n})$ is an orthogonal tensor, thus $\mathbf{Q}(\mathbf{n})^T\,\mathbf{Q}(\mathbf{n}) = \mathbf{1}$.

2.1.2 Plane strain deformation and principal stress states

The cases of plane strain deformation and principal stress states coincident with the coordinate directions perpendicular to the square facets of the cell, require 1/8 (Figure 4) of the 3D V-BCC cell to be modeled. The coordinate planes are symmetry planes, and the general periodic boundary conditions (6), together with appropriate reflections (7) give rise to the following boundary conditions (8), (9),

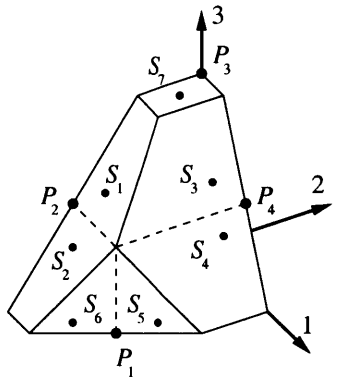

Figure 4: The (undeformed) 3D V-BCC cell model used for plane strain deformation and principal stress states.

$$
\begin{aligned}
\mathbf{u}(S_6) + \mathbf{Q}(\mathbf{e}_3)\mathbf{u}(S_5) &= 2\mathbf{u}(P_1) \\
\mathbf{u}(S_1) + \mathbf{Q}(\mathbf{e}_1)\mathbf{u}(S_2) &= 2\mathbf{u}(P_2) \\
\mathbf{e}_3 \cdot \mathbf{u}(S_7) &= \mathbf{e}_3 \cdot \mathbf{u}(P_3) \\
\mathbf{u}(S_3) + \mathbf{Q}(\mathbf{e}_2)\mathbf{u}(S_4) &= 2\mathbf{u}(P_4)
\end{aligned}
\tag{8}
$$

$$
(\mathbf{F} - \mathbf{1})\mathbf{p}(P_i) = \mathbf{u}(P_i), \quad i = 1..4 \tag{9}
$$

where S_1-S_7 are points on the facets of the 3D V-BCC cell (Figure 4).

2.1.3 Simple shear deformation

For the case of simple shear deformation in the 23-plane, 1/4 of the 3D V-BCC cell is modeled (Figure 5). The 23-plane is here a plane of symmetry, and the 12-plane is a plane of antisymmetry. The boundary conditions for this case are summarized below (10), (11),

$$
\begin{aligned}
\mathbf{u}(S_6) - \mathbf{Q}(\mathbf{e}_1)\mathbf{u}(S_{11}) &= 2\mathbf{u}(P_1) \\
\mathbf{u}(S_1) + \mathbf{Q}(\mathbf{e}_1)\mathbf{u}(S_2) &= 2\mathbf{u}(P_2) \\
\mathbf{u}(S_7) + \mathbf{Q}(\mathbf{e}_1)\mathbf{u}(S_8) &= 2\mathbf{u}(P_3) \\
\mathbf{u}(S_4) + \mathbf{u}(S_9) &= 2\mathbf{u}(P_4) \\
\mathbf{u}(S_3) + \mathbf{u}(S_{10}) &= 2\mathbf{u}(P_4) \\
\mathbf{u}(S_{12}) - \mathbf{Q}(\mathbf{e}_1)\mathbf{u}(S_5) &= 2\mathbf{u}(P_5) \\
\mathbf{u}(S_{15}) + \mathbf{Q}(\mathbf{e}_1)\mathbf{u}(S_{16}) &= 2\mathbf{u}(P_6) \\
\mathbf{u}(S_{13}) + \mathbf{Q}(\mathbf{e}_1)\mathbf{u}(S_{14}) &= \mathbf{0}
\end{aligned}
\tag{10}
$$

$$
(\mathbf{F} - \mathbf{1})\mathbf{p}(P_i) = \mathbf{u}(P_i), \quad i = 1..6 \tag{11}
$$

where S_1-S_{16} are points on the facets of the 3D V-BCC cell (Figure 5).

2.2 Macroscopic cell response

To calculate the overall mechanical response of the cell model under loading, we use the principle of virtual work,

$$
\delta W^{int} = \delta W^{ext}. \tag{12}
$$

The external virtual work may be written as

$$
\delta W^{ext} = \int_{S_0} \tilde{\mathbf{S}}\mathbf{n}_0 \cdot \delta\mathbf{u}(\mathbf{p})\mathrm{d}S_0 = \int_{S_0} \tilde{\mathbf{s}} \cdot \delta\mathbf{u}(\mathbf{p})\mathrm{d}S_0, \tag{13}
$$

where $\tilde{\mathbf{S}}$ is the (local) first Piola-Kirchhoff stress tensor, $\mathbf{n}_0$ is the outward unit normal to the surface area, S_0, in the reference configuration. $\delta\mathbf{u}(\mathbf{p})$ is the virtual displacement of a point $\mathbf{p}$ in the reference configuration, and $\tilde{\mathbf{s}}$ is the surface traction in the

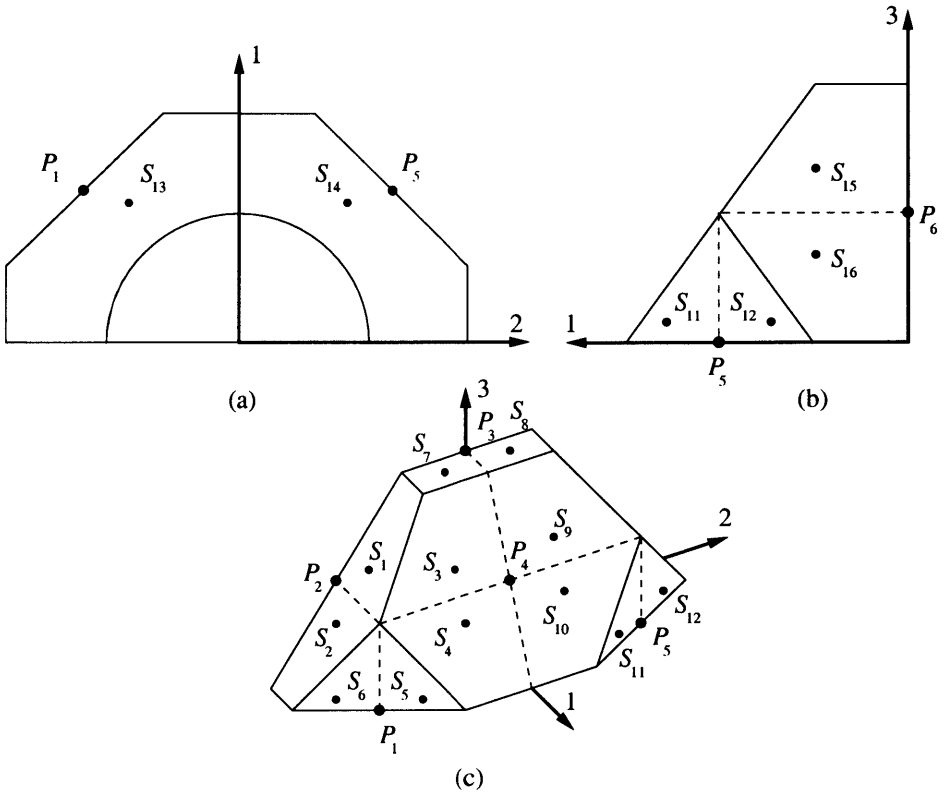

Figure 5: The (undeformed) 3D V-BCC cell model used for simple shear deformation: (a) 12-orthographic view; (b) 13-orthographic view; (c) 3D view.

reference configuration. The macroscopic (average) first Piola-Kirchhoff stress, $\mathbf{S}$, is given by

$$\mathbf{S} = \frac{1}{V_0} \int_{V_0} \tilde{\mathbf{S}} \, \mathrm{d}V_0, \tag{14}$$

where V_0 is the volume in the reference configuration. The first Piola-Kirchhoff stress is work conjugate to the deformation gradient. Hence, the internal virtual work can be written as

$$\delta W^{int} = V_0 \mathbf{S} \cdot \delta \mathbf{F}. \tag{15}$$

By using equations (12), (13) and (15), we get

$$V_0 \mathbf{S} \cdot \delta \mathbf{F} = \int_{S_0} \tilde{\mathbf{s}} \cdot \delta \mathbf{u}(\mathbf{p}) \mathrm{d}S_0. \tag{16}$$

Hence, the macroscopic first Piola-Kirchhoff stress tensor, $\mathbf{S}$, is expressed in terms of the surface tractions, $\tilde{\mathbf{s}}$. The components of the macroscopic deformation gradient, $\mathbf{F}$, are the quantities that drive the cell deformation (equations (9) and (11)) in the finite element analysis. Operationally, the components of $\mathbf{F}$ are provided to the cell model by introducing nine generalized degrees of freedom, ξ_i,

$$\begin{bmatrix} \xi_1 & \xi_2 & \xi_3 \\ \xi_4 & \xi_5 & \xi_6 \\ \xi_7 & \xi_8 & \xi_9 \end{bmatrix} = \begin{bmatrix} (F_{11} - 1) & F_{12} & F_{13} \\ F_{21} & (F_{22} - 1) & F_{23} \\ F_{31} & F_{32} & (F_{33} - 1) \end{bmatrix}. \tag{17}$$

These ξ_i are assigned to be the displacement components of three fictitious nodes in the finite element model, thus giving the $\mathbf{F}$ in equations (9) and (11). Virtual work is then used to determine the stress. The external virtual work (equation (13)) may be restated in terms of the generalized degrees of freedom, ξ_i, and their work conjugate

generalized forces, Ξ_i,

$$\delta W^{ext} = \sum_{i=1}^{9} \Xi_i \, \delta\xi_i. \tag{18}$$

Therefore, the Ξ_i are the "reaction forces" corresponding to the assigned "displacement components", ξ_i of the fictitious nodes. By using equations (15) and (18), the components of the macroscopic first Piola-Kirchhoff stress tensor, $\mathbf{S}$, are identified as

$$\begin{bmatrix} S_{11} & S_{12} & S_{13} \\ S_{21} & S_{22} & S_{23} \\ S_{31} & S_{32} & S_{33} \end{bmatrix} = \frac{1}{V_0} \begin{bmatrix} \Xi_1 & \Xi_2 & \Xi_3 \\ \Xi_4 & \Xi_5 & \Xi_6 \\ \Xi_7 & \Xi_8 & \Xi_9 \end{bmatrix}. \tag{19}$$

The macroscopic Cauchy stress tensor, $\mathbf{T}$, is calculated from $\mathbf{S}$ and $\mathbf{F}$ as

$$\mathbf{T} = \frac{V_0}{V} \mathbf{S}\,\mathbf{F}^T, \tag{20}$$

where V is the volume in the current (deformed) configuration.
Finally, the macroscopic logarithmic strain tensor, $\mathbf{E}$, can be calculated from

$$\mathbf{E} = \ln \mathbf{U}, \tag{21}$$

where $\mathbf{U}$ is the (macroscopic) right stretch tensor based on a polar decomposition of the macroscopic deformation gradient, $\mathbf{F} = \mathbf{R}\,\mathbf{U}$.

2.3 Loading conditions

2.3.1 Triaxial equi-lateral loading

The triaxiality of macroscopic stress is defined as

$$T_\Sigma = \frac{T_{kk}}{3\,T_{eq}}, \tag{22}$$

where $T_{kk}/3 = (T_{11} + T_{22} + T_{33})/3$ is the macroscopic hydrostatic stress, and T_{eq} is the macroscopic equivalent tensile (Mises) stress. The case of uniaxial tension corresponds to a macroscopic stress triaxiality of $T_\Sigma = 1/3$. A principal stress state for which $T_{11} = T_{22}$ results in a macroscopic stress triaxiality given by

$$T_\Sigma = \frac{2\,T_{11} + T_{33}}{3\,|T_{33} - T_{11}|}. \tag{23}$$

During triaxial loading, the 3D V-BCC cell model is subjected to a constant macroscopic axial strain rate, $\dot{E}_{33} = 0.01s^{-1}$, and the triaxiality of macroscopic stress, T_Σ, is kept constant throughout the deformation history. This is done by utilizing a technique similar to that used by Tzika, et al. (2000), where a user-defined element is introduced to monitor the axial macroscopic stress level, and apply lateral tractions accordingly.

2.3.2 Plane strain deformation

During plane strain deformation, the 3D V-BCC cell model is subjected to a constant macroscopic axial strain rate, $\dot{E}_{33} = 0.01s^{-1}$, and the 1-direction is confined, $E_{11} = 0$. The stress acting in the constrained direction, T_{11}, is given by the solution itself, and cannot be imposed. The in-plane lateral stress, T_{22}, is controlled through a stress biaxiality parameter B_Σ defined as

$$B_\Sigma = \frac{T_{22}}{T_{33}}. \tag{24}$$

The purpose of introducing a stress biaxiality parameter is to study the macroscopic stress triaxiality in the vicinity of a plane strain notch or a crack tip at different levels of in-plane stress biaxiality.

2.3.3 Simple shear deformation

Simple shear (plane strain) deformation in the 23-plane corresponds to a time-dependent macroscopic deformation gradient according to

$$\mathbf{F} = \mathbf{1} + \Gamma \cdot \mathbf{e}_2 \otimes \mathbf{e}_3 \tag{25}$$

where $\mathrm{d}\Gamma/\mathrm{d}t = 0.0173s^{-1}$ is the nominal shear strain rate. The macroscopic deformation gradient is imposed through the method described in Section 2.2.

2.4 Matrix constitutive behavior

The large-strain elastic-viscoplastic behavior of glassy polymers has been found to be well-described by the constitutive model of Boyce, et al. (1988), later modified by Arruda and Boyce (1993). Material constants for annealed polycarbonate are, for comparative reasons, in correspondence with those used by Socrate and Boyce (2000).

3 Results

3.1 Uniaxial (tensile) loading

The 3D V-BCC cell model was subjected to uniaxial tension for a range of initial void volume fractions, $f_0 = V_0^{void}/V_0^{cell}$; values studied were $f_0 = \{0.05, 0.10, 0.15, 0.20, 0.25\}$[2]. The macroscopic stress-strain response is represented by plotting macroscopic axial stress-axial strain curves (Figure 6a). The macroscopic volumetric strain, $E_{kk} = E_{11} + E_{22} + E_{33}$, plotted as a function of macroscopic axial strain, is shown in Figure 6b. The macroscopic yield stress for the different blends is defined as the point where the stress-strain response exhibits a peak in axial stress, followed by softening. The microscopic response, in terms of contours of plastic shear strain rate, $\dot{\gamma}^p$ (Arruda

[2]All cases were analyzed using the same mesh density. The case of $f_0 = 0.25$ was analyzed using a mesh four times denser than the original mesh. The macroscopic response of the refined mesh solution was identical to that of the original mesh, and the microscopic response was nearly identical.

and Boyce (1993)), is shown in Figure 7 for $f_0 = 0.05$. Figures 8 and 9 show the corresponding contours for $f_0 = 0.25$. Figures 7 and 8 depict the microscopic behavior at strain levels near macroscopic yield of the blends for $f_0 = 0.05$ and $f_0 = 0.25$, respectively, whereas Figure 9 shows the microscopic response at higher macroscopic axial strains for $f_0 = 0.25$.

The contour plots (Figures 7 and 8) show that plastic flow initiates in the equatorial region (a), as expected. At this point in the deformation, most of the surrounding matrix material is still in the elastic region. A close examination of the stress-strain curves (Figure 6) shows that, even prior to macroscopic yield, the curves deviate slightly from linearity[3]. This is due to the initial local plastic deformation in the equatorial region of the void, which begins to soften the voided material. As the yielded material strain-hardens due to molecular orientation, surrounding matrix material starts to flow. Eventually, shear bands develop across inter-particle ligaments. This "net section" yielding corresponds to macroscopic yield of the blend. Figure 6 shows that the macroscopic axial strain at yield for the blend with $f_0 = 0.05$ is $E_{33} \simeq 0.038$, and that of the blend with $f_0 = 0.25$ is $E_{33} \simeq 0.041$. It is seen in Figure 6a, that the macroscopic yield stress of the voided material decreases with increasing void volume fraction, as expected, due to the reduction in matrix net section. The macroscopic stress-strain response also shows that the post-yield softening, which is apparent in the homopolymer, is reduced through the introduction of voids, and that it decreases with increasing void volume fraction.

The contours of plastic shear strain rate for $f_0 = 0.25$ explain the reduction in post-yield softening compared to the homopolymer. The difference in deformation pattern between the voided polymer and the homopolymer is that the voided material undergoes plastic deformation through a succession of events, rather than undergoing plastic deformation uniformly. In other words, the intrinsic softening is not reached simultaneously everywhere in the matrix, as it would be in a homogeneous material.

[3]The homopolymer also exhibits slight pre-peak nonlinearity that is not captured in the Arruda-Boyce model for $f_0 = 0$; the cell model results indicate that enhanced pre-peak nonlinearity is to be expected in the voided blends.

Macroscopic softening is observed to occur between $E_{33} = 0.04$ and $E_{33} = 0.13$, approximately. At macroscopic yield ($E_{33} \simeq 0.04$), a shear band has fully developed across an inter-particle ligament. However, the development of the shear band was progressive and, at macroscopic yield, regions of the material in the shear band are already strain-hardening. Therefore, the macroscopic composite response exhibits less softening than the homopolymer since the entire net section is not softening homogeneously. For $f_0 = 0.05$, the net section plastic flow is more homogeneous, which results in an increased post-yield softening of the blend.

The hardening behavior of the different blends is consistent over the studied range of initial void volume fractions. As the shear bands strain-harden, surrounding material yields. The plastic flow then propagates up and down the ligaments in a manner similar to the stable necking of a tensile bar (Figure 9). As the plastic flow propagates up and down the inter-particle ligaments, an increasing volume of matrix material is being encompassed by the flow. This increases the total plastic flow resistance of the blend, which results in macroscopic strain-hardening, since more matrix material is forced to undergo plastic deformation simultaneously. For low void volume fractions, the increase in fraction of matrix material encompassed by the plastic flow occurs more rapidly with applied macroscopic axial strain (Figure 7), which results in a higher hardening rate than for the blends with high initial void volume fractions.

The predictions of the evolution of macroscopic volumetric strain with macroscopic axial strain, shown in Figure 6b, reflect the initial elastic Poisson effect of the porous material, followed by the plastic expansion of the void due to plastic deformation of the matrix. The predicted magnitude and evolution of volumetric strain, are in good agreement with the predictions by Socrate and Boyce (2000) for the axisymmetric V-BCC cell model; small discrepancies ($10-15\%$) are due to the axisymmetric formulation vs. the fully three-dimensional formulation.[4] The predicted evolution of volumetric strain is consistent with measurements of van der Sanden, et al. (1994).

[4]Note that a stacked hexagonal array (SHA) model has been found to provide unrealistic dramatic increases in dilatation when $f_0 > 0.1$. For an initial void volume fraction $f_0 = 0.20$, the prediction of the SHA model is about twice that of the present 3D V-BCC cell model.

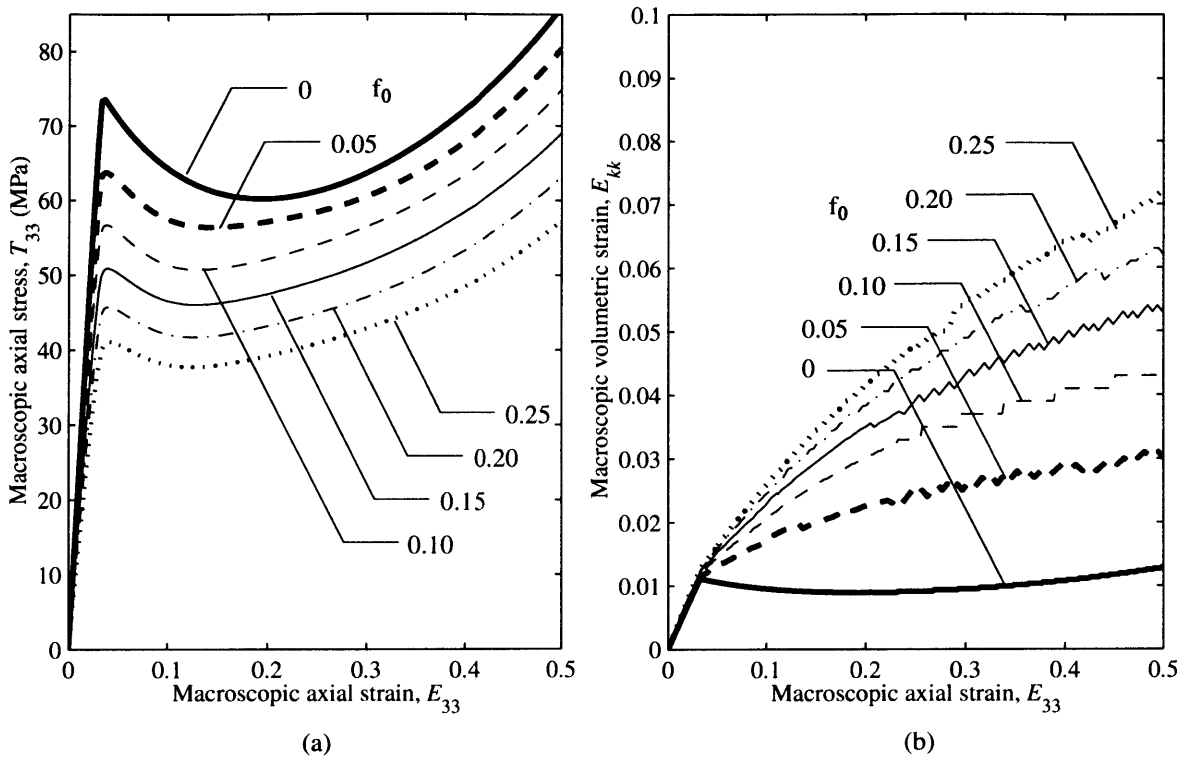

Figure 6: Macroscopic responses of the cell models under uniaxial tensile loading at different initial void volume fractions f_0: (a) evolution of macroscopic axial stress, T_{33}, with macroscopic axial strain, E_{33}, (b) evolution of macroscopic volumetric strain, E_{kk}, with macroscopic axial strain, E_{33}.

The predicted stress-strain curves for uniaxial tension of the 3D V-BCC cell model are in good agreement with those of the axisymmetric V-BCC cell model by Socrate and Boyce (2000). This shows that, for uniaxial tension and states of triaxial loading with equal lateral stresses, the modeling simplification to an axisymmetric version of the three-dimensional cell model can be done satisfactorily. A similar conclusion was drawn by Hom (1992), who modeled whisker-reinforced metal matrix composites. The author concluded that axisymmetric models of the three-dimensional microstructure are reasonable alternatives to three-dimensional micromechanical models, in axisymmetric loading situations.

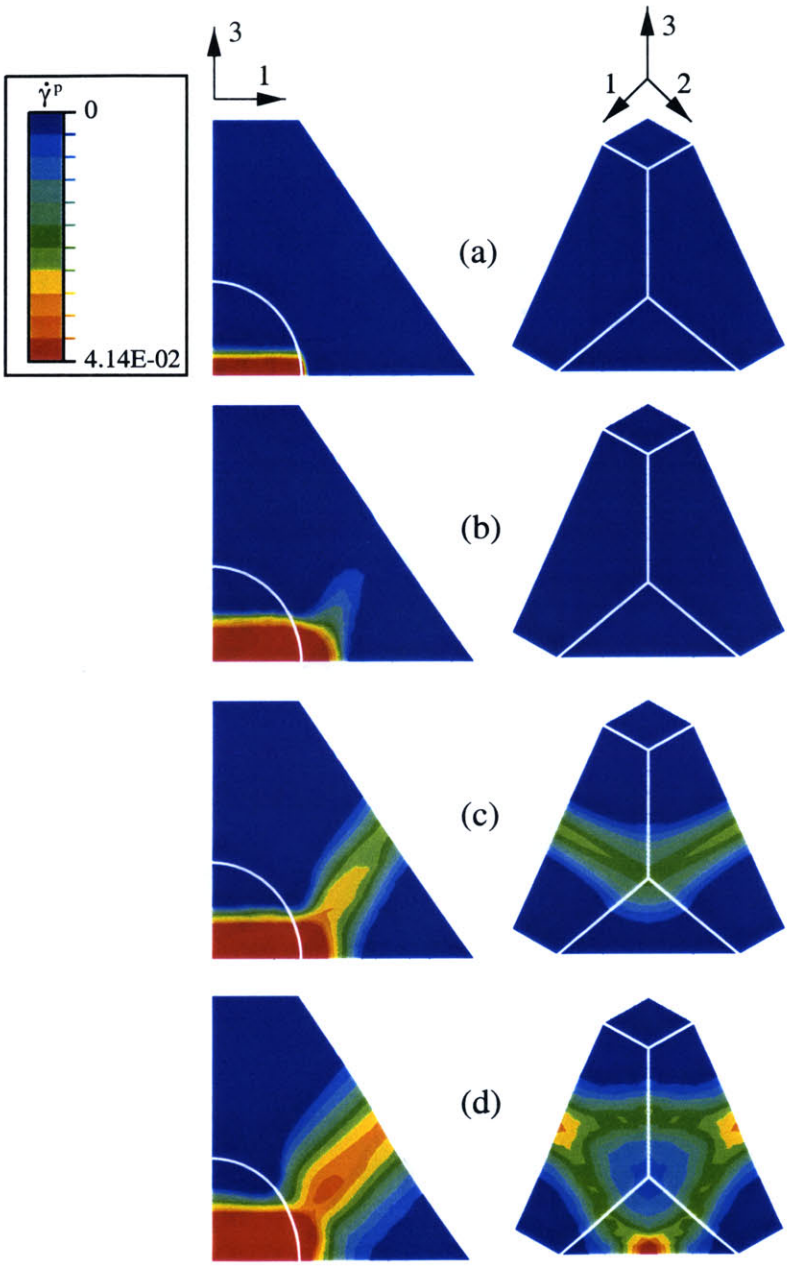

Figure 7: Contours of $\dot{\gamma}^p$ under uniaxial loading, for an initial void volume fraction $f_0 = 0.05$. The development of shear bands is shown for increasing levels of macroscopic axial strain: (a) $E_{33} \simeq 0.02$, (b) $E_{33} \simeq 0.03$, (c) $E_{33} \simeq 0.033$, (d) $E_{33} \simeq 0.06$. The macroscopic axial strain at yield was found to be $E_{33} \simeq 0.038$.

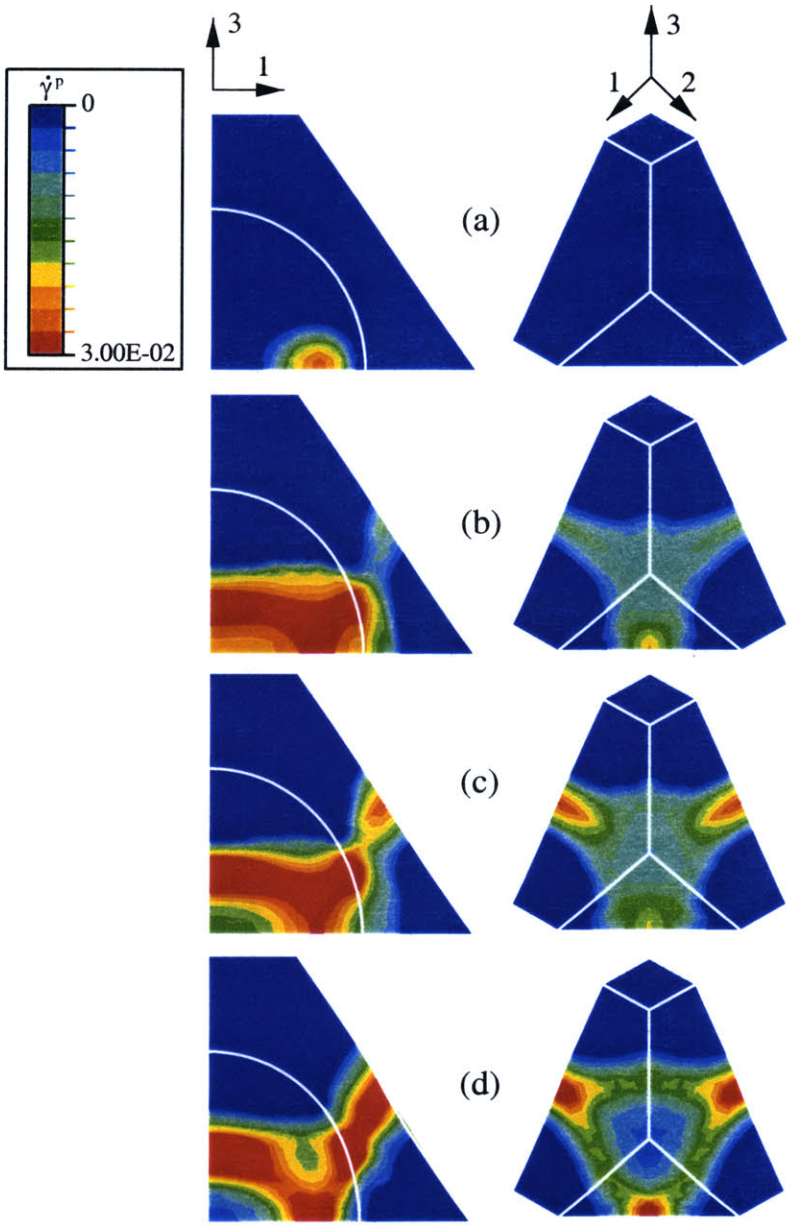

Figure 8: Contours of $\dot{\gamma}^p$ under uniaxial loading, for an initial void volume fraction $f_0 = 0.25$. The development of plastic shear strain localization is shown for increasing levels of macroscopic axial strain: (a) $E_{33} \simeq 0.02$, (b) $E_{33} \simeq 0.035$, (c) $E_{33} \simeq 0.039$, (d) $E_{33} \simeq 0.059$. The macroscopic axial strain at yield was found to be $E_{33} \simeq 0.041$.

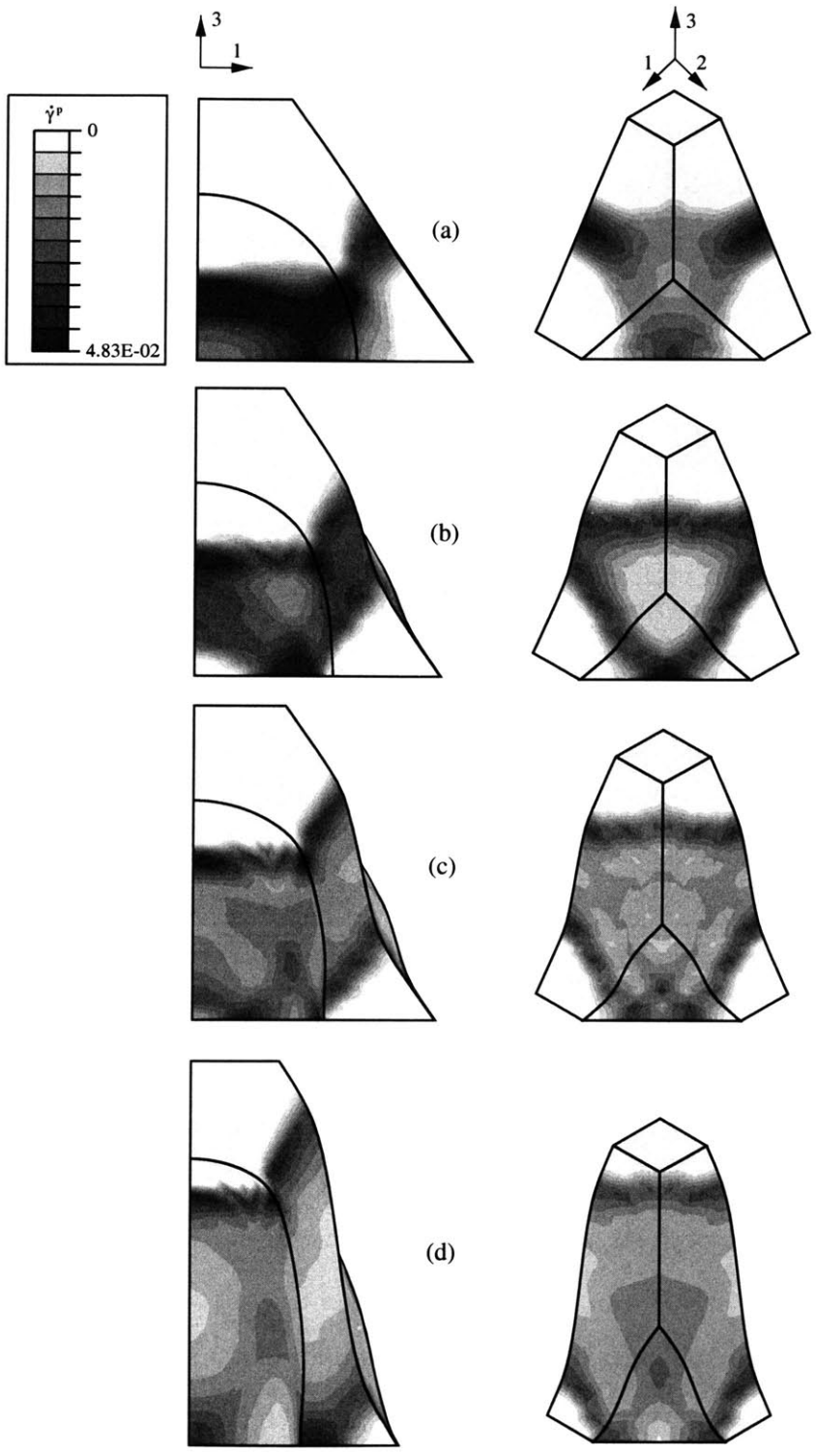

Figure 9: Contours of $\dot{\gamma}^p$ under uniaxial loading, for an initial void volume fraction $f_0 = 0.25$. The development of plastic shear strain localization is shown for increasing levels of macroscopic axial strain: (a) $E_{33} \simeq 0.039$, (b) $E_{33} \simeq 0.14$, (c) $E_{33} \simeq 0.23$, (d) $E_{33} \simeq 0.41$.

3.2 Plane strain deformation

In order to investigate how the blend responds to plane strain loading conditions, the 3D V-BCC cell model ($f_0 = 0.25$) was subjected to plane strain tension for a range of macroscopic stress biaxialities: $B_\Sigma = \{0, 0.25, 0.5\}$. The main loading direction is the 3-direction, and the constrained direction is the 1-direction (Figure 4). The stress in the 2-direction is controlled through the macroscopic stress biaxiality parameter B_Σ (24). The macroscopic equivalent tensile (Mises) stress vs. axial strain response is shown in Figure 10a for a range of stress biaxialities. The underlying microscopic behavior for two different stress biaxialities, $B_\Sigma = 0$ and $B_\Sigma = 0.5$, is characterized by plotting the contours of plastic shear strain rate at different levels of macroscopic axial strain (Figures 11 and 12). The macroscopic yield stress for the material is defined as the point where the stress-strain response exhibits a peak in equivalent tensile (Mises) stress, followed by softening.

Figure 10a shows that, prior to macroscopic yield, the stress-strain curves deviate slightly from linearity. Similar to the case of uniaxial tension, where local yielding of the matrix material in the equatorial region of the void gave rise to the non-linearity, the contours of plastic shear strain rate for the cases of $B_\Sigma = 0$ and $B_\Sigma = 0.5$ also show this initial local yielding of the matrix.

For the case of $B_\Sigma = 0$ (Figure 11), the contours of plastic shear strain rate reveal that plastic flow of the matrix initiates in the equatorial region of the void, and then successively spreads and grows across the inter-particle ligament in the constrained direction (Figure 11a). At this point the inter-particle ligament in the unconstrained direction is still in the elastic region. (This is a feature of the deformation pattern which could not have been captured in a traditional two-dimensional plane strain analysis in which the filler particles are approximated as cylindrical voids.) As the macroscopic axial strain continues to increase, the plastic flow spreads across the inter-particle ligament in the (unconstrained) 2-direction (Figure 11a,b). At this point, macroscopic yield of the blend is reached (Figure 10a). Interestingly, the interaction of the plastic flow in the constrained direction with that in the unconstrained

direction results in the formation of two separate shear bands across the ligament in the unconstrained direction (Figure 11c). This distributed yielding reduces the amount of strain softening as compared to that of the homopolymer, as was also observed in the case of uniaxial tension. As the deformation progresses, all of the shear bands strain-harden and then propagate up and down the ligament in a manner analogous to stable neck propagation during cold drawing of polymers. This propagation coincides with the macroscopic strain-hardening (Figure 10a).

For a higher macroscopic stress biaxiality, $B_\Sigma = 0.5$, the contours of plastic shear strain rate qualitatively resemble the contours for uniaxial tension (Figure 9). The deformation initiates at four distinct points of the equator of the void (Figure 12). The plastic flow then spreads across the two inter-particle ligaments simultaneously, which corresponds to macroscopic yield of the blend. Both shear bands then strain-harden and propagate up and down the ligaments.

The stress-strain curves shown in Figure 10a show that the post-yield softening of the blend increases with increasing imposed stress biaxiality. A close examination of the contour plots for $B_\Sigma = 0$ and $B_\Sigma = 0.5$ shows that in the case of $B_\Sigma = 0.5$, both ligaments (in the constrained and unconstrained directions) yield at approximately the same macroscopic axial strain and thus soften together, producing the greater strain softening with increased B_Σ.

The macroscopic hardening rate decreases with an increase in imposed stress biaxiality, B_Σ (Figure 10a). The higher stress biaxiality increases the dilatation of the blend (Figure 10b). The dilatation increases the macroscopic cross-section area of the cell, tending to decrease the macroscopically applied stress, T_{33}. The contours of plastic shear strain rate (Figures 11 and 12) show that in the case of the higher stress biaxiality, distinct shear bands propagate up and down the inter-particle ligaments. This 'drawing', which is more pronounced in the case of $B_\Sigma = 0.5$ than in the case of $B_\Sigma = 0$, thins the ligaments (Figure 12c,d).

The prediction of volumetric strain in the case of plane strain tension (Figure 10b) is higher than in the case of uniaxial tension, and, as expected, it is seen to increase with increasing stress biaxiality. In the case of $B_\Sigma = 0$, the plane strain constraint

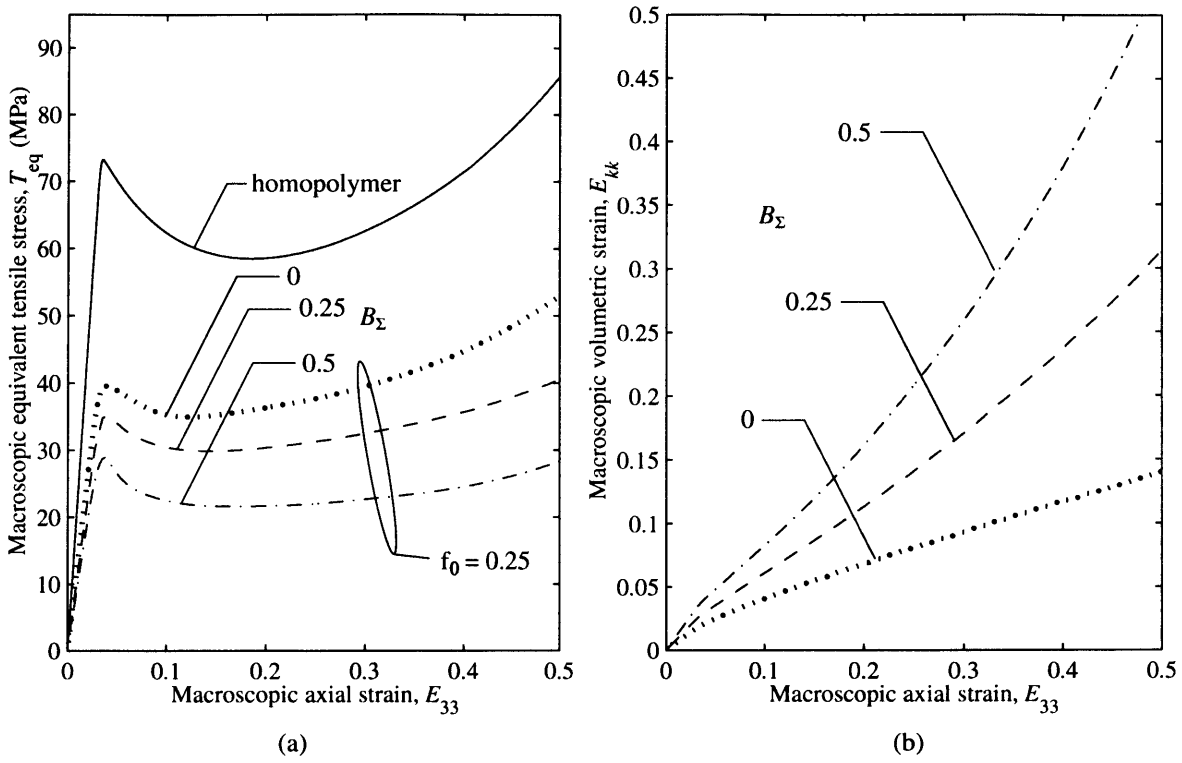

Figure 10: Macroscopic responses of the cell models under plane strain deformation: (a) evolution of macroscopic equivalent tensile (Mises) stress, T_{eq}, with macroscopic axial strain, E_{33}, (b) evolution of macroscopic volumetric strain, E_{kk}, with macroscopic axial strain.

restricts the lateral contraction of the cell upon (tensile) loading, which results in a higher dilatation of the cell. When positive stress biaxialities are imposed, the dilatation of the cell increases significantly (Figure 10b). The resulting triaxiality of the applied stress state increases (Figure 13) with increasing stress biaxialities, and this promotes dilatation of the blend. Note that a significant level of stress biaxiality ($B_\Sigma = 0.5$) in the voided polymer produces only modest levels of plane strain stress triaxiality, $T_\Sigma \simeq 1.5$; in a solid incompressible matrix material, the corresponding stress triaxiality would be $T_\Sigma = \sqrt{3}$. The internal traction-free surfaces limit the maximum achievable macroscopic stress triaxiality and promote macroscopic inelastic dilatation.

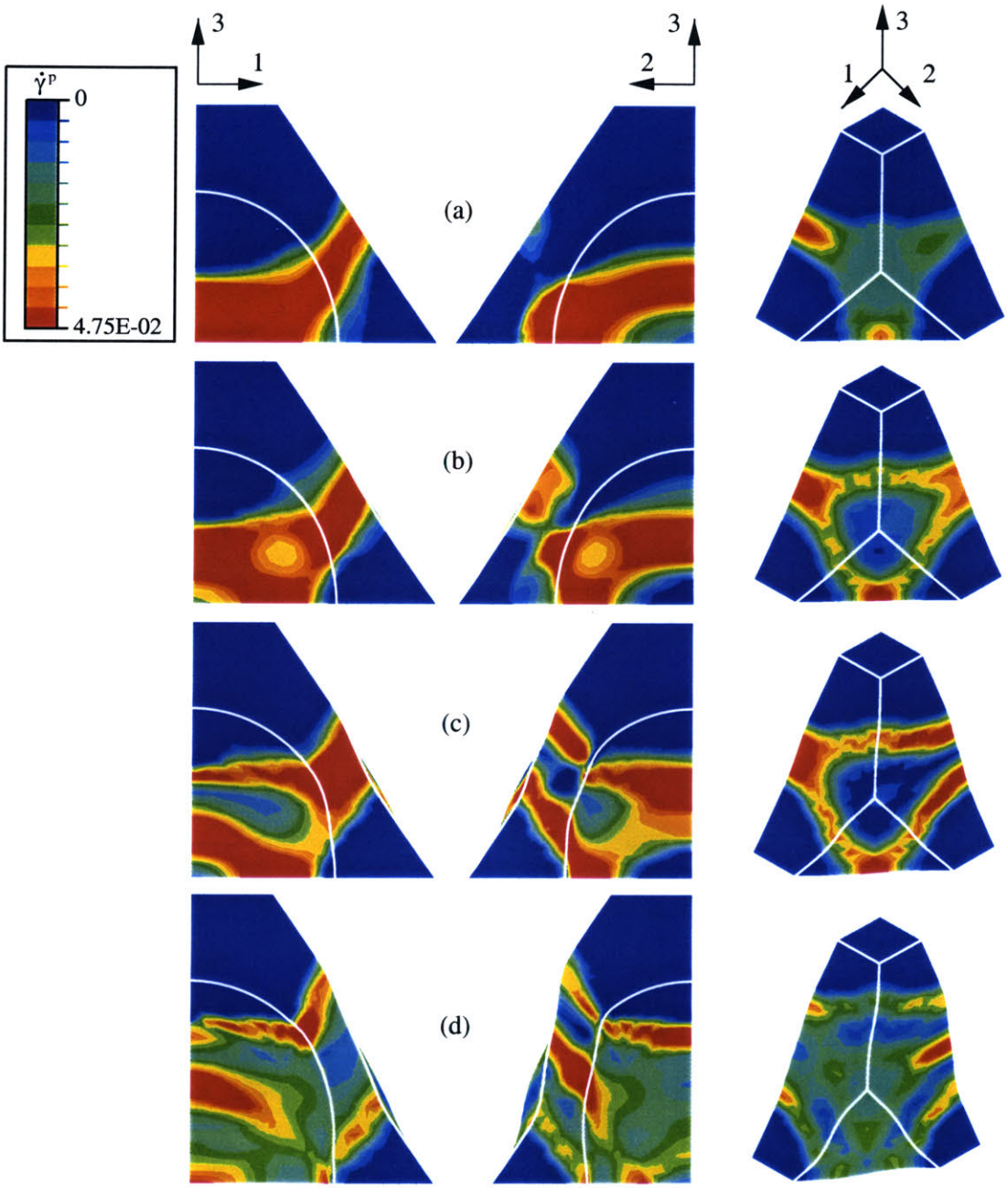

Figure 11: Contours of $\dot{\gamma}^p$ under plane strain deformation ($B_\Sigma = 0$), for an initial void volume fraction $f_0 = 0.25$. The development of plastic shear strain localization is shown for increasing levels of macroscopic axial strain: (a) $E_{33} \simeq 0.04$, (b) $E_{33} \simeq 0.057$, (c) $E_{33} \simeq 0.11$, (d) $E_{33} \simeq 0.23$. The macroscopic axial strain at yield was found to be $E_{33} \simeq 0.039$.

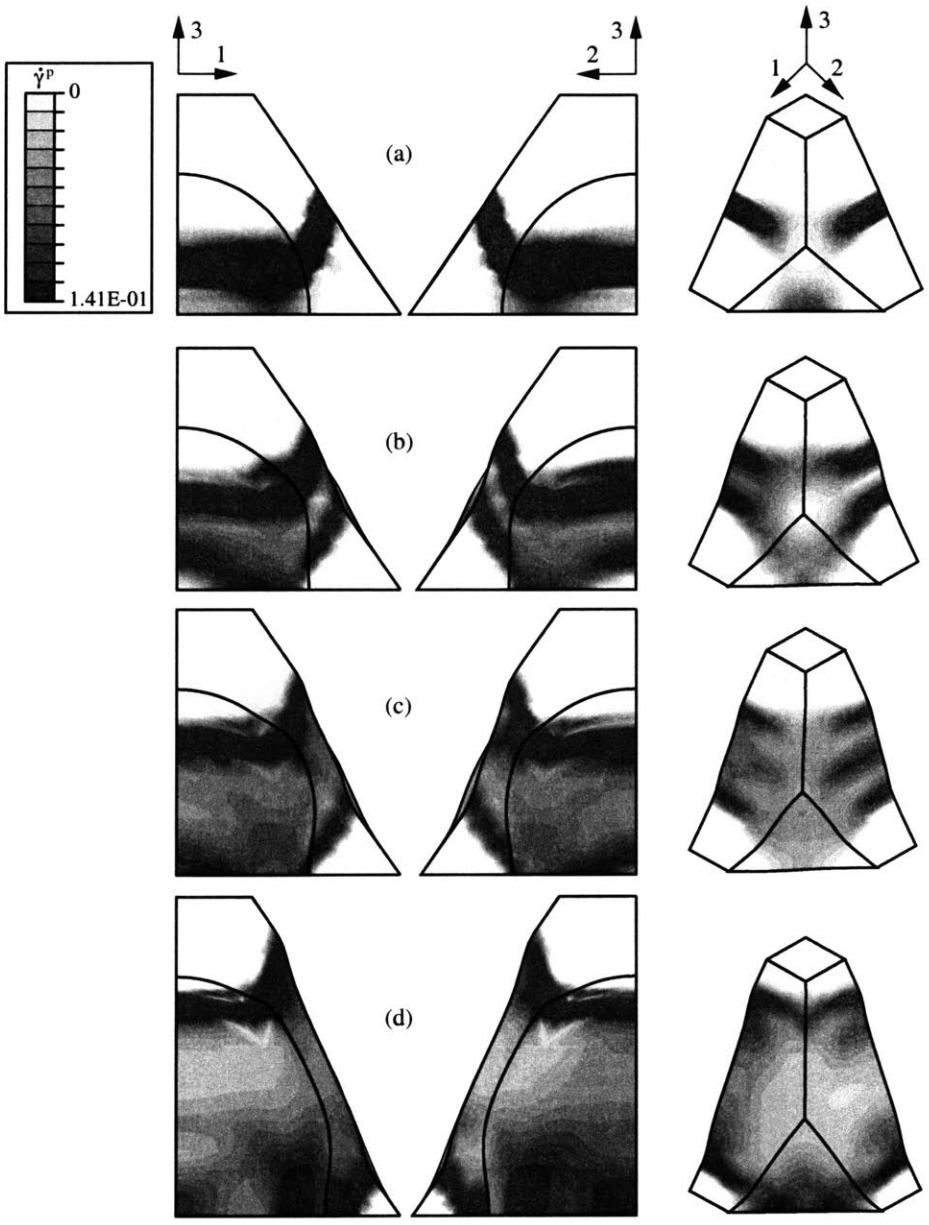

Figure 12: Contours of $\dot{\gamma}^p$ under plane strain deformation ($B_\Sigma = 0.5$), for an initial void volume fraction $f_0 = 0.25$. The development of plastic shear strain localization is shown for increasing levels of macroscopic axial strain: (a) $E_{33} \simeq 0.04$, (b) $E_{33} \simeq 0.14$, (c) $E_{33} \simeq 0.23$, (d) $E_{33} \simeq 0.42$. The macroscopic axial strain at yield was found to be $E_{33} \simeq 0.037$.

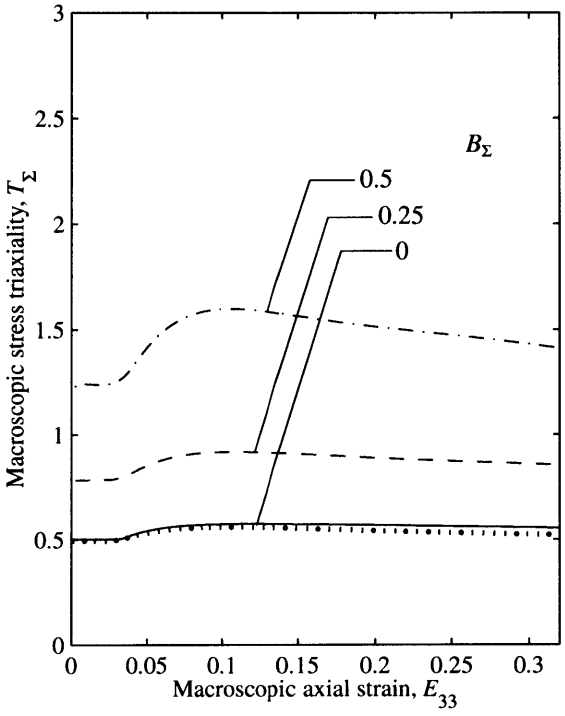

Figure 13: Macroscopic responses of the cell models under plane strain deformation ($f_0 = 0.25$): evolution of macroscopic stress triaxiality, T_Σ, with macroscopic axial strain.

3.3 Simple shear deformation

The cell models were subjected to simple shear deformation in the 23-plane, with the 1-direction constrained, to a final nominal shear strain $\Gamma = 0.5$. Cell models of two different initial void volume fractions, $f_0 = \{0.15, 0.25\}$, were analyzed. The composite response is computed in terms of the macroscopic nominal shear stress, S_{23}, as a function of the macroscopic nominal shear strain, Γ (Figure 14). Contours of plastic shear strain rate for the case of $f_0 = 0.25$ are shown in Figure 15. The plastic flow initiates at two locations of the particle equator (Figure 15a). At this point in the deformation, the onset of macroscopic yield of the blend has not yet been reached; the matrix is still predominantly in the elastic region. As the deformation progresses, the plastic flow spreads in a Y-shaped manner until it penetrates the ligament thickness (Figure 15b). As discussed above, the local plastic flow prior to macroscopic yield of the blend appears in the slight non-linearity in the stress strain response. The plastic flow then spreads across the inter-particle ligament in the vertical direction. This net section yield corresponds to macroscopic yield of the blend. The stress-strain response reveals that in the case of $f_0 = 0.25$, the macroscopic nominal shear strain at yield was $\Gamma \simeq 0.051$, and in the case of $f_0 = 0.15$, the corresponding value was $\Gamma \simeq 0.05$. Immediately after macroscopic yield, the stress-strain curves display an abrupt drop (Figure 14). This drop corresponds to the localization of yield (and strain softening) to a thin vertical band (Figure 15c) which penetrates the entire ligament thickness. The sudden drop in the stress-strain response immediately after yield is thought to be an artifact of the specific choice of loading direction relative to the BCC arrangement of voids. Once the vertical shear band strain-hardens, plastic deformation propagates left and right in the form of two shear bands.

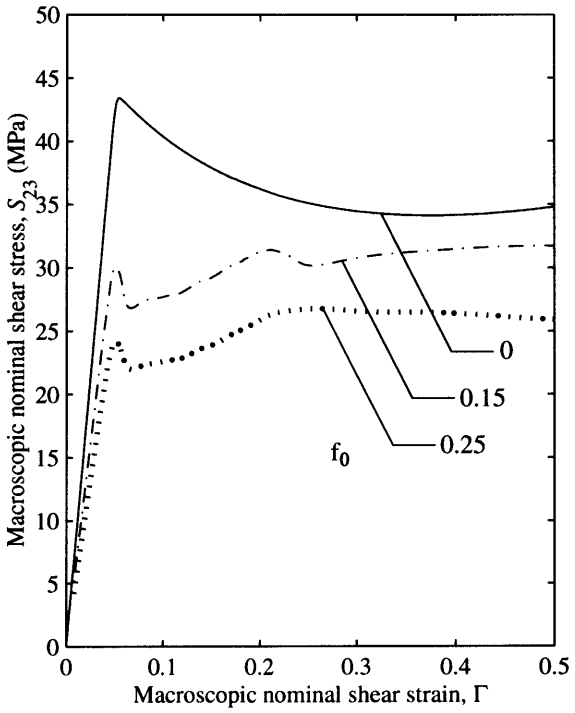

Figure 14: Macroscopic responses of the cell models under simple shear (plane strain) deformation: evolution of macroscopic nominal shear stress, S_{23}, with macroscopic nominal shear strain. The macroscopic nominal shear strain at yield was found to be $\Gamma \simeq 0.051$ for the voided polymers.

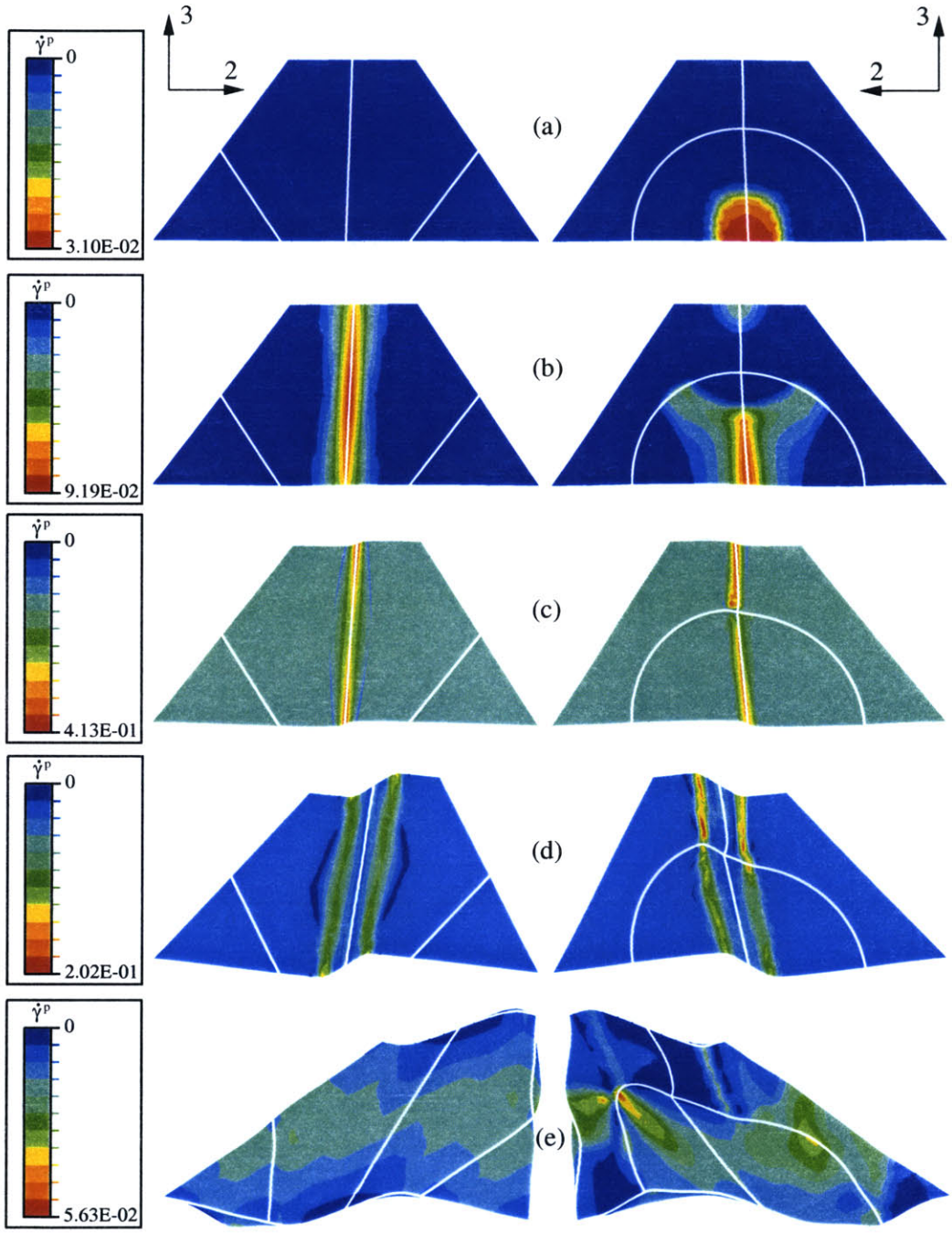

Figure 15: Contours of $\dot{\gamma}^p$ under simple shear (plane strain) deformation, for an initial void volume fraction $f_0 = 0.25$. The development of shear bands is shown for increasing levels of macroscopic nominal shear strain: (a) $\Gamma \simeq 0.033$, (b) $\Gamma \simeq 0.047$, (c) $\Gamma \simeq 0.066$, (d) $\Gamma \simeq 0.16$, (e) $\Gamma \simeq 0.36$. The macroscopic nominal shear strain at yield was found to be $\Gamma \simeq 0.051$.

4 Discussion

4.1 Implications for tensile loading

In order to investigate how the initial void volume fraction affects the macroscopic behavior of the blend, we use a modified Considère construction to predict the macroscopic neck propagation behavior of the blend. The Considère construction is modified to account for the volumetric strains associated with the growth of voids and with dilatation of the matrix material. This construction provides information for how the void volume fraction affects the natural draw ratio of the blend. The standard Considère construction, for rigid/plastic, incompressible, pressure-insensitive behavior, gives the following expression for the point at which a macroscopic neck initiates (Figure 16):

$$T_{33}\Big|_{initiation} = \frac{\mathrm{d}T_{33}}{\mathrm{d}E_{33}}\Big|_{initiation}, \tag{26}$$

where T_{33} is the macroscopic axial stress and E_{33} is the macroscopic axial strain. Deformation then localizes within the necked region until the strain-hardening slope, $\mathrm{d}T_{33}/\mathrm{d}E_{33}$, increases to the level of the stress, T_{33}, at which point the neck will stabilize and begin to propagate (Figure 16),

$$T_{33}\Big|_{stabilization} = \frac{\mathrm{d}T_{33}}{\mathrm{d}E_{33}}\Big|_{stabilization}. \tag{27}$$

For compressible materials, equations (26) and (27) must both be modified to account for the volume change, which gives

$$T_{33} = \frac{\mathrm{d}T_{33}}{\mathrm{d}E_{33}} \frac{1}{(1 - \frac{\mathrm{d}E_{kk}}{\mathrm{d}E_{33}})}. \tag{28}$$

where E_{kk} is the macroscopic volumetric strain.

Figure 16 plots both the left and right hand sides of (28) versus macroscopic axial

strain, and the respective intersections of these curves determine the axial strains at which the macroscopic neck will initiate, and at which it will begin to propagate stably. Curves are shown for the case of uniaxial tension and a range of initial void volume fractions. The levels of macroscopic axial strain at neck stabilization are used to calculate the natural draw ratio of the blends,

$$\lambda_{draw} = e^{E_{33}^{(s)}}, \tag{29}$$

where $E_{33}^{(s)}$ is the macroscopic axial strain at which the neck amplitude stabilizes and instead the neck begins to propagate stably. The predicted natural draw ratios are tabulated in Table 1. Figure 16 shows there to be a decrease in natural draw ratio with an increase in f_0, with $f_0 = 0.05$ being an exception. A close examination of the different stress-strain curves (Figures 6 and 16) reveals that at the point in the deformation where stable macroscopic neck propagation begins, the macroscopic hardening rate differs between the blends. In the case of the homopolymer, the strain-hardening is stronger than in the blend with $f_0 = 0.05$; therefore macroscopic neck stabilization occurs sooner, and the natural draw ratio of the material is slightly lower. For the cases of $f_0 > 0.05$, the natural draw ratio decreases with increasing f_0, and we note that the stabilized strain-hardening slope of the voided materials is close to that of the homopolymer, but both the drop in macroscopic stress and the increase in volumetric strain with increasing initial porosity produce macroscopic neck stabilization at a lower macroscopic strain. While this effect is not large for polycarbonate, due to the low natural draw ratio of the homopolymer, it is notable and would be more significant in polymers with higher natural draw ratios. For example, Bartczak, et al. (1999) measured significantly lower natural draw ratios in rubber-filled high-density polyethylene (HDPE), than in the homopolymer.

A lower natural draw ratio indicates that the introduction of voids promotes the propagation of plastic flow through the matrix at lower macroscopic strains than in the homopolymer under uniaxial and plane strain tension. The controlled introduction

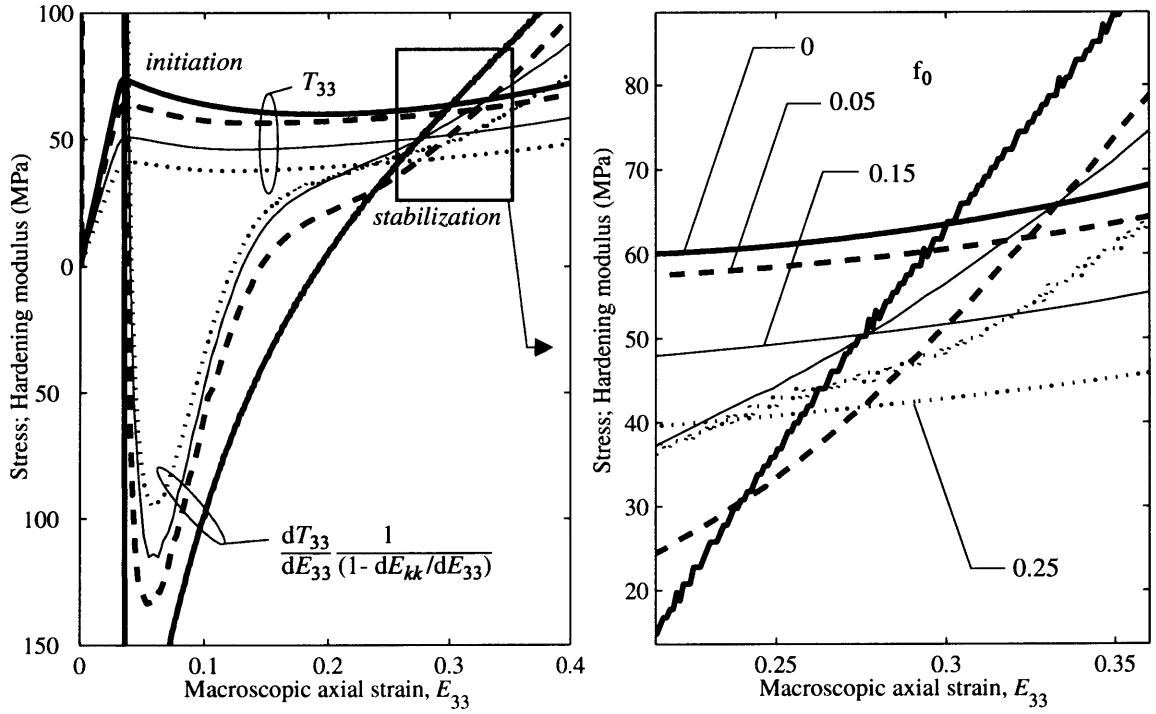

Figure 16: Considère construction for the case of uniaxial tension at different initial void volume fractions.

Table 1: Summary of the calculated natural draw ratios, λ_{draw}, for the case of uniaxial tension.

f_0	Uniaxial tension
0	1.35
0.05	1.38
0.15	1.32
0.25	1.27

of voids to the matrix may act to alter the distribution and propagation of plastic deformation under more complicated loading conditions such as occur at notch tips. To further understand the role of the altered macroscopic response on improving toughness under notch-like conditions, a three-dimensional constitutive model of the blend is required, as discussed further in Section 4.3.

4.2 Implications for toughening

The macroscopic behavior of the blend results in different stress and strain fields at a notch or a crack tip than what would be observed in the homopolymer. This requires the development of a continuum-level constitutive model (see Section 4.3 below) for these materials. The different macroscopic stress-strain response (i.e. lower yield point, reduced strain softening, volumetric straining, lower natural draw ratio) is likely to result in less severe stress conditions at a notch or a crack tip. To further address the potential of brittle failure due to crazing and/or cavitation in the matrix material, we monitored peak values of hydrostatic stress for a macroscopic stress triaxiality $T_\Sigma = 1.25$ (Figure 13), using both the plane strain cell model ($B_\Sigma = 0.5$) and the cell model with imposed (and equal) lateral stresses. We note that specific quantitative craze criteria are available in the literature for polystyrene and poly(methyl methacrylate), but these criteria have not been applied to polycarbonate. Therefore, the level of hydrostatic stress is used here to indicate the potential of brittle failure. The plane strain simulation resulted in a peak local hydrostatic

stress $\tilde{T}_{kk}^{(ps)}/3 = 64$ MPa at macroscopic yield, while the corresponding simulation using the cell with equal imposed lateral stresses resulted in a peak local hydrostatic stress $\tilde{T}_{kk}^{(triax)}/3 = 39$ MPa at macroscopic yield, where $\tilde{T}_{kk}/3$ denotes local matrix hydrostatic (Cauchy) stress. In both cases, the peak local hydrostatic stress in the matrix is observed at four locations in the equatorial region of the void, just below the surface. It is interesting to note that the plane strain cell model nonetheless predicts a significantly higher peak hydrostatic stress than the cell model with equal imposed lateral stresses. Socrate and Boyce obtained, for the axisymmetric V-BCC cell model under triaxial loading ($T_\Sigma = 1.3$), a peak local hydrostatic stress $\tilde{T}_{kk}^{(as)}/3 \simeq 70$ MPa at macroscopic yield. The 3D V-BCC cell model predicts a significantly lower peak local hydrostatic stress, when compared to the axisymmetric V-BCC cell, for the same macroscopic loading conditions.

4.3 Implications for constitutive modeling

Several studies on the mechanical behavior of materials containing internal cavities have been carried out over the past few decades within the context of metal plasticity: McClintock (1968) studied the behavior of a cylindrical cavity in an infinite matrix, and found an exponential dependence of the void growth rate on bi-axial stress. Rice and Tracey (1969) considered a spherical void in an infinite matrix, and found a similar dependence of void growth rate on triaxial stress. Gurson (1977) proposed a constitutive model for a rigid, perfectly-plastic matrix containing spherical voids[5], which has been widely used in the field of porous metal plasticity. The Gurson model assumes (1) small void volume fractions, (2) rigid, perfectly-plastic matrix, and that (3) spherical voids remain spherical throughout the deformation. Tvergaard (1981) used micromechanical modeling to study the interaction between neighboring voids in a porous material, and proposed a modification to the original Gurson model. The mechanical behavior of particle-filled polymers is characterized by large elastic and plastic strains, large void volume fractions of the second phase (so that voids interact

[5]Gurson also developed a constitutive model for a matrix containing cylindrical voids. The most frequently used, though, is the model based on a periodic array of spherical voids.

strongly), non-spherical void growth, and evolving matrix anisotropy. These major differences suggest that mere fitting of the Gurson model to the study of voided polymeric materials is very problematic. Authors have modified the original Gurson model to eliminate some of the differences: high elastic yield strains have been accounted for by Steenbrink, et al. (1997), and the pressure dependence of yield has been accounted for by Lazzeri and Bucknall (1993). These modifications might make the Gurson model more suitable for the application to particle-filled polymers. However, there is no 'Gurson-like' model that fully accounts for *all* of the differences between the original Gurson model and the characteristics of particle-filled polymers. In order to develop a more fundamental understanding of the mechanics of deformation of particle-filled polymers, we presented a cell model which appears to give realistic predictions of the micromechanical and macromechanical behavior of rubber-filled polycarbonate. The results constitute a first, and important, step towards establishing a constitutive model for particle-filled polymers, and in particular, voided polycarbonate. The different load cases in this study allow for a preliminary macroscopic "yield locus" to be constructed. While we note that the rate-dependent material does not possess a yield locus, it is instructional to view a surface in order to demonstrate the strong hydrostatic stress dependence on plastic flow. Each macroscopic yield point (for $f_0 = 0.25$) is plotted in macroscopic hydrostatic-deviatoric stress space (Figure 17). We note that the norm of [deviatoric plus dilatational] macroscopic strain rate varies over the studied range of macroscopic stress triaxialities, but we expect that effects of deformation rate on flow strength will be small. For the case of hydrostatic tension, the applied macroscopic dilatational strain rate was $\dot{E}_{kk} = 0.03s^{-1}$. When this rate was decreased by a factor of 3, the macroscopic yield stress of the material decreased by less than 3%. Apart from the studied loading cases, the case of macroscopic hydrostatic tension ($T_\Sigma \to \infty$) and the cases of principal loading with $T_\Sigma = 2$ and $T_\Sigma = 5$, were also studied in order to obtain points for the yield locus at higher stress triaxialities. The yield locus shows a strong dependence on hydrostatic stress, where the deviatoric stress required to reach macroscopic yield of the blend decreases with increasing hydrostatic tension. Indeed, the blend will yield under the

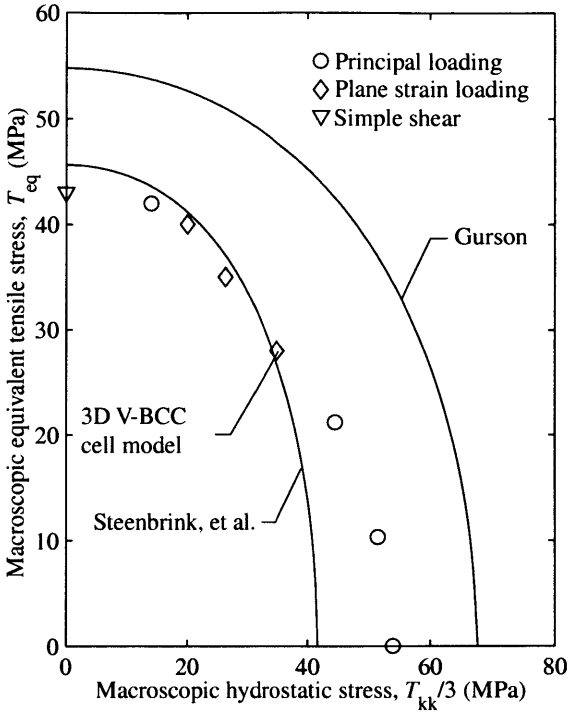

Figure 17: Different yield loci for voided polycarbonate having an initial void volume fraction $f_0 = 0.25$.

action of hydrostatic stress alone. This general shape of yield locus was also found by Gurson (1977) and by Steenbrink, et al. (1997). As one would expect, the Gurson model shows poor agreement with the cell model predictions, because of its inherent limitations. The model by Steenbrink, et al. shows considerable improvement over the Gurson model in predicting initial yield of the blend. However, under hydrostatic tension, the 3D V-BCC cell model predicts a higher yield stress than the model by Steenbrink, et al. (Figure 17). The yield loci for the models by Gurson and Steenbrink, et al. are briefly summarized in Appendix A. The improvement of the model by Steenbrink, et. al over that of Gurson is due to (1) the Tvergaard parameter q_1, which lowers the yield strength of the material, and (2) the fact that elasticity is accounted for through the parameter e (see Appendix A).

4.4 Anisotropy of the 3D V-BCC cell model

The 3D V-BCC cell is intrinsically anisotropic because of the cubic symmetry of the underlying BCC-arrangement of particles. The choice of coordinate directions should thus influence the predicted response of the voided material upon macroscopic loading. In the present study, the coordinates (which were taken as the principal loading directions) in Figure 1 were employed. Other coordinate directions could have been used to investigate the response of the voided material. This would have required additional finite element modeling, and has not been carried out in the present study.

4.5 Implications of a periodic cell model

Smit, et al. (1999) presented a two-dimensional plane-strain cell model based on a random distribution of cylindrical voids in a polycarbonate matrix. They argued that the post-yield softening predicted by one-particle simple cubic cell models is an artifact of the assumed periodicity of the structure. Deformation events in a periodic structure will be periodic; i.e., they will occur at the same position in however many cells comprise the body. Smit, et al. argued that it is only through the introduction of a spatially random distribution of second-phase particles that a model can capture the stable macroscopic blend behavior which results from the successive percolation of plastic flow through the matrix. From a computational standpoint, two-dimensional models of the spatially random structure are feasible. However, a detailed three-dimensional large-strain model of the voided elastic-plastic matrix material introduces considerable computational requirements, and solving such problems would prove a cumbersome task. While the two-dimensional multi-particle model captures the successive percolation of plastic flow through the matrix, it significantly over-predicts the evolution of volumetric strain of the blend due to its two-dimensional assumption vs. the three-dimensional reality. Two-dimensional models also cannot capture important trends in the constrained direction which may be important in understanding toughness. The present "one-particle" model captures the evolution

of volumetric strain well, and since the high levels of hydrostatic stress in the matrix ahead of notches and crack tips produce dilatation of the blend, a good model of the voided material should be able to predict this. Future work could address the further implications of the randomness of the particle distribution on the micromechanical and macromechanical behavior, through multi-particle models and/or multi-level modeling schemes.

5 Concluding Remarks

A three-dimensional cell model based on a BCC arrangement of particles was introduced. The cell model realistically predicts patterns of matrix deformation and the macroscopic response of rubber-filled polycarbonate (where the rubber phase is taken to be cavitated). It shows good agreement with the macroscopic behavior predicted by the two-dimensional axisymmetric V-BCC cell model introduced by Socrate and Boyce (2000). However, on a microscopic level, details of the deformation are resolved that cannot be captured using an axisymmetric cell model. The three-dimensional cell model also shows improvement over the two-dimensional cell model in that it allows for modes of deformation beyond that of axisymmetric modes, such as plane strain and simple shear deformation. The 3D V-BCC cell model is applicable not only to rubber-filled polycarbonate, but to other particulate materials with similar morphology, such as semi-crystalline polymer blends and metal matrix composites of high second-phase fractions.

Acknowledgments This work was supported by the MIT Center for Materials Science and Engineering, NSF MRSEC Grant No. DMR-98-08941. The authors wish to acknowledge stimulating and encouraging discussions with Prof. S. Socrate.

References

Arruda, E. M. and Boyce, M. C. (1993). Evolution of plastic anisotropy in amorphous polymers during finite straining. Int. J. Plasticity 9 (6), 697–720.

Bartczak, Z., Argon, A. S., Cohen, R. E., and Weinberg, M. (1999). Toughness mechanism in semi-crystalline polymer blends: I. high-density polyethylene toughened with rubbers. Polymer 40, 2331–2346.

Boyce, M. C., Parks, D. M., and Argon, A. S. (1988). Large inelastic deformation of glassy polymers. part 1: Rate dependent constitutive model. Mech. Mater. 7 (1), 15–33.

Dib, M. W. and Rodin, G. J. (1993). Three-dimensional analysis of creeping polycrystals using periodic arrays of truncated octahedra. J. Mech. Phys. Solids 41 (4), 725–747.

Gurson, A. L. (1977). Continuum theory of ductile rupture by void nucleation and growth: Part 1 - yield criteria and flow rules for porous ductile media. ASME Trans., J. Eng. Mater. Technol. 99 Ser. H 1, 2–15.

Hom, C. L. (1992). Three-dimensional finite element analysis of plastic deformation in a whisker-reinforced metal matrix composite. J. Mech. Phys. Solids. 40 (5), 991–1008.

Ishikawa, N., Parks, D. M., Socrate, S., and Kurihara, M. (2000). Micromechanical modeling of ferrite-pearlite steels using finite element unit cell models. ISIJ Int. 40 (11), 1170–1179.

Koplik, J. and Needleman, A. (1988). Void growth and coalescence in porous plastic solids. Int. J. Solids Struct. 24 (8), 835–853.

Lazzeri, A. and Bucknall, C. B. (1993). Dilatational bands in rubber-toughened polymers. J. Mater. Sci. 28 (24), 6799–6808.

McClintock, F. A. (1968). A criterion for ductile fracture by the growth of holes. J. Appl. Mech. 35, 363–371.

Nimmer, R. P. and Woods, J. T. (1992). An investigation of brittle failure in ductile notch-sensitive thermoplastics. Polym. Eng. Sci. 32 (16), 1126–1137.

Rice, J. R. and Tracey, D. M. (1969). On the ductile enlargement of voids in triaxial stress fields. J. Mech. Phys. Solids 17, 201–217.

Smit, R. J. M., Brekelmans, W. A. M., and Meijer, H. E. H. (1999). Prediction of the large-strain mechanical response of heterogeneous polymer systems: local and global deformation behaviour of a representative volume element of voided polycarbonate. J. Mech. Phys. Solids 47 (2), 201–221.

Socrate, S. and Boyce, M. C. (2000). Micromechanics of toughened polycarbonate. J. Mech. Phys. Solids 48 (2), 233–273.

Socrate, S., Boyce, M. C., Kear, K., and Shaw, K. (2001). Micromechanics and macromechanics of thermoplastic vulcanizates during uniaxial compression, submitted. Polymer.

Steenbrink, A. C., van der Giessen, E., and Wu, P. D. (1997). Void growth in glassy polymers. J. Mech. Phys. Solids 45 (3), 405–437.

Tvergaard, V. (1981). Influence of voids on shear band instabilities under plane strain conditions. Int. J. Fracture 17 (4), 389–407.

Tvergaard, V. (1982). On localization in ductile materials containing spherical voids. Int. J. Fracture 18 (4), 237–252.

Tzika, P. A., Boyce, M. C., and Parks, D. M. (2000). Micromechanics of deformation in particle-toughened polyamides. J. Mech. Phys. Solids 48 (9), 1893–1929.

van der Sanden, M. C. M., de Kok, J. M. M., and Meijer, H. E. H. (1994). Deformation and toughness of polymeric systems: 7. influence of dispersed rubbery phase. Polymer 35 (14), 2995–3004.

Wigner, E. and Seitz, F. (1933). On the constitution of metallic sodium. Phys. Rev. 43, 804–810.

Yee, A. (1977). The yield and deformation behaviour of some polycarbonate blends. J. Mater. Sci. 12, 757–765.

A Yield loci of existing constitutive models

Gurson (1977) proposed a constitutive model for a rigid, perfectly plastic matrix containing low fractions of either spherical or cylindrical voids. The yield locus for the model with spherical voids is given by

$$\Phi_G = \left(\frac{T_{eq}}{T_Y}\right)^2 + 2f\cosh\left(\frac{T_{kk}}{2T_Y}\right) - (1+f^2) = 0, \tag{A. 1}$$

where T_Y is the yield strength of the matrix material and f is the void volume fraction. The locus is bounded in the direction of hydrostatic stress by the second term in (A. 1). If the void volume fraction, f, is set to zero, this term vanishes, and the pressure-independent Mises yield locus is retained.

The modification of the Gurson model to account for large elastic strains associated with the deformation of polymeric materials (Steenbrink, et al. (1997)) gave rise to the (initial) yield locus

$$\Phi_S = \left(\frac{T_{eq}}{T_Y}\right)^2 + 2q_1 f\cosh\left(e\ln\left(1+\frac{1}{e}\frac{T_{kk}}{2T_Y}\right)\right) - (1+(q_1 f)^2) = 0, \tag{A. 2}$$

where T_{eq} is the equivalent tensile (Mises) stress and f is the void volume fraction. The parameter q_1 was originally introduced by Tvergaard (1981). Tvergaard compared predictions of the Gurson model to results of finite element analyses, and suggested $q_1 = 1.5$, which is also used in this study. The term e in A. 2, which accounts for the elasticity, is defined as

$$e = \ln\left(\frac{T_Y}{\sqrt{3}E^*}\right) \tag{A. 3}$$

where E^* is the effective Young's modulus of the blend, based on a self-consistent estimate (see Steenbrink, et al. (1997)):

$$E^* = \frac{2E(7-5\nu)(1-f)}{2(7-5\nu)+(1+\nu)(13-15\nu)f}. \tag{A. 4}$$

Using this estimate together with the Young's modulus $E = 2.3$ GPa and the Pois-

son's ratio $\nu = 0.33$ of the homopolymer, the effective (initial) Young's modulus is calculated as $E^* = 1.38$ GPa, which agrees well with the value 1.35 GPa given by the slope of the stress-strain curve for uniaxial tension with $f_0 = 0.25$ (Figure 6a). For $q_1 = 1$ and when elasticity is neglected, $E^* \to \infty$, the original Gurson model (A. 1) is recovered.

In the present application of (A. 1) and (A. 2) to voided polycarbonate ($f_0 = 0.25$), the yield strength, T_Y, is taken to be the stress at initial yield of the homopolymer subjected to uniaxial tension at a macroscopic strain rate $\dot{E}_{33} = 0.01 s^{-1}$ (Figure 6a).

Appendix B

Paper II

Article accepted for publication in Mech. Mater., M. Danielsson, D.M. Parks and M.C. Boyce, "Constitutive modeling of porous hyperelastic materials", 2003.

CONSTITUTIVE MODELING OF POROUS HYPERELASTIC MATERIALS

M. Danielsson, D.M. Parks[1] and M.C. Boyce

Department of Mechanical Engineering,
Center for Materials Science and Engineering,
Massachusetts Institute of Technology,
Cambridge, MA 02139, USA,
November 2002.

Abstract

A micromechanics framework for the development of continuum-level constitutive models for the large-strain deformation of porous hyperelastic materials is presented. A kinematically admissible deformation field is assumed which enables the derivation of a strain energy density function for the porous material. The strain energy density function depends on the properties of the incompressible hyperelastic matrix material, the initial level of porosity, and the macroscopic deformation. Differentiation of the strain energy density function, with respect to deformation, provides an expression for the stress-strain behavior of the porous hyperelastic material. Example calculations are carried out for porous hyperelastic materials with a Neo-Hookean matrix. The constitutive model is used to predict the stress-strain behavior of the pore-containing matrix as a function of initial porosity and macroscopic loading conditions. Predictions of the dependence of the small-strain elastic response on porosity are compared to various estimates of effective elastic moduli for porous materials found in the literature. Constitutive model predictions of the small to large-strain deformation behavior compare well with results from numerical three-dimensional micromechanical multi-void cell models.

Keywords: Constitutive modeling, Hyperelasticity, Porous material, Elastomer.

[1]Corresponding author. E-mail: dmparks@mit.edu, Telephone: +1 617 253 0033, Facsimile: +1 617 258 8742.

1 Introduction

Although the mechanics of low-density elastomeric foams has been widely investigated (e.g., Gibson and Ashby (1997)), the effects of low levels of porosity on the mechanical behavior of elastomeric materials is a subject that has been poorly covered in the literature. Low levels of porosity in elastomers may arise due to defects, from processing, or may have been deliberately introduced as part of the manufacturing process to create high-density foams. It is well-recognized that the introduction of even low levels of porosity alters the mechanical properties of the material, when compared to the homogeneous elastomer. When porosity is introduced, the elastic moduli of the material change: the shear and bulk moduli decrease, the latter markedly, and the common assumption of incompressibility breaks down. There is considerable qualitative understanding of these effects of porosity on the mechanical behavior of porous elastomers, but a quantitative understanding is largely lacking; very little information and very few models exist in the literature. Many models of porous elastomeric materials have been geared toward practical engineering situations, such as vibration dampers. The models typically try to predict the effective compression and shear moduli of rubber blocks between metal platens (see Kasner and Meinecke (1996) for a review of these models). These models are hence very specific, and can only be applied to a limited number of loading situations. Attempts have been made, with a continuum mechanics approach, to model the constitutive behavior of porous elastomers (see, for example, Blatz and Ko (1962), Kakavas (2002)). These models are more general than the "engineering-type" models, since they model the material behavior rather than the structural component behavior. They can therefore be implemented directly into finite element software packages where they can be used to simulate arbitrary component geometries under various loading conditions. However, the models often require empirical fitting of material parameters, which limits their usefulness (see, for example, Blatz and Ko (1962)).

In this work, we develop a general micromechanics framework for the development of constitutive models of the large-strain deformation of porous elastomeric materi-

als. The framework is applicable to any type of isotropic hyperelastic matrix material which obeys pointwise incompressibility, such as the Neo-Hookean, Mooney-Rivlin, Ogden, and eight-chain models for rubber elasticity (see Boyce and Arruda (2000) for a review). A strain energy density function for the porous material is derived from an assumed kinematically admissible deformation field in a model of the pore-containing matrix. The strain energy density function enables the calculation of a stress-strain relationship for the porous elastomer, using virtual work. As an example, a constitutive model is analytically developed for a porous Neo-Hookean material. The stress is observed to depend on the material properties of the elastomer matrix, the initial void volume fraction (porosity), and the applied state of strain. Constitutive model predictions compare well with those obtained from a numerical three-dimensional micromechanical cell model for a range of initial void volume fractions and tensile load cases. We discuss the applicability of the model to compressive loading situations, such as uniaxial compression.

2 The representative volume element

In order to study the deformation of a porous hyperelastic solid, we take a thick-walled sphere to represent the undeformed porous material. This type of spherical volume element has been used frequently in the literature to represent a porous solid subjected to external pressure (see for example Gurson (1977), Haghi and Anand (1991), Kakavas (2002)). Under radial external traction, the spherically-symmetric deformation field in an incompressible hollow sphere is known, and the stress state in the sphere can be evaluated exactly. The spherical volume element is used in this work as well, but a more general state of deformation is allowed. The sphere is subjected to a macroscopic state of deformation given by three principal (generally un-equal) macroscopic stretches, $\{\overline{\lambda}_1, \overline{\lambda}_2, \overline{\lambda}_3\}$. This principal macroscopic stretch state corresponds to a macroscopic deformation gradient, $\overline{\mathbf{F}}$, whose Cartesian components

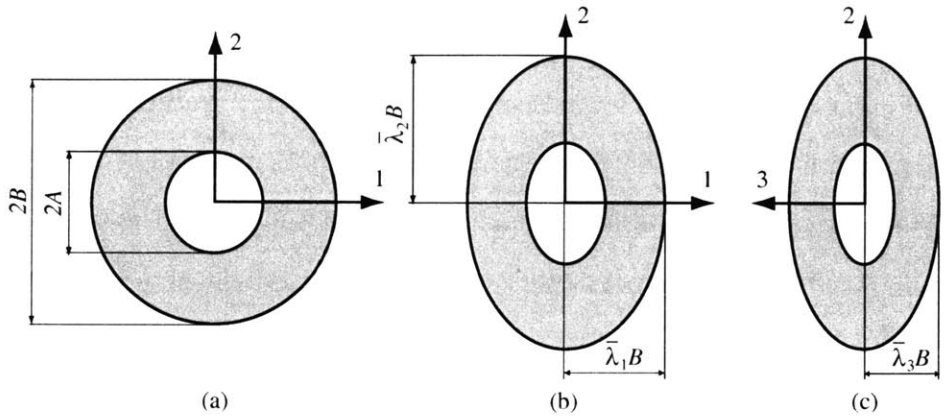

Figure 1: The spherical volume element: (a) undeformed configuration, (b-c) deformed configuration.

are given by

$$[\overline{\mathbf{F}}]_{ij} = \overline{\lambda}_i \delta_{ij} \quad \text{(no sum on } i\text{)}, \tag{1}$$

where δ_{ij} is the Kronecker delta. The initial material, whose matrix is taken to be pointwise incompressible, is characterized by an initial void volume fraction f_0, given by $f_0 = (A/B)^3$ (Fig. 1a), where A and B are, respectively, the inner and outer radii of the sphere. When subjected to the principal macroscopic stretch state, the outer surface of the sphere transforms into an ellipsoid with its three principal axes given by these stretches (Fig. 1b-c).

2.1 Deformation fields

The displacement field for a purely hydrostatic expansion of a sphere is known; every material point in the sphere moves radially because of the spherical symmetry. When the surface of the sphere transforms into an ellipsoid, material point displacements will, in general, not be only radial. However, finding an exact solution of the displacement of every point in the deformed sphere is very difficult. In a study of cavitation in hyperelastic solids, Hou and Abeyaratne (1992) proposed a set of kinematically

admissible *radial* deformation fields for the growth of a cavity in a solid, of the form

$$x_i = \psi_i \, X_i = \hat{\psi}_i(R) \, X_i \quad \text{(no sum on } i\text{)}, \tag{2}$$

where $x_i = \mathbf{x}\cdot\mathbf{e}_i$ is the ith Cartesian component of the deformed position $\mathbf{x}$, $X_i = \mathbf{X}\cdot\mathbf{e}_i$ is the ith Cartesian component of the reference position $\mathbf{X}$, and $R = \sqrt{\mathbf{X}\cdot\mathbf{X}}$ is the radial distance from the origin in the reference configuration. The components X_i are given in a spherical coordinate system by

$$X_1 = R\sin\Theta\sin\Phi, \tag{3}$$

$$X_2 = R\sin\Theta\cos\Phi, \tag{4}$$

$$X_3 = R\cos\Theta, \tag{5}$$

where $0 \leq \Theta \leq \pi$ and $0 \leq \Phi \leq 2\pi$ are standard spherical angles, measured in the reference configuration. Cartesian components of the local deformation gradient are then given by

$$[\mathbf{F}]_{ij} = \frac{\partial x_i}{\partial X_j} = \psi_i' \frac{X_i X_j}{R} + \psi_i \, \delta_{ij} \quad \text{(no sum on } i\text{)}, \tag{6}$$

where $(\dots)'$ denotes differentiation with respect to R. The deformation is said to be locally isochoric (volume-preserving) if

$$J \equiv \det \mathbf{F} = \lambda_1\lambda_2\lambda_3 = 1, \tag{7}$$

where $\{\lambda_1, \lambda_2, \lambda_3\}$ are principal stretches. The principal stretches are the eigenvalues of the stretch tensors $\mathbf{V}$ and $\mathbf{U}$, which can be obtained through a polar decomposition of $\mathbf{F}$,

$$\mathbf{F} = \mathbf{V}\,\mathbf{R} = \mathbf{R}\,\mathbf{U}, \tag{8}$$

where $\mathbf{R}$ is a proper orthogonal tensor. By combining Eqs. (6) and (7), a system of differential equations is obtained (Hou and Abeyaratne (1992)):

$$\begin{aligned} \psi_1\,\psi_2\,\psi_3 + R\,\psi_1\,\psi_2\,\psi_3' &= 1, \\ \psi_1'\,\psi_3 - \psi_1\,\psi_3' &= 0, \\ \psi_2'\,\psi_3 - \psi_2\,\psi_3' &= 0. \end{aligned} \tag{9}$$

The solution of these differential equations renders three unknown integration constants. These constants can be determined from boundary conditions. When the sphere is subjected to a macroscopic state of deformation[2], given by three principal stretches, $\{\overline{\lambda}_1, \overline{\lambda}_2, \overline{\lambda}_3\}$, the following boundary conditions are identified (Fig. 1b-c),

$$\overline{\lambda}_i = \hat{\psi}_i(B). \tag{10}$$

The solution of the system of differential equations (Eq. 9), together with the boundary conditions (Eq. 10) is given by

$$x_i = \frac{\overline{\lambda}_i}{\overline{J}^{1/3}} \left(1 + \frac{B^3\,(\overline{J}-1)}{R^3}\right)^{1/3} X_i \quad \text{(no sum on } i\text{)}, \tag{11}$$

where $\overline{J} \equiv \det \overline{\mathbf{F}} = \overline{\lambda}_1\overline{\lambda}_2\overline{\lambda}_3$. By using Eqs. (6) and (11), the components of the deformation gradient, $\mathbf{F}$, at every point in the matrix, can then be expressed as

$$[\mathbf{F}]_{ij} = \frac{\overline{\lambda}_i}{\overline{J}^{2/3}} \left(\frac{1-\psi^3}{\psi^2\,R^2} X_i X_j + \psi \delta_{ij}\right) \quad \text{(no sum on } i\text{)}, \tag{12}$$

where $\psi = \hat{\psi}(R) = \left(1 + (\overline{J}-1)\,(B/R)^3\right)^{1/3}$. The expression for the deformation gradient at every material point in the matrix (Eq. 12) can be used to calculate any measure of strain for use in constitutive model development, including expressions for the stretch invariants and the principal stretches.

[2] *Notation*: Throughout, macroscopic (cell-average) quantities will be distinguished from local quantities by a bar, e.g. $\overline{\lambda}_i$ and $\overline{J}$ denote "macroscopic principal stretch in the ith principal direction" and "macroscopic volume change", etc.

The stretch invariants I_1 and I_2 are defined as

$$I_1 \equiv \operatorname{tr} \mathbf{B} = \lambda_1^2 + \lambda_2^2 + \lambda_3^2, \tag{13}$$

$$I_2 \equiv \frac{1}{2}\left(I_1^2 - \operatorname{tr}(\mathbf{B}^2)\right) = \lambda_1^2\lambda_2^2 + \lambda_2^2\lambda_3^2 + \lambda_3^2\lambda_1^2, \tag{14}$$

where $\mathbf{B} \equiv \mathbf{F}\,\mathbf{F}^T = \mathbf{V}^2$ is the left Cauchy-Green strain tensor. Using Eqs. (6) and (11), the first and second invariants of stretch can be expressed at every point, $\mathbf{X}$, in the reference sphere, by

$$I_1 = \frac{1}{\overline{J}^{2/3}}\left\{\overline{I}_1\,\psi^2 + \frac{1}{R^2}\left(\overline{\lambda}_1^2 X_1^2 + \overline{\lambda}_2^2 X_2^2 + \overline{\lambda}_3^2 X_3^2\right)\left(\frac{1}{\psi^4} - \psi^2\right)\right\}, \tag{15}$$

$$I_2 = \overline{J}^{2/3}\left\{\frac{\overline{I}_2}{\overline{J}^2\psi^2} + \frac{1}{R^2}\left(\frac{X_1^2}{\overline{\lambda}_1^2} + \frac{X_2^2}{\overline{\lambda}_2^2} + \frac{X_3^2}{\overline{\lambda}_3^2}\right)\left(\psi^4 - \frac{1}{\psi^2}\right)\right\}, \tag{16}$$

where $\overline{I}_1 \equiv \operatorname{tr}\overline{\mathbf{B}} = \overline{\lambda}_1^2 + \overline{\lambda}_2^2 + \overline{\lambda}_3^2$ is the first invariant of macroscopic stretch, $\overline{I}_2 \equiv \frac{1}{2}\left(\overline{I}_1^2 - \operatorname{tr}(\overline{\mathbf{B}}^2)\right) = \overline{\lambda}_1^2\overline{\lambda}_2^2 + \overline{\lambda}_2^2\overline{\lambda}_3^2 + \overline{\lambda}_3^2\overline{\lambda}_1^2$ is the second invariant of macroscopic stretch, and $\overline{\mathbf{B}} \equiv \overline{\mathbf{F}}\,\overline{\mathbf{F}}^T$ is the macroscopic left Cauchy-Green strain tensor.

The principal stretches, λ_i, can be determined as the square-roots of the eigenvalues of $\mathbf{B}$. The principal stretches, λ_i, are then expressed as functions of position in the reference sphere, $\mathbf{X}$, and the macroscopically-applied deformation. Any other strain measure may be similarly obtained at every point in the matrix for use in the development of the constitutive model for the porous material if the matrix constitutive model is formulated in terms of that particular strain measure. We present the general framework next for the case where the matrix strain energy density is expressed in terms of the stretch invariants.

3 Constitutive models for porous hyperelastic materials

In the previous section, a class of deformation fields was adopted to describe the locally isochoric motion of every material point as the sphere undergoes a macroscopic state of stretch given by $\{\overline{\lambda}_1, \overline{\lambda}_2, \overline{\lambda}_3\}$. In this section, we describe how to obtain the macroscopic state of stress corresponding to the macroscopically-applied stretches. The methodology outlined below can be applied to any incompressible isotropic matrix material, such as the stretch-invariant based Neo-Hookean, Mooney-Rivlin and eight-chain material models, and the principal-stretch based Ogden material model. As an example, we study a specific material model for the sphere, the Neo-Hookean material model. Using this matrix material model, we obtain an explicit expression for the stress as a function of macroscopic deformation, matrix material properties and initial level of porosity.

3.1 General case

The pointwise strain energy density function for an incompressible isotropic hyperelastic material can be expressed in terms of the stretch invariants I_1 and I_2 as

$$W = \hat{W}(I_1\,,\, I_2\,;\, \mathcal{P}), \tag{17}$$

or, alternatively, in terms of the principal stretches, as

$$W = \hat{W}(\lambda_1\,,\lambda_2\,,\, \lambda_3\,;\, \mathcal{P}), \tag{18}$$

where, in either case, $\mathcal{P}$ represents a general list of scalar material properties, and in Eq. (18), and subsequently, the three principal stretches are subject to the incompressibility constraint given by Eq. (7).

In the case of a stretch-invariant based matrix material model, Eqs. (17), (15)

and (16) can be combined to determine the strain energy density, W, at every point in the sphere. The homogenized strain energy density of the sphere, $\overline{W}$, is obtained by integrating the pointwise strain energy density function, W, over the reference volume, and dividing by the reference volume,

$$\overline{W} = \frac{1}{V_0} \int_{Bf_0^{1/3}}^{B} \int_0^{2\pi} \int_0^{\pi} \hat{W}(I_1, I_2; \mathcal{P})\, R^2 \sin\Theta \, \mathrm{d}\Theta \, \mathrm{d}\Phi \, \mathrm{d}R, \tag{19}$$

where the reference volume is given by $V_0 = 4\pi B^3/3$, and I_1 and I_2 are given by Eqs. (15) and (16), respectively. The macroscopic Cauchy stress, $\overline{\mathbf{T}}$, corresponding to the applied macroscopic deformation can be readily obtained (see, for example, Malvern (1969)) by evaluating:

$$\overline{\mathbf{T}} = \frac{2}{\overline{J}} \frac{\partial \overline{W}}{\partial \overline{\mathbf{B}}} \overline{\mathbf{B}} = \frac{2}{\overline{J}} \frac{\partial \overline{W}}{\partial \overline{I}_1} \overline{\mathbf{B}} + \frac{2}{\overline{J}} \frac{\partial \overline{W}}{\partial \overline{I}_2} \left(\overline{I}_1 \overline{\mathbf{B}} - \overline{\mathbf{B}}^2 \right) + \frac{\partial \overline{W}}{\partial \overline{J}} \mathbf{1}, \tag{20}$$

where $\mathbf{1}$ is the second-order identity tensor.

3.2 Example case: Neo-Hookean matrix material

The strain energy density for a Neo-Hookean material is a linear function of the first invariant of stretch,

$$W_{NH} = \frac{\mu}{2} (I_1 - 3), \tag{21}$$

where μ is the infinitesimal shear modulus. Upon integrating the pointwise strain energy density function given by Eq. (21) over the reference volume according to Eq. (19), the strain energy density, $\overline{W}_{NH}$, of the hollow Neo-Hookean sphere subjected to a macroscopic state of stretch can be evaluated as

$$\overline{W}_{NH} = \frac{\mu}{2} \left\{ \overline{I}_1 \left(2 - \frac{1}{\overline{J}} - \frac{f_0 + 2(\overline{J} - 1)}{\overline{J}^{2/3} \eta^{1/3}} \right) - 3(1 - f_0) \right\}, \tag{22}$$

where $\eta \equiv \left(1 + (\overline{J} - 1)/f_0\right)$. The explicit occurrences of $\overline{\lambda}_i$ found in Eq. (15) vanish, and the strain energy density $\overline{W}_{NH}$ becomes a function only of the matrix properties (here μ), the initial void volume fraction, f_0, and the macroscopic stretch invariants $\overline{J}$ and $\overline{I}_1$. The macroscopic Cauchy stress tensor, $\overline{\mathbf{T}}$, can then be readily obtained by evaluating

$$\overline{\mathbf{T}} = \frac{2}{\overline{J}} \frac{\partial \overline{W}_{NH}}{\partial \overline{I}_1} \overline{\mathbf{B}} + \frac{\partial \overline{W}_{NH}}{\partial \overline{J}} \mathbf{1}. \tag{23}$$

The derivatives of the strain energy density in Eq. (23) are given by

$$\frac{\partial \overline{W}_{NH}}{\partial \overline{I}_1} = \frac{\mu}{2} \left\{ 2 - \frac{1}{\overline{J}} - \frac{f_0 + 2\,(\overline{J} - 1)}{\overline{J}^{2/3} \eta^{1/3}} \right\}, \tag{24}$$

$$\frac{\partial \overline{W}_{NH}}{\partial \overline{J}} = \frac{\mu}{2} \overline{I}_1 \left\{ \frac{1}{\overline{J}^2} - \frac{1}{3\,\overline{J}^{2/3} \eta^{1/3}} \left(\frac{(4 - f_0)\eta + (1 - f_0)}{f_0 \eta^2 + (1 - f_0)\eta} \right) \right\}. \tag{25}$$

Upon combining Eqs. (23), (24) and (25), the macroscopic Cauchy stress tensor, $\overline{\mathbf{T}}$, is given by

$$\begin{aligned} \overline{\mathbf{T}} = \frac{\mu}{2} \left(\frac{4}{\overline{J}} - \frac{2}{\overline{J}^2} - 2\,\frac{f_0 + 2\,(\overline{J} - 1)}{\overline{J}^{5/3} \eta^{1/3}} \right) \overline{\mathbf{B}} + \\ \frac{\mu}{2} \overline{I}_1 \left(\frac{1}{\overline{J}^2} - \frac{1}{3\,\overline{J}^{2/3} \eta^{1/3}} \left(\frac{(4 - f_0)\eta + (1 - f_0)}{f_0 \eta^2 + (1 - f_0)\eta} \right) \right) \mathbf{1}. \end{aligned} \tag{26}$$

For the case of a purely deviatoric state of macroscopic deformation, $\overline{J} = 1$, Eq. (26) reduces to

$$\mathrm{dev}(\overline{\mathbf{T}}) = \mu\,(1 - f_0)\mathrm{dev}(\overline{\mathbf{B}}), \tag{27}$$

where $\mathrm{dev}(\dots)$ denotes the deviatoric part of the argument. In the limit of zero porosity, $f_0 = 0$, the deviatoric Cauchy stress becomes $\mathrm{dev}(\overline{\mathbf{T}}) = \mu\,\mathrm{dev}(\overline{\mathbf{B}})$. The total Cauchy stress in an incompressible elastic material can be determined only to within an arbitrary (workless) hydrostatic stress, $-\overline{p}\mathbf{1}$. In the limit of zero porosity, the total Cauchy stress is therefore given by the well-known constitutive equation for a

Neo-Hookean material,

$$\overline{\mathbf{T}} = \mu\,\mathrm{dev}(\overline{\mathbf{B}}) - \bar{p}\mathbf{1}. \tag{28}$$

4 Results using a Neo-Hookean matrix material

In this section, the proposed constitutive model (Eq. 26) is used to study the porous elastomer stress-strain response under different types of loading conditions, and the dependence of this behavior on the level of porosity. First, constitutive model predictions of the infinitesimal shear and bulk moduli, as functions of porosity, are compared to the estimates of Budiansky, Hill and Mori-Tanaka. The large-strain behavior of the porous elastomer is then studied under hydrostatic tension and under plane strain tension. Constitutive model predictions of the large-strain behavior are compared to results from a numerical three-dimensional micromechanical multi-void cell model. The multi-void cell model is shown in Fig. (2). It consists of an assembly of cubes that are either fully dense or contain a void. The number of voids, and the void size relative to the cube that contains it, determine the macroscopic initial void volume fraction f_0. Periodic boundary conditions are applied to the surfaces of the cell model. The deformation of the cell model can then be solved numerically as a boundary value problem, and the macroscopic stress-strain response can be extracted. For details on the cell model, boundary conditions and the calculation of the macroscopic stress-strain response, see Danielsson (2003) and Danielsson et al. (2003a).

4.1 Infinitesimal elastic moduli

The constitutive model (Eq. 26) provides a stress-strain relationship for a porous hyperelastic material in the context of large-strain kinematics. The voids are assumed to be initially spherical, rendering the porous material initially isotropic. In the limit of small strains, the elastic response can therefore be characterized by two infinitesimal elastic moduli. From an engineering standpoint, it is instructive to determine these elastic moduli, and compare them to estimates of elastic moduli for porous materials

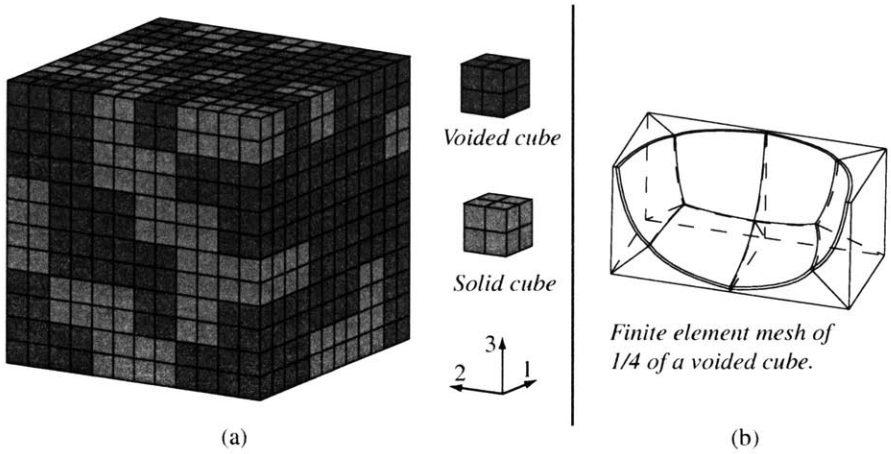

Figure 2: The micromechanical cell model: (a) the whole model, (b) a quarter of a void-containing cube.

reported in the literature.

The self-consistent estimates by Budiansky (1965) and Hill (1965), for an incompressible matrix material containing a volume fraction, f_0, of spherical voids, are given by

$$\overline{\mu}_{BH} = \mu \frac{3\,(1-2f_0)}{3-f_0}, \tag{29}$$

$$\overline{\kappa}_{BH} = \mu \frac{4\,(1-2f_0)(1-f_0)}{(3-f_0)f_0}, \tag{30}$$

where $\overline{\mu}_{BH}$ and $\overline{\kappa}_{BH}$ are the effective shear and bulk moduli, respectively. The Budiansky-Hill estimates predict both moduli to decrease with an increase in f_0, with the bulk modulus exhibiting a precipitous drop upon the introduction of voids (Fig. 3). However, in the self-consistent scheme, the elastic moduli approach zero as f_0 approaches $1/2$, and the stiffness of the material is lost. This limits the range of porosities that can be studied using the self-consistent scheme by Budiansky and Hill.

The work of Mori and Tanaka (1973) concerned the calculation of the average internal stress in the matrix of a material containing misfitting inclusions. The Mori-Tanaka theory has been applied to the calculation of the effective elastic properties of composites (Benveniste (1987)). Using the Mori-Tanaka approach, the elastic moduli

for the case of spherical voids in an incompressible matrix are given by

$$\overline{\mu}_{MT} = \mu \frac{1 - f_0}{1 + \frac{2}{3} f_0}, \tag{31}$$

$$\overline{\kappa}_{MT} = \mu \frac{4}{3} (\frac{1}{f_0} - 1), \tag{32}$$

where $\overline{\mu}_{MT}$ and $\overline{\kappa}_{MT}$ are the effective shear and bulk moduli, respectively. Fig. (3) shows that the Mori-Tanaka estimates predict monotonically decreasing bulk and shear moduli, with increasing initial level of porosity. The Mori-Tanaka theory covers the full range of porosities, as the predicted moduli approach zero only when f_0 approaches zero.

The infinitesimal shear and bulk moduli as predicted by the constitutive model are denoted $\overline{\mu}$ and $\overline{\kappa}$, respectively. They are obtained by differentiation of stress (Eq. 23) with respect to strain, evaluated in the small strain limit. The infinitesimal macroscopic shear modulus can be calculated, for example, as

$$\overline{\mu} = \left. \frac{\mathrm{d}(\overline{T}_{12})}{\mathrm{d}(\overline{B}_{12})} \right|_{\substack{\overline{J}=1 \\ \overline{I}_1=3}} = \mu\,(1 - f_0), \tag{33}$$

and the infinitesimal bulk modulus can be calculated as

$$\overline{\kappa} = \left. \frac{\mathrm{d}(\mathrm{tr}\,\overline{\mathbf{T}})}{\mathrm{d}(\ln \overline{J})} \right|_{\substack{\overline{J}=1 \\ \overline{I}_1=3}} = \frac{4}{3} \mu\,(\frac{1}{f_0} - 1). \tag{34}$$

The constitutive model predicts the monotonic decrease in shear and bulk moduli with an increase in f_0, and also shows the precipitous drop in bulk modulus upon the introduction of voids. The infinitesimal bulk modulus, $\overline{\kappa}$, approaches infinity as the initial void volume fraction approaches zero, thus recovering the incompressibility of the matrix material. The expression for the infinitesimal shear modulus, $\overline{\mu}$, shows that for zero void content, the matrix shear stiffness is recovered. As the void volume fraction approaches one, the infinitesimal bulk and shear moduli approach zero, and the stiffness of the porous elastomer is lost. Eq. (15) shows that under a macroscopic pure deviatoric state of deformation, where $\overline{J} = 1$, the pointwise first invariant of

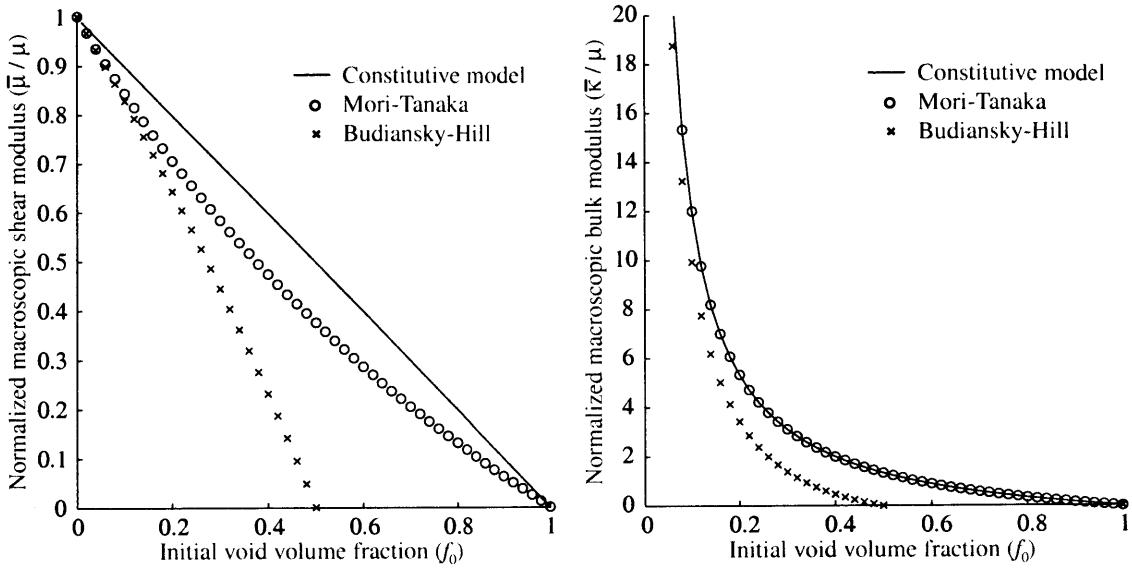

Figure 3: Infinitesimal elastic moduli: (a) shear modulus, (b) bulk modulus

stretch becomes independent of position in the sphere, and equal to the macroscopic first invariant of stretch; i.e., $I_1 = \overline{I}_1$. This state of constant strain in the matrix results in an upper bound on the infinitesimal shear modulus, and Eq. (33) is indeed equal to the Voigt upper bound, $\overline{\mu}_V = \mu(1 - f_0)$. The infinitesimal bulk modulus predicted by the constitutive model, $\overline{\kappa}$, is identical to the Mori-Tanaka bulk modulus, $\overline{\kappa}_{MT}$. The explanation for this is that the latter was obtained by solving the problem of a particle, surrounded by a matrix shell, embedded in an effective medium under external pressure. In the limit of zero particle stiffness and an incompressible matrix material, this reduces to the cell model in the present study, subjected to an external pressure (Fig. 1).

4.2 Large-strain volumetric expansion

The constitutive model is used to study the large-strain macroscopic volumetric expansion for materials with initial void volume fractions $f_0 = \{0.05, 0.15, 0.25\}$. The results are compared to results from the numerical micromechanical cell model. The response of the two models is characterized by plotting the normalized negative pres-

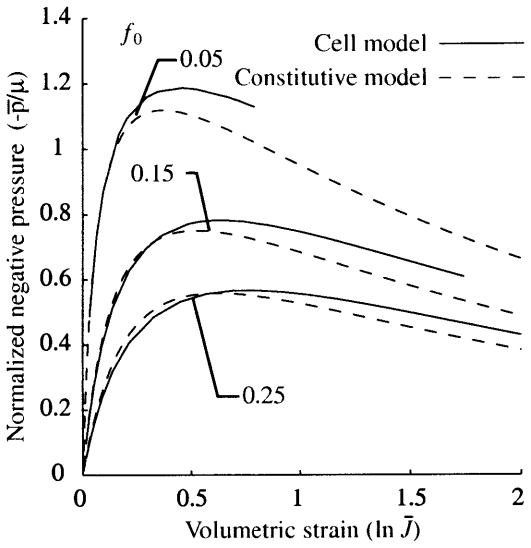

Figure 4: Hydrostatic tension. (- -) Constitutive model predictions, (-) RVE predictions.

sure, $-\overline{p}/\mu = \operatorname{tr}\overline{\mathbf{T}}/3\mu$, versus logarithmic volumetric strain, $\ln\overline{J}$, (Fig. 4). The constitutive model is deformed up to a volumetric strain $\overline{J} = 2$, but excessive finite element distortions in the cell models at high levels of volumetric strain prevent the analyses of $f_0 = 0.05$ and $f_0 = 0.15$ from reaching $\overline{J} = 2$. At these levels of volumetric strain, the finite element analyses would require re-meshing, and this is not addressed in the present work. Fig. (4) shows the nonlinear relationship between negative pressure and volumetric strain predicted by the constitutive model. The initial slopes of the curves in Fig. (4) correspond to the infinitesimal bulk moduli of the porous material at the different levels of porosity. An analytical expression for the infinitesimal bulk modulus, $\overline{\kappa}$, as a function of void volume fraction and matrix shear modulus was determined (Eq. 34), and this agrees with the initial slopes in Fig. (4), as expected. As the deformation progresses, the predicted tangent bulk modulus of the constitutive model decreases with increasing volumetric strain, and the negative pressure reaches a limit point beyond which it decreases with increasing volumetric strain. A parallel can be drawn to the instability associated with the inflation of a balloon[3]. The same

[3]This behavior depends on the constitutive behavior of the matrix material. As the porous material expands hydrostatically, the most highly deformed matrix material (on the pore surface)

basic features in the negative-pressure/volumetric-strain curves are observed for all studied levels of initial porosity, f_0. Fig. (4) shows that the predictions of the constitutive model are in very good agreement with the predictions of the cell model, over the studied range of porosities, for volumetric strains up to $\overline{J} = 0.3$. Beyond this strain, the predictions of the constitutive model and the cell model begin to deviate, but basic features of deformation are retained, and the agreement is reasonable.

4.3 Plane strain tension

The constitutive model (Eq. 26) accounts for the anisotropic growth of voids with macroscopic deformation. In the previous case of volumetric expansion, where the voids grow spherically, this feature of the constitutive model is not apparent. In order to elucidate this feature, we study the case of macroscopic plane strain tension, and compare predictions of the constitutive model to cell model predictions. Plane strain deformation is kinematically enforced by driving the deformation in one direction (the axial direction; $\overline{\lambda}_A$), and prescribing the strain in one of the lateral directions to be identically zero (the constraint direction; $\overline{\lambda}_C = 1$). The remaining lateral direction (the free direction; $\overline{\lambda}_L$) is left unprescribed. Fig. (5a) shows the true-stress/true-strain response of the constitutive model and of the cell model for the three different initial void volume fractions, $f_0 = \{0.05, 0.15, 0.25\}$. The plane strain constraint results in a tensile stress in the constraint direction, in addition to the stress in the axial direction (Fig. 5a). The stress in the axial and constraint directions both decrease, with an increasing level of initial porosity, as the elastic compliance of the porous elastomer increases. Fig. (5b) shows that the dilatation of the porous elastomer increases with increasing initial porosity, as the porous elastomer is able to accommodate larger volumetric strains through void growth. The stress-strain response (Fig. 5a) of the constitutive model is in excellent agreement with the cell model results, both in the

may approach a limiting extensibility and "lock". Since the matrix material itself is incompressible, this would cause an upturn in the predicted macroscopic hydrostatic stress. If the volumetric strain level associated with such a "macroscopic locking" precedes the limit point observed in the case of a non-locking material, such as the present Neo-Hookean matrix, the latter limit point may be eliminated altogether.

axial and constraint directions, for all studied values of initial porosity, f_0. The lowest initial void volume fraction, $f_0 = 0.05$, provides the best agreement.

Fig. (5b) shows the evolution of volumetric strain with applied deformation. As the material extends in the axial direction, it contracts in the free direction, which corresponds to a negative strain. The volumetric strain, in the case of plane strain tension (Fig. 5b), is the sum of the axial strain and the strain associated with the lateral contraction,

$$\ln \overline{J} = \overline{E}_A + \overline{E}_L, \tag{35}$$

where $\overline{E}_A = \ln \overline{\lambda}_A$ and $\overline{E}_L = \ln \overline{\lambda}_L$. The dilatational response of the constitutive model is in reasonable agreement with the cell model predictions over the studied range of void volume fractions and deformations. The evolution of lateral strain in the free direction (Fig. 5b) is predicted well for the lowest initial void volume fraction, $f_0 = 0.05$, but there is an increasing discrepancy between the constitutive model predictions and the cell model predictions as the initial void volume fraction increases. The largest discrepancy occurs at the highest level of macroscopic axial strain, $\overline{E}_A = 1.1$, in the case of $f_0 = 0.25$, where the difference between the lateral strain prediction of the constitutive model and that of the cell model is $\overline{E}_L^{const} - \overline{E}_L^{cell} \simeq 0.1$.

As mentioned previously, the constitutive model accounts for the pore-shape anisotropy accompanying void growth. Under a non-hydrostatic state of deformation, the voids assume the shapes of ellipsoids. Eq. (11), evaluated on the inside of the sphere where $X_i = A = Bf_0^{1/3}$, shows that the ratios between the principal axes of the ellipsoidal voids, $\{a_1, a_2, a_3\}$, are identical to the ratios between the macroscopic principal stretches,

$$\frac{a_j}{a_i} = \frac{\overline{\lambda}_j}{\overline{\lambda}_i}, \tag{36}$$

where a_i and a_j are any two of the principal axes of the ellipsoidal void. By using the fact that the matrix material is incompressible, the current size and shape of the

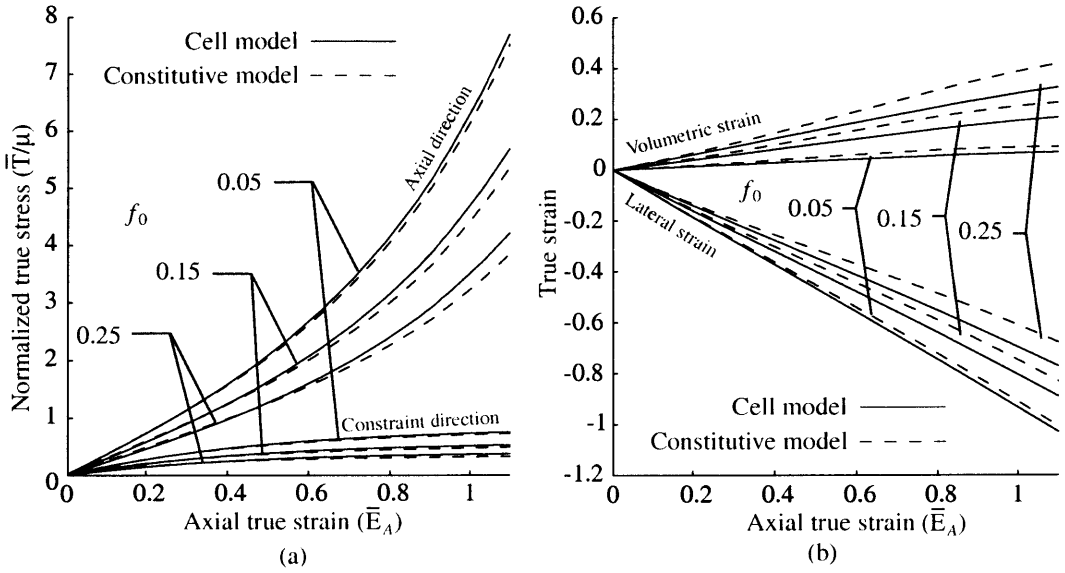

Figure 5: Plane strain tension. (- -) Constitutive model predictions, (-) RVE predictions.

void can be expressed in terms of the macroscopic state of deformation,

$$\overline{\alpha}_i = \overline{\lambda}_i \left(\frac{\eta}{\overline{J}} \right)^{1/3}, \tag{37}$$

where $\overline{\alpha}_i = a_i / f_0^{1/3}$ is a measure of stretch of the ellipsoidal void in the ith principal direction. Eq. (37) shows that in the case of plane strain tension, discussed previously, the void expands also in the direction of constraint in order to accommodate the macroscopic (positive) volumetric strain, $\ln \overline{J} > 0$.

5 Conclusions

A large-strain continuum mechanics framework for the development of constitutive models for porous hyperelastic materials was presented. The framework is applicable to any type of stretch-invariant based, or principal-stretch based isotropic hyperelastic matrix material which obeys pointwise incompressibility, such as the Neo-Hookean, Mooney-Rivlin, Ogden and eight-chain material models for rubber elasticity. An ini-

tially spherical unit cell was taken to represent the initial porous material, and the strain energy density function for the unit cell was derived and expressed in terms of the matrix properties, the initial porosity and the applied macroscopic deformation. The example case of a Neo-Hookean matrix material was studied, and a constitutive model using this matrix material was derived using virtual work arguments. The model accounts for the finite straining of the matrix, and the non-spherical growth of voids in the matrix which is expected under deviatoric states of deformation. Predictions of the constitutive model were compared to predictions of a numerical three-dimensional micromechanical cell model using the same matrix properties. The agreement between the models was good for a range of void volume fractions and load cases. The constitutive model successfully predicted the non-spherical void growth accompanying the evolving matrix anisotropy.

The studied load cases were all tensile in nature. Under small to moderate compressive deformations, the model will also be applicable. However, deformation events such as local buckling of matrix ligaments would be anticipated to occur as compressive deformations become large, especially in the case of high levels of porosity. Such phenomena are not accounted for in the present model. It is therefore doubtful that the application of the developed framework to large compressive deformations, at high levels of porosity, will be successful.

The example case concerned a specific matrix material model, the Neo-Hookean material model. The strain energy density in this model is a simple linear function of the first invariant of stretch, I_1 (Eq. 21). By using this matrix material model, it was possible to derive an analytical expression for the strain energy density in the spherical unit cell (Eq. 22). An analytical stress-strain relationship was then extracted through straight-forward differentiation of the strain energy density function with respect to the macroscopically-applied deformation (Eq. 26). In cases where the functional form of the pointwise strain energy density function is more complicated, such as in the eight-chain model, numerical quadrature may be required to obtain a stress-strain relationship for the porous material. Details on the numerical quadrature in such cases are outlined in Appendix A.

The developed framework can be extended to other classes of materials. For example, constitutive modeling of large-strain deformation of porous glassy polymers requires a constitutive description of the orientation hardening associated with plastic flow. For non-voided glassy polymers, the orientation hardening has been successfully treated within the context of rubber elasticity (e.g., Arruda and Boyce (1993)). The present framework therefore provides a means of approximating the average orientation hardening of *porous* glassy polymers, in which the behavior of the matrix is given, albeit neglecting specifics regarding the localized and propagating aspects of plastic deformation in the matrix. Such investigations are underway, and the results will be reported elsewhere (Danielsson et al. (2003b)).

6 Acknowledgments

This work was supported by the MIT Center for Materials Science and Engineering (CMSE), NSF MRSEC Grant No. DMR-98-08941.

References

Arruda, E. M., Boyce, M. C., 1993. Evolution of plastic anisotropy in amorphous polymers during finite straining. Int. J. Plasticity. 9 (6), 697–720.

Benveniste, Y., 1987. A new approach to the application of Mori-Tanaka's theory in composite materials. Mech. Mater. 6, 147–157.

Blatz, P. J., Ko, W. L., 1962. Application of finite elastic theory to the deformation of rubbery materials. Trans. Soc Rheol. 6, 223–251.

Boyce, M. C., Arruda, E. M., 2000. Constitutive models of rubber elasticity: A review. Rubber Chem. Tech. 73, 504–523.

Budiansky, B., 1965. On the elastic moduli of some heterogeneous materials. J. Mech. Phys. Solids 13, 223–227.

Danielsson, M., June 2003. Micromechanics, Macromechanics and Constitutive Modeling of the Elasto-Viscoplastic Deformation of Rubber-Toughened Glassy Polymers. Ph.D. thesis, Massachusetts Institute of Technology.

Danielsson, M., Boyce, M. C., Parks, D. M., 2003a. Micromechanical modeling of porous glassy polymers: The effects of a random microstructure. Under preparation; to be submitted for journal publication .

Danielsson, M., Parks, D. M., Boyce, M. C., 2003b. A constitutive model for the ductile behavior of voided glassy polymers. Under preparation; to be submitted for journal publication .

Gibson, L. J., Ashby, M. F., 1997. Cellular solids. Cambridge University Press, Cambridge, UK.

Gurson, A. L., 1977. Continuum theory of ductile rupture by void nucleation and growth: Part I – Yield criteria and flow rules for porous ductile media. ASME Trans., J. Eng. Mater. Technol. 99 Ser. H 1, 2–15.

Haghi, M., Anand, L., 1991. Analysis of strain-hardening viscoplastic thick-walled sphere and cylinder under external pressure. Int. J. Plasticity 7, 123–140.

Hill, R., 1965. A self-consistent mechanics of composite materials. J. Mech. Phys. Solids 13, 213–222.

Hou, H., Abeyaratne, R., 1992. Cavitation in elastic and elastic-plastic solids. J. Mech. Phys. Solids 40 (3), 571–592.

Kakavas, P. A., 2002. Influence of the cavitation on the stress-strain fields of compressible Blatz-Ko materials at finite deformation. Int. J. Solids Struct. 39, 783–795.

Kasner, A. I., Meinecke, E. A., 1996. Porosity in rubber, a review. Rubber Chem. Tech. 69, 424–443.

Malvern, L. E., 1969. Introduction to the mechanics of a continuous medium. Prentice-Hall, Englewood Cliffs N.J.

Mori, T., Tanaka, K., 1973. Average stress in matrix and average elastic energy of materials with misfitting inclusions. Acta Metal. 21, 571–574.

Stroud, A. H., Secrest, D., 1966. Gaussian quadrature formulas. Prentice-Hall, Englewood Cliffs N.J.

A Numerical integration of the stress-strain relationship

In cases where the expression for the pointwise strain energy function is complicated[4], it may be necessary to integrate the stress-strain relationship for the porous material numerically. In this appendix, we outline the steps involved in this procedure.

The macroscopic left Cauchy-Green strain tensor, $\overline{\mathbf{B}}$, can be decomposed into an orthogonal rotation tensor, $\overline{\mathbf{Q}}$ and a diagonal tensor $\tilde{\overline{\mathbf{B}}}$, as

$$\overline{\mathbf{B}} = \overline{\mathbf{Q}}\,\tilde{\overline{\mathbf{B}}}\,\overline{\mathbf{Q}}^T, \tag{38}$$

where $\tilde{\overline{\mathbf{B}}}$ is the macroscopic principal left Cauchy-Green strain tensor. The diagonal components of $\tilde{\overline{\mathbf{B}}}$ are expressed in terms of the macroscopically-applied stretches, $\overline{\lambda}_i$, as

$$[\tilde{\overline{\mathbf{B}}}]_i = \overline{\lambda}_i^2. \tag{39}$$

Since the principal directions of the macroscopic Cauchy stress tensor, $\overline{\mathbf{T}}$, and the macroscopic left Cauchy-Green strain tensor, $\overline{\mathbf{B}}$, coincide, the latter may be decomposed as,

$$\overline{\mathbf{T}} = \overline{\mathbf{Q}}\,\tilde{\overline{\mathbf{T}}}\,\overline{\mathbf{Q}}^T, \tag{40}$$

where $\tilde{\overline{\mathbf{T}}}$ is the macroscopic principal Cauchy stress tensor. By combining Eqs. (20), (38) and (40), the macroscopic principal Cauchy stress tensor can be expressed as

$$\tilde{\overline{\mathbf{T}}} = \frac{2}{\overline{J}}\,\overline{\mathbf{Q}}^T \frac{\partial \overline{W}}{\partial \overline{\mathbf{B}}}\,\overline{\mathbf{Q}}\,\overline{\mathbf{Q}}^T\,\overline{\mathbf{B}}\,\overline{\mathbf{Q}} = \frac{2}{\overline{J}} \frac{\partial \overline{W}}{\partial \tilde{\overline{\mathbf{B}}}}\,\tilde{\overline{\mathbf{B}}}. \tag{41}$$

[4]For example, if the strain energy density of the matrix material is expressed in terms of higher order terms and/or exponential terms of either stretch invariants (Eq. 17) or principal stretches (Eq. 18), the closed-form integration of the matrix strain energy density over the spherical domain may be cumbersome.

Using Eq. (41), the diagonal components, $[\tilde{\overline{\mathbf{T}}}]_i$, of the macroscopic principal Cauchy stress tensor, $\tilde{\overline{\mathbf{T}}}$, are then expressed as

$$[\tilde{\overline{\mathbf{T}}}]_i = \left[\frac{2}{\overline{J}}\frac{\partial \overline{W}}{\partial \tilde{\overline{\mathbf{B}}}}\tilde{\overline{\mathbf{B}}}\right]_i = \frac{2}{\overline{J}}\frac{\partial \overline{W}}{\partial(\overline{\lambda}_i^2)}\overline{\lambda}_i^2 = \frac{\overline{\lambda}_i}{\overline{J}}\frac{\partial \overline{W}}{\partial \overline{\lambda}_i} \quad \text{(no sum on } i\text{)}. \tag{42}$$

By using Eqs. (42) and (19), the components of the macroscopic principal Cauchy stress tensor can, in the case of a stretch-invariant based matrix material, be expressed as

$$[\tilde{\overline{\mathbf{T}}}]_i = \frac{\overline{\lambda}_i}{\overline{J}V_0}\int_{Bf_0^{1/3}}^{B}\int_0^{2\pi}\int_0^{\pi}\left(\frac{\partial \hat{W}}{\partial I_1}\frac{\partial I_1}{\partial \overline{\lambda}_i} + \frac{\partial \hat{W}}{\partial I_2}\frac{\partial I_2}{\partial \overline{\lambda}_i}\right) R^2 \sin\Theta \, \mathrm{d}\Theta \, \mathrm{d}\Phi \, \mathrm{d}R. \tag{43}$$

In the case of a principal-stretch based matrix material, this integral becomes

$$[\tilde{\overline{\mathbf{T}}}]_i = \frac{\overline{\lambda}_i}{\overline{J}V_0}\int_{Bf_0^{1/3}}^{B}\int_0^{2\pi}\int_0^{\pi}\left(\frac{\partial \hat{W}}{\partial \lambda_1}\frac{\partial \lambda_1}{\partial \overline{\lambda}_i} + \frac{\partial \hat{W}}{\partial \lambda_2}\frac{\partial \lambda_2}{\partial \overline{\lambda}_i} + \frac{\partial \hat{W}}{\partial \lambda_3}\frac{\partial \lambda_3}{\partial \overline{\lambda}_i}\right) R^2 \sin\Theta \, \mathrm{d}\Theta \, \mathrm{d}\Phi \, \mathrm{d}R. \tag{44}$$

The integrals in Eqs. (43) and (44) can be evaluated numerically using an appropriate numerical quadrature rule, such as Gauss-Legendre quadrature (Stroud and Secrest (1966)). Details on the choice of a suitable quadrature rule, as well as suitable order of quadrature for each of the variables $\{\Theta, \Phi, R\}$ will be reported elsewhere (Danielsson et al. (2003b)). The macroscopic Cauchy stress tensor, $\overline{\mathbf{T}}$, can be readily obtained through the rotation of $\tilde{\overline{\mathbf{T}}}$ by $\overline{\mathbf{Q}}$ (Eq. 40).

Bibliography

[1] ABAQUS Inc., Pawtucket, R.I., USA. *ABAQUS Reference manuals.*

[2] L. Anand. On Hencky's approximate strain-energy function for moderate deformations. *J. Appl. Mech*, 46:78–82, 1979.

[3] L. Anand and M. Kothari. A computational procedure for rate-independent crystal plasticity. *J. Mech. Phys. Solids.*, 44(4):525–558, 1996.

[4] A. S. Argon. A theory for the low-temperature plastic deformation of glassy polymers. *Philos. Mag.*, 28:839–865, 1973.

[5] A. S. Argon and R. E. Cohen. Toughenability of polymers. *Submitted to Polymer for publication.*, 2003.

[6] E. M. Arruda. *Characterization of the strain hardening response of amorphous polymers.* PhD thesis, M.I.T., 1992.

[7] E. M. Arruda and M. C. Boyce. Evolution of plastic anisotropy in amorphous polymers during finite straining. *Int. J. Plasticity*, 9(6):697–720, 1993.

[8] E. M. Arruda and M. C. Boyce. A three-dimensional constitutive model for the large stretch behavior of rubber elastic materials. *J. Mech. Phys. Solids*, 41(2):389–412, 1993.

[9] U. D. Baumann. The role of particle cavitation in the toughening of polymers. Master's thesis, M.I.T., 1998.

[10] Y. Benveniste. A new approach to the application of Mori-Tanaka's theory in composite materials. *Mech. Mater*, 6:147–157, 1987.

[11] M. C. Boyce, E. L. Montagut, and A. S. Argon. The effects of thermomechanical coupling on the cold drawing process of glassy polymers. *Polym. Eng. Sci.*, 32(16):1073–1085, August 1992.

[12] M. C. Boyce, D. M. Parks, and A. S. Argon. Large inelastic deformation of glassy polymers. part 1: Rate dependent constitutive model. *Mech. Mater.*, 7(1):15–33, 1988.

[13] M. C. Boyce, G. G. Weber, and D. M. Parks. On the kinematics of finite strain plasticity. *J. Mech. Phys. Solids*, 37(5):647–665, 1989.

[14] C. B. Bucknall. *Toughened Plastics.* Applied Science Publishers Ltd. London, 1977.

[15] C. B. Bucknall. Applications of microscopy to the deformation and fracture of rubber-toughened polymers. *J. of Microsc.-Oxford*, 201(2):221–229, 2001.

[16] C. B. Bucknall and R. R. Smith. Stress-whitening in high-impact polystyrenes. *Polymer*, 6(8):437–446, 1965.

[17] B. Budiansky. On the elastic moduli of some heterogeneous materials. *J. Mech. Phys. Solids*, 13:223–227, 1965.

[18] C. Cheng, N. Peduto, A. Hiltner, E. Baer, P.R. Soskey, and S.G. Mylonakis. Comparison of some butadiene-based impact modifiers for polycarbonate. *J. Appl. Polym. Sci.*, 53:513–525, 1994.

[19] A. C. F. Cocks. Inelastic deformation of porous materials. *J. Mech. Phys. Solids.*, 37(6):693–715, 1989.

[20] M. E. Cruz and A. T. Patera. A parallel Monte-Carlo finite-element procedure for the analysis of multi-component random media. *Int. J. Numer. Meth. Eng.*, 38:1087–1121, 1995.

[21] M. Danielsson, D. M. Parks, and M. C. Boyce. Three-dimensional micromechanical modeling of voided polymeric materials. *J. Mech. Phys. Solids*, 50(2):351–379, 2002.

[22] M. Danielsson, D. M. Parks, and M. C. Boyce. Constitutive modeling of porous hyperelastic materials. *Accepted for publication in Mech. Mater.*, 2003.

[23] M. W. Dib and G. J. Rodin. Three-dimensional analysis of creeping polycrystals using periodic arrays of truncated octahedra. *J. Mech. Phys. Solids*, 41(4):725–747, 1993.

[24] A. R. Duckett, editor. *11th international conference on deformation, yield and fracture of polymers.* IOM Communications, 2000.

[25] J. M. Duva and J. W. Hutchinson. Constitutive potentials for dilutely voided non-linear materials. *Mech. Mater.*, 3:41–54, 1984.

[26] H. J. Eyring. Viscosity, plasticity and diffusion as examples of absolute reaction rates. *J. Chem. Phys.*, 4:283–291, 1936.

[27] B. P. Gearing. *Constitutive equations and failure criteria for amorphous polymeric materials.* PhD thesis, Massachusetts Institute of Technology, 2002.

[28] B. P. Gearing and L. Anand. Notch-sensitive fracture of polycarbonate. *Submitted to Int. J. Solids Struct. for publication.*, 2003.

[29] S. Ghosh, K. Lee, and S. Moorthy. Two scale analysis of heterogeneous elastic-plastic materials with asymptotic homogenization and voronoi cell finite element model. *Comput. Methods Appl. Mech. Engrg.*, 132:63–116, 1996.

[30] C. G'Sell and J. J. Jonas. Determination of the plastic behaviour of solid polymers at constant true strain rate. *J. Mater. Sci.*, 14:583–591, 1979.

[31] A. L. Gurson. Continuum theory of ductile rupture by void nucleation and growth: Part 1 - yield criteria and flow rules for porous ductile media. *ASME Trans., J. Eng. Mater. Technol.*, 99 Ser. H 1:2–15, 1977.

[32] M. Haghi and L. Anand. A constitutive model for isotropic, porous elasto-viscoplastic metals. *Mech. Mater.*, 13:37–53, 1991.

[33] R. N. Haward and G. Thackray. The use of a mathematical model to describe isothermal stress-strain curves in glassy thermoplastics. *Proc. Roy. Soc. A*, 302:453–472, 1968.

[34] R. Hill. A self-consistent mechanics of composite materials. *J. Mech. Phys. Solids*, 13:213–222, 1965.

[35] H. S. Hou and R. Abeyaratne. Cavitation in elastic and elastic plastic solids. *J. Mech. Phys. Solids.*, 40(3):571–592, 1992.

[36] J. W. Hutchinson. Bounds and self-consistent estimates for creep of polycrystalline materials. *Proc. Roy. Soc. London*, 348(1652):101–127, 1976.

[37] H. Hyakutake and H. Nisitani. Conditions for ductile and brittle fracture in notched polycarbonate bars. *JSME Int. J.*, 30(259):29–36, 1987.

[38] M. D. Johnson. Deformation and fracture of polycarbonate and rubber-modified polycarbonate under controlled temperature, deformation rate, and notch stress triaxiality. Master's thesis, Massachusetts Institute of Technology, 2001.

[39] H. H. Kausch. *Polymer Fracture.* Springer-Verlag Berlin Heidelberg, 2nd edition, 1987.

[40] S.W. Kim, F.J. McGarry, and C.K. Riew. Enhanced polycarbonate toughness 2: Mechanisms. *Polym. Eng. Sci.*, 35(6):477–482, 1995.

[41] J. Koplik and A. Needleman. Void growth and coalescence in porous plastic solids. *Int. J. Solids Struct.*, 24(8):835–853, 1988.

[42] J. Lai and E. van der Giessen. A numerical study of crack-tip plasticity in glassy polymers. *Mech. Mater.*, 25:183–197, 1997.

[43] A. Lazzeri and C. B. Bucknall. Dilatational bands in rubber-toughened polymers. *J. Mater. Sci.*, 28(24):6799–6808, 1993.

[44] E. H. Lee. Elastic-plastic deformation at finite strains. *J. Appl. Mech.*, 36:1–6, 1969.

[45] P. A. Lovell, J. McDonald, D. E. J. Saunders, M. N. Sherratt, and R. J. Young. Mechanical properties of rubber-toughened poly(methyl methacrylate). *Plast. Rubb. Compos. Process. Appl.*, 16:37, 1991.

[46] J. T. Lutz and R. F. Grossman, editors. *Polymer modifiers and additives.* Marcel Dekker, Inc. New York, 2001.

[47] F. A. McClintock. A criterion for ductile fracture by the growth of holes. *J. Appl. Mech.*, 35:363–371, 1968.

[48] J. C. Michel and P. Suquet. The constitutive law of non-linear viscous and porous materials. *J. Mech. Phys. Solids.*, 40(4):783–812, 1992.

[49] C. Miehe, editor. *IUTAM Symposium on Computational Mechanics of Solid Materials at Large Strains.* Kluwer Academic Publications, 2001.

[50] T. Mori and K. Tanaka. Average stress in matrix and average elastic energy of materials with misfitting inclusions. *Acta. Metall.*, 21:571–574, 1973.

[51] R. P. Nimmer and J. T. Woods. An investigation of brittle failure in ductile notch-sensitive thermoplastics. *Polym. Eng. Sci.*, 32(16):1126–1137, 1992.

[52] M. Nygårds and P. Gudmundson. Micromechanical modeling of ferritic / pearlitic steels. *Mat. Sci. Eng. A-Struct.*, 325(1-2):435–443, 2002.

[53] M. Nygårds and P. Gudmundson. Three-dimensional periodic voronoi grain models and micromechanical fe-simulations of a two-phase steel. *Comp. Mater. Sci.*, 24(4):513–519, 2002.

[54] D. M. Parks, A. S. Argon, and B. Bagepalli. Large elastic-plastic deformation of glassy polymers, Part I: Constitutive modeling. Technical report, Department of Mechanical Engineering, MIT, March 1985.

[55] M. Parvin and J. G. Williams. Ductile-brittle transitions in polycarbonate. *Int. J. Fract.*, 11:963–972, 1975.

[56] K. G. W. Pijnenburg and E. Van der Giessen. Macroscopic yield in cavitated polymer blends. *Int. J. Solids Struct.*, 38:3575–3598, 2000.

[57] P. PonteCastañeda and J.R. Willis. On the overall properties of non-linearly viscous composites. *Proc. R. Soc. London*, A416:217–244, 1988.

[58] S. Quilici and G. Cailletaud. FE simulation of macro-, meso- and micro-scales in polycrystalline plasticity. *Comp. Mater. Sci.*, 16:383–390, 1999.

[59] G. Rodin and D. M. Parks. On constistency relations in nonlinear fracture mechanics. *J. Appl. Mech.*, 53:834–838, 1986.

[60] B. Rosen, editor. *Fracture processes in polymeric solids.* John Wiley and Sons, Inc. New York, 1964.

[61] J. Segurado and J. Llorca. A numerical approximation to the elastic properties of sphere-reinforced composites. *J. Mech. Phys. Solids.*, 50(10):2107–2121, 2002.

[62] R. J. M. Smit, W. A. M. Brekelmans, and H. E. H. Meijer. Prediction of the large-strain mechanical response of heterogeneous polymer systems: local and global deformation behaviour of a representative volume element of voided polycarbonate. *J. Mech. Phys. Solids*, 47(2):201–221, 1999.

[63] S. Socrate and M. C. Boyce. Micromechanics of toughened polycarbonate. *J. Mech. Phys. Solids*, 48(2):233–273, 2000.

[64] P. Sofronis and R. M. McMeeking. Creep of a power-law material containing spherical voids. *J. Appl. Mech.*, 59:S88–S95, 1992.

[65] A. C. Steenbrink, E. van der Giessen, and P. D. Wu. Void growth in glassy polymers. *J. Mech. Phys. Solids*, 45(3):405–437, 1997.

[66] A. H. Stroud and D. Secrest. *Gaussian quadrature formulas.* Prentice-Hall, Englewood Cliffs N.J., 1966.

[67] S. Torquato. *Random Heterogeneous Materials: Microstructure and Macroscopic Properties.* Springer Verlag New York, Inc., 2001.

[68] L. R. G. Treloar. *The physics of rubber elasticity.* Clarendon Press, Oxford, 1975.

[69] K. Tsuji, K. Iwase, and K. Ando. An investigation into the location of crack initiation sites in alumina, polycarbonate and mild steel. *Fatigue Fract. Engng. Mater. Struct.*, 22:509–517, 1999.

[70] V. Tvergaard. On localization in ductile materials containing spherical voids. *Int. J. Fracture*, 18(4):237–252, 1982.

[71] V. Tvergaard and A. Needleman. Analysis of the cup-cone fracture in a round tensile bar. *Acta Metall.*, 32:157–169, 1984.

[72] M. C. M. van der Sanden. *Ultimate toughness of amorphous polymers.* PhD thesis, Eindhoven University of Technology, 1993.

[73] J. A. W. van Dommelen. *Micromechanics of Particle-Modified Semicrystalline Polymers.* PhD thesis, Eindhoven University of Technology, 2003.

[74] J. A. W. van Dommelen, W. A. M. Brekelmans, and F. P. T. Baaijens. Micromechanical modeling of particle-toughening of polymers by locally induced anisotropy. *Mech. Mater.*, 35:845–863, 2003.

[75] M. C. Wang and E. J. Guth. Statistical theory of networks of non-Gaussian flexible chains. *J. Chem. Phys.*, 20:1144, 1952.

[76] E. Wigner and F. Seitz. On the constitution of metallic sodium. *Phys. Rev.*, 43:804–810, 1933.

[77] A. F. Yee. The yield and deformation behaviour of some polycarbonate blends. *J. Mater. Sci.*, 12:757–765, 1977.

[78] A. Zavaliangos and L. Anand. Thermo-elasto-viscoplasticity of isotropic porous metals. *J. Mech. Phys. Solids.*, 41(6):1087–1118, 1993.

[79] A. I. Zavaliangos. *Elasto-viscoplasticity of isotropic porous metals.* PhD thesis, M.I.T., 1992.

[80] S. N. Zhurkov. Kinetic concept of the strength of solids. *Int. J. Fract. Mech.*, 1:311–323, 1965.

[81] S. N. Zhurkov. Atomic mechanism for the destruction of stressed polymers. *Sov. Phys. Solid State*, 15(7):1379–1384, 1974.